NANYANG
TECHNOLOGICAL
UNIVERSITY
SINGAPORE

MAGNETIC SKYRMION
STABILIZATION, NUCLEATION, AND DYNAMICS ON MAGNETIC MULTILAYER THIN FILMS

CALVIN ANG CHING IAN

SCHOOL OF PHYSICAL AND MATHEMATICAL SCIENCES

2021

MAGNETIC SKYRMION STABILIZATION, NUCLEATION, AND DYNAMICS ON MAGNETIC MULTILAYER THIN FILMS

CALVIN ANG CHING IAN

SCHOOL OF PHYSICAL AND MATHEMATICAL SCIENCES

A thesis submitted to the Nanyang Technological
University in partial fulfilment of the requirement for the
degree of Doctor of Philosophy

2021

Statement of Originality

I hereby certify that the work embodied in this thesis is the result of original research done by me except where otherwise stated in this thesis. The thesis work has not been submitted for a degree or professional qualification to any other university or institution. I declare that this thesis is written by myself and is free of plagiarism and of sufficient grammatical clarity to be examined. I confirm that the investigations were conducted in accord with the ethics policies and integrity standards of Nanyang Technological University and that the research data are presented honestly and without prejudice.

1 AUG 2021

. . . .
Date

. . . .
CALVIN ANG CHING IAN

Supervisor Declaration Statement

I have reviewed the content and presentation style of this thesis and declare it of sufficient grammatical clarity to be examined. To the best of my knowledge, the thesis is free of plagiarism and the research and writing are those of the candidate's except as acknowledged in the Author Attribution Statement. I confirm that the investigations were conducted in accord with the ethics policies and integrity standards of Nanyang Technological University and that the research data are presented honestly and without prejudice.

5 Aug 2021

. . . .

Date

. . . .

PROF. LEW WEN SIANG

Authorship Attribution Statement

This thesis contains material from 3 paper(s) published in the following peer-reviewed journal in which I am listed as an author.

Chapter 5 is published as C. C. I. Ang, W. L. Gan, G. D. H. Wong, and W. S. Lew. Temperature-modulated magnetic skyrmion phases and transformations analysis from first-order reversal curve study. *Physical Review B* **103**, 144409 (2021). DOI: 10.1103/PhysRevB.103.144409

The contributions of the co-authors are as follows:

- I designed the experiment and prepared the manuscript drafts.
- Mr. Grayson Dao Hwee Wong assisted in sample fabrication.
- Dr. Weiliang Gan provided guidance in experimental setup and Kerr microscopy.
- Dr. Weiliang Gan, Mr. Grayson Dao Hwee Wong, and I analyzed the first-order reversal curve data.
- Prof. Lew Wen Siang supervised the study.
- All authors contributed to the discussion and preparation of the manuscript.

Chapter 6 is published as C. C. I. Ang, W. L. Gan, G. D. H. Wong, and W. S. Lew. Electrical Control of Skyrmion Density via Skyrmion-Stripe Transformation. *Physical Review Applied* **14**, 054048 (2020). DOI: 10.1103/PhysRevApplied.14.054048

The contributions of the co-authors are as follows:

- I designed the experiment and prepared the manuscript drafts.
- I performed the electrical characterization and Kerr microscopy with assistance by Dr. Weiliang Gan.
- Mr. Grayson Dao Hwee Wong assisted in electron beam lithography of the sample.
- Dr. Weiliang Gan, Mr. Grayson Dao Hwee Wong, and I analyzed the skyrmion transformation results.
- Prof. Lew Wen Siang supervised the study.

- All authors contributed to the discussion and preparation of the manuscript.

Chapter 7 is published as C. C. I. Ang, W. L. Gan, and W. S. Lew. Bilayer skyrmion dynamics on a magnetic anisotropy gradient. *New Journal of Physics* **21**, 043006 (2019). DOI: 10.1088/1367-2630/ab1171

The contributions of the co-authors are as follows:

- I co-designed the study with Dr Weiliang Gan.
- I performed the micromagnetic simulations on Mumax3.
- I developed the analytical model with help by Dr. Weiliang Gan.
- Prof. Lew Wen Siang supervised the study.
- All authors contributed to the discussion and preparation of the manuscript.

1 AUG 2021

. . . .
Date

. . . .
CALVIN ANG CHING IAN

Abstract

Magnetic skyrmions are particle-like nanoscale magnetic structures currently surging in interest in the spintronics field. Their small size combined with topological stability and efficient manipulation by various electromagnetic excitations make them promising next-generation high-density information carriers. Beyond data storage and memory applications, the diverse magnetic skyrmion interactions and excitations can be further exploited for conventional logic computing and unconventional computing like neuromorphic, probabilistic, and Brownian computing. Skyrmion research is advancing on many fronts to bring these technological ideas into reality, including stabilisation in materials and conditions, reliable nucleation techniques, and precise control of magnetic skyrmions.

In this thesis, the spin texture evolution between the labyrinth, stripe, skyrmion, and ferromagnetic states in magnetic multilayer $[Pt/Co/Fe/Ir]_2$ under the first-order reversal curve (FORC) magnetic field sweeps was investigated. Temperature modulation was performed to tune skyrmion phases and acquire their corresponding FORC signatures. Using magneto-optical Kerr microscopy, an analysis technique based on the sweeping field was developed and applied in the derivation of the skyrmion phase. A technique for skyrmion nucleation and deletion by current density modulation independent of current polarity in magnetic multilayer $[Pt/Co/Fe/Ir]_2$ was demonstrated. A high current density induces the nucleation of skyrmions via spin-orbit torque acting on defects. In contrast, the low current density causes a volatile skyrmion-stripe transformation at pinning sites that annihilates other skyrmions. A voltage-induced magnetic skyrmion motion based on voltage-controlled magnetic anisotropy gradients was investigated towards a more energy-efficient skyrmion propagation technique. The dynamics of synthetic antiferromagnetic skyrmions on a magnetic anisotropy gradient was investigated numerically, and an analytical model was developed to describe their motion accurately.

Acknowledgements

I am deeply grateful for the support, encouragement, and companionship given by everybody who had been part of my four-year-long PhD journey.

I would like to thank my supervisor, Prof. Lew Wen Siang, for recognising my abilities and granting me the opportunity to pursue research in his group. He supported me since my involvement in URECA 2014/2015 and URECA-FYP 2016/2017 as an undergraduate. He provided valuable guidance and direction to my work during the ups and downs of this whole journey.

I would like to thank my mentor, Dr. Gan Weiliang, who kickstarted my journey into research ever since my undergraduate years and continued to support me throughout my PhD years. His technical expertise and deep knowledge in the field of spintronics leaves many in awe and was invaluable in overcoming many of the setbacks faced. It had been a great privilege to had worked alongside him.

I would like to thank Dr. Gerard Joseph Lim, who entertained my endless questions and led me through the complete ins and outs of almost every piece of equipment in the laboratory. He was the most reliable and adaptive person around; all sorts of odd issues and breakdowns can be resolved with his assistance. His extensive knowledge beyond spintronics also offered valuable insights and discussions.

I would like to thank my peer, Grayson Wong Dao Hwee, who also started his PhD at the same time. We ploughed through the years, watching each other's back and lending a helping hand whenever needed. Also, the invaluable companionship for the countless dinners and breaks with the rest.

I would like to wholeheartedly thank all the members of our group, past and present, who made the moments outside of research ever so fun and enjoyable. There are my graduated seniors, Dr. Tan Funan, Dr. Putu Andhita Dananjaya, Dr. Law Wai Cheung, Dr. Shawn Wong De Wei, Dr. Jin Tianli, Dr. Desmond Loy Jia Jun, and Dr. Shane Wong Qi Ying. Also, my juniors, Birte Coester, Samuel Chow Chen Wai, Ang Jia Min, Liu Lingli, Chee Mun Yin, Hou Kunqi, Poh Han Yin, Thong Jia Rui, Calvin Lee Xiu Xian, and Wu Shuo. The ever-helpful

project officers Hoo Siew Wei, Zhong Xiaoyang, and Henry Kwang Yap Chuan. Several members on exchange at our laboratory, Dr. Xu Zhan, Prof. Wang Xuan, and Namita Bindal. Trainees who joined us a year ago, Eugene Koh Chin Sing, and Zhou Sunzhong. Everybody, in one way or another, perhaps even unknowingly, helped me catch an extra breath.

Finally, I would like to thank my family for their unwavering support.

Table of Contents

Acronyms

AC	Alternating Current
AHE	Anomalous Hall Effect
ANE	Anomalous Nernst Effect
AO-HDS	All-Optical Helicity Dependent Switching
BDMI	Bulk Dzyaloshinskii-Moriya Interaction
CW	Clockwise
CCW	Counterclockwise
DC	Direct Current
DDI	Dipole-Dipole Interaction
DMI	Dzyaloshinskii-Moriya Interaction
DP	Depinned state
DPC	Differential Phase Contrast
EBL	Electron Beam Lithography
FFT	Fast Fourier Transform
FM	Ferromagnet
FORC	First-order Reversal Curve
HM	Heavy Metal
HTST	Harmonic Transition State Theory
IBE	Ion Beam Etching
IC	Incommensurate spin state
IDMI	Interfacial Dzyaloshinskii-Moriya Interaction
IF	Integrate-and-Fire
IMA	In-Plane Magnetic Anisotropy
IP	In-Plane
IPA	Isopropanol
LIF	Leaky Integrate-and-Fire
LLG	Landau-Lifshitz Gilbert
LTEM	Lorentz Transmission Electron Microscopy
MAG	Magnetic Anisotropy Gradient
MFM	Magnetic Force Microscopy
MIBK	Methyl Isobutyl Ketone
MOKE	Magneto-optical Kerr Effect
MTJ	Magnetic Tunnel Junction

NCMR	Non-Collinear MagnetoResistance
NDD	Nonreciprocal Directional Dichroism
NV-SPM	Nitrogen-Vacancy Scanning Probe Microscopy
OHE	Ordinary Hall Effect
PID	Proportional-Integral-Derivative
PMA	Perpendicular Magnetic Anisotropy
PMMA	Polymethyl methacrylate
REXS	Resonant Elastic X-ray Scattering
RF	Radio Frequency
RKKY	Ruderman-Kittel-Kasuya-Yosida
SAF	Synthetic AntiFerromagnet
SANS	Small-Angle Neutron Scattering
SAW	Surface Acoustic Wave
SEM	Scanning Electron Microscopy
SEMPA	Scanning Electron Microscopy with Polarization Analysis
SHE	Spin Hall Effect
SIMS	Secondary Ion Mass Spectrometer
SKHE	Skyrmion Hall Effect
SOT	Spin-Orbit Torque
SOC	Spin-Orbit Coupling
SPLEEM	Spin-Polarized Low-Energy Electron Microscopy
SP-STM	Spin-polarized Scanning Tunnelling Microscopy
SSVT	Single Stage Variable Temperature
STEM	Scanning Transmission Electron Microscopy
STT	Spin-Transfer Torque
STXM	Scanning Transmission X-ray Microscopy
THE	Topological Hall Effect
TMR	Tunneling MagnetoResistance
UHV	Ultra-High Vacuum
VCMA	Voltage-Controlled Magnetic Anisotropy
VSM	Vibrating Sample Magnetometer
XMCD	X-ray Magnetic Circular Dichroism
X-PEEM	X-ray Photoemission Electron Microscopy

Chapter 1 Introduction

1.1 Historical Advances

The idea of skyrmions originated from the field of particle physics back in 1961 by Tony Hilton Royle Skyrme[1-4]. In search of the fundamental structure of atoms and sub-atomic particles, Skyrme found the model of elementary particles being in some form of point-like objects unreasonable. He viewed these models as "*just a very good and useful way of enabling us to live with our ignorance of what really goes on at short distances*"[4]. As opposed to the forced discretized description of the atom, he mathematically demonstrated that the manifestation of particles in the form of topological solitons could be derived from a continuous field theory[3]. These topological solitons can be visualized as stable knots or singularities in a vector field that cannot smoothly unwind to annihilate and is named after Skyrme as skyrmions. The general concept of quantized, countable, and particle-like states emerging from continuous fields subsequently found applications in several other fields of physics, such as liquid crystals[5], Bose-Einstein condensates[6-8], quantum Hall magnets[9,10] and even cosmology[11,12].

In 1989, the same idea was extended to magnetism, where Bogdanov and Yablonskii first proposed stabilising the skyrmion structure in magnetic materias[13-15]. In magnets with non-centrosymmetric crystallography and the inhomogeneous relativistic exchange interaction, which was coined Dzyaloshinskii-Moriya interaction (DMI), can lower the skyrmion configuration's energy to be more energetically favourable than the uniform or the ferromagnetic state across a specific magnetic field range. In 2001, Bogdanov and Rößler predicted the stabilization of skyrmions in magnetic thin films and multilayers by interfacial DMI (IDMI) induced similarly by spin-orbit coupling (SOC) but with broken inverse symmetry at the interfaces[16]. The use of IDMI became a critical turning point that propelled the field of magnetic skyrmion research into the room temperature regime and gained the significant attention as potential nanoscale information carriers today.

A magnetic skyrmion can be visualized as a point of reversed magnetization in a perpendicular ferromagnetic state, with a finite radius where the magnetization gradually reverses in a chiral manner, as shown in Fig. 1.1. Two main types of magnetic skyrmions configurations are the Bloch skyrmions and the Néel skyrmions. The two configurations differ in how the magnetization vector rotates from its centre to the peripheral uniform state. A Bloch skyrmion is also known as the 'swirling' or 'vortex' configuration; its magnetization rotates perpendicular to the plane between the opposite magnetizations. A Néel skyrmion, referred to as the 'spiky' configuration, has its magnetization rotating parallel to the plane between the opposite magnetizations[17,18]. The magnetic skyrmion configuration is determined by the interactions and conditions stabilizing them and are not exclusively restricted to being either the Bloch or Néel; they can also be in intermediate states. In the simplest terms, the stabilization of magnetic skyrmions is realized by the competition between the interactions favouring in-plane (IP) or rotating magnetization and the interactions favouring perpendicular or ferromagnetic magnetization. Bloch skyrmions are generally stabilized by dipolar interaction and bulk-DMI (BDMI), while Néel skyrmions are mainly stabilized by IDMI. Detailed discussion on the stabilization of magnetic skyrmions is given in Chapter 3.1.

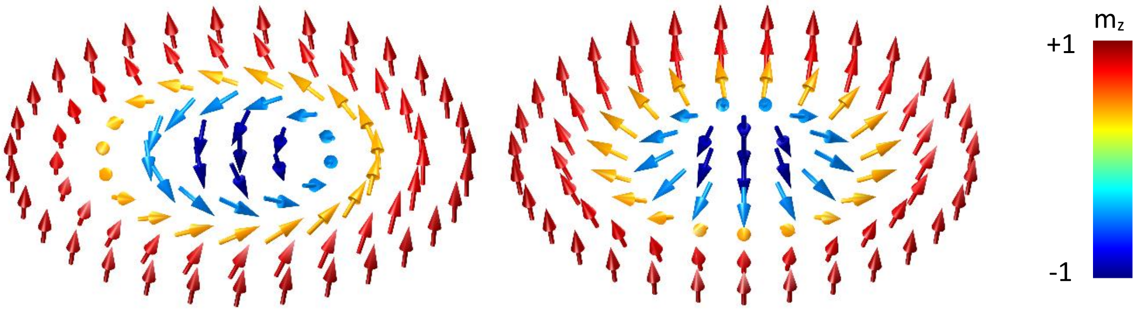

Figure 1.1| Two general magnetic skyrmion configurations: Bloch skyrmion (left) and Néel skyrmion (right).

In 2009, the first experimental evidence of magnetic skyrmions was published by Mühlbauer *et al.* in MnSi using neutron scattering data at low temperatures just below 30K[19]. The cubic B20 crystal structure of MnSi with the lack of space-inversion symmetry induces the chiral spin-orbit interaction, BDMI, favouring rotating or non-linear adjacent spins arrangement. Hence, the magnetic configuration of MnSi in the absence of a magnetic field is the helical structure with a chiral periodic rotating structure, as shown in Fig. 1.2(b). With a magnetic field, magnetization is tilted in the magnetic field direction and leads to the transition into the conical phase, as shown in Fig. 1.2(b). Magnetic skyrmions are stabilized in the range of conditions referred to as the A phase in Fig. 1.2(a). The small-angle neutron scattering (SANS) results at the A phase shown in Fig. 1.2(c) showed a consistent long-range sixfold intensity pattern perpendicular to the magnetic field regardless of the sample orientation, presenting the magnetic skyrmion lattice decoupled from the atomic lattice. Figure 1.2(d) gives the predicted real space magnetic configuration in the A phase without direct imaging. In work shortly after, the Hall effect measurement of MnSi in the A phase returned additional signal unaccounted for by the ordinary Hall effect or anomalous Hall effect[20] (AHE). The additional Hall voltage aligned closely with the expected magnitude of topological Hall effect (THE) from a chiral skyrmion lattice with the skyrmion density measured using SANS[19]. With both these works, the magnetic lattice configuration detected by SANS in MnSi was unambiguously identified to be the topological lattice of magnetic skyrmions.

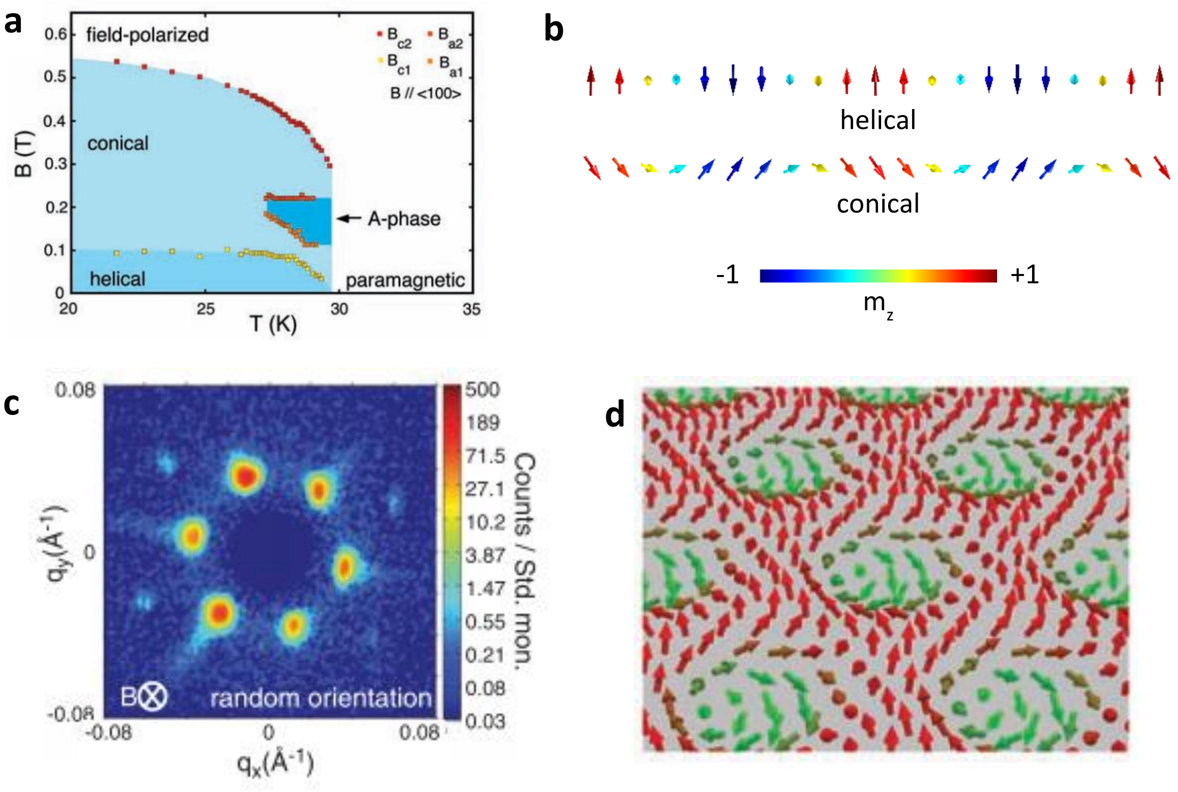

Figure 1.2| First experimental detection of magnetic skyrmions. (a) Magnetic configuration phase diagram across magnetic field and temperature[19]. (b) Helical and conical phase structure. (c) Sixfold neutron small-angle scattering intensity pattern in the A phase for random orientation of the sample[19]. (d) Real-space depiction of magnetic configuration in the A phase[19].

Skyrmion observation had been challenging and was only achieved approximately 20 years after its first proposal due to the stringent conditions required to stabilize them, as seen in Fig. 1.2(a). The A phase exists only in a small pocket of magnetic field and temperature. The stabilization of skyrmion requires the combination of DMI that is typically weak with a similarly weak Heisenberg exchange interaction. Hence, the A phase was found in materials with low Curie temperature like MnSi. Following the first skyrmion detection in MnSi[19-23], the discovery of magnetic skyrmions in many other materials with the same B20 crystal structure like FeGe[24-27], $Fe_{1-x}Co_xSi$[28-31], $Mn_xCo_{1-x}Si$[32,33], $Mn_{1-x}Fe_xGe$[34], and insulating multiferroic ferrimagnetic Cu_2OSeO_3[23,35-37].

The first direct real-space observation of magnetic skyrmions was performed by Yu *et. al.* using Lorentz transmission electron microscopy (LTEM) on $Fe_{0.5}Co_{0.5}Si$ thin film in 2010[29]. The LTEM images in Fig. 1.3(a) and (b) shows the IP spin configuration, essential in proving the topological nature of the circular domains, previously inaccessible using the combination of SANS[19] and Hall effect[20] results. The range of magnetic field and temperature stabilizing magnetic skyrmions was significantly widened for a thin film compared to its bulk, as shown in Fig. 1.3(c) due to substantially larger demagnetization effects[24,29].

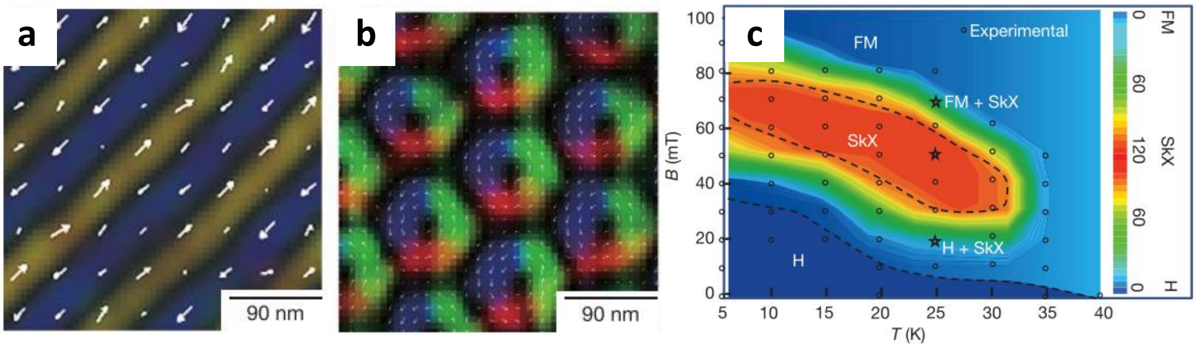

Figure 1.3| Experimental Lorentz transmission electron microscopy real-space images of (a) helical and (b) skyrmion crystal in $Fe_{0.5}Co_{0.5}Si$. (c) Phase diagram of magnetic structure in $Fe_{0.5}Co_{0.5}Si$.[29]

The milestone of magnetic skyrmion observation paved the way for exciting developments in scientific research of their topological properties and exploration for their possible technological applications. Abundant physics surrounding the stabilization of magnetic skyrmions and their emergent interactions arising from its topological structure with magnetic, electrical, thermal, mechanical, and even chemical remain to be explored. These early observations of magnetic skyrmions detected in material with B20 crystals presented several main challenges for technological applications. The stringent conditions required for stabilization with low Curie temperature, and narrow range of magnetic field and temperature, limits their viability for room-temperature devices.

Besides the investigation on skyrmion stability, early experiments on current-induced skyrmion motion revealed surprisingly low pinning current in the order of 10^6 A/m^2 for MnSi[25,38,39] and FeGe[26], giving them a stark advantage over domain walls that typically has a pinning current of 10^{11} A/m^2. The first experimental demonstration involved the current-induced rotation of the skyrmion lattice under a slight temperature gradient observed using SANS[38]. Further work using LTEM to image skyrmion motion in FeGe also showed similar order of pinning current[25]. A moving lattice of skyrmions induced an emergent electric field detectable via the Hall voltage[39] and revealed a similar pinning current of 10^6 A/m^2. The low pinning current in skyrmions further boosted their prospects as nanoscale information carriers over their close rival, domain wall. Even though skyrmions have significantly lower pinning current than domain walls, similar current densities are still required to drive both at comparable velocities[17].

1.2 Room-temperature magnetic skyrmions

The next milestone in magnetic skyrmion research was stabilising magnetic skyrmions in magnetic thin films and multilayers using IDMI at a heavy metal (HM) and ferromagnet (FM) interface. The IDMI strength induced at the HM/FM interface due to the strong SOC in the HM layer can be at the order of the exchange interaction sufficient to stabilize magnetic skyrmions at room temperature. Hence, the temperature ceiling limited by the Curie temperature of BDMI materials, typically in the tens of Kelvin, was overcome, and room-temperature magnetic skyrmions were made easily accessible.

Even though IDMI-stabilized magnetic skyrmions were first reported earlier in 2011 in monolayer Fe films on Ir(111) surface[40] and followed by PdFe bilayer on Ir(111) in 2013[41], these films were still required low temperatures and epitaxial film growth by molecular beam epitaxy, which was not suitable for industrial production. Beyond 2015, the range of material stabilizing magnetic skyrmion expanded by utilizing IDMI in HM/FM thin films and multilayers fabricated by sputtering, a fabrication technique already extensively used in the semiconductor industry. The variety in HM offered many opportunities to explore the different magnetic skyrmions stabilized using different combinations of HM/FM. Examples of HM/FM thin films include Ta/CoFeB/TaO[42], Ir/Co/Pt[43], Pt/Co/MgO[44], Pt/Co/Ta[45], Pt/CoFeB/MgO[45,46], Ta/CoFeB/MgO[47] and Pt/Co/Fe/Ir[48-50]. Two HM layers typically sandwich the FM layer to optimize IDMI, as seen in the list of examples.

The room temperature magnetic skyrmions in thin films and multilayers coupled with their production-ready fabrication technique, sputtering, the technological implementation of magnetic skyrmions were brought much closer within grasp. Opportunities to investigate magnetic skyrmions widen significantly with the relative ease in sputtering these materials and experiments being possible under ambient conditions instead of cryogenic ones. Skyrmion research quickly branched and progressed on all fronts to bring the first magnetic skyrmion based technological device, also referred to as skyrmionic devices, into reality. Thus, a complete understanding of the physical phenomena surrounding the properties and manipulation of skyrmions is necessary.

First, the most crucial criterion is the stability of the magnetic skyrmions. The HM/FM structure also provided an advantage on this front. Magnetic anisotropy, dipolar and DMI are all tunable by choice of material and their thickness. The tuning of these interactions can provide magnetic skyrmions of suitable stability for their desired applications. Different extent of skyrmion stability will determine the skyrmion phases between isolated skyrmions and skyrmion lattices. A new characterization technique of skyrmion phases using the first-order reversal curve distribution was introduced in this thesis and discussed in Chapter 6.

Second, a reliable technique of nucleating and annihilating single skyrmions will be crucial in most skyrmionic devices. The use of skyrmions as information carriers ideally utilize each skyrmion as a single bit of information instead of a cluster or lattice of skyrmions. Nucleation techniques pursued primarily use electrical current injections to integrate with electronics for control of the device[42,51-54]. Various other skyrmion nucleation techniques such as tilted magnetic fields[55-58], laser illumination[59-61], X-ray[62], electric field[63,64], and strain[65-67] were also explored. The demonstration of both skyrmion nucleation and annihilation using a unipolar current injection via skyrmion-stripe transformations and its mechanism is presented in Chapter 7 of this thesis.

Third, precise control and motion of magnetic skyrmions. Similar to nucleation techniques, electrical current injection is the primary method of choice to propagate skyrmions.

The HM/FM structure brings a complementary advantage for skyrmion propagation using spin-orbit torque (SOT) induced by spin current injection from the adjacent HM layer into the FM layer under an in-plane current injection. Even though SOT has better efficiency in driving skyrmions compared to just spin-transfer torque (STT) in the FM layer, the general use of electrical current remains energetically consuming and not ideal. Hence, a new approach to driving skyrmions using voltages instead of current was introduced to reduce skyrmionic devices' energy costs. In addition, skyrmion propagation also involves a special phenomenon induced by its topological configuration, the skyrmion Hall effect, where skyrmions travel with a transverse velocity relative to their driving force. The skyrmion Hall effect causes skyrmions to be driven towards the edges of nanotracks and annihilate at sufficiently high speeds. The synthetic antiferromagnet (SAF) structure for skyrmions was proposed to mitigate the skyrmion Hall effect using the restoring force between a pair of antiferromagnetically coupled skyrmions. Incorporating SAF skyrmions in a voltage-driven system, an analytical model for the dynamics of SAF skyrmions on a magnetic anisotropy gradient was developed and presented in Chapter 8 of this thesis.

Finally, a reliable detection technique for single or clusters of skyrmions is necessary. Typical electrical means of magnetic domain detection are magnetoresistance and Hall voltages. A magnetic tunnel junction (MTJ) structure fabricated above a segment along a nanotrack uses the change in tunnelling magnetoresistance (TMR) when a reversed domain is driven across it. Similarly, a Hall bar fabricated across a small segment along a nanotrack uses the change in Hall voltage due to AHE to detect the existence of reversed domains at its junction. A possible alternative to TMR is the tunnelling non-collinear magnetoresistance (NCMR) to simplify its structure by removing the need for a reference magnetic layer[68]. NCMR is a form of magnetoresistance induced by the non-collinearity of the spin structure of the skyrmion, i.e. the rotating segment of the skyrmion around its core. These detection techniques cannot directly prove the topological nature of the domain detected. The topological Hall effect (THE) is one technique that can definitively identify topological spin textures.

1.3 Objective of this thesis

This thesis aims to advance the understanding of magnetic skyrmions for the technological development of skyrmionic devices. Therefore, the objectives are tailored to investigate several key aspects and processes, including skyrmion stability, nucleation, annihilation, and motion, necessary for the functions of most skyrmionic devices. The main objectives of this thesis are as follows:

1) Develop a model skyrmion stability and phase characterization via the first-order reversal curve technique.

2) Demonstrate skyrmion nucleation and annihilation by unipolar current injection via current-induced skyrmion-stripe transformation.

3) Formulate a model for dynamics of synthetic antiferromagnetically coupled skyrmion motion on a magnetic anisotropy gradient.

The remainder of this thesis is organized as follows:

Chapter 2 provides background information that includes magnetism fundamentals, interactions, and dynamics helpful in understanding the rest of the thesis.

Chapter 3 discusses the literature review of magnetic skyrmions that includes skyrmion material, stabilization mechanism, nucleation, control, motion, and detection techniques applicable to skyrmionic technologies.

Chapter 4 describes the experimental techniques performed in this thesis, including sputtering, electron beam lithography, ion beam etching, vibrating sample magnetometry, magneto-optical Kerr microscopy, and electrical Hall resistance measurement.

Chapter 5 describes the numerical techniques employed for the micromagnetic simulation work on synthetic antiferromagnetically coupled skyrmion dynamics on a magnetic anisotropy gradient.

Chapter 6 presents the characterization of skyrmion phases and transformations based on the first-order reversal curve technique. Using temperature modulation to vary skyrmion stability and Kerr imaging, a new form of analysis of the first-order reversal curve diagram based on the sweeping field was introduced and applied in a model for skyrmion stability and phases.

Chapter 7 presents a new skyrmion density modulation technique driven by current density control. The reversible transformation between skyrmion and stripe domains induced by current injection was investigated, and their corresponding mechanisms were revealed.

Chapter 8 presents the analytical analysis of the synthetic antiferromagnetic skyrmion dynamics driven by a magnetic anisotropy gradient. The accuracy of the analytical expressions was supported by numerical results.

Chapter 9 summarizes this thesis's main findings and conclusions and proposes several future works on magnetic skyrmion towards technological development.

References

1 T. H. R. Skyrme & B. F. J. Schonland. A non-linear theory of strong interactions. *Proceedings of the Royal Society of London. Series A. Mathematical and Physical Sciences* **247**, 260-278, doi:doi:10.1098/rspa.1958.0183 (1958).

2 T. H. R. Skyrme & B. F. J. Schonland. A unified model of K- and π-mesons. *Proceedings of the Royal Society of London. Series A. Mathematical and Physical Sciences* **252**, 236-245, doi:doi:10.1098/rspa.1959.0149 (1959).

3 T. H. R. Skyrme & B. F. J. Schonland. A non-linear field theory. *Proceedings of the Royal Society of London. Series A. Mathematical and Physical Sciences* **260**, 127-138, doi:doi:10.1098/rspa.1961.0018 (1961).

4 T. H. R. Skyrme. The origins of skyrmions. *International Journal of Modern Physics A* **03**, 2745-2751, doi:10.1142/S0217751X88001156 (1988).

5 D. C. Wright & N. D. Mermin. Crystalline liquids: the blue phases. *Reviews of Modern Physics* **61**, 385-432, doi:10.1103/RevModPhys.61.385 (1989).

6 U. Al Khawaja & H. Stoof. Skyrmions in a ferromagnetic Bose-Einstein condensate. *Nature* **411**, 918-920, doi:10.1038/35082010 (2001).

7 U. A. Khawaja & H. T. C. Stoof. Skyrmion physics in Bose-Einstein ferromagnets. *Physical Review A* **64**, 043612, doi:10.1103/PhysRevA.64.043612 (2001).

8 T.-L. Ho. Spinor Bose Condensates in Optical Traps. *Phys. Rev. Lett.* **81**, 742-745, doi:10.1103/PhysRevLett.81.742 (1998).

9 S. L. Sondhi, A. Karlhede, S. A. Kivelson, *et al.* Skyrmions and the crossover from the integer to fractional quantum Hall effect at small Zeeman energies. *Phys. Rev. B* **47**, 16419-16426, doi:10.1103/PhysRevB.47.16419 (1993).

10 L. Brey, H. A. Fertig, R. Côté, *et al.* Skyrme Crystal in a Two-Dimensional Electron Gas. *Phys. Rev. Lett.* **75**, 2562-2565, doi:10.1103/PhysRevLett.75.2562 (1995).

11 R. Ouyed & M. Butler. Skyrmion Stars. *The Astrophysical Journal* **522**, 453-459, doi:10.1086/307618 (1999).

12 R. Durrer, M. Kunz & A. Melchiorri. Cosmic structure formation with topological defects. *Physics Reports* **364**, 1-81, doi:10.1016/S0370-1573(02)00014-5 (2002).

13 A. N. Bogdanov & D. A. Yablonskii. Thermodynamically stable "vortices" in magnetically ordered crystals. The mixed state of magnets *Soviet Physics Journal of Experimental and Theoretical Physics* **68**, 101-103 (1989).

14 A. Bogdanov & A. Hubert. Thermodynamically stable magnetic vortex states in magnetic crystals. *J. Magn. Magn. Mater.* **138**, 255-269, doi:10.1016/0304-8853(94)90046-9 (1994).

15 A. Bocdanov & A. Hubert. The Properties of Isolated Magnetic Vortices. *physica status solidi (b)* **186**, 527-543, doi:10.1002/pssb.2221860223 (1994).

16 A. N. Bogdanov & U. K. Rößler. Chiral Symmetry Breaking in Magnetic Thin Films and Multilayers. *Phys. Rev. Lett.* **87**, 037203, doi:10.1103/PhysRevLett.87.037203 (2001).

17 A. Fert, V. Cros & J. Sampaio. Skyrmions on the track. *Nat. Nanotech.* **8**, 152-156, doi:10.1038/nnano.2013.29 (2013).

18 X. Zhang, Y. Zhou, K. Mee Song, *et al.* Skyrmion-electronics: writing, deleting, reading and processing magnetic skyrmions toward spintronic applications. *Journal of Physics: Condensed Matter* **32**, 143001, doi:10.1088/1361-648x/ab5488 (2020).

19 S. Mühlbauer, B. Binz, F. Jonietz, *et al.* Skyrmion Lattice in a Chiral Magnet. *Science* **323**, 915, doi:10.1126/science.1166767 (2009).

20 A. Neubauer, C. Pfleiderer, B. Binz, *et al.* Topological Hall Effect in the A Phase of MnSi. *Phys. Rev. Lett.* **102**, 186602, doi:10.1103/PhysRevLett.102.186602 (2009).

21 A. Tonomura, X. Yu, K. Yanagisawa, *et al.* Real-Space Observation of Skyrmion Lattice in Helimagnet MnSi Thin Samples. *Nano Lett.* **12**, 1673-1677, doi:10.1021/nl300073m (2012).

22 Y. Li, N. Kanazawa, X. Z. Yu, *et al.* Robust Formation of Skyrmions and Topological Hall Effect Anomaly in Epitaxial Thin Films of MnSi. *Phys. Rev. Lett.* **110**, 117202, doi:10.1103/PhysRevLett.110.117202 (2013).

23 M. Mochizuki, X. Z. Yu, S. Seki, *et al.* Thermally driven ratchet motion of a skyrmion microcrystal and topological magnon Hall effect. *Nat. Mater.* **13**, 241-246, doi:10.1038/nmat3862 (2014).

24 X. Z. Yu, N. Kanazawa, Y. Onose, *et al.* Near room-temperature formation of a skyrmion crystal in thin-films of the helimagnet FeGe. *Nat. Mater.* **10**, 106-109, doi:10.1038/nmat2916 (2011).

25 X. Z. Yu, N. Kanazawa, W. Z. Zhang, *et al.* Skyrmion flow near room temperature in an ultralow current density. *Nat. Commun.* **3**, 988, doi:10.1038/ncomms1990 (2012).

26 S. X. Huang & C. L. Chien. Extended Skyrmion Phase in Epitaxial FeGe(111) Thin Films. *Phys. Rev. Lett.* **108**, 267201, doi:10.1103/PhysRevLett.108.267201 (2012).

27 N. Kanazawa, M. Kubota, A. Tsukazaki, *et al.* Discretized topological Hall effect emerging from skyrmions in constricted geometry. *Phys. Rev. B* **91**, 041122, doi:10.1103/PhysRevB.91.041122 (2015).

28 W. Münzer, A. Neubauer, T. Adams, *et al.* Skyrmion lattice in the doped semiconductor FeCoSi. *Phys. Rev. B* **81**, 041203, doi:10.1103/PhysRevB.81.041203 (2010).

29 X. Z. Yu, Y. Onose, N. Kanazawa, *et al.* Real-space observation of a two-dimensional skyrmion crystal. *Nature* **465**, 901-904, doi:10.1038/nature09124 (2010).

30 P. Milde, D. Köhler, J. Seidel, *et al.* Unwinding of a Skyrmion Lattice by Magnetic Monopoles. *Science* **340**, 1076-1080, doi:10.1126/science.1234657 (2013).

31 H. S. Park, X. Yu, S. Aizawa, *et al.* Observation of the magnetic flux and three-dimensional structure of skyrmion lattices by electron holography. *Nat. Nanotech.* **9**, 337-342, doi:10.1038/nnano.2014.52 (2014).

32 N. Kanazawa, Y. Onose, T. Arima, *et al.* Large Topological Hall Effect in a Short-Period Helimagnet MnGe. *Phys. Rev. Lett.* **106**, 156603, doi:10.1103/PhysRevLett.106.156603 (2011).

33 J. Kindervater, T. Adams, A. Bauer, *et al.* Evolution of magnetocrystalline anisotropies in $Mn_{1-x}Fe_xSi$ and $Mn_{1-x}Co_xSi$ as inferred from small-angle neutron scattering and bulk properties. *Phys. Rev. B* **101**, 104406, doi:10.1103/PhysRevB.101.104406 (2020).

34 K. Shibata, X. Z. Yu, T. Hara, *et al.* Towards control of the size and helicity of skyrmions in helimagnetic alloys by spin–orbit coupling. *Nat. Nanotech.* **8**, 723-728, doi:10.1038/nnano.2013.174 (2013).

35 S. Seki, X. Z. Yu, S. Ishiwata, *et al.* Observation of Skyrmions in a Multiferroic Material. *Science* **336**, 198, doi:10.1126/science.1214143 (2012).

36 T. Adams, A. Chacon, M. Wagner, *et al.* Long-Wavelength Helimagnetic Order and Skyrmion Lattice Phase in Cu2OSeO3. *Phys. Rev. Lett.* **108**, 237204, doi:10.1103/PhysRevLett.108.237204 (2012).

37 J. S. White, K. Prša, P. Huang, *et al.* Electric-Field-Induced Skyrmion Distortion and Giant Lattice Rotation in the Magnetoelectric Insulator Cu_2OSeO_3. *Phys. Rev. Lett.* **113**, 107203, doi:10.1103/PhysRevLett.113.107203 (2014).

38 F. Jonietz, S. Mühlbauer, C. Pfleiderer, *et al.* Spin Transfer Torques in MnSi at Ultralow Current Densities. *Science* **330**, 1648, doi:10.1126/science.1195709 (2010).

39 T. Schulz, R. Ritz, A. Bauer, *et al.* Emergent electrodynamics of skyrmions in a chiral magnet. *Nat. Phys.* **8**, 301-304, doi:10.1038/nphys2231 (2012).

40 S. Heinze, K. von Bergmann, M. Menzel, *et al.* Spontaneous atomic-scale magnetic skyrmion lattice in two dimensions. *Nat. Phys.* **7**, 713-718, doi:10.1038/nphys2045 (2011).

41 N. Romming, C. Hanneken, M. Menzel, *et al.* Writing and Deleting Single Magnetic Skyrmions. *Science* **341**, 636, doi:10.1126/science.1240573 (2013).

42 W. Jiang, P. Upadhyaya, W. Zhang, *et al.* Blowing magnetic skyrmion bubbles. *Science* **349**, 283, doi:10.1126/science.aaa1442 (2015).

43 C. Moreau-Luchaire, C. Moutafis, N. Reyren, *et al.* Additive interfacial chiral interaction in multilayers for stabilization of small individual skyrmions at room temperature. *Nat. Nanotech.* **11**, 444, doi:10.1038/nnano.2015.313 (2016).

44 O. Boulle, J. Vogel, H. Yang, *et al.* Room-temperature chiral magnetic skyrmions in ultrathin magnetic nanostructures. *Nat. Nanotech.* **11**, 449-454, doi:10.1038/nnano.2015.315 (2016).

45 S. Woo, K. Litzius, B. Krüger, *et al.* Observation of room-temperature magnetic skyrmions and their current-driven dynamics in ultrathin metallic ferromagnets. *Nat. Mater.* **15**, 501-506, doi:10.1038/nmat4593 (2016).

46 K. Litzius, I. Lemesh, B. Krüger, *et al.* Skyrmion Hall effect revealed by direct time-resolved X-ray microscopy. *Nat. Phys.* **13**, 170, doi:10.1038/nphys4000 (2016).

47 G. Yu, P. Upadhyaya, X. Li, *et al.* Room-Temperature Creation and Spin–Orbit Torque Manipulation of Skyrmions in Thin Films with Engineered Asymmetry. *Nano Lett.* **16**, 1981-1988, doi:10.1021/acs.nanolett.5b05257 (2016).

48 A. Soumyanarayanan, M. Raju, A. L. Gonzalez Oyarce, *et al.* Tunable room-temperature magnetic skyrmions in Ir/Fe/Co/Pt multilayers. *Nat. Mater.* **16**, 898-904, doi:10.1038/nmat4934 (2017).

49 M. Raju, A. Yagil, A. Soumyanarayanan, *et al.* The evolution of skyrmions in Ir/Fe/Co/Pt multilayers and their topological Hall signature. *Nat. Commun.* **10**, 696, doi:10.1038/s41467-018-08041-9 (2019).

50 C. C. I. Ang, W. Gan, G. D. H. Wong, *et al.* Temperature-modulated magnetic skyrmion phases and transformations analysis from first-order reversal curve study. *Phys. Rev. B* **103**, 144409, doi:10.1103/PhysRevB.103.144409 (2021).

51 G. Yu, P. Upadhyaya, Q. Shao, *et al.* Room-Temperature Skyrmion Shift Device for Memory Application. *Nano Lett.* **17**, 261-268, doi:10.1021/acs.nanolett.6b04010 (2017).

52 Z. Wang, X. Zhang, J. Xia, *et al.* Generation and Hall effect of skyrmions enabled using nonmagnetic point contacts. *Phys. Rev. B* **100**, 184426, doi:10.1103/PhysRevB.100.184426 (2019).

53 A. Hrabec, J. Sampaio, M. Belmeguenai, *et al.* Current-induced skyrmion generation and dynamics in symmetric bilayers. *Nat. Commun.* **8**, 15765, doi:10.1038/ncomms15765 (2017).

54 S. Finizio, K. Zeissler, S. Wintz, *et al.* Deterministic Field-Free Skyrmion Nucleation at a Nanoengineered Injector Device. *Nano Lett.* **19**, 7246-7255, doi:10.1021/acs.nanolett.9b02840 (2019).

55 S. Zhang, J. Zhang, Y. Wen, *et al.* Determination of chirality and density control of Néel-type skyrmions with in-plane magnetic field. *Commun. Phys.* **1**, 36, doi:10.1038/s42005-018-0040-5 (2018).

56 C. Wang, H. Du, X. Zhao, *et al.* Enhanced Stability of the Magnetic Skyrmion Lattice Phase under a Tilted Magnetic Field in a Two-Dimensional Chiral Magnet. *Nano Lett.* **17**, 2921-2927, doi:10.1021/acs.nanolett.7b00135 (2017).

57 Z. Qin, Y. Wang, S. Zhu, *et al.* Stabilization and Reversal of Skyrmion Lattice in Ta/CoFeB/MgO Multilayers. *ACS Applied Materials & Interfaces* **10**, 36556-36563, doi:10.1021/acsami.8b12694 (2018).

58 M. Li, A. Rai, A. Pokhrel, *et al.* Formation of zero-field skyrmion arrays in asymmetric superlattices. *Appl. Phys. Lett.* **117**, 112403, doi:10.1063/5.0024265 (2020).

59 T. Ogasawara, N. Iwata, Y. Murakami, *et al.* Submicron-scale spatial feature of ultrafast photoinduced magnetization reversal in TbFeCo thin film. *Appl. Phys. Lett.* **94**, 162507, doi:10.1063/1.3123256 (2009).

60 W. Koshibae & N. Nagaosa. Creation of skyrmions and antiskyrmions by local heating. *Nat. Commun.* **5**, 5148, doi:10.1038/ncomms6148 (2014).

61 M. Finazzi, M. Savoini, A. R. Khorsand, *et al.* Laser-Induced Magnetic Nanostructures with Tunable Topological Properties. *Phys. Rev. Lett.* **110**, 177205, doi:10.1103/PhysRevLett.110.177205 (2013).

62 Y. Guang, I. Bykova, Y. Liu, *et al.* Creating zero-field skyrmions in exchange-biased multilayers through X-ray illumination. *Nat. Commun.* **11**, 949, doi:10.1038/s41467-020-14769-0 (2020).

63 P.-J. Hsu, A. Kubetzka, A. Finco, *et al.* Electric-field-driven switching of individual magnetic skyrmions. *Nat. Nanotech.* **12**, 123-126, doi:10.1038/nnano.2016.234 (2017).

64 M. Schott, A. Bernand-Mantel, L. Ranno, *et al.* The Skyrmion Switch: Turning Magnetic Skyrmion Bubbles on and off with an Electric Field. *Nano Lett.* **17**, 3006-3012, doi:10.1021/acs.nanolett.7b00328 (2017).

65 M. Lee, W. Kang, Y. Onose, *et al.* Unusual Hall Effect Anomaly in MnSi under Pressure. *Phys. Rev. Lett.* **102**, 186601, doi:10.1103/PhysRevLett.102.186601 (2009).

66 R. Ritz, M. Halder, C. Franz, *et al.* Giant generic topological Hall resistivity of MnSi under pressure. *Phys. Rev. B* **87**, 134424, doi:10.1103/PhysRevB.87.134424 (2013).

67 T. Yokouchi, S. Sugimoto, B. Rana, *et al.* Creation of magnetic skyrmions by surface acoustic waves. *Nat. Nanotech.* **15**, 361-366, doi:10.1038/s41565-020-0661-1 (2020).

68 C. Hanneken, F. Otte, A. Kubetzka, *et al.* Electrical detection of magnetic skyrmions by tunnelling non-collinear magnetoresistance. *Nat. Nanotech.* **10**, 1039-1042, doi:10.1038/nnano.2015.218 (2015).

Chapter 2 Magnetism Background

This chapter provides the fundamental magnetic background helpful in understanding the remaining parts of the thesis. Readers with adequate magnetism background may proceed directly to Chapter 3 for the detailed review on magnetic skyrmions.

2.1 Magnetism

Magnets and magnetism are essential and integrated into many aspects of our lives today. In our homes, we have magnets used to hold notes on the refrigerator, keep cupboard doors closed firmly, and spin the fans' blades. There are also less visible but essential magnets in the speakers, microphones, and hard disk drives in our computers. In hospitals, we have magnetic resonance imaging that lets us image our internal organs safely and unintrusively. In our transport system, we have magnetically levitated high-speed trains achieved by letting go of the traditional wheel-based trains. Finally, the Earth is also a giant magnet; thus, we have magnetic compass needles aligning towards the geographical north pole.

We begin with an intuitive picture of magnetism close to our daily lives. From a typical first interaction with magnets like the disc refrigerator magnets, we can deduce that magnets are attracted to certain “magnetic” items like the refrigerator wall and paper clips but not other “non-magnetic” items like wooden furniture or brick wall. When playing around with a pair of magnets, one will quickly realise they not only attract but also repel against one another, depending on how you orientate them. Thus, there exist directionality or polarity in its behaviour. By adopting the directionality associated with the magnetic compass, the polarities are named the north and south poles. The attraction and repulsion arise from the alignment of opposite poles and like poles, respectively. However, both faces of the disc magnet are attracted to the refrigerator wall, regardless of polarity. This observation implies the idea of magnetic induction, where magnets can induce an opposite polarity on another “magnetic” material in proximity. In addition, these “magnetic” items like paper clips do not attract each other but are attracted to magnets. Hence, these magnetic properties seemingly can be created, changed, and annihilated.

While the attractive and repulsive magnetic properties can disappear at times, nothing is physically created or annihilated. A magnet consists of numerous microscopic magnets of atomic origin that form internally co-aligned fragments, referred to as domains. Depending on how all the domains are aligned, they can complement each other to exhibit magnetic forces or cancel each other to show no force, like that between paper clips. The disc magnets that show sturdy polarity and magnetic force are referred to as hard magnets. On the other hand, paper clips are referred to as soft magnets because an external magnetic field easily reorients their domains. Soft magnets also easily return to an unoriented state showing little to no magnetic force after the hard magnets are removed.

Beyond the simplistic categorization of "magnetic" and "non-magnetic" materials, all materials are magnetic in the sense that they exhibit a response under magnetic fields, just that the response may be minuscule and not easily observable. Materials can be categorized into five main categories: ferromagnet, ferrimagnet, antiferromagnet, diamagnet, and paramagnet[1,2]. Ferromagnets and ferrimagnets are the categories of materials associated with the layman's description of "magnetic" material due to their strong response to magnetic fields and easily observable magnetic forces. Ferromagnet and antiferromagnet describe the atomic magnetic moments' behaviour of favouring parallel and antiparallel alignment. The parallel alignment in ferromagnets complement each other to generate a larger total magnetic moment, and the opposite is true for antiferromagnets. Ferrimagnets are compounds that have an unbalanced antiparallel alignment of magnetic moments, giving a weaker but non-zero total magnetic moment. Paramagnets has atoms with randomly oriented magnetic moment across the material. Thus, not generating any total magnetic moment as a whole material. The magnetic moments in paramagnets only begin to align parallel under substantial magnetic fields. Diamagnets do not contain atoms with a magnetic moment and only produce a minuscule magnetic moment that aligns antiparallel to very strong magnetic fields. Hence, the study of magnetic materials for technological applications focuses on ferromagnet, ferrimagnet, and antiferromagnets that exhibit magnetic interactions and order under small or no magnetic fields.

Before delving into the origin of magnetic moments in the materials, we will first discuss the close relationship between electrical charges and magnetic fields that will form the framework explaining atomic magnetic moments. Charged particles like electrons experience a force under magnetic fields named the Lorentz force $\vec{F}_q$ given by,

$$\vec{F}_q = q\vec{E} + q\vec{v}_q \times \vec{B}, \tag{2.1.1}$$

where q is the particle's electrical charge, $\vec{E}$ is the electric field strength, $\vec{v}_q$ is the velocity of the charged particle, $\vec{B}$ is the magnetic flux density. Equation 2.1.1 gives the force exerted by an electric field and magnetic field in the first and second terms. On the other hand, a moving charged particle, which is most easily found as electrical currents in a conducting wire, also generates a magnetic field in space around itself, quantified by the Biot-Savart law,

$$d\vec{B} = \frac{\mu_0 I d\vec{L} \times \hat{r}}{4\pi r^2}, \tag{2.1.2}$$

where μ_0 is the permeability of free space, I is the electrical current magnitude, $d\vec{L}$ is the infinitesimal length of the wire, $\hat{r}$ is the direction from the $d\vec{L}$ element to the position of interest in space, and r is the distance between the $d\vec{L}$ element and the position of interest in space. Equation 2.1.2 is useful as a generalized equation for complex configurations of electrical currents. For a more straightforward case of a straight wire, the Ampere's law can be applied and is given by,

$$\int_C \vec{B} \cdot d\vec{l} = \mu_0 I, \tag{2.1.3}$$

where the integral is performed around a closed loop orientated on the plane perpendicular to the current direction, and $d\vec{l}$ is the infinitesimal length around the same closed loop. Equation 2.1.3 gives a helpful picture of the magnetic field generated being orientated circularly on the plane perpendicular to the current with a decreasing magnitude as it gets further from the current-carrying conductor. The direction of the circular magnetic fields is also fixed and easily deduced using the right-hand grip rule. With the thumb directed along the current direction, the remaining fingers in the gripped state point along the magnetic field direction around the wire. Most crucially, we focus on the case for a wire in a loop. A circular current flow generates a magnetic field perpendicular to the loop plane, analogous to a physical magnet. The wire can be looped many times into a solenoid to achieve stronger magnetic fields and used as an electromagnet where the magnetic field is generated and controlled by applying an electrical current through the solenoid.

With the critical picture of moving charges as the source of magnetic fields, we return to the origin of magnetic moments in an atom. The atomic magnetic moment arises from two sources: the electron itself and the orbital motion of electrons around the atomic nucleus. Electrons with their intrinsic angular momentum named spin, and their electrical charge generate the magnetic moment. Contrary to the name spin used to describe the electron's intrinsic angular momentum, a simple picture of electrons having charges accumulated on its surface and spinning about an axis is inaccurate as the charges will require unphysical velocities. Spin is an intrinsic property of electrons whose origin is not yet fully elucidated[3,4]. Within the atom, electrons move around the atomic nucleus within regions referred to as orbitals where there is a high probability exceeding 90% of finding the electron. The angular momentum associated with the orbital motion coupled with the charged electron provides the second source of the atomic magnetic moment. Note that the term orbital does not imply electron motion following circular orbits. Atomic orbitals exist in different shapes like spherical, dumbbells, etc. Not all electron orbitals have non-zero angular momentum. Only the set of degenerate orbitals that are not precisely half-filled or fully-filled has a finite angular momentum. Hence, the magnetic properties of the atom are closely tied to its electronic configuration[1,2,5].

2.2 Magnetic interactions

The magnetic moments and angular momentum within each atom undergo various magnetic interactions discussed in this section. The combination of these interactions results in many different configurations and states like skyrmions and other magnetic textures that will be discussed in Chapter 3.1.

2.2.1 Heisenberg exchange interaction

The essential magnetic interaction that allows for the ordered magnetic moments in a material is the Heisenberg exchange interaction between the atoms[6]. The Heisenberg exchange interaction's energy is given by,

$$E_{ex} = -J_{ex}\left(\vec{S}_1 \cdot \vec{S}_2\right), \tag{2.2.1}$$

where J_{ex} is the exchange integral, $\vec{S}_1$ and $\vec{S}_2$ are the spins of the interacting atoms. From Eq. 2.2.1, the Heisenberg exchange interaction favours either the parallel or antiparallel alignment of adjacent atoms. The positive and negative sign of J_{ex} determines the ferromagnetic and antiferromagnetic nature of the interaction, respectively. Ferrimagnetic materials have a negative J_{ex} but unequal spin magnitude between the interacting atoms, found in compounds with a mixture of different elements[7].

The Heisenberg exchange interaction competes with a disorder caused by thermal energy. Above the temperature named the Curie temperature T_C, a ferromagnetic material transitions into a paramagnet where the magnetic moments no longer exhibit order and generate little to no total magnetic moment in the material[8]. The Heisenberg exchange interaction arises from the quantum mechanical effect of particles with overlapping wave functions, where the term exchange here refers to the swapping of indistinguishable particles. The condition of indistinguishability requires the system to remain unchanged before and after the swapping of particles. With the inclusion of Pauli's exclusion principle that restricts particles from occupying identical states in both spin and spatial states, the spin alignment dependent energy manifests even without considering spin interaction[9].

2.2.2 Dzyaloshinskii-Moriya interaction

Dzyaloshinskii-Moriya interaction (DMI) is described by a 3-site indirect exchange mechanism between two magnetic sites with a third atom with strong spin-orbit coupling, given by,

$$E_{DM} = -\vec{D}_{12} \cdot \left(\vec{S}_1 \times \vec{S}_2 \right), \tag{2.2.2}$$

where $\vec{D}_{12}$ is the DMI vector and its magnitude referred to as the DMI strength. Comparing DMI to the Heisenberg exchange interaction, the stark contrast lies in the cross product between the atomic spins in Eq. 2.2.2 instead of the dot product in Eq. 2.2.1. Thus, DMI not only favours a perpendicular alignment between adjacent spins but also with a fixed handedness. The handedness will be critical in fixing the chirality of domain walls to stabilize topological structures and inhibit the formation of non-topological ones. Thus, the first observations of magnetic skyrmions were performed in materials with DMI[10-15]. The importance of DMI in the role of skyrmion stabilization is detailed in Section 3.1.

DMI was first proposed by Dzyaloshinskii as an antisymmetric spin-coupling interaction to account for the weak ferromagnetism observed in antiferromagnetic crystals of Fe_2O_3 and $MnCO_3$[16]. Moriya later formulated E_{DM} by the inclusion of spin-orbit interaction using Anderson's formalism for microscopic magnetic model[17,18]. Thus, this interaction was later named after the key contributions by both scientists.

2.2.3 Dipole-dipole interaction

The magnetic dipole-dipole interaction (DDI) describes the interaction between the magnetic field exerted by one magnetic dipole on another magnetic dipole, where each electron or atom can be viewed as a magnetic dipole that would generate the identical magnetic field. This interaction is also referred to as demagnetizing interaction and magnetostatic interaction that stems from the same idea. The magnetic field exerted by one magnetic dipole would favour the antiparallel alignment of another magnetic dipole, leading to the minimization of stray magnetic fields and demagnetizing effects.

The potential energy of a dipole under a magnetic field is given by,

$$E_{DDI} = -\vec{\mu} \cdot \vec{B}_{\text{int}}, \tag{2.2.3}$$

where $\vec{\mu}$ is the magnetic dipole moment and $\vec{B}_{\text{int}}$ is the internal magnetic flux density generated by the material itself. To evaluate the total energy cost of DDI, the energy of each dipole due to the magnetic field of every other magnetic dipole needs to be considered due to its long-range nature compared to the Heisenberg exchange interaction and DMI where only nearest neighbours are relevant[1].

2.2.4 Magnetic Anisotropy

Magnetic anisotropy refers to the directional preference of magnetic moments. It exists in various forms like magnetocrystalline anisotropy, shape anisotropy, interfacial magnetic anisotropy, and stress anisotropy. Two main orientations of magnetic anisotropy important for magnetic skyrmions are the uniaxial perpendicular magnetic anisotropy and in-plane magnetic anisotropy. The uniaxial perpendicular magnetic anisotropy energy is given by,

$$E_{Ku} = -\int K_u m_z^2 \, dV, \tag{2.2.4}$$

where K_u is the magnetic anisotropy strength, and m_z is the normalized perpendicular magnetic moment component[19].

Perpendicular magnetic anisotropy can be found in magnetic thin films and multilayers like Pd/Co, Pt/Co, Au/Co, Ir/Co, Ru/Co[20,21]. The long-range DDI generally contributes to an in-plane magnetic anisotropy in the bulk of thick films, while the broken symmetry at interfaces induces a perpendicular magnetic anisotropy of spin-orbit interaction origins[21]. Thus, the transition from an in-plane to perpendicular magnetic anisotropy can be found in those magnetic multilayers with decreasing thickness[22]. The interplay between the in-plane and perpendicular magnetic anisotropy will later become a critical component in stabilizing magnetic skyrmions discussed in Chapter 3.1[23-26].

Apart from the metallic multilayers, magnetic metal/oxide interfaces were later discovered to display strong perpendicular magnetic anisotropy despite the lack of strong spin-orbit interactions in oxides. Examples of these oxides include AlO_x, MgO, TaO_x, and HfO_x[27,28]. The perpendicular magnetic anisotropy in these systems alternatively arises from electronic hybridization between the magnetic transition metal orbit with the oxygen across the interface[19].

More importantly, the perpendicular magnetic anisotropy at the magnetic metal/oxide interface was demonstrated to be tunable by applying a voltage across the insulating interface, referred to as voltage-controlled magnetic anisotropy (VCMA)[29-31]. VCMA has opened avenues for ultralow current-induced magnetization reversal for magnetic tunnel junction technologies[31]. Similarly, VCMA is a valuable tool for possible application in low energy skyrmion nucleation[32,33]. By further exploiting VCMA to form a magnetic anisotropy gradient, we propose a pure voltage-driven scheme for skyrmion propagation presented in Chapter 7.

2.2.5 Zeeman Interaction

The Zeeman interaction refers to the potential energy of the magnetic moment in an external magnetic field, given by,

$$E_{Zee} = -\vec{\mu} \cdot \vec{B}_{ext}, \tag{2.2.5}$$

where $\vec{\mu}$ is the magnetic moment, and $\vec{B}_{ext}$ is the magnetic flux density generated externally applied onto the material. From Eq. 2.2.5, the relation is simple and displays the preference for alignment of magnetic moments along the magnetic field direction[34-36].

2.2.6 RKKY Interaction

The Ruderman-Kittel-Kasuya-Yosida (RKKY) interaction is an indirect exchange interaction spanning several lattice sites via free itinerant conduction electrons, unlike the direct electron orbital overlap for the Heisenberg exchange interaction[37-40]. The indirect exchange interaction takes a similar form given in Eq. 2.2.1 where the exchange constant is oscillatory with the distance between the atoms and even possibly changes sign. Thus, one atom can have ferromagnetic coupling with the nearest atom but antiferromagnetic coupling with another atom at a further distance. The oscillatory behaviour is critical for competing interactions that is one of the means to stabilize magnetic skyrmions. The RKKY interaction is also applied in the formation of synthetic antiferromagnets. In a synthetic antiferromagnet, two ferromagnetic layers sandwich a metallic layer with itinerant electrons like iridium and ruthenium that displays RKKY interaction. By tuning the metallic layer thickness, the two ferromagnetic layers can achieve either ferromagnetic or antiferromagnetic coupling[41,42].

2.3 Magnetization Dynamics

Magnetization dynamics were first modelled by Landau and Lifshitz following the expression,

$$\frac{\partial \vec{M}}{\partial t} = -|\gamma| \vec{M} \times \vec{H}_{eff} - \frac{|\lambda|}{M_s} \vec{M} \times \left(\vec{M} \times \vec{H}_{eff} \right), \tag{2.3.1}$$

where $\vec{M}$ is the magnetization vector, γ is the gyromagnetic ratio, $\vec{H}_{eff}$ is the effective magnetic field, λ is a phenomenological constant of the material. Note that the modulus terms are added to avoid confusion due to the occasional conflicting sign conventions of these two terms. Magnetization refers to the effective magnetic moment per unit volume. All the internal magnetic interactions can be condensed into an effective magnetic field included in $\vec{H}_{eff}$. Magnetization dynamics are characterized by two main processes, precessional motion and damping, represented as the first and second terms in Eq. 2.3.1.

The magnetization precessional instead of a linear one with the effective magnetic field is in analogy with the precessional motion of a spinning gyroscope under a torque. For an intuitive picture of the precessional motion in a magnetic field, we return to the source of the magnetic moment being associated with a charged particle with angular momentum or a set of magnetic dipoles. A torque orientated perpendicular to the magnetization and magnetic field instead of a net force will be exerted on the magnetization in both these scenarios. Thus, the evolution of magnetization associated with the angular momentum follows this torque direction corresponding to a precessional motion.

The precessional motion does not proceed indefinitely and is accounted for by the phenomenological damping term in Eq. 2.3.1. The damping process physically arises from dissipative processes. From Eq. 2.3.1, the damping torque is perpendicular to the precessional torque and $\vec{M}$, and points towards the $\vec{H}_{eff}$. Thus, this torque diminishes the precessional motion over time and aligns $\vec{M}$ along $\vec{H}_{eff}$ eventually. As both precessional and damping torques being always orthogonal to $\vec{M}$, the magnitude of $\vec{M}$ is always preserved.

Gilbert later introduces the damping term alternatively as a viscous source, given by,

$$\frac{\partial \vec{M}}{\partial t} = -|\gamma| \vec{M} \times \vec{H}_{eff} + \frac{|\alpha|}{M_s} \vec{M} \times \frac{\partial \vec{M}}{\partial t} , \tag{2.3.2}$$

where α is the Gilbert damping parameter. Again the modulus terms are used to avoid confusion due to the sign convention of those terms. Equation 2.3.2 can be expressed into a similar form as that proposed by Landau and Liftshitz, given by,

$$\frac{\partial \vec{M}}{\partial t} = -\frac{|\gamma|}{1+\alpha^2} \vec{M} \times \vec{H}_{eff} - \frac{|\alpha\gamma|}{M_s\left(1+\alpha^2\right)} \vec{M} \times \left(\vec{M} \times \vec{H}_{eff}\right), \tag{2.3.3}$$

where the difference lies in the pre-factors of the two terms[43]. The Gilbert form of the magnetization dynamics provides a more accurate, and thus used as the prime equation referred to as Landau-Lifshitz-Gilbert (LLG) equation[44,45].

The discussion on the conversion of the internal magnetic interaction and external magnetic fields are presented in Section 4.3.1, while current-induced magnetization dynamics are presented in Section 4.3.2. Thus, these items are omitted in this section.

References

1 M. Getzlaff. *Fundamentals of Magnetism*. (Springer Berlin Heidelberg, 2007).

2 W. Nolting & A. Ramakanth. *Quantum Theory of Magnetism*. (Springer Berlin Heidelberg, 2009).

3 J. C. A. Boeyens. Understanding Electron Spin. *Journal of Chemical Education* **72**, 412, doi:10.1021/ed072p412 (1995).

4 E. D. Commins. Electron Spin and Its History. *Annual Review of Nuclear and Particle Science* **62**, 133-157, doi:10.1146/annurev-nucl-102711-094908 (2012).

5 R. Shankar. *Fundamentals of Physics II: Electromagnetism, Optics, and Quantum Mechanics*. (Yale University Press, 2016).

6 W. Heisenberg. Zur Theorie des Ferromagnetismus. *Zeitschrift für Physik* **49**, 619-636, doi:10.1007/BF01328601 (1928).

7 S. Woo, K. M. Song, X. Zhang, *et al.* Deterministic creation and deletion of a single magnetic skyrmion observed by direct time-resolved X-ray microscopy. *Nat. Electron* **1**, 288-296, doi:10.1038/s41928-018-0070-8 (2018).

8 J. Nelson & S. Sanvito. Predicting the Curie temperature of ferromagnets using machine learning. *Phys. Rev. Mater.* **3**, 104405, doi:10.1103/PhysRevMaterials.3.104405 (2019).

9 A. N. W, N. W. Ashcroft, N. D. Mermin, *et al. Solid State Physics*. (Holt, Rinehart and Winston, 1976).

10 S. Mühlbauer, B. Binz, F. Jonietz, *et al.* Skyrmion Lattice in a Chiral Magnet. *Science* **323**, 915, doi:10.1126/science.1166767 (2009).

11 A. Neubauer, C. Pfleiderer, B. Binz, *et al.* Topological Hall Effect in the A Phase of MnSi. *Phys. Rev. Lett.* **102**, 186602, doi:10.1103/PhysRevLett.102.186602 (2009).

12 A. Tonomura, X. Yu, K. Yanagisawa, *et al.* Real-Space Observation of Skyrmion Lattice in Helimagnet MnSi Thin Samples. *Nano Lett.* **12**, 1673-1677, doi:10.1021/nl300073m (2012).

13 Y. Li, N. Kanazawa, X. Z. Yu, *et al.* Robust Formation of Skyrmions and Topological Hall Effect Anomaly in Epitaxial Thin Films of MnSi. *Phys. Rev. Lett.* **110**, 117202, doi:10.1103/PhysRevLett.110.117202 (2013).

14 M. Mochizuki, X. Z. Yu, S. Seki, *et al.* Thermally driven ratchet motion of a skyrmion microcrystal and topological magnon Hall effect. *Nat. Mater.* **13**, 241-246, doi:10.1038/nmat3862 (2014).

15 X. Z. Yu, Y. Onose, N. Kanazawa, *et al.* Real-space observation of a two-dimensional skyrmion crystal. *Nature* **465**, 901-904, doi:10.1038/nature09124 (2010).

16 I. Dzyaloshinsky. A thermodynamic theory of “weak” ferromagnetism of antiferromagnetics. *J. Phys. Chem. Solids* **4**, 241-255, doi:10.1016/0022-3697(58)90076-3 (1958).

17 P. W. Anderson. New Approach to the Theory of Superexchange Interactions. *Phys. Rev.* **115**, 2-13, doi:10.1103/PhysRev.115.2 (1959).

18 T. Moriya. Anisotropic Superexchange Interaction and Weak Ferromagnetism. *Phys. Rev.* **120**, 91-98, doi:10.1103/PhysRev.120.91 (1960).

19 B. Dieny & M. Chshiev. Perpendicular magnetic anisotropy at transition metal/oxide interfaces and applications. *Reviews of Modern Physics* **89**, 025008, doi:10.1103/RevModPhys.89.025008 (2017).

20 P. J. H. Bloemen & W. J. M. de Jonge. Magnetic anisotropy of Co/Ni/Co/Pt multilayers. *J. Magn. Magn. Mater.* **116**, L1-L6, doi:10.1016/0304-8853(92)90130-G (1992).

21 M. T. Johnson, P. J. H. Bloemen, F. J. A. d. Broeder, *et al.* Magnetic anisotropy in metallic multilayers. *Reports on Progress in Physics* **59**, 1409-1458, doi:10.1088/0034-4885/59/11/002 (1996).

22 D. T. Ngo, Z. L. Meng, T. Tahmasebi, *et al.* Interfacial tuning of perpendicular magnetic anisotropy and spin magnetic moment in CoFe/Pd multilayers. *J. Magn. Magn. Mater.* **350**, 42-46, doi:10.1016/j.jmmm.2013.08.063 (2014).

23 R. Tolley, S. A. Montoya & E. E. Fullerton. Room-temperature observation and current control of skyrmions in Pt/Co/Os/Pt thin films. *Phys. Rev. Mater.* **2**, doi:10.1103/PhysRevMaterials.2.044404 (2018).

24 R. Juge, S.-G. Je, D. d. S. Chaves, *et al.* Current-Driven Skyrmion Dynamics and Drive-Dependent Skyrmion Hall Effect in an Ultrathin Film. *Phys. Rev. Appl.* **12**, 044007, doi:10.1103/PhysRevApplied.12.044007 (2019).

25 S. D. Pollard, J. A. Garlow, J. Yu, *et al.* Observation of stable Néel skyrmions in cobalt/palladium multilayers with Lorentz transmission electron microscopy. *Nat. Commun.* **8**, 14761, doi:10.1038/ncomms14761 (2017).

26 J. Brandão, D. A. Dugato, R. L. Seeger, *et al.* Observation of magnetic skyrmions in unpatterned symmetric multilayers at room temperature and zero magnetic field. *Sci. Rep.* **9**, 4144, doi:10.1038/s41598-019-40705-4 (2019).

27 S. Monso, B. Rodmacq, S. Auffret, *et al.* Crossover from in-plane to perpendicular anisotropy in Pt/CoFe/AlOx sandwiches as a function of Al oxidation: A very accurate control of the oxidation of tunnel barriers. *Appl. Phys. Lett.* **80**, 4157-4159, doi:10.1063/1.1483122 (2002).

28 A. Manchon, C. Ducruet, L. Lombard, *et al.* Analysis of oxygen induced anisotropy crossover in Pt/Co/MOx trilayers. *J. Appl. Phys.* **104**, 043914, doi:10.1063/1.2969711 (2008).

29 M. Endo, S. Kanai, S. Ikeda, *et al.* Electric-field effects on thickness dependent magnetic anisotropy of sputtered MgO/$Co_{40}Fe_{40}B_{20}$/Ta structures. *Appl. Phys. Lett.* **96**, 212503, doi:10.1063/1.3429592 (2010).

30 K. Kita, D. W. Abraham, M. J. Gajek, *et al.* Electric-field-control of magnetic anisotropy of $Co_{0.6}Fe_{0.2}B_{0.2}$/oxide stacks using reduced voltage. *J. Appl. Phys.* **112**, 033919, doi:10.1063/1.4745901 (2012).

31 W.-G. Wang, M. Li, S. Hageman, *et al.* Electric-field-assisted switching in magnetic tunnel junctions. *Nat. Mater.* **11**, 64-68, doi:10.1038/nmat3171 (2012).

32 M. Schott, A. Bernand-Mantel, L. Ranno, *et al.* The Skyrmion Switch: Turning Magnetic Skyrmion Bubbles on and off with an Electric Field. *Nano Lett.* **17**, 3006-3012, doi:10.1021/acs.nanolett.7b00328 (2017).

33 C. Ma, X. Zhang, J. Xia, *et al.* Electric Field-Induced Creation and Directional Motion of Domain Walls and Skyrmion Bubbles. *Nano Lett.* **19**, 353-361, doi:10.1021/acs.nanolett.8b03983 (2019).

34 P. Zeeman. The Effect of Magnetisation on the Nature of Light Emitted by a Substance. *Nature* **55**, 347-347, doi:10.1038/055347a0 (1897).

35 P. Zeeman. XXXII. On the influence of magnetism on the nature of the light emitted by a substance. *The London, Edinburgh, and Dublin Philosophical Magazine and Journal of Science* **43**, 226-239, doi:10.1080/14786449708620985 (1897).

36 P. Zeeman. VII. Doublets and triplets in the spectrum produced by external magnetic forces. *The London, Edinburgh, and Dublin Philosophical Magazine and Journal of Science* **44**, 55-60, doi:10.1080/14786449708621028 (1897).

37 M. A. Ruderman & C. Kittel. Indirect Exchange Coupling of Nuclear Magnetic Moments by Conduction Electrons. *Phys. Rev.* **96**, 99-102, doi:10.1103/PhysRev.96.99 (1954).

38 T. Kasuya. A Theory of Metallic Ferro- and Antiferromagnetism on Zener's Model. *Progress of Theoretical Physics* **16**, 45-57, doi:10.1143/ptp.16.45 (1956).

39 K. Yosida. Magnetic Properties of Cu-Mn Alloys. *Phys. Rev.* **106**, 893-898, doi:10.1103/PhysRev.106.893 (1957).

40 Y. Yafet. Ruderman-Kittel-Kasuya-Yosida range function of a one-dimensional free-electron gas. *Phys. Rev. B* **36**, 3948-3949, doi:10.1103/PhysRevB.36.3948 (1987).

41 T. Dohi, S. DuttaGupta, S. Fukami, *et al.* Formation and current-induced motion of synthetic antiferromagnetic skyrmion bubbles. *Nat. Commun.* **10**, 5153, doi:10.1038/s41467-019-13182-6 (2019).

42 W. Legrand, D. Maccariello, F. Ajejas, *et al.* Room-temperature stabilization of antiferromagnetic skyrmions in synthetic antiferromagnets. *Nat. Mater.* **19**, 34-42, doi:10.1038/s41563-019-0468-3 (2020).

43 T. L. Gilbert. A phenomenological theory of damping in ferromagnetic materials. *IEEE Trans. Magn.* **40**, 3443-3449, doi:10.1109/TMAG.2004.836740 (2004).

44 M. D. Stiles & J. Miltat. in *Spin dynamics in confined magnetic structures III* 225-308 (Springer, 2006).

45 D. C. Mattis. *The theory of magnetism I: Statics and Dynamics*. Vol. 17 (Springer Science & Business Media, 2012).

Chapter 3 Review of Magnetic Skyrmion Stabilization, Control, and Applications

In this chapter, a literature review of the magnetic skyrmions is consolidated. Section 3.1 discusses the topological property of skyrmions, and the range of different configurations considered skyrmions mathematically. This section discusses the different stabilizing interactions, conditions, and materials in which the different types of skyrmions are observed. Section 3.2 presents skyrmion nucleation techniques. Section 3.3 presents the various forms of skyrmion excitations and responses crucial for reliable control of skyrmions. Section 3.4 presents the experimental techniques used in the imaging and detection of skyrmions. Section 3.5 presents the proposed technological application of skyrmions.

3.1 Skyrmion Properties & Stabilization

In this section, the topological nature and corresponding range of possible configurations of skyrmions are described mathematically. Magnetic skyrmion materials are presented and categorized based on their configuration and the dominant magnetic interactions stabilizing them, including BDMI, IDMI, DDI, and frustration. In addition, other conditions such as temperature, pressure, magnetic field, electrical field, geometrical constraint, and strain also play a role in stabilizing skyrmions. Finally, the metastability of magnetic skyrmions outside of their thermodynamically stable conditions critical for technological applications is discussed. The origin of skyrmion stability not only from an energy barrier but also significant entropic contributions are highlighted.

3.1.1 Topology

The stability of magnetic skyrmions had been closely linked to the topological configuration of their vector field of magnetic moments. In mathematics, topology refers to the study of geometric properties preserved under continuous deformations such as stretching, twisting, and bending without tearing. An example of a pair of topologically equivalent two-dimensional shapes is an ellipse and a circle that can be transformed into each other by stretching. Another less intuitive example of topologically equivalent shapes is a doughnut and coffee mug. As shown in Fig. 3.1.1, a doughnut can be transformed into a coffee mug by deforming the side of a doughnut into a cylindrical section and subsequently depressing the top face to form the mug's body. As deformations can perform this transformation without tearing, a doughnut and coffee mug are topologically equivalent. The critical implication here is that transformations between topologically inequivalent geometries cannot be achieved by continuous deformation alone and hence offers additional stability to the incumbent geometry.

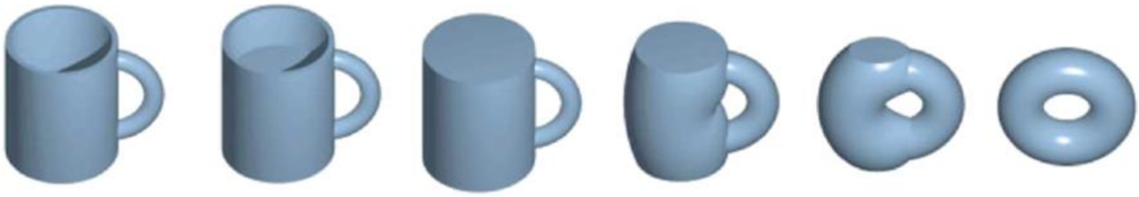

Figure 3.1.1| Illustration of the topological equivalence between a doughnut and coffee mug through a process of continuous transformations[1].

For two-dimensional magnetic skyrmions on a film, its topology is quantified by the winding number, also known as skyrmion topological number N_{sk} given by

$$N_{sk} = \frac{1}{4\pi}\iint \vec{m} \bullet \left(\frac{\partial \vec{m}}{\partial x} \times \frac{\partial \vec{m}}{\partial y} \right) dxdy \ , \tag{3.1.1}$$

where $\vec{m}(x,y)$ is the normalized magnetization with the magnitude of 1 [2-4]. This expression computes the number of times $\vec{m}$ wraps around a unit sphere. Hence the structure of a skyrmion have N_{sk} of ± 1. In contrast, the winding number of a plane with uniform magnetization is 0. Thus, continuous transformations between these two states are prohibited, and skyrmions can resist annihilation by minor deformations. This stability arising from the geometry or configuration of the skyrmion is referred to as topological stability.

Theoretically, a skyrmion described by a continuous vector field is topologically protected because its annihilation requires the transformation into a topologically trivial state. However, full topological protection is broken in real physical magnetic systems due to the discretized magnetic moments at the atomic scale. Even so, a finite energy barrier that suppresses the annihilation process remains and offers topological stability[5,6].

3.1.2 Skyrmion Configuration

The magnetization $\vec{m} = (m_x, m_y, m_z)$ configuration of a two-dimensional skyrmion is preferably described by polar coordinates over cartesian coordinates given the skyrmion's circular symmetry[7]. The assumption of circular symmetry is valid for a magnetic skyrmion at equilibrium without an in-plane magnetic field. The transformation of spatial coordinates between cartesian $\vec{r}(x,y)$ and polar $\vec{r}(\mathrm{r},\varphi)$ coordinates is given by,

$$x = r\cos\varphi \quad , \quad y = r\sin\varphi \ , \tag{3.1.2}$$

where r is the radial distance from the centre of the skyrmion, and φ is the azimuthal angle in space. The direction of $\vec{m}(\theta,\phi)$ vector is described using spherical coordinates given by,

$$\vec{m}\left(\theta(r,\varphi),\phi(r,\varphi)\right) = \left(\sin\theta\cos\phi, \sin\theta\sin\phi, \cos\theta\right) \ , \tag{3.1.3}$$

where θ is the polar angle and ϕ is the azimuthal angle of the vector.

With the assumption of circular symmetry, the dependence of $\theta(\mathrm{r},\varphi)$ and $\phi(\mathrm{r},\varphi)$ are both simplified to $\theta(\mathrm{r})$ and $\phi(\varphi)$ respectively. By substituting $\vec{m}\left(\theta(r),\phi(\varphi)\right)$ into the Eq. 3.1.1 we obtain

$$N_{sk} = -\frac{1}{4\pi}\left[\cos\theta(r)\right]_{r=0}^{r=R}\left[\phi(\varphi)\right]_{\varphi=0}^{\varphi=2\pi} \ , \tag{3.1.4}$$

where R corresponds to the radial distance at which $\vec{m}$ becomes fully antiparallel to its core. The term $\left[\cos\theta(r)\right]_{r=0}^{r=R} = \pm 2$ depends on the polarity or orientation of the skyrmion core. A core in the positive $\hat{z}$ direction returns the value of –2 and vice versa. The term $\left[\phi(\varphi)\right]_{\varphi=0}^{\varphi=2\pi} = \pm 2\pi$ depends on the skyrmion's vorticity ω defined as $\omega = \left[\phi(\varphi)\right]_{\varphi=0}^{\varphi=2\pi} / 2\pi$. ω describes the relative direction of change in the azimuthal angles φ and ϕ of space and magnetization vector, respectively. ω is +1 if they are unidirectional and –1 if they are in opposite directions. Based on Eq. 3.1.4, an additional phase term γ defined as the skyrmion helicity can be introduced to $\phi(\varphi)$ while conserving the magnitude of N_{sk}, to give,

$$\phi(\varphi,\gamma) = \omega\varphi + \gamma \, , \tag{3.1.5}$$

where $\gamma = (-\pi, \pi]$.

Figure 3.1.2 shows a list of topologically equivalent skyrmion configurations with $\gamma = \{-\pi/2, 0, \pi/2, \pi\}$. Bloch and Néel skyrmions both have positive ω but differ in γ as shown in the first and third row of Fig. 3.1.2. Bloch skyrmions have $\gamma = \{+\pi/2, -\pi/2\}$ that manifest as clockwise (CW) or counterclockwise (CCW) vortex-like configurations, while Néel skyrmions have $\gamma = \{0, \pi\}$ that manifest as spike-like configurations. It is important to note that skyrmions can have any γ between $-\pi$ and π, and Bloch and Néel skyrmions are merely nomenclature used to describe several specific cases of γ. The second and final row of skyrmions with negative ω shown in Fig. 3.1.2 correspond to antiskyrmions. Antiskyrmions are topologically equivalent to skyrmions but have alternating Bloch and Néel characters around their core. The configuration of antiskyrmions is independent of γ due to its rotational symmetry, and hence are effectively characterized by its vorticity alone.

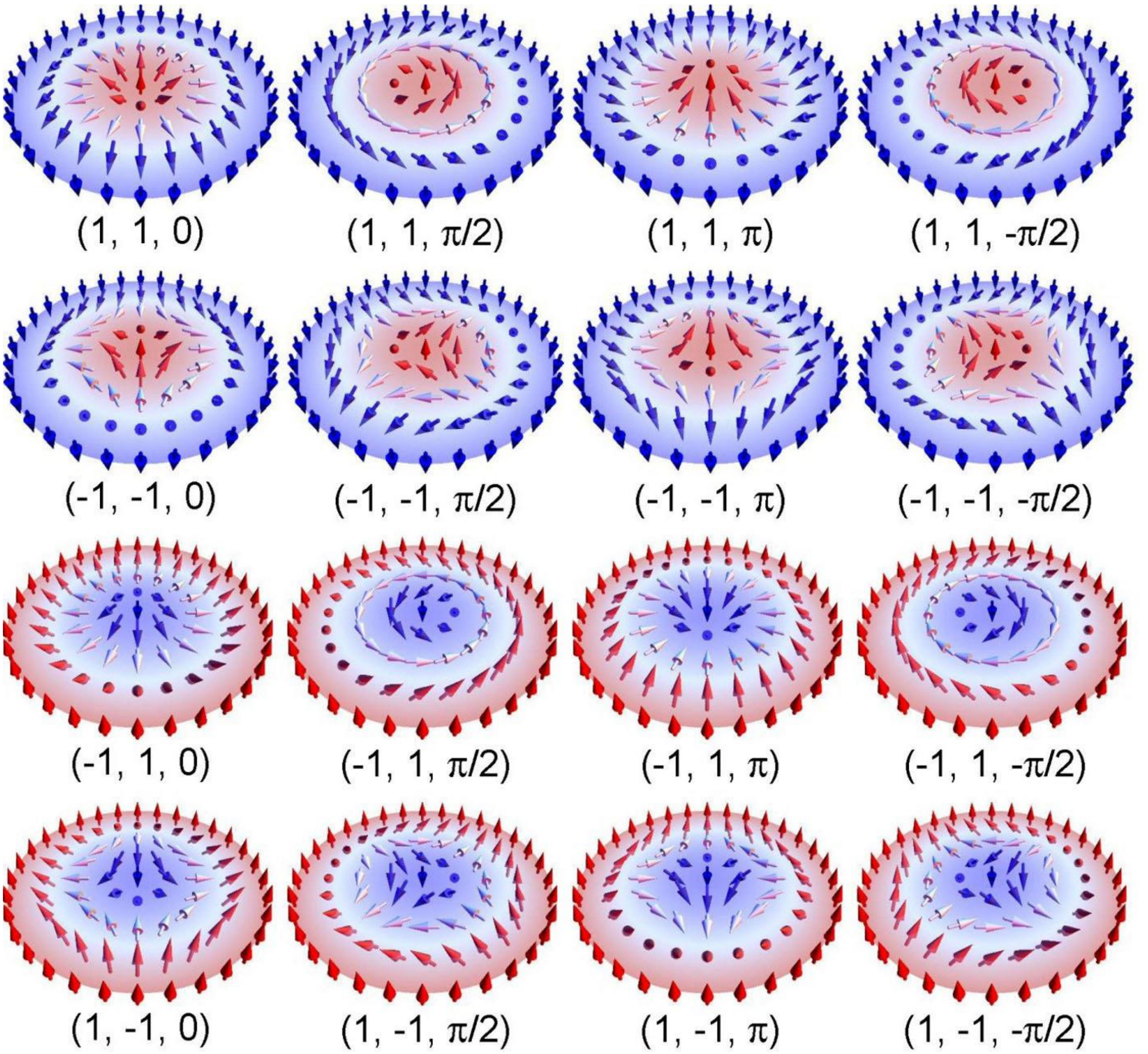

Figure 3.1.2| Illustrations of magnetic skyrmions described by the skyrmion number N_{sk}, vorticity ω, and helicity γ. The arrow denotes the spin direction while the color denotes the out-of-plane spin value, where red is out of plane, white is IP and blue is into the plane[17].

The topological nature of skyrmions is also seen from the dependence of N_{sk} on $\theta(\mathrm{r})$ in Eq. 3.1.4. N_{sk} is always conserved assuming a monotonic function of $\theta(\mathrm{r})$, $\theta(\mathrm{r})$ can vary over large values or small of r corresponding to expansion or contraction. In summary, ω

determines the topology of the skyrmion, γ determines the extent of Bloch or Néel character of the skyrmion body, and $\theta(\mathrm{r})$ determines the skyrmion size and rate of switching from the skyrmion core to its periphery.

Even though there is no exact analytical expression to describe $\theta(\mathrm{r})$, several models offer useful approximations, such as the $360°$ domain wall model[7-9] and the Belavin-Polyakov skyrmion model. In the $360°$ domain wall model[6,7,10], the skyrmion configuration is approximated as the summation of two overlapping $180°$ domain walls. A one-dimensional domain wall profile's polar angle θ_{DW} that switches from 0 to π along the positive x axis is given by,

$$\theta_{DW}(x,c,w)=2\arctan\left(\exp\left(\frac{x-c}{w}\right)\right)=\arcsin\left(\tanh\left(\frac{x-c}{w}\right)\right)+\frac{\pi}{2}, \tag{3.1.6}$$

where c is the domain wall's position defined as the position where $\theta_{DW}=\pi/2$, and w is the domain wall width. The skyrmion configuration is then described by,

$$\theta_{360}(r,R_0,w)=\theta_{DW}(r-R_0,w)+\theta_{DW}(r+R_0,w)-\pi, \tag{3.1.7}$$

for skyrmion with positive polarity and,

$$\theta_{360}(r,R_0,w)=\theta_{DW}(r-R_0,w)+\theta_{DW}(r+R_0,w), \tag{3.1.8}$$

for skyrmion with negative polarity, where R_0 is the characteristic size of the skyrmion. The skyrmion radius R, typically defined as the distance from the skyrmion core where $m_z=0$, is related to R_0 by,

$$R_0=\ln\left(\sinh R+\sqrt{\sinh^2 R-1}\right). \tag{3.1.9}$$

The $360°$ domain wall model has been demonstrated to accurately fit experimental skyrmion configurations[7].

On the other hand, the Belavin-Polyakov skyrmion model[11] offers a more simplified expression given by,

$$\theta_{BP}=2\arctan\left(\frac{R}{r}\right)=\arccos\left(\frac{R^2-r^2}{R^2+r^2}\right). \tag{3.1.10}$$

Belavin and Polyakov analytically derived this solution by approximating the energy functional of the skyrmion to only the strongest interaction, Heisenberg exchange interaction. This approximation is valid for the case of isotropic ferromagnets where the other magnetic interactions are insignificant. The other magnetic interactions like DMI, DDI, and Zeeman interaction constitute perturbations to the Belavin-Polyakov skyrmion model under most conditions. Hence, it has been commonly used in theoretical and analytical work to minimize skyrmion energy functionals[12-16]. The simplification in Belavin-Polyakov removes the freedom in w, resulting in poor modelling of larger skyrmions compared to the 360° domain wall model, as illustrated in Fig. 3.1.3. The 360° domain wall model approaches the Belavin-Polyakov model with increasing w.

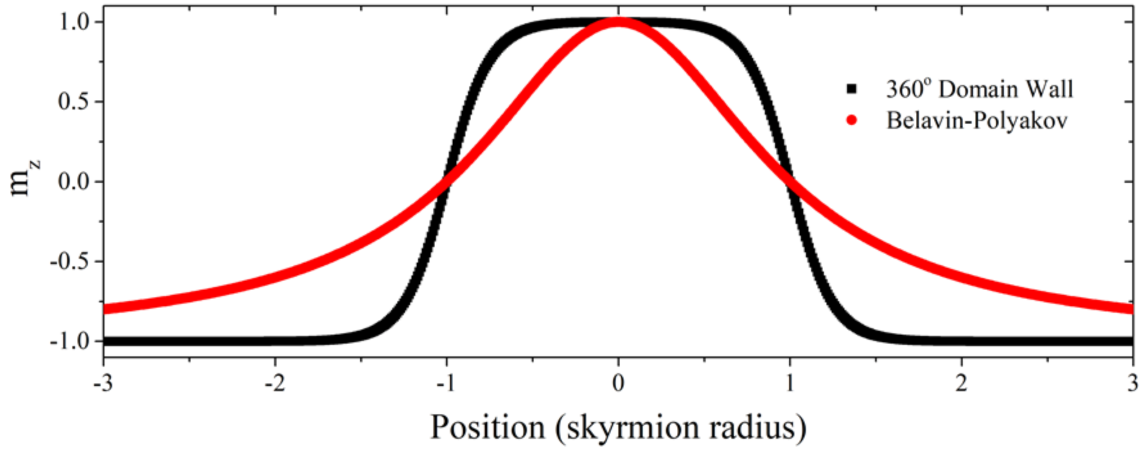

Figure 3.1.3| Comparison of the magnetization profile based on the 360° domain wall model and Belavin Polyakov model-based skyrmion profiles with a common skyrmion radius.

3.1.3 Bulk Dzyaloshinskii-Moriya Interaction Stabilized

The materials stabilizing magnetic skyrmions using predominantly BDMI induced by the lack of space inversion symmetry in their bulk crystal structure includes several main groups: B20-type compounds, β-Mn-type, and polar magnets. A wide variety of spin textures can be found in BDMI materials apart from the most common Bloch magnetic skyrmions, such as three-dimensional hedgehog-antihedgehog lattice[18], meron-antimeron lattice[19], Néel skyrmions[20], and antiskyrmions[21]. Multiferroicity in Cu_2OSeO_3[22] and polar magnets[23] also provides exciting possibilities for electric field control of these spin textures. The range of skyrmion properties found in BDMI materials varies significantly with Curie temperature as low as 2 Kelvins[24,25] to temperatures well above room temperature[26], and sizes from hundreds of nanometres down to 5 nm[27].

The earliest observations of magnetic skyrmions were performed on the group of B20-type transition metal compounds in 2009[28]. B20 compounds consist of transition metals such as Mn, Fe, Co and group 14 elements such as Si, and Ge in a cubic crystal lattice with the $P2_13$ space group. A list of B20 compounds with reported skyrmion observations and experiments are: MnSi[28-40], FeGe[41-53], MnGe[18,31,41,54-58], $Fe_xCo_{1-x}Si$[31,35,59-63], $Co_{1+x}Si_{1-x}$[64], $Mn_xFe_{1-x}Si$[27,31,65,66], $Mn_xCo_{1-x}Si$[27,31], $Mn_xFe_{1-x}Ge$[67-69], $Mn_xSi_{1-x}Ge$[70], $Fe_xCo_{1-x}Ge$[71-73]. Table 3.1.1 provides a summarized list of these compounds with their transition temperature, modulation period, and reported spin textures.

Most of the B20 compounds stabilize two-dimensional Bloch skyrmion lattices and share a common magnetic field-temperature phase diagram in terms of the spin textures as shown in Fig. 3.1.4(a), except MnGe and compounds close to its composition[18]. The spin textures include helical, conical, A-phase or skyrmion lattice, ferromagnetic and paramagnetic. In the absence of a magnetic field, the helical state is stabilized for temperatures below the paramagnetic phase. The helical state has a chiral winding of the spins perpendicular to its helix or propagation vector **q**, arising from the competition between the exchange interaction and BDMI. Under an applied magnetic field, the winding spins undergo a tilt towards the magnetic field described as the conical state. Under increasing magnetic field, the tilt in the conical state increases and transitions into the ferromagnetic state. The skyrmion lattice phase is found within a field slightly above the helical phase and temperatures bordering the paramagnetic phase. The orientation and sign of the BDMI fix the skyrmion helicity. The skyrmion spin structure is generally invariant across the bulk and approximated to form skyrmion tubes, as shown in Fig. 3.1.4(b). The skyrmion lattice corresponds to the manifestation of the thermodynamically stable superposition of three chiral helices induced by thermal fluctuations[28,74,75]. These helices are thermally driven into an ordered state with relative angles of 120° on a plane perpendicular to the magnetic field where the three **q** sum up to the zero vector. Hence, the skyrmion lattice phase are hexagonally arranged and described as the thermodynamically stable coplanar 3**q** state, where the propagation vectors lie on the same plane.

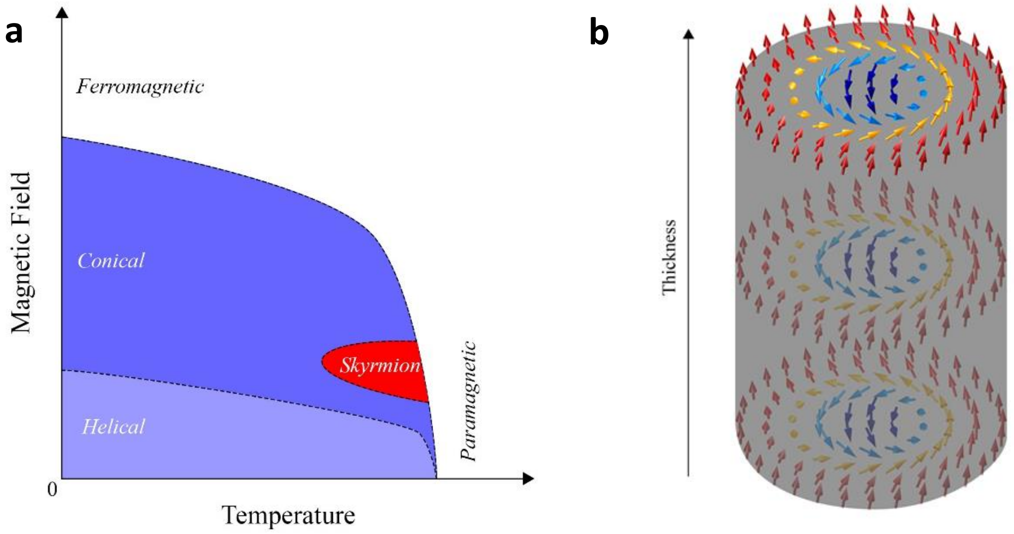

Figure 3.1.4| (a) General schematic of magnetic field-temperature spin phase diagrams of B20 compounds stabilizing two-dimensional skyrmions. (b) Structure of Bloch skyrmion tube through the bulk of the crystal.

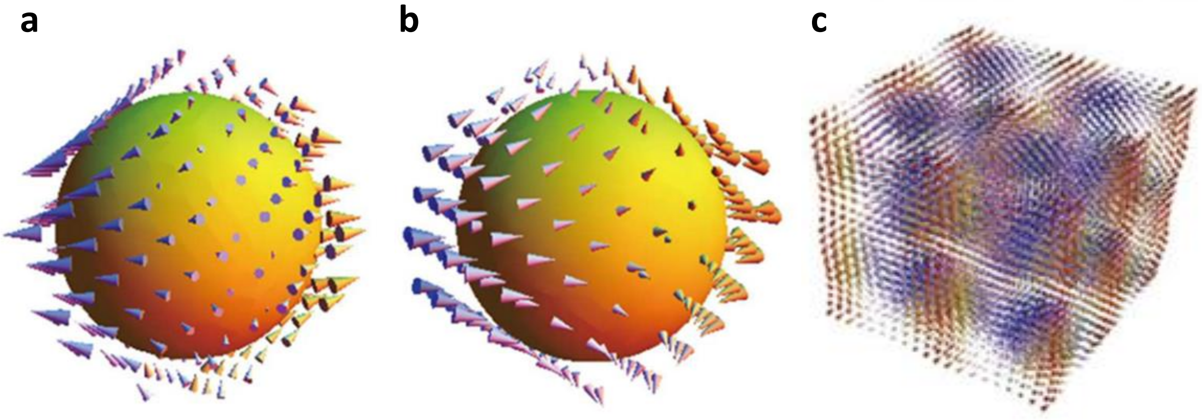

Figure 3.1.5| Magnetic configurations of (a) hedgehog, (b) antihedgehog, and (c) hedgehog-antihedgehog cubic lattice[18].

MnGe and compounds close to this composition stabilize the skyrmion-antiskyrmion or spin hedgehog-antihedgehog cubic-lattice, in short, hedgehog lattice (HL) as shown in Fig. 3.1.5(a)–(c)[18]. HL comprises three orthogonal helices and is also known as the cubic 3**q**-HL. The 3**q**-HL state dominates the phase diagram apart from the ferromagnetic and paramagnetic states. A superposition of 4**q**-HL where the helices align in the apical directions of a tetrahedron was observed in $MnSi_{1-x}Ge_x$[70] for $0.3 \leq x \leq 0.6$. The tetrahedral 4**q**-HL corresponds to a face-centered-cubic array of hedgehogs and anti-hedgehogs. The helical periods of these 3**q**-HL and 4**q**-HL were extremely small at 2.0 nm to 3.0 nm and cannot be accounted for by just the competition of BDMI and the ferromagnetic exchange interaction. Several other interactions like magnetic frustration and Ruderman-Kittel-Kasuya-Yosida (RKKY) interaction had been proposed as possible mechanism[70], but the complete understanding awaits further investigation.

One of the first bulk materials reporting the observation of skyrmions besides B20 compounds is the ferrimagnetic insulator Cu_2OSeO_3 with the same space group as the B20 compounds and exhibits a spin texture phase closely resembling B20 compounds[22]. A disordered skyrmion phase and tilted conical phase was revealed in Cu_2OSeO_3 at low temperatures and high magnetic fields applied in the $\langle 100 \rangle$ direction[76,77]. Its multiferroicity with both magnetic and dielectric order gained significant attention for investigations of magnetoelectric coupling effects[22,35,76-96].

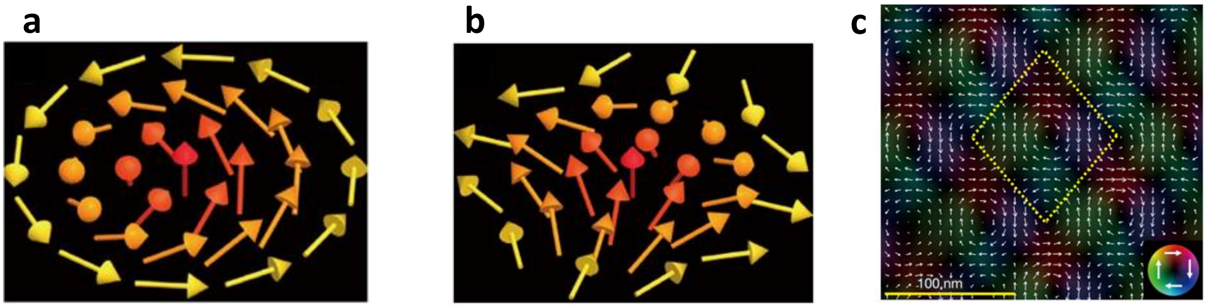

Figure 3.1.6| Magnetic configuration of (a) meron, (b) antimeron, and (c) meron-antimeron square lattice[19].

β-Mn-type compounds such as CoZnMn alloys and molybdenum nitrides[97] were the next class of bulk materials reporting skyrmion observation beyond the B20 compounds and Cu_2OSeO_3. β-Mn-type compounds have the cubic chiral space group $P4_132$ or $P4_332$, which are non-centrosymmetric like B20 compounds where BDMI can be induced. Bloch skyrmions were found in a wide range of $Co_{10-x/2}Zn_{10-x/2}Mn_x$[19,97-101] alloys for $x \leq 6$ [97], with transition temperatures up to 400 K. Frustrated magnetism at low temperatures for $Co_{10-x/2}Zn_{10-x/2}Mn_x$ where $3 \leqslant x \leqslant 7$[100-102] forms a new three-dimensional disordered skyrmion phase at low temperatures disconnected from A phase. $Co_8Zn_9Mn_3$ also reported a meron-antimeron square lattice stabilised by IP magnetic anisotropy can be transformed into the Bloch skyrmion lattice by applying perpendicular magnetic fields[19]. With the substitution of Co by Fe, the $Co_{8-x}Fe_xZn_8Mn_4$[103] alloys have diverging magnetic modulation period due to decreasing BDMI strength and BDMI sign change when x ~ 2.7, reminiscent of the similar trend in $Fe_xCo_{1-x}Ge$’[95] and $Mn_{1-x}Fe_xGe$[67] that undergo BDMI sign change with composition.

Molybdenum nitrides are a class of materials with β-Mn structure with the composition of A_2Mo_3N where A is Fe, Co, Rh, Pd, Pt, Pa, Ni[26,104-106]. The helical and skyrmion phases were identified in $Fe_xCo_{1-x}Rh_{0.5}Mo_3N$ for x = 1 using LTEM in 2016[104]. In $Fe_{2-x}Pd_xMo_3N$, the substitution of Fe by Pd aimed at enhancing BDMI was showed two new forms of skyrmion phases, a high skyrmion density phase at low temperatures below 100K and a low skyrmion density-helical mixed state that persists up to the maximum temperature investigated, 350 K[106]. Skyrmions had also been reported in $FePd_{1-x}Pt_xMo_3N$[105] and $FePtMo_3N$[26]. Molybdenum nitrides remain an intriguing class of material yet to be fully explored for potentially new skyrmion phases or more favourable skyrmion properties for technological applications.

In 2015, magnetic skyrmions were reported in polar magnets with C_{nv} crystal symmetry[20,108], as theoretically predicted based on crystallography back in 1989[109]. This material class stabilizes Néel skyrmions instead of Bloch skyrmions. GaV_4S_8[20], and GaV_4Se_8[107] are molecular magnets in the class of Lacunar spinels with the composition of AM_4X_8 (A =Ga, Ge; M=V, Mo, Nb, Ta; X = S, Se)[23]. Spin modulation in these materials is restricted within the plane perpendicular to the polar axis. Under a magnetic field along the polar axis, the spin textures transition between cycloidal, Néel skyrmion lattice and ferromagnetic phase as shown in Fig. 3.1.7 (a) and (b). The cycloidal phase has spins rotating within the plane parallel to its modulation direction is stabilized. Under a magnetic field perpendicular to the polar axis, the conical phase formed by tilted cycloids is stabilized instead[110]. The spin textures phase of GaV_4S_8 and GaV_4Se_8 span significantly different conditions, as shown in Fig. 3-7(c) and (d), respectively. The easy axis anisotropy in GaV_4S_8 restricts skyrmion lattice stability while GaV_4Se_8 with easy-plane anisotropy supports skyrmion lattice stability to span almost the full range of temperatures below Curie temperature[111]. The Jahn-Teller transition of Lacunar spinels at low temperatures also results in the induction of ferroelectric polarization due to the distortion of the crystal along <111>, making GaV_4S_8[23] and GaV_4Se_8[110] another group of multiferroic materials like Cu_2OSeO_3[79], but with significantly stronger electric polarization[23].

Another polar magnet, $VOSe_2O_5$, with a tetragonal C_{4v} point group and P_4cc space group, reported the Néel Skyrmion observation in 2017[108]. Figure 3.1.8(a) shows the spin texture phase diagram of $VOSe_2O_5$ with two cycloid phases IC-1 and IC-2, A phase, ferromagnetic, and paramagnetic phases. The phase diagram of $VOSe_2O_5$ with the A phase found only in a small range of temperature just below the transition temperature bears a closer resemblance to B20 compounds[28] than the polar magnets[20,107]. While the IC-1 phase has been identified as a single-**q** cycloidal state, the IC-2 phase has yet to be definitively identified and is currently proposed to be an anisotropic double-**q** state[112] as shown in Fig. 3.1.8(b).

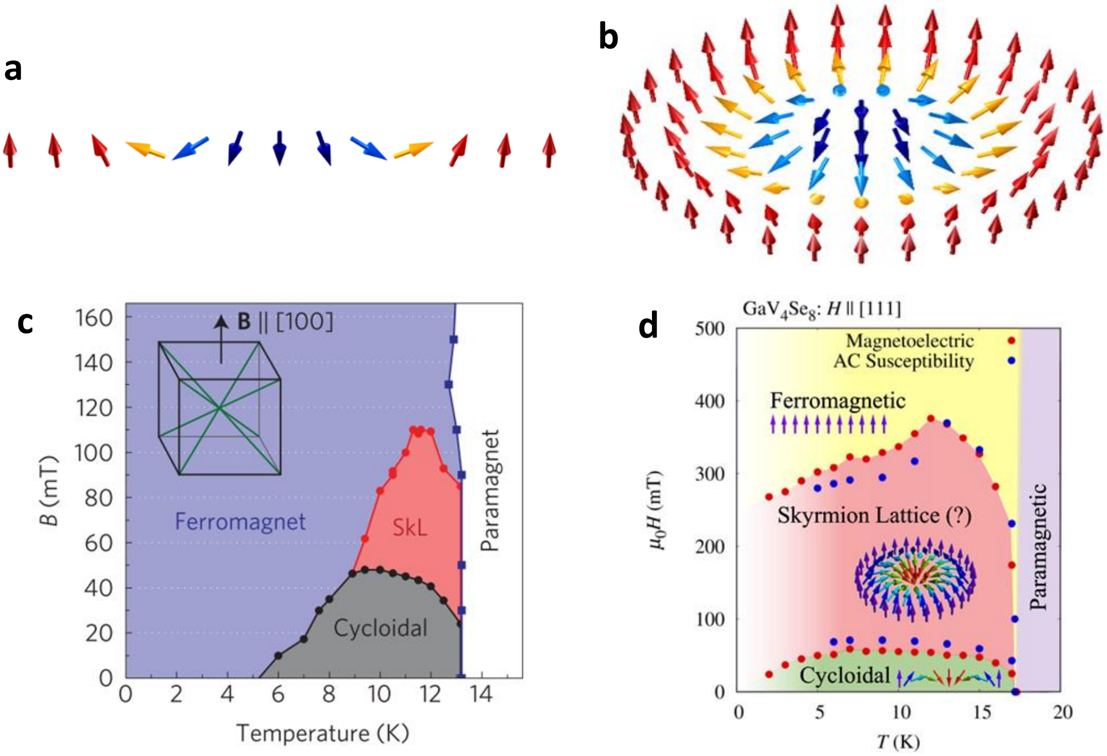

Figure 3.1.7| Magnetic configuration of (a) Cycloid, and (b) Néel magnetic skyrmion. Spin texture phase diagram of (c) GaV_4S_8[20], and (d) GaV_4Se_8[107]. SkL corresponds to the skyrmion lattice.

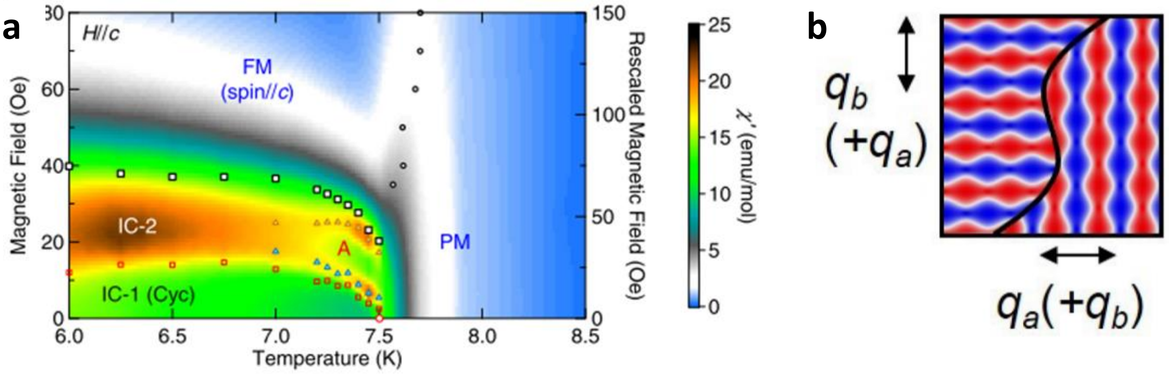

Figure 3.1.8| (a) Spin texture phase diagram of $VOSe_2O_5$. IC, A, FM, and PM corresponds to incommensurate state, skyrmion lattice, ferromagnet, and paramagnet, respectively. (b) Top view of the magnetic configuration of IC-2 phase where the red, white, and blue corresponds to positive out-of-plane, IP, and negative out-of-plane magnetization[108].

$Mn_{1.4}Pt_{0.9}Pd_{0.1}Sn$ is a non-centrosymmetric tetragonal Heusler compound with the crystal symmetry, D_{2d}[21]. Like the polar magnets with C_{nv} crystal symmetry, the D_{2d} symmetry induces BDMI that confines modulation directions within the plane perpendicular to the *c* axis. In addition, D_{2d} symmetry induces an anisotropic BDMI along [010] and [100] with opposite BDMI signs[21]. Hence, Bloch domain walls of opposite helicities are stabilized along these axes, and a continuous transition in helicities can only occur via Néel walls along the diagonal to form an antiskyrmion[113]. Figure 3.1.9 shows the complex phase diagram of the diverse spin textures in this material[113]. Only with an IP magnetic field perpendicular to the *c* axis or tilting of the sample, antiskyrmions lattices are formed[21]. The antiskyrmions can also be transformed into Bloch skyrmions using a strong IP magnetic field sweep via an intermediate non-topological bubble[113,114]. The complexity in spin textures available in $Mn_{1.4}Pt_{0.9}Pd_{0.1}Sn$ provides valuable opportunities for further studies and practical applications with viability at room temperature.

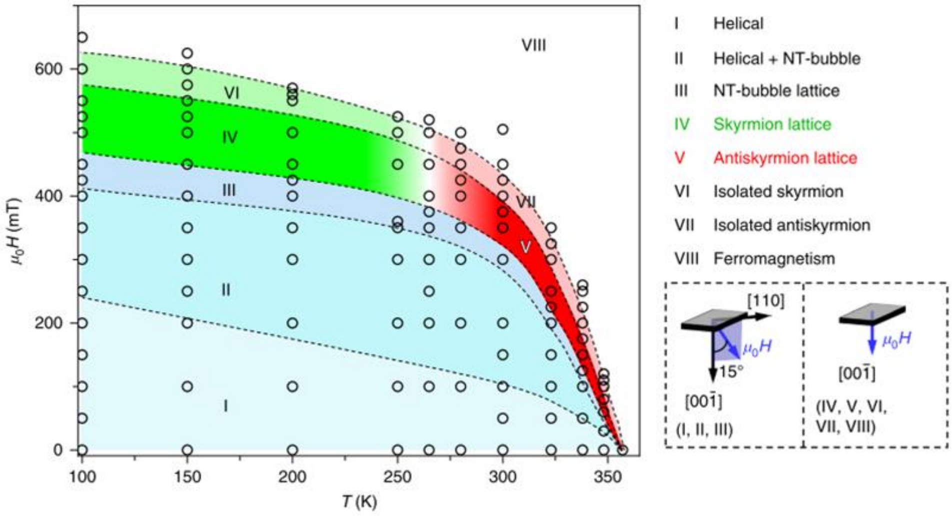

Figure 3.1.9| Spin texture phase diagram of $Mn_{1.4}Pt_{0.9}Pd_{0.1}Sn$ where a tilted magnetic field illustrated in the bottom right of the figure was applied for phases I, II, and III, and a perpendicular magnetic field was applied for phases IV, V, VI, VII, and VIII[113].

Table 3.1.1| List of materials with magnetic skyrmions predominantly stabilized by BDMI and their key parameters transition temperature, magnetic modulation, and the type of spin texture found.

Material	**Content**	**Transition temperature (K)**	**Magnetic modulation (nm)**	**Spin texture**
MnSi[28]		30	18	Bloch Sk
$Mn_{1-x}Fe_xSi$[65,75,115]	$0 \le x \le 0.12$	6.0 – 30	10 – 18	Bloch Sk
FeSi[116]	*Paramagnetic*			
$Fe_{1-x}Co_xSi$[24,59]	$0.05 \le x \le 0.7$	2 – 50	30 – 230	Bloch Sk
CoSi[117]	*Diamagnetic*			
$Co_{1+x}Si_{1-x}$[64]	$0.028 \le x \le 0.043$	275 – 328	17	Bloch Sk
FeGe[118]		280	70	Bloch Sk
$Fe_xCo_{1-x}Ge$[71-73,119]	$0 \le x \le 0.5$	180 – 280	70 – 192	Bloch Sk
	$x \sim 0.6$	125	∞	Ferromagnet
	$0.7 \le x \le 0.8$	21 – 125	46 – 110	Bloch Sk
CoGe[120]	*Diamagnetic*			
MnGe[54]		170	3 – 6	3**q** – HL
$Mn_{1-x}Fe_xGe$[67,68]	$0 \le x \le 0.3$	150 – 170	3 – 4	HL
	$0.3 \le x < 0.8$	170 – 220	4 – 160	Bloch Sk
	$x \sim 0.8$	220	∞	Ferromagnet
	$0.8 < x \le 1$	220 – 280	220 – 70	Bloch Sk
$MnSi_{1-x}Ge_x$[70]	$0 \le x \le 0.25$	30	9 – 18	Bloch Sk
	$0.3 \le x \le 0.6$	30 – 100	2.0 – 2.5	4**q** – HL
	$0.7 \le x \le 1$	150 – 170	2.5 – 3.0	3**q** – HL
$Mn_{1-x}Co_xSi$[27,75]	$0 \le x \le 0.04$	5 – 30	9 – 18	Bloch Sk
Cu_2OSeO_3[22]		60	63	Bloch Sk
$Co_{10}Zn_{10}$[97,101]		414	156	Bloch Sk
$Co_9Zn_9Mn_2$[97,101]		396	132	Bloch Sk
$Co_8Zn_8Mn_4$[97,101]		299	125	Bloch Sk
$Co_7Zn_7Mn_6$[97,101]		158	112	Bloch Sk (Frus)
$Co_6Mn_6Zn_8$[97]	*Non-ferromagnetic*			
$Co_8Zn_{10}Mn_2$[97]		345	120	Bloch Sk
$Co_8Zn_9Mn_3$[97]		320	165	Bloch Sk/ Meron-antimeron
$Co_{8-x}Fe_xZn_8Mn_4$[103]	$0 \le x < 2.7$	240 – 300	109 – 370	Bloch Sk
	$x \sim 2.7$	240	∞	Ferromagnet
	$2.7 < x \le 4.5$	135 – 230	262 – 98	Bloch Sk
$FeRh_{0.5}Mo_3N$[104]		120	110	Bloch Sk
$Fe_{2-x}Pd_xMo_3N$[26]	$0 \le x \le 0.15$	-	-	Ferromagnet
	0.32	600	60	Bloch Sk
$FePtMo_3N$[26]		222	120	Bloch Sk
GaV_4S_8[20]		13	17.7	Néel Sk
GaV_4Se_8[110]		18	19.4	Néel Sk
$VOSe_2O_5$[108]		7.5	125	Néel Sk
$Mn_{1.4}Pt_{0.9}Pd_{0.1}Sn$[21]		360	150	Bloch Sk/ Antiskyrmion lattice

3.1.4 Interfacial Dzyaloshinskii-Moriya Interaction Stabilized

In this section, we loosely classify IDMI stabilized magnetic skyrmion materials as materials with IDMI, regardless of IDMI being the dominant interaction stabilizing the magnetic skyrmions. These materials utilize the broken space inversion symmetry found at interfaces and the strong spin-orbit coupling strength of the heavy metal to induce IDMI. IDMI can be optimized using HMs that induce opposite IDMI signs at the top and bottom FM interfaces[121,122]. The IDMI vector always aligns along the interface plane and stabilizes Néel skyrmions. The materials in this category exist in HM/FM or $HM_1/FM/HM_2$ structures and possibly with repetitions. In these structures, IDMI, magnetic anisotropy, and DDI can be effectively tuned via the choice of FM, HM, thicknesses, and repetitions. Most IDMI materials stabilize skyrmions at room temperature. The stabilization of magnetic skyrmions under ambient conditions without a magnetic field is highly desirable and demonstrated using exchange bias and structural confinement techniques. Furthermore, most of these materials can also be fabricated efficiently by sputtering, which is compatible with present-day semiconductor industry production processes, making them the prime material category for technological applications.

The list of reporting magnetic skyrmion observations and other experimental investigations in IDMI materials that will be further discuss in their relevant chapters is given as follows: Ir(111)/Fe[3,123,124], Ir(111)/Fe/Pd[5,125,126], Pt/FM/Au/FM/Pt[127], Ir/Co/Pt[128], $Pt/Co/Al_2O_3$[129], Ir/Fe/Co/Pt[122,130-134], Pt/CoFeB/MgO[135-139], Pt/Co/Ir[140-145], Pt/Co/Ta[139,146-153], Ru(0001)/Co[154], $Ta/CoFeB/TaO_x$[155-158], Pt/Co/MgO[159,160], Ta/CoFeB/MgO[139,161-164], Pt/Co/Os/Pt[165], IrMn/CoFeB/MgO[166,167], Pt/GdFeCo/MgO[168-170], $SrRuO_3/BaTiO_4$[171], W/CoFeB/MgO[137], Pt/CoB/Ir[172,173], W/FeB/Ir[174], $SrIrO_3/SrRuO_3$[175], Pt/Co/Ni[176], Pt/Co/IrMn[177], Pt/Co/Ru[178,179], Pt/Co/Ni/Ir[178], Pd/Co[180,181], WTe_2/Fe_3GeTe_2[182], and Co/Pd/FeGeTe[183].

The first IDMI material reporting the observation of magnetic skyrmions consists of a single monolayer(ML) of Fe deposited on Ir(111) single crystal substrate denoted as Ir(111)/Fe(1ML) in 2011 at temperatures below 28 K[3]. A square lattice of skyrmions with an atomic-scale periodicity of 1 nm was observed as the spontaneous ground state. It was stabilized primarily by the four-spin interaction, IDMI, and a weak exchange interaction[184].

With the addition of a Pd monolayer on this material, Ir(111)/Fe(1ML)/Pd(1ML) have a cycloidal ground state. Skyrmions only gradually form under an increasing magnetic field from the cycloids and achieving a pure skyrmion state at large magnetic fields of 1.4 T. The skyrmion size remains very small, below 5 nm. While Ir(111)/Fe(1ML) led to the new class of four-spin interaction stabilized skyrmions, this material remains far from suitable for practical applications due to its extremely low temperature requirement.

Epitaxial oxides heterostructures of $SrRuO_3/BaTiO_3$[171] and $SrIrO_3/SrRuO_3$[175] are another pair of materials with skyrmion observation at slightly higher temperatures of up to 100 K. In $SrRuO_3/BaTiO_3$, the ferroelectric proximity effect induced by the ferroelectric $BaTiO_3$ layer on $SrRuO_3$ was used to control DMI in $SrRuO_3$ by ionic displacements. Thus the DMI and magnetic skyrmions in $SrRuO_3$ can be controlled by electric field [171]. $SrIrO_3/SrRuO_3$, on the other hand, stabilizes skyrmions using the strong spin-orbit interaction of $SrIrO_3$ to induce IDMI on the adjacent $SrRuO_3$. Both $SrRuO_3/BaTiO_3$[171] and $SrIrO_3/SrRuO_3$[175] offer competitive skyrmion sizes as small as 50 nm and 6 nm, respectively.

The stabilization of magnetic skyrmions was recently expanded into 2-dimensional van der Waals materials like Fe_3GeTe_2[182]. The PMA in Fe_3GeTe_2 was tuned by temperature and the number of layers. IDMI was induced by interfacing with WTe_2, and magnetic skyrmions were successfully stabilized between 94 K and 198 K with sizes close to 100 nm[182]. Ionic gating on this material had also been shown to strongly modulate magnetic interactions and raise its Curie temperature to room temperature[185].

A general approach to tuning the materials and structure to acquire the skyrmion state is to minimize domain wall energy density given by,

$$\sigma_{DW} = 4\sqrt{A_{ex}K_{eff}} - \pi D, \tag{3.1.11}$$

where A_{ex} is the exchange stiffness constant, K_{eff} is the effective perpendicular magnetic anisotropy, and D is DMI strength[186,187]. From Eq. 3.1.11, σ_{DW} can be minimized by having low K_{eff} or even become negative with sufficiently large D [13]. Note that skyrmions are stabilized as the ground state when $\sigma_{DW} < 0$. However, skyrmions can still be stabilized as metastable states when $\sigma_{DW} > 0$ [13,122]. The first term in Eq. 3.1.11 A_{ex} is essential for ferromagnetism but opposes the formation of non-collinear spin configurations.

$K_{eff} = K_{MC} - \mu_0 M_S^2 / 2$ must be positive with K_{MC} being stronger than the IP magnetic anisotropy due to DDI in thin films, $\mu_0 M_S^2 / 2$ [188,189]. The quality factor defined as $Q = 2K_{MC} / \mu_0 M_S^2$ is also commonly used to represent the same condition. Overly strong PMA inhibits the formation of domain walls and small domains. In the intermediate range where $Q \approx 1$, the labyrinth, stripe, bubble states with Bloch type domain walls can be induced[188]. The non-chiral nature of DDI forms small circular bubble domains that can be Bloch skyrmions with either $\pi/2$ or $-\pi/2$ helicities, or just a non-topological circular domain[190,191]. The chiral IDMI restricts the bubble domains to a single helicity[190,192]. DDI favors Bloch skyrmions, while IDMI favors Néel skyrmions. The critical IDMI strength at which the skyrmion becomes Néel skyrmions is given by $D_{Neel} > 3\pi^2 / (32dK_d)$ for d is the film thickness and $K_d = \frac{1}{2}\mu_0 M_S^2$ is the DDI induced demagnetizing or shape anisotropy[16,188].

Most of the room-temperature skyrmions reported in this category are primarily stabilized by DDI instead of IDMI[10]; DDI induces the local skyrmion energy minimum. The IDMI-induced local energy minimum exists at smaller skyrmion sizes but is suppressed by DDI. Experimentally, a skyrmion stabilized by the DDI or IDMI cannot be distinguished by the skyrmion size and shape. However, only IDMI can stabilize skyrmions with diameters less than 10 nm[10]. Mixed-use of terms bubble and skyrmion are present in literature. This thesis will use the term bubbles or bubble state to refer to all small circular reversed domains without specific configuration details.

In minimizing σ_{DW} towards zero, not only skyrmions but the labyrinth and stripe domains become increasingly stabilized[188]. With a low K_{eff} without any magnetic field, the spins form a demagnetized labyrinth state with a complex interconnected network of stripes. Under a perpendicular magnetic field, the stripes aligned antiparallel to the magnetic field shrink toward a minimum width before fracturing into stripe segments and skyrmions[193].

It is desirable to optimize IDMI by choice of HM or oxides depending on the FM layer, noting to have complementary IDMI with opposite signs on either interface of the FM layer if possible[122,194139121,140]. Symmetry in the material at both interfaces also does not necessitate the nullification of IDMI; for instance, Pd/Co/Pd exhibits strong IDMI due to large lattice mismatch at the top and bottom interfaces[180]. σ_{DW} is tuned by bringing the material close to the point of orientation transition from PMA to IMA, typically using insertion layers[165,195] or

FM thickness modulation[146,156,196]. Other techniques like hydrogenation of interfaces[197] and ion irradiation had also demonstrated similar skyrmion stabilizing properties[160,198]. The increase in repetitions can also be applied to enhance DDI to lower σ_{DW} and improve thermal stability while preserving the PMA and IDMI of the structure[199,200].

One highly desirable skyrmion property is stabilization under ambient conditions at room temperature without a magnetic field. The low σ_{DW} in these materials primarily driven by DDI inevitably introduces the labyrinth state as seen in most materials[155,192,201,202]. This challenge can be overcome by exchange bias as demonstrated in IrMn/CoFeB/MgO[167], $[Pt/Co/IrMn]_{11}$ [177], and Pt/Co/NiFe/IrMn[203]. The exchange bias from IrMn provides an effective field that can replace the required magnetic field. An exchange-coupled underlayer in Cu(001)/Ni/Cu/Ni/Fe was also demonstrated to provide a similar effective field on FM to acquire zero-field skyrmions[204]. Skyrmions can also be stabilized at zero magnetic fields within nanostructures due to the chiral tilt induced by IDMI at the edges[140,194,202,205]. Skyrmion lattices commensurate with the confining geometry initially formed using a magnetic field in nanostructures can persist after removing the magnetic field instead of extending into stripe domains[194,206,207].

Magnetic skyrmions are 2-dimensional spin textures and are typically considered to be translational invariant across the FM thickness. This assumption is valid for magnetic thin films of thickness less than the exchange length $l_{ex} = \sqrt{2A_{ex} / \left(\mu_0 M_S^2\right)}$ [16]. However, for magnetic multilayers with many repetitions[122,169,176], variation in spin texture across its thickness is reported[147,190,208,209]. DDI stabilizes the Bloch-type winding close to the middle layers of the FM but gradually transitions into the Néel-type winding at the top and bottom layers with opposite helicities to minimize stray fields referred to as Néel caps[190]. However, homogeneous helicity across all the layers is possible under sufficiently large IDMI[147,209].

With increasing temperature, a decrease in σ_{DW} and improved skyrmion stability occurs due to the different rate of change in all the magnetic interactions with temperature. While A_{ex}, K_{eff} and D decrease with temperature, the faster decay rate of K_{eff} compared to A_{ex} and D causes the resulting decrease in σ_{DW} and favouring skyrmions[148,210].

Apart from using ferromagnetic multilayers, ferrimagnetic skyrmions stabilized in materials like $Pt/GdCo/TaO_x$[211] and $[Pt/GdFeCo/MgO]_{20}$[168-170] had been reported. These materials can also be tuned into antiferromagnets by temperature modulation to their magnetization compensation temperature[212,213]. DDI is significantly suppressed in antiferromagnets to allow for skyrmion stabilized by IDMI energy well at diameters below 10 nm[10,211]. Ferrimagnetic skyrmions also have the critical advantage of diminished skyrmion Hall effect, which refers to the deviation of skyrmions in motion from the driving force that is detrimental to the stability of high-speed skyrmions[168] and will be further discussed in section 3.3.

The ferromagnetic multilayer structure can also be tuned to form synthetic antiferromagnet (SAF) using Ruderman–Kittel–Kasuya–Yoshida (RKKY) interaction between the FM layers through non-magnetic spacer layers[214]. Stabilization of SAF skyrmions had been demonstrated in Pt/Co/Ru[215], Pt/Co/Ni/Ir/Co/Ni/Ta[216], and Pt/Co/CoFeB/Ir/Co/CoFeB/W[217]. Similar to the ferrimagnetic skyrmions, SAF skyrmions benefit from the reduced DDI combined with strong IDMI to stabilize smaller skyrmions[215], and reduced skyrmion Hall effect crucial for skyrmion motion[217]. SAF skyrmions also hold the advantage for room temperature applications over the reported ferrimagnetic skyrmions that require a restrictive temperature range close to the magnetization compensation temperature.

Table 3.1.2| List of materials with IDMI that stabilize magnetic skyrmions regardless of the dominant stabilizing interaction like DDI and 4-spin interaction. The range of magnetic field, temperatures, and sizes of magnetic skyrmions observed is provided alongside the materials. The final column highlights the key material properties of the materials that differ from the majority. The zero magnetic field labelled with a star indicates these materials reported zero-field magnetic skyrmions as ground state or isolated magnetic skyrmions without stripe domains. RT refers to room temperature.

Material	**Magnetic Field (mT)**	**Temperature (K)**	**Skyrmion Size (nm)**	**Material Property**
Ir(111)/Fe(1ML)[3,218]	0*	< 28	1	4-spin interaction
Si(111)/YSZ/Ir(111)/Fe(1ML)[219]	0*	< 26.4	1	4-spin interaction
Ir(111)/Fe(1ML)/Pd(1ML)[5,7]	1400	< 8	1 – 5	4-spin interaction
$SrRuO_3/BaTiO_4$[171]	0 – 3000	5 – 80	50 – 100	
$SrIrO_3/SrRuO_3$[175]	0 – 40	<10 – 100	< 10 – 14	
WTe_2/Fe_3GeTe_2[182]	51 – 60	180 – 197	80 – 150	Van der Waals
Cu(001)/Ni/Cu/Ni/Fe[204]	0*	RT	200	
Pt/Co/Os/Pt[165]	0.05 – 2	299 – 301	1500 – 2000	
$Ta/CoFeB/TaO_x$[192,201]	0.48 – 0.54	RT	700 – 2000	
$Pt/Co/Al_2O_3$[129]	0.15 – 0.3	RT	~2000	
W/FeB/Ir/MgO[174]	0.4	RT	2000	
Ta/CoFeB/Ta/MgO[195]	0.48	RT	1500	
Pt/Co/CoFeB/Ir/Co/CoFeB/W[217]	0.2 – 0.3	RT	1000	Synthetic Antiferromagnet
[Pt/CoNi]$_2$[220]	0 – 0.2	RT	500 – 1000	
[CoB/Ir/Pt]$_3$[172]	0	RT	600 – 800	
[Pt/Co/W]$_8$[221]	7 – 26	RT	220 – 580	
[Pd/Co]$_5$[180,196]$_n$	0^c – 75	RT	180 – 500	
[Pt/CoFeB/MgO]$_{15}$[222,223]	0^c – 30	RT	113 – 400	
[Pt/Co/W]$_5$[199]	100 – 150	RT	300	
W/CoFeB/MgO[224]	0 – 40	RT	170 – 250	
[Pt/Co/Ta]$_{15}$[194]	0 – 7	RT	50 – 220	
[Pt/GdFeCo/MgO]$_{20}$[169]	110 – 130	RT	100 – 200	Ferrimagnet
Pt/Co/MgO[159,202]	0^c – 4	RT	130 – 190	
Pt/Ni/Co/Ni/Au/Ni/Co/Ni/Pt[127]	6	RT	160	
[Co/Tb/Ni/Pt]$_{20}$[176]	30 – 47	RT	140	
[Pt/Co/Ru]$_2$[215]	0 – 60	RT	30 – 100	Synthetic Antiferromagnet
[Pt/Co]$_{15}$[225]	0 – 200	RT	100	
[Ir/Co/Pt]$_{10}$[121,140]	10 – 80	RT	30 – 90	
[Pt/[Co/Ni]$_2$/Ir]$_{20}$[200]	144	RT	80	
[Ir/Fe/Co/Pt]$_{20}$[122]	0 – 200	RT	55 – 75	
[Co/Ni/Pt]$_{20}$[176]	50 – 120	RT	69	
[Pt/Co/Ta]$_6$[146]	100 – 150	RT	50	
Ru(0001)/Co(1ML)[154]	100 – 200	RT	40 – 50	
$Pt/GdCo/TaO_x$[211]	0 – 450	RT	10 – 30	Ferrimagnet
IrMn/CoFeB/MgO[167]	0	RT	400	Exchange Bias
[Pt/Co/IrMn]$_{11}$ [177]	0	RT	99 – 113	Exchange Bias
Pt/Co/NiFe/IrMn[203]	0	RT	46 – 86	Exchange Bias

3.1.5 Dipole-dipole Interaction Stabilized

In this section, the materials exhibit magnetic skyrmions stabilized by DDI without IDMI to distinguish the materials from the previous section. Here, we categorize these two classes of materials by the helicity degeneracy induced by IDMI. Materials in this section have Bloch-type domain walls, skyrmions, and other textures with freedom in helicities. This freedom plays a vital role in realizing new spin textures like biskyrmions and higher-order skyrmions discussed in this section.

The stabilization of magnetic skyrmions in this class occurs due to the competition between PMA and DDI and low domain wall energy[190,226-228]. These materials have the labyrinth ground state that transitions into stripes segments and eventually skyrmions with an increasing magnetic field, as shown in Fig. 3.1.10. More importantly, magnetic skyrmions with both helicities are stabilized simultaneously, as shown in Fig. 3.1.10(c)[190]. Thermally-induced switching of helicity of skyrmions was also demonstrated in $BaFe_{10.15}Sc_{1.8}Mg_{0.05}O_{19}$ with increasing temperature[228]. In sufficiently thick materials such as $[Fe/Gd]_{100}$, chiral Néel caps form at the top and bottom layers that can be driven by SOT[191]. The materials, TbFeCo[226], $[Fe/Gd]_N$[190,229], $Tm_3Fe_5O_{12}$[227], $BaFe_{10.15}Sc_{1.8}Mg_{0.05}O_{19}$[228] are suitable for room temperature applications, but the nature of DDI limits the minimum skyrmion sizes and have generally larger skyrmions than that with IDMI[10]. In the frustrated magnet, Fe_3Sn_2[230-233], the magnetic skyrmions and spin textures reported are still primarily stabilized by DDI as those in this category as opposed to competing exchange interaction, hence show very distinct properties from the frustrated magnets discussed in Section 3.1.6.

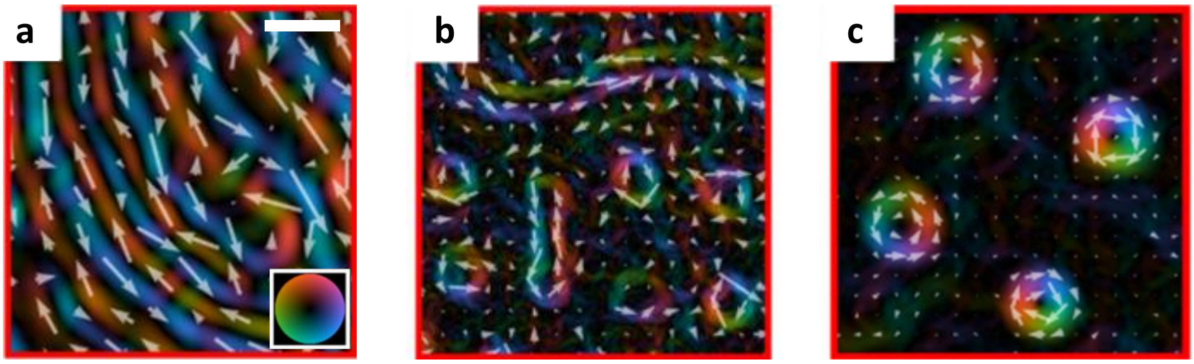

Figure 3.1.10| IP spin configuration of $[Fe/Gd]_{80}$ under an increasing out-of-plane magnetic field of (a) 0mT, (b) 145mT, and (c) 220mT[229]. The scale bar represents 150 nm.

The stability of magnetic skyrmions had been attributed to the topology of the skyrmions for many years. Still, a direct experimental comparison between a topological and non-topological structure had been challenging. This was possible in DDI materials due to the ability to stabilize both skyrmions and non-topological bubbles in the same material using different magnetic field sequences[234]. The experiment provided clear enhanced stability of skyrmions over non-topological bubbles by annihilating at higher fields and shrinking down to smaller sizes by magnetic fields before annihilation.

The exploration of skyrmions materials into two-dimensional van der Waals materials yield $Cr_2Ge_2Te_6$[235] and Fe_3GeTe_2[236]. These materials demonstrate the same labyrinth, stripe and skyrmion textures like the other DDI materials but only at a low temperature of 60 K and 150 K for $Cr_2Ge_2Te_6$[235], and Fe_3GeTe_2[236], respectively. However, an interesting observation of single helicity skyrmions was observed in $Cr_2Ge_2Te_6$ compared to the DDI materials with helicity degeneracy and generally showed equal populations of both helicities. This homochiral nature of the skyrmions in $Cr_2Ge_2Te_6$ was attributed to the emergence of Bloch lines along stripe domains wall that undergoes unwinding into a single helicity when in proximity.

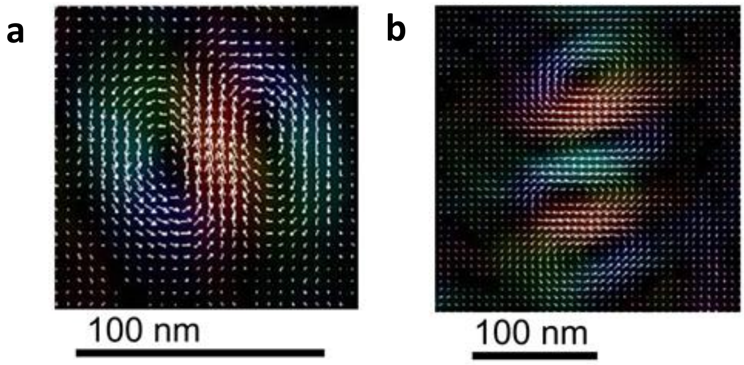

Figure 3.1.11| IP spin configuration of (a) biskyrmion and (b) four skyrmions chain[237].

The freedom of helicities in DDI materials also gives rise to the stabilization of new spin texture of biskyrmions reported in MnNiGa[238], $La_{1.37}Sr_{1.63}Mn_2O_7$[239] and $La_{0.7}Sr_{0.3}Mn_{0.95}Ru_{0.05}O_3$[237]. The configuration of biskyrmions comprises of two skyrmions with opposite helicities interlocked side-by-side with a common form of winding along their intersections, as shown in Fig 3.1.11(a). In $La_{0.7}Sr_{0.3}Mn_{0.95}Ru_{0.05}O_3$, the bounding of four skyrmions with alternating helicities was also observed, as shown in Fig. 3.1.11(b)[237]. These textures bear implications of forming a much stronger topological Hall effect than one can achieve in a skyrmion lattice. Possible applications of these properties remain to be explored.

Table 3.1.3| List of DDI skyrmions and biskyrmion materials without IDMI and their corresponding magnetic field, temperature and skyrmions sizes ranges. Remarks are added as useful additional characteristics of the materials.

Material	**Magnetic Field (mT)**	**Temperature (K)**	**Skyrmion Size (nm)**	**Remarks**
TbFeCo[226]	0	RT	200	Ferrimagnetic, Skyrmonium
$[Fe/Gd]_N$[190,229]	0 – 185	RT	71 – 230	Ferrimagnetic
$Tm_3Fe_5O_{12}$[227]	3.5 – 4.5	RT	500	Ferrimagnetic
$BaFe_{10.15}Sc_{1.8}Mg_{0.05}O_{19}$[228]	110 – 200	RT	100 – 300	
Fe_3Sn_2[230,231]	0 – 800	130 - 630	160 – 380	Frustrated
$Cr_2Ge_2Te_6$[235]	12 – 200	17 – 60	77 – 121	Van der Waals
Fe_3GeTe_2[236]	68 – 92	93 – 150	120	Van der Waals
MnNiGa[238]	50 – 500	16 – 338	120 – 200	Biskyrmion
$La_{1.37}Sr_{1.63}Mn_2O_7$[239]	350 – 400	20 – 60	130 – 150	Biskyrmion
$La_{0.7}Sr_{0.3}Mn_{0.95}Ru_{0.05}O_3$[237]	70 – 300	RT	90 – 200	Biskyrmion
$La_{1.2}Sr_{1.8}Mn_{1.8}Ru_{0.2}O_7$[240]	0 – 300	5 – 70	75 – 200	

3.1.6 Magnetic Frustration Stabilized

Magnetic frustration is another interaction that stabilizes magnetic skyrmions apart from IDMI, DDI, and four-spin interactions discussed thus far. Magnetic frustration refers to the circumstance where localized spins experience competing exchange interactions that cannot satisfy all spins simultaneously and lead to a huge number of possible degenerate ground states[25,241,242]. Such circumstances can arise from antiferromagnetic coupling in specific geometries, like triangular, Kagome, tetrahedral, spinel, pyrochlore lattices[243], and/or the RKKY interaction that exhibits oscillatory exchange interaction[244]. Within the highly degenerate ground states, modulated spin order can arise and even stabilize skyrmion lattices under a magnetic field[245]. With the inclusion of PMA, the range of possible multiple-**q** states are extended[246]. Even three-dimensional spin textures are expected to be found in these materials[247]. Frustrated magnets are theoretically proposed to host the widest range of spin textures. It has the freedom in both helicity and vorticity compared to DMI materials with fixed helicity and DDI materials that have freedom between a pair of helicity but not vorticity[246]. Among the materials reported thus far includes, Gd_2PdSi_3[248-250], $Gd_3Ru_4Al_{12}$[251], $GdRu_2Si_2$[252], and $SrFeO_3$[253].

The frustrated Gd_2PdSi_3 with a triangular lattice and RKKY interaction stabilized four key spin textures including a Bloch skyrmion lattice, and three other incommensurate spin states (IC) labelled IC-1, IC-2, depinned (DP) as shown in Fig. 3.1.12(b) and (c)[248-250]. Deduced from the resonant x-ray scattering results, IC-1 had been identified as a triple-q with no net scalar spin chirality, likely being a meron-antimeron lattice. IC-2 corresponds to fan-like state with an oscillatory IP and constant out-of-plane magnitude as shown in Fig. 3.1.12(e). DP closely relates to IC-2 with a tilted modulation vector from the plane. The Bloch-type winding skyrmions arise due to DDI. The modulation periods were extremely small at 2.5nm, at the length scale of the RKKY interaction. In addition, the skyrmion phase extending down to the lowest temperatures suggests that it is not thermal fluctuation-induced in contrast to that found in bulk DMI materials[248].

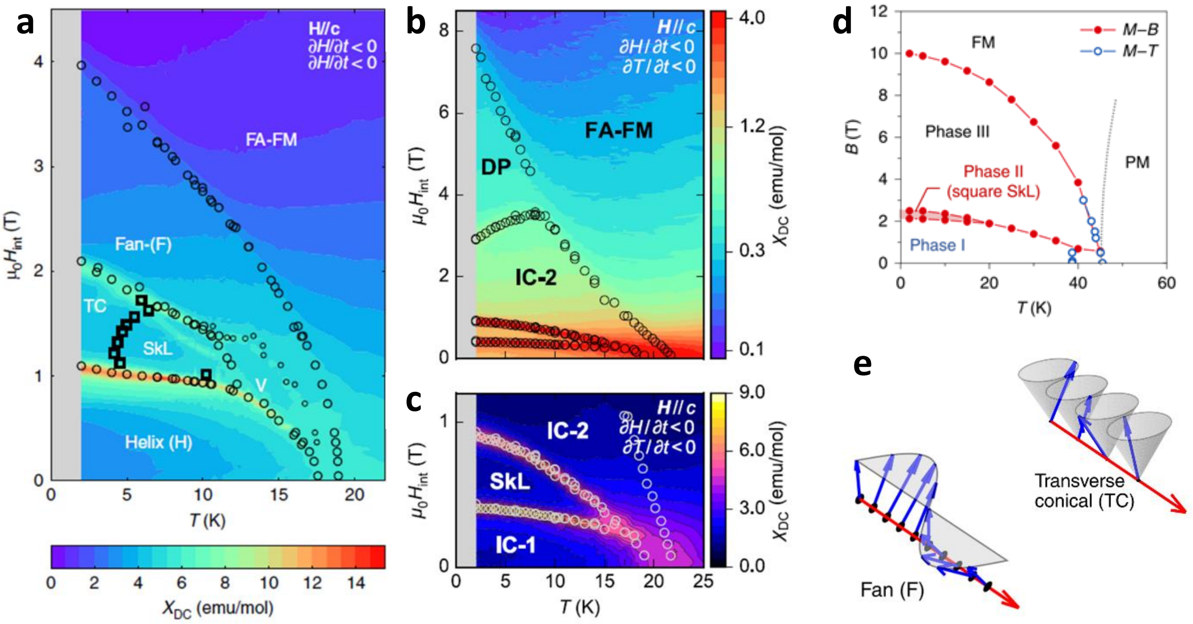

Figure 3.1.12| Spin texture phase diagram of (a) Gd$_3$Ru$_4$Al$_{12}$[251], (b-c) Gd$_2$PdSi$_3$[248,249], and (d) GdRu$_2$Si$_2$[252]. In (a-c) TC, SkL, FA-FM and V corresponds to transverse conical, skyrmion lattice, field-aligned ferromagnet and a yet to be identified state, respectively. In (b) IC, and DP corresponds to incommensurate state, and depinned state, respectively. In (d), FM and PM correspond to ferromagnet, and paramagnet state, respectively. (e) Spin configuration of the fan and transverse conical states.

In Gd$_3$Ru$_4$Al$_{12}$[251] with the breathing Kagome lattice in conjunction with RKKY interaction stabilizes similar spin textures like the Bloch skyrmion lattice and fan state, but also a multi-domain helical, transverse conical, and a yet-to-be-identified V phase shown in Fig. 3.1.12(a). A transverse conical state impedes the skyrmion lattice phase from extending down to the lowest temperatures due to IP anisotropy, and thermal fluctuations are required to overcome this anisotropy. The modulation periods are also very small at 2.8 nm[251].

$GdRu_2Si_2$[252] demonstrated the possibility of skyrmion stabilization by magnetic frustration from RKKY interaction even without geometric frustration. The spin textures labelled phase I, II and III correspond to the helical, square Bloch skyrmion lattice, and fan states, bearing close resemblance to the other magnetically frustrated systems. The manifestation of the square lattice, instead of the hexagonal one, is postulated to arise from the four-spin interaction also found in Ir(111)/Fe(1ML)[3,218]. The freedom in spin helicity was also found from the LTEM imaging of the skyrmion lattice that showed skyrmions with both CW and CCW winding around their cores. Even smaller modulation periods were detected in this material at 1.9 nm.

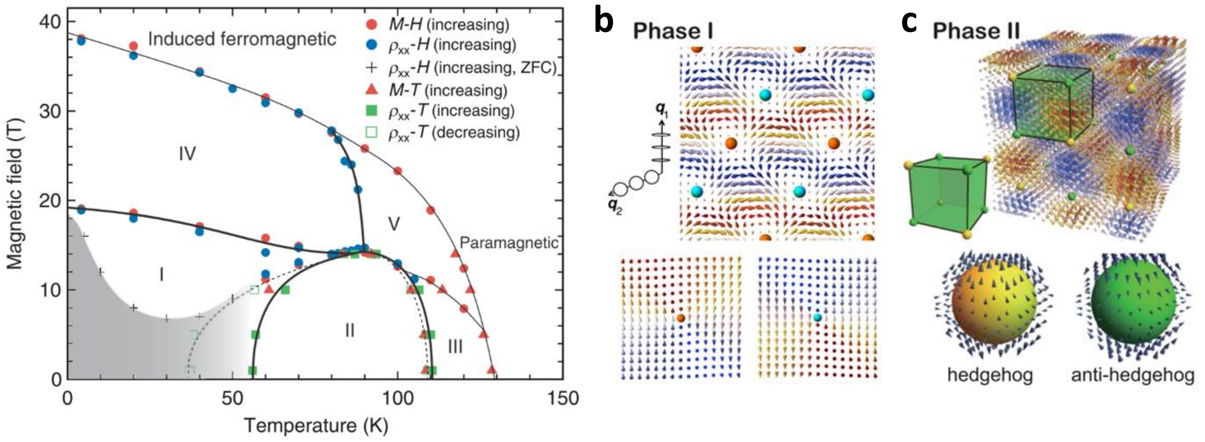

Figure 3.1.13| (a) Magnetic field-temperature spin texture phase diagram of $SrFeO_3$[253]. Spin texture of (b) Phase I and (c) Phase II.

In the centrosymmetric cubic $SrFeO_3$, magnetic frustration arises from possibly competing exchange interactions[254] or the double-exchange mechanism considering the itinerant oxygen p-holes[255] to stabilize spin spirals. The spin spirals modulation along $\langle 111 \rangle$ in the cubic structure with freedom in helicity manifests one of the most complex and yet fully elucidated set of spin textures across temperature and magnetic field labelled as phases I to V in Fig 3.1.13(a). Phase I, II and III has been identified as the anisotropic double-**q**, isotropic quadruple-**q** structures, and single-**q** helical state parallel to $\langle 111 \rangle$, respectively[256]. The anisotropic double-**q** state consists of both a Bloch and Néel type spin helices along different modulation vectors. The quadruple-q structure corresponds to a hedgehog-antihedgehog lattice reminiscent of that found in MnGe[18,70]. Further investigations are required to comprehensively understand the interplay of magnetic interactions in $SrFeO_3$ and conclusively determined all the spin textures.

Table 3.1.4| List of DDI skyrmions and biskyrmion materials without IDMI with their corresponding magnetic field, temperature and skyrmions size ranges. Remarks are added as useful additional characteristics of the materials.

Material	**Magnetic Field (mT)**	**Temperature (K)**	**Skyrmion Size (nm)**	**Remarks**
$Gd_3Ru_4Al_{12}$[251]	1000 – 2000	5 – 12	2.8	
Gd_2PdSi_3[248]	500 – 1000	0 – 15	2.5	
$GdRu_2Si_2$[252]	2000 - 2400	46	1.9	Four-spin interaction
$SrFeO_3$[253]	0 – 10000	80 – 120	1.8	HL

3.1.7 Metastable Magnetic Skyrmions

The magnetic skyrmion lattice phase stabilization is primarily tuned under the constraining conditions of temperature and magnetic field, but is also possible by pressure[32-34] and electric fields[171]. Beyond investigating the skyrmion lattice as the ground state, metastable magnetic skyrmions beyond their thermodynamically stable conditions are the ones useful as nanoscale information carriers[164,257-260]. The investigations of metastable skyrmions are highly non-trivial with a wide range of spin textures bordering the skyrmions lattice phase, including, but not limited to, helical, conical[28,118], cycloid[20,108,110], stripes[122,146,192,201], and ferromagnetic states. The annihilation of the metastable skyrmions into other ground-state spin textures depends on the material and conditions via several possible mechanisms, such as Bloch point formation[261,262], antiskyrmion formation, symmetric shrinking[263-266], edge escape, vortex formation, or non-magnetic defects. In addition to this, a significant contribution of configurational entropy to skyrmion lifetime further inflates the complexity required for skyrmion lifetime modelling beyond just the energy barrier[62,267,268].

The venture into metastable magnetic skyrmions begun in the class of BDMI materials. The skyrmion lattice being a thermal fluctuation induced state, is only accessible at high temperatures. However, by performing cooling under a magnetic field, the skyrmion lattice phase can persist to the lowest temperature as first reported by Münzer *et al.* in $Fe_{0.8}Co_{0.2}Si$, as shown in Fig. 3.1.14(a)[269]. Similar observations were later reported in MnSi[39,74], Co-Zn-Mn alloys [98,99], and Cu_2OSeO_3[76] as shown in Fig. 3.1.14(b)–(d). The skyrmion lattice is stabilized from collapse into the helical and conical states by an energy barrier. The skyrmion lattice annihilates at a maximum rate just below the equilibrium skyrmion lattice phase. Using fast cooling rates, the dwell time at these unstable temperatures is minimized before reaching sufficiently low temperatures where thermal energy can no longer overcome the energy barrier. Depending on the metastability of the skyrmion lattice, higher cooling rates are required for MnSi[25,39,74], compared to that for $Fe_{1-x}Co_xSi$[61] and $Co_8Zn_8Mn_4$[99]. Field cooling offers a vital pathway to access zero-field magnetic skyrmions, as illustrated in Fig. 3.1.14(b) and (c)[39,98]. Metastable skyrmion lattice at low temperatures transitions into a square lattice, induced by magnetic anisotropy along the crystal lattice[39,98,99].

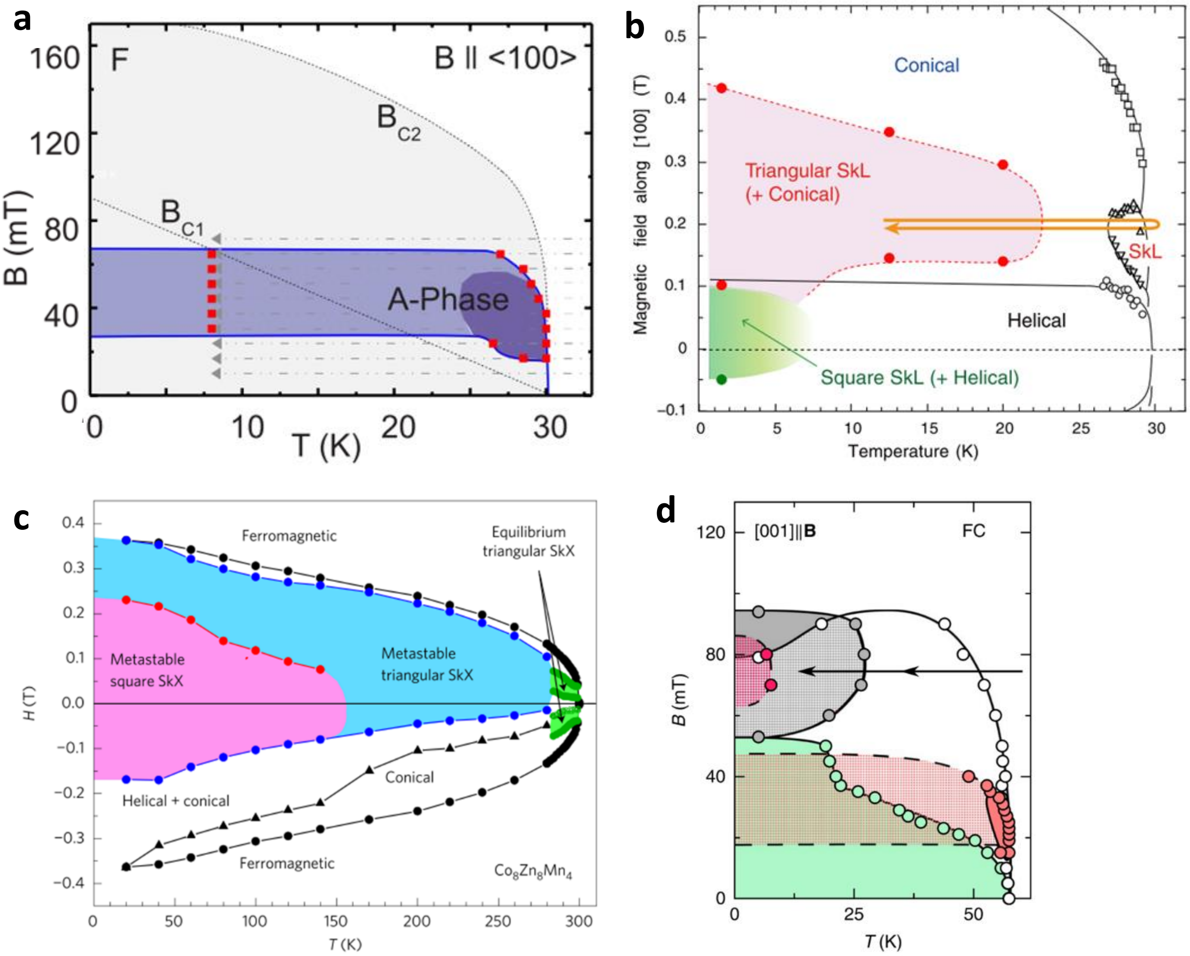

Figure 3.1.14| (a) Magnetic phase diagram of $Fe_{0.8}Co_{0.2}Si$ under field cooling where the blue shaded regions represent the skyrmion metastable lattice phase[269]. (b) MnSi[39]. (c) Co8Zn8Mn4[98]. (d) Cu_2OSeO_3[76]

In thick materials that form skyrmion tubes through their bulk, the annihilation of skyrmions into other states are characterized by the formation of Bloch points or hedgehogs defects triggered by transverse fluctuations[62,270]. These defects propagate across the skyrmion tube leading to annihilation. This propagation can be pinned and suppressed by defects in the bulk to boost skyrmions' metastability. The role of defects was initially proposed to explain the high metastability found in $Co_8Zn_8Mn_4$[99] and $Fe_{1-x}Co_xSi$[61] compared to MnSi[74], and later explicitly demonstrated 50 times increment of skyrmion lifetime in Cu_2OSeO_3 with 2.5% doping of Zn[92].

In 2017, a critical experiment that highlights the importance of entropy on skyrmion lifetime was reported by Wild *et al.*[62]. In this experiment, the temperature dependence of skyrmion lifetime τ follows the Arrhenius equation, given by,

$$\tau = \tau_0 e^{E_a/(k_B T)}, \tag{3.1.12}$$

where τ_0 is the attempt time, and E_a is the energy barrier. E_a in this system displayed magnetic field dependence that decays sharply at large positive fields and negative fields while τ_0 increases dramatically from 10^{-37} s to 10^{-2} s simultaneously. This phenomenon is referred to as the enthalpy-entropy compensation or Meyer-Neldel rule. Lifetime increments from a larger E_a are partly negated by entropic effects that increase the number of pathways across the barrier[62]. Thus τ_0 cannot be trivialized for skyrmion lifetime.

Atomistic numerical works derive τ_0 using rate theories, like harmonic transition state theory(HTST)[271] or Langer's theory[268]. In these theories, the term τ_0 rely on the entropic difference between the initial skyrmions state and the saddle point state with maximum energy during the annihilation process. Skyrmions in thin films annihilate via few main mechanisms, including defects, escape through a boundary, and radial collapse by symmetrical shrinking, in order of decreasing tendency[263,264,268,272]. Notably, escaping through a boundary remains more likely than radial collapse, even though it has a higher energy barrier, highlighting the significance of the entropic contribution to the overall metastability[268]. Thus, the degree of freedom in skyrmion fluctuations that increases with its size is favourable[265]. Recent work by Varentcova *et al*. concluded that the contribution of the energy barrier to skyrmion lifetime is insignificant compared to the skyrmion entropy at room temperature. Thus, to maximize skyrmion entropy, the narrowest and bubble-like skyrmion body is ideal as it carries the maximum number of magnon modes.

3.2 Skyrmion Nucleation

This section presents the experimental demonstrations of skyrmion nucleation techniques via the interplay of skyrmion stability under various conditions and excitations. These conditions and excitations include magnetic field, temperature, electrical currents, spin currents, electrical field, laser, X-ray, stress, and pressure. The ideal nucleation technique would be one that can nucleate single skyrmions at precise positions within nanoseconds or faster and perform selective annihilation of skyrmions. The ease of integration into devices and energy efficiency are also vital for technological applications.

3.2.1 Magnetic Field

A magnetic field is essential to stabilize magnetic skyrmions as the equilibrium ground state for most magnetic skyrmion materials, other than materials like Ir(111)/Fe(1ML)[3,218] and possibly in engineered exchange-biased structures IrMn/CoFeB/MgO[167], $[\mathrm{Pt/Co/IrMn}]_{11}$ [177], and Pt/Co/NiFe/IrMn[203]. Here, we present the use of magnitude, direction, and sequential magnetic field sweeps to obtain metastable magnetic skyrmions.

The use of tilted magnetic fields with an IP component was demonstrated to nucleate isolated skyrmions effectively[149,161,178,273]. The addition of an IP magnetic field reduces the role of effective magnetic anisotropy that impedes skyrmion stability, hence improving skyrmion density up to several multiples[149] or even the emergence of a previously inaccessible skyrmion lattice via perpendicular magnetic fields alone[273]. In work by Qin *et al.*, nucleation of a metastable skyrmion lattice by a highly tilted magnetic field sweep at an angle close to the plane and subsequent polarity reversal of the skyrmion lattice were demonstrated[161]. The tilted magnetic field in materials without DMI or weak DMI can nucleate non-topological bubbles instead of skyrmions[234].

In confined structures, skyrmions nucleation and their subsequent stabilization at zero-field can be accessed easily[140,194,202,205]. The confining potential at the structure edge induced by DMI allows for the nucleation of skyrmions by magnetic field pulses that remain stable without a magnetic field[205]. Woo *et al.* demonstrated the nucleation of a skyrmion lattice commensurate to a 2 μm disc initially in a labyrinth state using a bipolar magnetic field pulse[194]. When the nanostructure dimensions are comparable to the skyrmion size, it can only form a single skyrmion or be in a ferromagnetic state; hence magnetic field pulses can be applied as a switch between the two states[140,202].

A localized magnetic field can be used to switch magnetization within a narrow region at the order of the skyrmion size and perform skyrmion nucleation. Zhang *et al*. demonstrated nucleation using the stray field of a magnetic force microscopy tip to induce localized fields[150]. The ambient labyrinth domains are sliced into an array of skyrmions by performing scans across it[150,274]. For a high remnant material of $Co_{45}Pt_{55}$, isolated skyrmion can be nucleated from an ambient ferromagnetic state[275]. Casiraghi *et al.* later also showed that under an external magnetic field, these skyrmions could even be reliably moved using a tip by the repulsion with the skyrmion core[137].

Spin textures and skyrmions are hysteretic and display magnetic field history dependence. Skyrmion density acquired from a positive and negative field sweep differs; More skyrmions are formed during the fracturing of stripe domains than nucleation from the ferromagnetic state. Exploiting magnetic skyrmions’ metastability, a perpendicular magnetic field sweep to an intermediate field instead of saturation before removing the magnetic field can obtain higher zero-field skyrmion density[130,133,134,152,276]. A characterization technique that can optimize this intermediate field is the FORC technique. This technique, in short, reveals the irreversibility of magnetization with reversal fields to identify skyrmion or other spin texture transformations[130]. The FORC technique is fully detailed in section 4.2.4. Our work on further unravelling the information derivable and understanding the FORC results are presented in Chapter 6.

Defects can be used as nucleation sites with a pathway of lower energy barrier[268,272,277]. For increased reliability, intentional defects can be fabricated, as demonstrated by Fallon *et al*. using Ga^+ beam localized illumination. Subsequently, skyrmions are reliably nucleated at the defect sites by magnetic field pulses and persist after the magnetic field is removed[198].

3.2.2 Electrical and Spin Current

Electrical and spin currents are the primary nucleation method of interest because they are comparatively easier to integrate and operate with electronics. Furthermore, these currents can also perform control, motion, and detection, providing opportunities for skyrmionic devices fully functional by electrical control. The use of current injections is also less perturbative compared to the magnetic field and temperature variations with thermodynamic changes on the material. Below we present several current-induced nucleation performed using constrictions of nanostructures, fabrication of skyrmion injection tips, or just homogeneous current across a nanotrack.

The use of geometrical constriction that affects the current distribution along the nanotrack for skyrmion nucleation was first demonstrated by Jiang *et al.*, as shown in Fig. 3.2.1(a)[192]. Under an applied perpendicular field close to saturation with sparse stripe and skyrmions, current injection drives the stripe domains on the left into the constriction. As the stripe domains exit the constriction on the right, the diverging current causes the stripe domains to snip into skyrmions, analogous to blowing a soap bubble[192,278]. A more simplified nanostructure with just a short constricting segment at the ends of the nanotrack shown in Fig. 3.2.1(b) was just as effective[260]. In this device, the skyrmion and stripes are generated by SOT that acts on the tilted magnetization at the device boundary induced by DMI. In a similar structure with a nonmagnetic conducting point contact at the constriction, as shown in Fig. 3.2.1(c), current-induced skyrmion nucleation is mediated by the formation of a skyrmion-antiskyrmion pair by a divergent SOT[157].

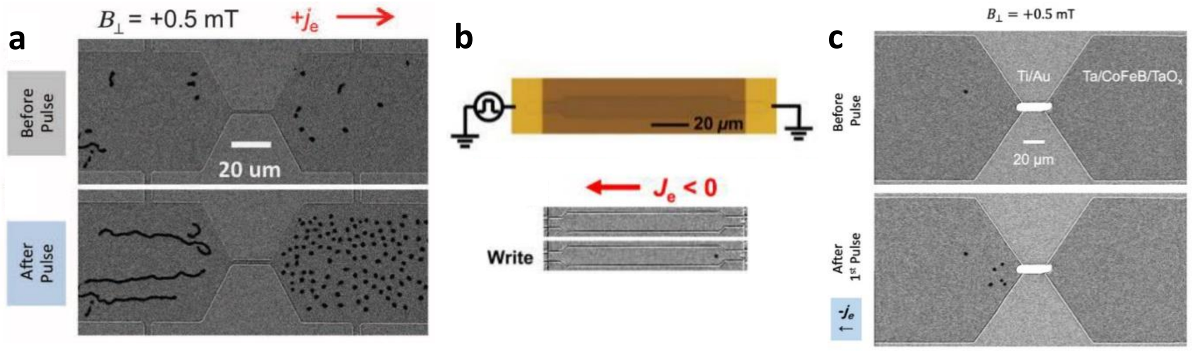

Figure 3.2.1 Current-induced skyrmion nucleation devices utilizing (a) a constriction between two wide regions[192], (b) short constriction segment at the ends of the track[260], and (c) nonmagnetic conducting point contact at the constriction[157].

A sharp conducting tip offers a small region of high current density used for nucleation before diverging into the nanotrack, as shown in Fig. 3.2.2(a)–(c)[127,172]. The mechanism for nucleation was a SOT-induced switching at the tip instead of purely a thermally induced phenomenon due to Joule heating. However, heating does assist in lowering the threshold current density for nucleation under longer pulses[172].

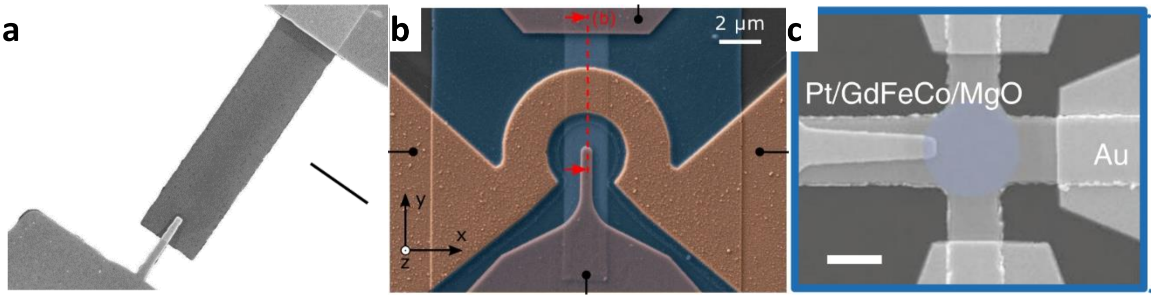

Figure 3.2.2 (a-c) Images of experimentally demonstrated nucleation devices utilizing a sharp current injection tip[127,170,172]. (a) Scale bar, 3 μm. (c) Scale bar, 4 μm.

Skyrmion nucleation has also been observed by a simple electrical current injection through a straight nanotrack. Many works attribute the nucleation process to a thermally induced phenomenon due to Joule heating[128,141,176,225]. The observed minimum current density and voltage relations with the thickness of sample and pulse durations support this mechanism[128]. An extensive investigation of current-induced skyrmion nucleation under different temperatures, magnetic fields, current densities, and current profiles further supports the observed nucleation to be thermally indcued[136]. Brock *et al*. demonstrated materials with lower saturation magnetization and perpendicular anisotropy favour this nucleation via Joule heating[176].

Besides Joule heating, the action of SOT on defects is another possible mechanism to trigger nucleation by homogeneous electrical currents[169,223,279]. Defects along a nanotrack lead to inhomogeneous material properties and magnetization. Homogenous SOT acting across these regions cause nucleation of intermediate non-topological bubbles or even skyrmion-antiskyrmion pairs that transition into skyrmions as they are driven out of the defects[169,223,279]. Artificial defects at sharp corners of a constriction along a track were also used as nucleation sources driven by current-induced SOT[223].

Perpendicular current injection for skyrmion nucleation in an MTJ was demonstrated via STT induced magnetization reversal[280]. Local spin current injection using an STM tip was also shown to both nucleate and annihilate skyrmions precisely and selectively[5].

The investigation on $Co_8Zn_9Mn_3$ crystal by Yu *et al.* reveals the emergence of dynamically induced skyrmions under a continuous flow of DC electrical current[281]. These skyrmions are stabilized within a limited current density range. This phenomenon arises from the fluctuations due to STT across the modulating helical or conical states that trigger the transition into isolated skyrmions or even skyrmion lattices[282]. These dynamic skyrmions annihilate after the removal of the electrical current.

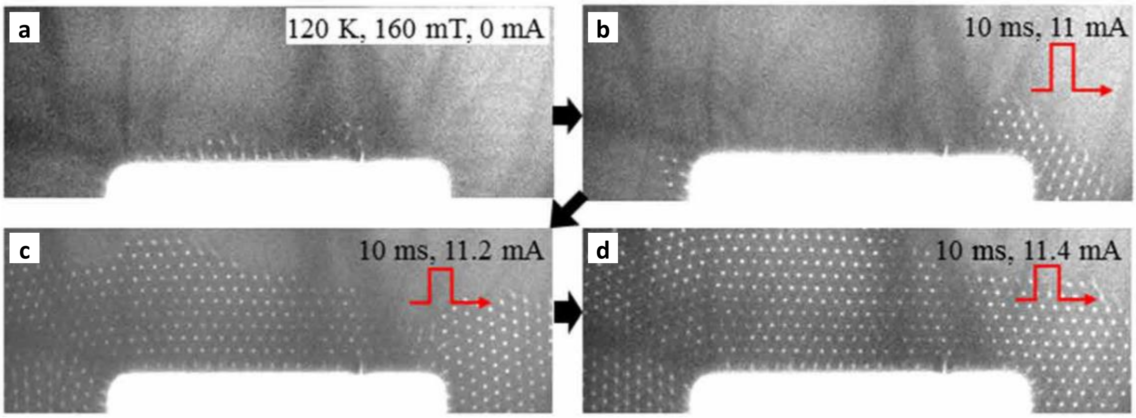

Figure 3.2.3 (a-d) Illustration of skyrmion nucleation using current pulses on FeGe thin plate.

BDMI materials like FeGe crystals cannot utilize SOT-related mechanisms. However, metastable skyrmions nucleation can still be performed by electrical current pulses, as demonstrated by Yu *et al.* shown in Fig. 3.2.3[52]. By fabricating a rectangular notch along the bottom edge of the track, the inhomogeneous current at the corners of the notch generates a spin current that excites skyrmions in its vicinity and extends away from the notch by additional pulses shown in Fig. 3.2.3(a)–(d). Annihilation of these skyrmions could also be performed using a reversed current[52].

The IDMI material has a clear advantage over the BDMI materials due to the availability of SOT that accompanies the materials used to induce IDMI. However, the BDMI materials show lower critical current densities for nucleation in less than 10^9 A/m^2 compared to the IDMI material, with a majority exceeding 10^{10} A/m^2 and up to 10^{12} A/m^2 shown in Table 3.2.1. As electrical currents can also drive skyrmion motion, decoupling the current paths for nucleation and motion will be necessary. For instance, a short nucleating segment that lies transverse to the track instead of the devices presented above.

Table 3.2.1| List of materials with their corresponding critical current density and mechanism involved in skyrmion nucleation.

Material	**Current density (A/m^2)**	**Mechanism/ Structure**
Ta/CoFeB/TaO$_x$[192]	6×10^8	Constriction
Ta/CoFeB/TaO$_x$[260]	2.3×10^{10}	Short constriction segment
Ta/CoFeB/TaO$_x$[157]	8.8×10^{10}	Non-magnetic constriction
Pt/Ni/Co/Ni/Au/Ni/Co/Ni/Pt [127]	2.6×10^{11}	Nucleation tip
[Co$_{68}$B$_{32}$/Ir/Pt]$_3$[172]	1.0×10^{12}	Nucleation tip
[Pt/GdFeCo/MgO]$_{20}$[170]	1.7×10^{10}	Nucleation tip
[Pt/Ir/Co]$_{10}$[128]	2.0×10^{11}	Joule heating
[Pt/Co]$_{15}$[225]	7.6×10^9	Joule heating
[Co/Ir/Pt]$_{20}$[141]	2.0×10^{11}	Joule heating
[Co/Ni/Pt]$_{20}$[176]	2.4×10^9	Joule heating
[Pt/CoFeB/MgO]$_{15}$[223]	2.6×10^{11}	Defect
[Pt/GdFeCo/Mgo]$_{20}$	2.5×10^{10}	Defect
Co$_8$Zn$_9$Mn$_3$[281]	2×10^8	Under DC current
FeGe[52]	1×10^9	Rectangular notch

3.2.3 Electric Field

Electric fields are another attractive means of electrical control due to their significantly less dissipative nature than electrical currents. An electric field can induce and control various magnetic interactions, including exchange interaction[283-285], magnetic anisotropy[286-289], and DMI[290-294], all critical in determining magnetic skyrmion stability.

Hsu *et al*. demonstrated electric field-controlled reversible skyrmion nucleation and annihilation on Ir(111)/Fe(3ML)[124]. The electric field was applied locally using the STM tip. Nucleation and annihilation occur via an electric field-induced relaxation of the Fe atom nuclei that modulates the exchange interaction to favour the ferromagnetic or skyrmion state[285,295].

Voltage-controlled magnetic anisotropy (VCMA) is the primary mechanism for the category of IDMI materials[129,167,220,296] where the skyrmions in magnetic multilayers are predominantly DDI stabilized and relied on its competition with perpendicular magnetic anisotropy to stabilize magnetic skyrmions. The first demonstration of skyrmion density modulation using electric fields was performed by Schott *et al*. on Pt/Co/Al$_2$O$_3$[129]. A decrease of K_{eff} and M_S by –47% and –64%, respectively, was measured under a voltage change from +20 V to –20 V. The substantial variation of M_S was attributed to the proximity of T_C to room temperature at low Co thickness, while the change in K_{eff} remains for thicker Co. Nonetheless, a consistent decrease or increase of σ_{DW} was achieved to nucleate and annihilate skyrmions, respectively. In another work by Ma *et al.*, electric field control was performed on a gradient sample of Pt/CoNi/Pt/CoNi/Pt with varying thickness[220]. As the electric field modulates K_{eff} across the gradient, skyrmions only existed along a particular section of the device with optimal K_{eff} that shifts following the magnitude of the electric field. Note that the skyrmion density directly correlates to the electric field; skyrmion density returns to the ambient state after removing the electric field.

Non-volatile nucleation and annihilation using voltage pulses were later demonstrated by Bhattacharya *et al.* on IrMn/CoFeB/MgO[167]. Nucleation could be performed using ±7 V pulses that correspond to 157 mV/nm without an external magnetic field due to exchange bias. In addition, the annihilation voltage pulse also triggered a stripe to skyrmion transformation[167]. Similar skyrmion nucleation and annihilation by voltage pulses were later demonstrated in Ta/CoFeB/MgO/CoFeB/W MTJ as well[296]. While a magnetic field is unnecessary for the nucleation process, a magnetic field aligned to the skyrmion core improves the nucleation probability.

In another approach to electric field control of skyrmions demonstrated by Ba *et al.*, the magnetic multilayer of $[Pt/Co/Ta]_5$ was deposited on a ferroelectric substrate $Pb(Mg_{1/3}Nb_{2/3})_{0.7}Ti_{0.3}O_3$ (PMN-PT). The electric field control of the magnetic layers was performed via an electric-field-induced strain in the substrate[286]. The tensile stress in the substrate is transferred onto the magnetic multilayer to weaken IDMI and K_{eff}. Non-volatile nucleation of skyrmions from a ferromagnetic state under a 60 mT magnetic field was demonstrated under a transient electric field of –4 kV/cm. This strain-mediated electric field control offers new opportunities for modulation across the whole magnetic multilayer compared to conventional means involving charge accumulation across only a particular interface.

Electric field control is also applicable to BDMI materials. Okamura *et al.* first reported the electrical field control of the skyrmion phase in the insulating multiferroic Cu_2OSeO_3 across magnetic field and temperature by magnetic susceptibility measurements[85]. Both the thermodynamically stable skyrmion phase and field cooled metastable skyrmion phase expanded (shrank) under +3.0 mV/nm (–3.0 mV/nm) electric field as shown in Fig 3.2.4(a)–

(c). The extended range of the magnetic field and temperature of the thermodynamically stable skyrmions induced by +3.0 mV/nm that intersects the range of metastable skyrmions under +0.0 mV/nm constitutes the range where non-volatile nucleation and annihilation can be performed, represented in green in Fig. 3.2.4(d)[85]. White *et al.* further investigated the same electric field control of the skyrmion phase in Cu_2OSeO_3 using the SANS imaging technique that resolves the mixed state of metastable skyrmions with helical and conical states[298]. Temporal measurement of the metastable skyrmions lifetime revealed only low temperatures below 40 K will be sufficient for technological applications but are not accessible for nucleation using an electric field due to the magnitude of electric field required[298]. Kruchkov *et al*. later provided a theoretical account and reported similar electric field control on the magnetic skyrmion phase in Cu_2OSeO_3[297]. The underlying mechanism involves the magnetoelectric coupling due to *d-p* hybridisation[299,300]. This coupling only constitutes a small perturbation of the free energy of the skyrmion and helical states that are already energetically comparable[297]. Further work on Cu_2OSeO_3 demonstrates an IP electric field continues to induce skyrmion nucleation via the same mechanism[88].

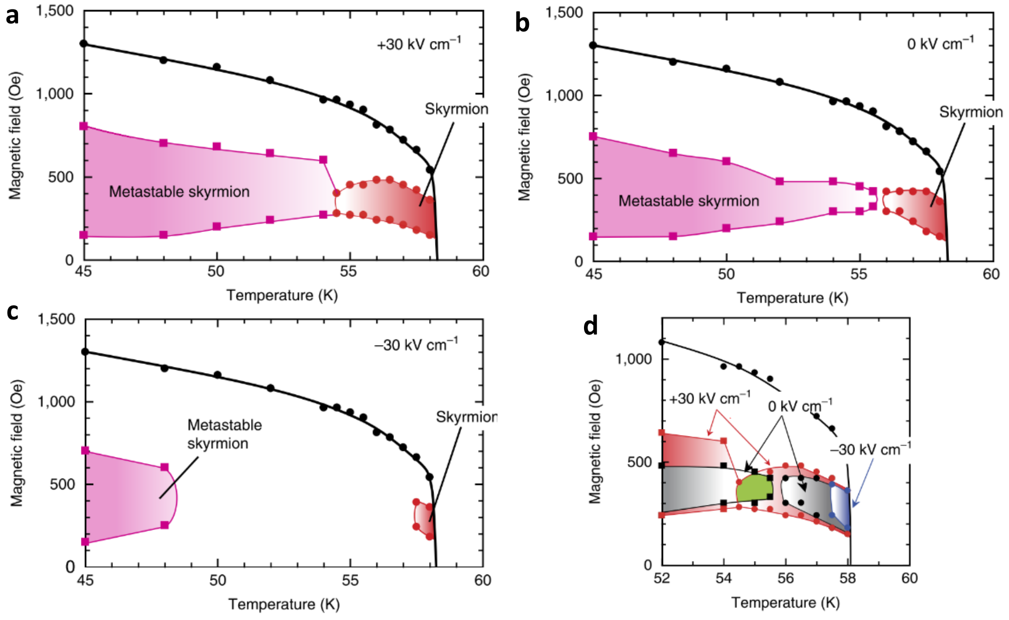

Figure 3.2.4| Magnetic phase diagram of Cu_2OSeO_3 under (a)positive, (b)zero and (c)negative electric field[297]. (d) Merged magnetic phase diagram under positive, zero, and negative electric fields. The green region indicates the range possible for non-volatile skyrmion nucleation and annihilation[85].

3.2.4 Laser and X-ray illumination

Optical control of magnetic materials offers the possibility for ultrafast transitions down to femtosecond regime[301] since the first observation of demagnetization effects using a 60 fs laser in 1996[302]. Following the all-optical helicity dependent switching (AO-HDS) that demonstrated controllable domain reversal using 40 fs circularly polarized light in GdFeCo, interest in optical control for application in magnetic recording technologies was boosted. While AO-HDS was initially demonstrated in ferrimagnetic rare earth-transition metal alloy films or heterostructures[303,304], ferromagnetic thin films and heterostructures are possible as well[305].

In the earlier work by Ogasawara *et al.*, 130 fs pulse laser was demonstrated to nucleate magnetic bubbles down to 400 µm in TbFeCo where DDI skyrmions are stabilized[306]. The nucleation mechanism involves thermal demagnetization induced by the laser followed by the relaxation into a reversed bubble due to DDI with the peripheral domain, as shown in Fig. 3.2.5(a)[307]. This relaxation time was found to be 750 ps for a 400 nm bubble. Finazzi *et al.* extended this study on TbFeCo to show the nucleation of higher-order skyrmions like skyrmionium depending on laser fluence[226]. Nucleation of skyrmions with increasing diameter occurs above the fluence of 4 mJ/cm^2 and up to 5 mJ/cm^2, above which skyrmionium and other higher-order spin textures emerge[226].

Optically induced skyrmion nucleation in FeGe investigated by Berruto *et al.* was also driven by the temperature increase from the light pulse[47]. The heat generated by the laser pulse raises the temperature to the thermodynamically stable skyrmion regime before cooling back as metastable skyrmions. Exceedingly high fluence causes skyrmion annihilation as the temperature was cycled past T_C. The transition time for this mechanism ranges close to 1 µs, limited by the cooling rate of the system. The optically nucleated BDMI skyrmions in FeGe displayed sizes that were independent of fluence, unlike DDI skyrmions[47].

In the IDMI material of Ta/CoFeB/TaO$_x$, Je *et al.* demonstrated 35 fs laser-induced skyrmion nucleation driven by thermal effects. Using a large laser spot size of 60 µm, a skyrmion cluster is produced from a ferromagnetic state initialized by a magnetic field, as shown in Fig. 3.2.5(b). Larger skyrmions are found at the cluster's periphery, and the overall skyrmion size reduces with fluence. No noticeable difference in nucleation by opposite circularly polarized light suggests that the nucleation process is similar to TbFeCo[306]. All the optical nucleation mechanisms discussed above are heat-induced rather than magneto-optical interactions.

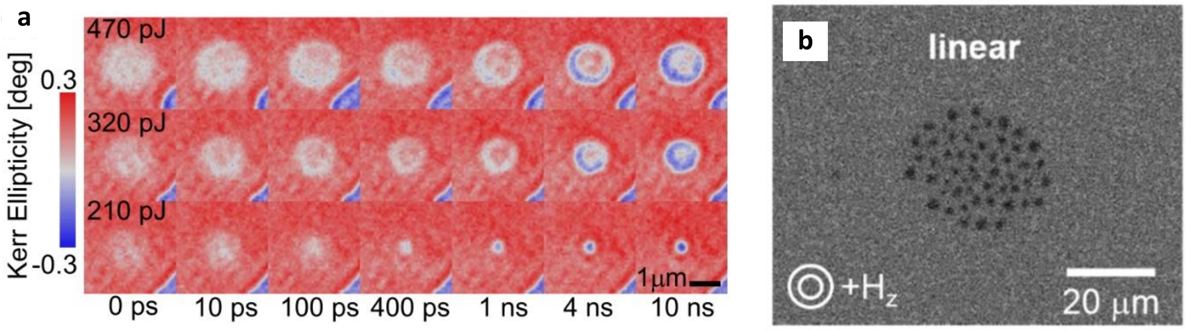

Figure 3.2.5| (a) Domain reversal on TbFeCo induced by 130 fs laser pulse with 1.3 µm spot size by different pump pulse energy[306]. (b) Nucleation of skyrmion cluster on Ta/CoFeB/TaO_x by 35 fs laser pulse with 60 µm spot size[155].

Recent work by Guang *et al.* demonstrated skyrmion nucleation on an exchange biased $[Pt/Co/IrMn]_{11}$ multilayers using X-ray illumination[177]. X-rays allowed the reduction of spot size down to 44 nm, and nucleation of 100 nm skyrmions was observed. The mechanism involved here differs from the prior works and is not thermally driven; Mn atoms strongly absorb the X-ray photons to cause exchange bias reorientation. However, these nucleated skyrmions that lie on exchange biased spots may lead to unintended pinning and instability of these skyrmions beyond these spots and remain to be further investigated.

3.2.5 Strain

Mechanical stress that induces crystallography deformation of bulk materials and interfaces allows for tuning various magnetic interactions critical for skyrmion stabilization such as BDMI[43], IDMI[286,308], and magnetic anisotropy[34,286]. Thus, nucleation techniques are possible via the interplay of the thermodynamically stable and metastable skyrmions. Furthermore, tunable stress can be applied mechanically or indirectly via electric field-induced strain in a ferroelectric substrate.

The studies of strain effects on magnetic skyrmions in BDMI materials were pioneered by Lee *et al*. on MnSi by hydrostatic pressure and later examined again by Ritz *et al.*[30,32]. Under increasing pressure, a fall of T_C accompanied by an increasing portion of the skyrmion lattice phase was observed, as shown in Fig. 3.2.6(a)–(b). Subsequently, Nii *et al*. and Chacon *et al*. performed a uniaxial compressive stress investigation of MnSi to reveal that the skyrmion phase is extended(diminished) by a strain perpendicular(parallel) to the magnetic field[33,34]. More importantly, they showed the magnetic phase changes originate from strain-induced magnetic anisotropy. A different mechanism was revealed by Shibata *et al.* in FeGe, where tensile strain-induced BDMI modulation[43]. Uniaxial tensile stress caused lateral deformation and elongation of the hexagonally packed skyrmions along the strain axis due to the diminished BDMI along the strain axis.

The investigation of another BDMI material, Cu_2OSeO_3, by Levatić *et al*. revealed a similar enhancement of the skyrmion phase across magnetic field and temperature like MnSi but differed with an increase in T_C [309]. Seki *et al*. showed the enhancement(reduction) of skyrmion stability in Cu_2OSeO_3 with uniaxial tensile strain perpendicular(parallel) to the magnetic field and displayed crystallography orientation dependence where enhancement is nil[310]. Under uniaxial compressive stress, Nakajima *et al*. similarly demonstrated the increase in skyrmion stability and identified an enhancement of BDMI along the strain axis[311]. The recent report by Deng *et al*. showed the enhancement of T_C from 60 K up to room temperature in Cu_2OSeO_3 under high pressures up to 42.1 GPa[312]. Alongside the increase of T_C, the skyrmion lattice phase was also extended across the entire temperature range without significant changes in the magnetic field range, as shown in Fig. 3.2.6(g)–(h). Using Raman spectroscopy, the crystal transitioned past three different crystallographic phases with increasing pressure from $P2_13$ to $P2_12_12_1$, $P2_1$ and P1, above pressures of 5.5 GPa, 7.3 GPa, and 24.3 GPa, respectively. The increase of T_C occurs abruptly from less than 100K to 300K at 7.9 GPa, while the sudden drop in the minimum temperature of the skyrmion phase occurs at 26.2 GPa, which relate closely to the transitions in crystallographic phases above. Notably, the skyrmion phase persisted and even improved under these crystal transitions, implying the possibility for similar behavior in other materials.

The investigation of strain on magnetic multilayers is less explored comparatively to that in BDMI materials. In work by Yokouchi *et al.*, skyrmion nucleation in Pt/Co/Ir was performed using surface acoustic waves(SAW)[145]. The skyrmion nucleation was triggered by spatially inhomogeneous strain-induced effective torque via magnetoelastic coupling and an intermediate skyrmion-antiskyrmion formation. Nucleation efficiency via this mechanism is optimal when the half-wavelength of the SAW is slightly larger than the skyrmion size, which is approximately 4 µm, as shown in Fig. 3.2.7(a). An alternative approach to applying and controlling strain on the magnetic multilayer is depositing on a ferroelectric substrate that can be strained using electric fields. This approach was demonstrated by Feng *et al.* using $[Pt/Co/Ta]_n$ on a TiNiNb substrate. TiNiNb additionally provides hysteretic and non-volatile strain that widen options for strain control. Skyrmion nucleation is suppressed by compressive stress but favoured by a tensile strain, as shown in Fig. 3.2.7(b). Both IDMI and K_{eff} decrease with tensile strain due to weakening of the out-of-plane hybridization of Pt at Pt/Co interface and emergence of anisotropic magnetic anisotropy that lies perpendicular to the strain, respectively. The lowering of the minimum magnetic field for skyrmion nucleation down to zero was also demonstrated[313].

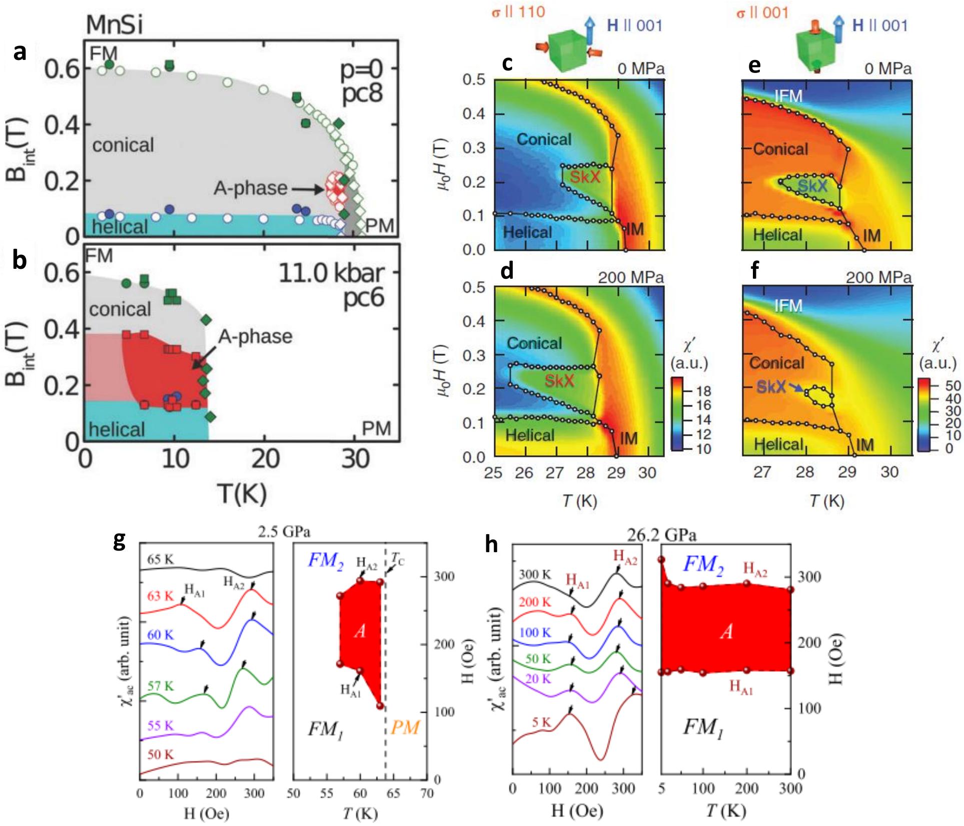

Figure 3.2.6| (a-b) Magnetic phase diagram of MnSi under hydrostatic pressure of (a) 0.0 kbar, and (b) 11.0 kbar[32]. (c-f) Magnetic phase diagram of MnSi under uniaxial compressive stress in orientation illustrated in schematic[34]. (g-h) AC susceptibility and magnetic phase diagram of Cu_2OSeO_3 under hydrostatic pressure of (g) 2.5 GPa and (h)26.2 GPa[312].

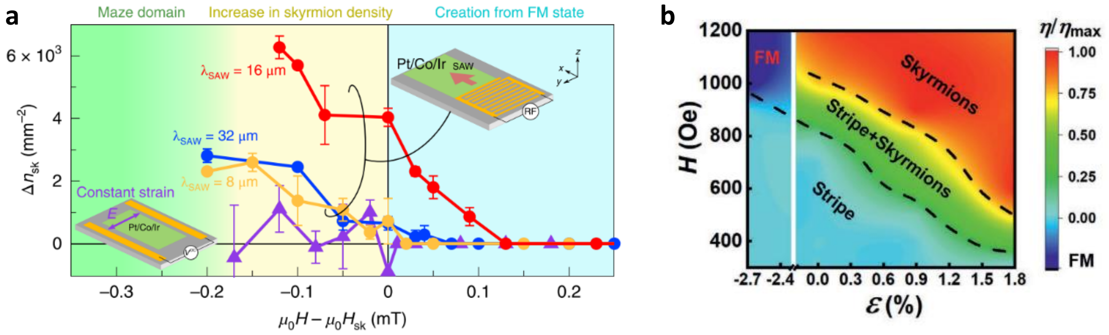

Figure 3.2.7| (a) Change in skyrmion density induced by different SAW wavelengths against magnetic field relative to the magnetic field at which isolated skyrmions exist Pt/Co/Ir[145]. (b) Magnetic phase diagram of [Pt/Co/Ta]$_{12}$ under magnetic field and strain[313].

3.3 Skyrmion Motion/Excitation

This section presents the theoretical description of skyrmion dynamics and experimental demonstration of skyrmion motion and excitations. The list of excitations for skyrmion motion includes electrical current, spin current, temperature, energy gradient, electric field, magnetic fields, and microwaves.

3.3.1 Thiele’s Equation

The dynamics of a single magnetic skyrmion can be described using Thiele’s equation derived from the Landau-Lifshitz Gilbert equation under several assumptions[314]. The first assumption is the magnetic skyrmion is not accelerating and translating with constant velocity or massless. The second assumption is the magnetic skyrmion has a rigid and uniform profile across the thickness that does not deform under forces and during motion. The first assumption can be satisfied when the magnetic skyrmions are driven in the flow regime with limited pinning interactions[201,315]. However, the deviations from the second assumption are typical for experiments at high velocity and thicknesses[138,191,222]. Nonetheless, Thiele’s equation remains the key equation of motion for magnetic skyrmions useful in capturing critical features of skyrmion dynamics.

The Thiele’s equation is given by,

$$\begin{gathered}\vec{F}_g + \vec{F}_d + \vec{F}_{ext} = 0 \\ \vec{G}\times\vec{v} - \vec{v}\cdot\overleftrightarrow{D} + \vec{F}_{ext} = 0\end{gathered}, \tag{3.3.1}$$

where $\vec{G}$ is the gyromagnetic coupling vector, $\vec{v}$ is the drift velocity of the centre of mass of the skyrmion, $\overleftrightarrow{D}$ is the dissipative tensor, and $\vec{F}$ is the conservative external forces acting on the skyrmion. The equation takes the form of a dynamic equation requiring the balance of the gyrotropic force $\vec{F}_g$, dissipative force $\vec{F}_d$ and the conservative external forces $\vec{F}_{ext}$.

For the $\vec{F}_g$ term in Eq. 3.3.1, $\vec{G} = (0,0,G)$ and,

$$G = -\frac{M_s d}{\gamma} \iint \vec{m} \cdot \left(\frac{\partial \vec{m}}{dx} \times \frac{\partial \vec{m}}{dy} \right) dxdy, \tag{3.3.2}$$

where $\vec{m}$ corresponds to the unit vector of magnetization, d is the thickness of the magnetic layer, M_S is the saturation magnetization, and γ is the gyromagnetic ratio. The integral in this term is related to the winding number or skyrmion number N_{sk} in Eq. 3.1.1 by a factor of 4π. For the case of a magnetic skyrmion that is defined by the topological structure with $N_{sk} = \pm 1$, Eq. 3.3.2 is simplified to,

$$G = \pm 4\pi N_{sk} M_s d / \gamma, \tag{3.3.3}$$

determined by N_{sk} which depends on the polarity and chirality of the magnetic skyrmion. The gyrotropic force is often referred to as the Magnus force as it is commonly orientated orthogonal to the velocity.

The second term in Eq.3.3.1 is the dissipative term where $\overleftrightarrow{D}$ is given by,

$$\overleftrightarrow{D} = \frac{\alpha M_s t}{\gamma} \begin{pmatrix} \int \frac{\partial \vec{m}}{\partial x} \cdot \frac{\partial \vec{m}}{\partial x} dxdy & \int \frac{\partial \vec{m}}{\partial x} \cdot \frac{\partial \vec{m}}{\partial y} dxdy \\ \int \frac{\partial \vec{m}}{\partial y} \cdot \frac{\partial \vec{m}}{\partial x} dxdy & \int \frac{\partial \vec{m}}{\partial y} \cdot \frac{\partial \vec{m}}{\partial y} dxdy \end{pmatrix} \quad \text{or} \quad D_{ij} = \frac{\alpha M_s t}{\gamma} \int \frac{\partial \vec{m}}{\partial i} \cdot \frac{\partial \vec{m}}{\partial j} dxdy, \tag{3.3.4}$$

where α is the Gilbert damping constant. Under the assumption of an axially symmetric skyrmion profile[316], $D_{xy} = D_{yx} = 0$ and $D_{xx} = D_{yy}$ the tensor can be further simplified down to a scalar term given by D_s,

$$\overleftrightarrow{D} = D_s = \frac{\alpha M_s t}{\gamma} \int \frac{\partial \vec{m}}{\partial x} \cdot \frac{\partial \vec{m}}{\partial x} dxdy. \tag{3.3.5}$$

The final term in Eq. 3.3.1 represents an equivalent conservative external force acting on the skyrmion by excitations such as energy gradients, electrical currents, and spin currents, described in general as,

$$\vec{F} = -\nabla U \,. \tag{3.3.6}$$

Given that $\vec{F}_g$ and $\vec{F}_d$ are orthogonal, it necessitates $\vec{F}_{ext}$ from being collinear with $\vec{v}$ and leads to the deviation in the motion of the skyrmion from its driving force, also referred to as the skyrmion Hall effect. By resolving Eq. 3.3.1, one can derive the angle of deviation will be given by,

$$\theta_{sk} = \frac{G}{D_s}\,, \tag{3.3.7}$$

referred to as the skyrmion Hall angle[201,222]. The skyrmion Hall effect poses a threat to the stability of magnetic skyrmion in confined structures like nanotracks, where the skyrmions can be driven to annihilation at the structure edges. The confining potential induced by DMI at the edges provides limited protection to the magnetic skyrmions and can be overcome at sufficient velocities[201].

Two main approaches are adopted to mitigate the skyrmion Hall effect, reducing $\vec{F}_g$ to zero or introducing stronger confining forces to mitigate $\vec{F}_g$. $\vec{F}_g$ is reduced in antiferromagnetic systems or synthetic antiferromagnets where there are two sublattices of skyrmions with a common chirality but opposite polarity that counteract to give a zero G [168,217]. Hence, the skyrmion motion $\vec{v}$ will be collinear with the driving force $\vec{F}_{ext}$ impeded by $\vec{F}_d$. Alternatively, confining potentials can be enhanced by fabricating track edges with either enhanced Ku or diminished DMI[164,317,318].

3.3.2 Electrical and Spin Current

The motion of skyrmion induced by electrical currents or spin currents can be categorized into two main categories, STT and SOT. SOT is the primary driving mechanism in IDMI materials due to their structure with a strong spin-orbit coupling layer adjacent to the FM that can induce spin current injection into the FM. Other materials are primarily be driven by STT, unless intentionally interfaced with another layer that can induce SOT. SOT is significantly more effective than STT for magnetic skyrmions and hence are the centre of attention[6,316].

SOT can drive skyrmions either along or against electron flow depending on the injected spin current's polarization and the skyrmion's chirality[316]. Considering the SOT generated by SHE, the effective field can be expressed as,

$$H_{SOT} = \frac{\hbar \theta_{SH} j}{2eM_s d}\left(\vec{m} \times \left(\hat{z} \times \hat{j}_e\right)\right), \tag{3.3.8}$$

where $\hbar$ is the reduced Planck's constant, θ_{SH} is the spin Hall angle, j is the charge current density, e is the charge of an electron, $\hat{j}_e$ is the unit vector along electron flow[192,319,320]. The term $\hat{z} \times \hat{j}_e$ corresponds to the injected spin current direction $\vec{\sigma}$ that lie along $\hat{y}$ assuming $\hat{j}_e$ flows along $\hat{x}$. Following Thiele's formulism, the force density $\vec{f}_{SOT}$ induced by H_{SOT} across the skyrmion can be derived by $\vec{f} = \nabla H \cdot M$. In addition, by taking $\hat{j}_e = +\hat{x}$ to simplify the formula and give a more intuitive view of the forces acting on the skyrmion, $\vec{f}_{SOT}$ is given by,

$$\vec{f}_{SOT} = \frac{\hbar \theta_H j}{2ed}\left(\left(m_z \frac{\partial m_x}{\partial x} - m_x \frac{\partial m_z}{\partial x}\right)\mathbf{\hat{x}} + \left(m_z \frac{\partial m_x}{\partial y} - m_x \frac{\partial m_z}{\partial y}\right)\mathbf{\hat{y}}\right). \tag{3.3.9}$$

Equation 3.3.9 highlights the importance of skyrmion's chirality for $\vec{f}_{SOT}$ to induce a unidirectional force along both skyrmion edges that result in translational motion. Without chirality, a bubble domain will either experience a converging force that annihilates it or diverging force that stretches the domain into a long stripe domain. Thus, the translational motion by SOT excitation was also used as a general rule to differentiate skyrmions from non-topological bubbles[192].

To initiate skyrmion motion, a minimum depinning current, is required to overcome the effects of pinnig due to disorder, defects, or inhomogeneity across the material, even more so for sputtered materials[194,321,322]. Just above the depinning current, skyrmions move in the creep regime[192,323] where their motion involve stochastic hopping from pining site to pinning site. Longer current pulses thermally assist with depinning[201]. Skyrmion speed in the creep regime is slow at the order of µm/s[165,192]. At higher current densities, skyrmions overcome the pinning interactions and propagate dominantly due to the driving forces. A challenge arises when the same current intended for motion can induce unintended nucleation and deletion of magnetic skyrmions, as discussed previously in Section 3.2.2. A mess of random nucleation and annihilation across the device can occur at higher current density dynamics[128,135,223,260]. One approach to overcome this is to use higher magnitude and shorter current pulses for motion[260]. Comparing the current-induced skyrmion motion on $[\mathrm{Pt/Co/Ta}]_{15}$ and $[\mathrm{Pt/CoFeB/MgO}]_{15}$ in work by Woo *et al.*, few skyrmions moved freely, and others were pinned or annihilated in $[\mathrm{Pt/Co/Ta}]_{15}$ while most skyrmions in $[\mathrm{Pt/CoFeB/MgO}]_{15}$ can be moved uniformly[194]. The amorphous CoFeB without grain boundaries like polycrystalline Co was shown to be more desirable.

The skyrmion Hall effect predicted by the Thiele's equation was absent at low driving currents. θ_{sk} increased and saturates with current density and skyrmion velocity in experiments, as shown in Fig. 3.3.1(a-b)[201,222]. The current dependent θ_{sk} was attributed to the transition from the creep to flow regime due to pinning interactions by Jiang *et al.*[201,315]. Soon after, Litzius *et al*. reported a linearly increasing θ_{sk} with skyrmion velocity and further proposed the increase in θ_{sk} was also attributed to the deformation of skyrmions at high velocities due to additional contribution by the field-like component of SOT[222]. A recent report by Litzius *et al*. further exemplifies in an even higher drive regime, not only the field-like component of SOT that induces small deformations, but the damping-like component of SOT causes even more significant deformation into a stripe along $\hat{y}$ that contributes to the increase in θ_{sk} [138]. As skyrmions inevitably transition from the creep to flow regime, current density dependent θ_{sk} is a general feature observed in later works on Pt/Co/MgO[221] and [Pt/GdFeCo/MgO]$_{20}$[217].

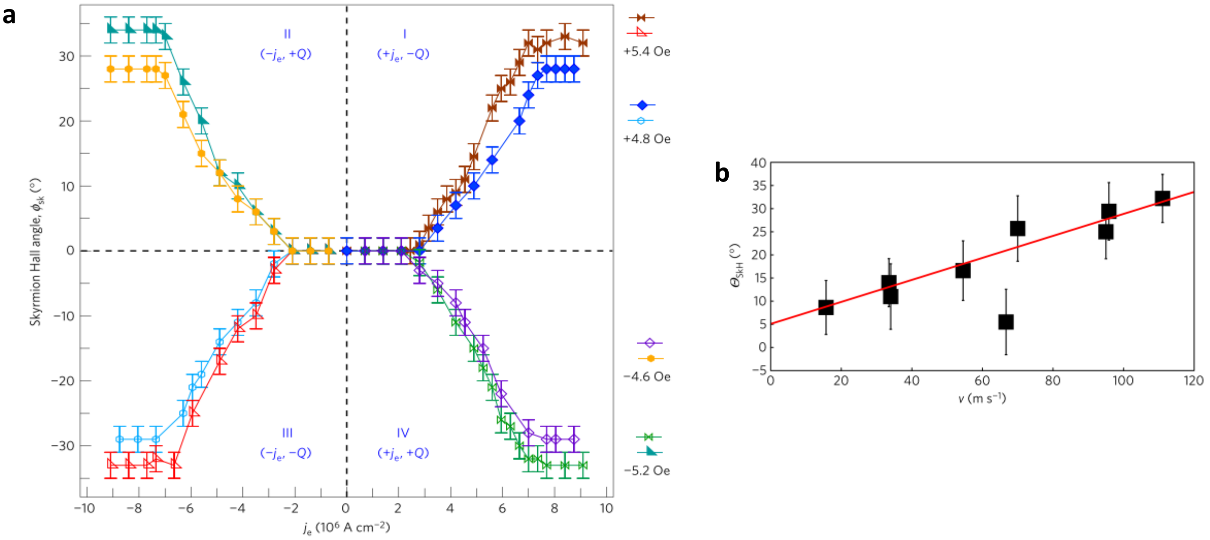

Figure 3.3.1| (a) Skyrmion Hall angle in Ta/CoFeB/TaO$_x$ across all four combinations between current directions and skyrmion polarities[201]. (b) Linear dependence of skyrmion Hall angle in [Pt/CoFeB/MgO]$_{15}$ with skyrmion velocity[222].

In Eq. 3.3.7, D increases linearly with skyrmion size for large skyrmions and thus θ_{sk} is expected to increase significantly at smaller sizes. However, the experimental observation of diameter-independent skyrmion Hall angle was reported by Zeissler *et al*. in [Pt/CoB/Ir]$_5$. Skyrmion ranging from 35 nm to 825nm showed a common θ_{sk} of 9^o at an average velocity of

6 m/s. The diameter independence arose from the dominant pinning landscape across the device. Hence, demonstrating pinning is a critical aspect that not only generates drive dependent θ_{sk} but also removes diameter dependence.

Because of the skyrmion Hall effect, skyrmions are driven towards and accumulate along one of the transverse edges of the track, and a qualitative sign of the skyrmion Hall effect can be derived. The work by Sugimoto on Pt/Co/Ir further demonstrated the accumulation and depletion of skyrmions could even be induced in regions with no current flow[143,144]. Figure 3.3.2(a) shows the device geometry used, where the current flows across the middle track while narrow 1μm bridges connect to the adjacent tracks. Under an applied current, skyrmion accumulation occurs in the top track, while depletion occurs in the bottom track. This behaviour was likened to a skyrmion chemical potential gradient transverse to the current and can be helpful in skyrmion injection or deletion applications.

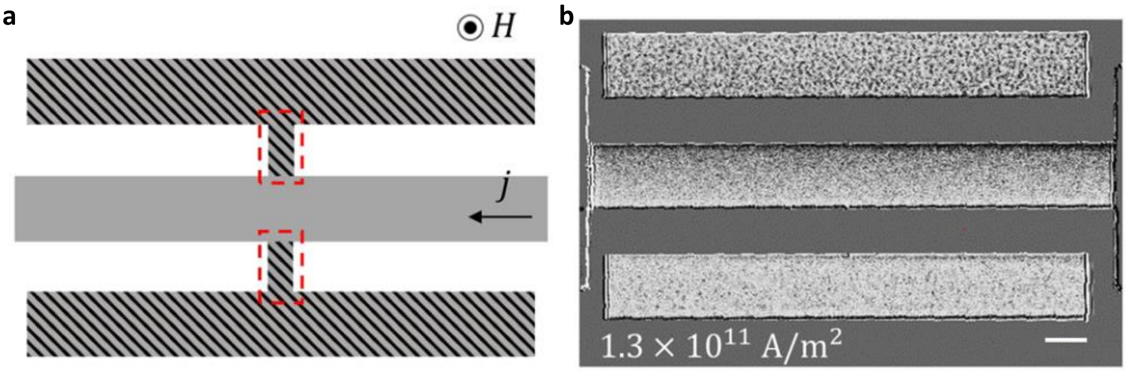

Figure 3.3.2| (a) Schematic of device structure where the current injection was only performed across the middle track but connected to adjacent tracks via a narrow bridge (b) MOKE image of skyrmion distribution across the device under electrical current flow[144]. Scale bar, 10 μm.

Antiferromagnetic skyrmions are theoretically predicted to produce no gyrotropic forces and skyrmion Hall effect. The work by Woo *et al.* in the ferrimagnetic multilayer [Pt/GdFeCo/MgO]$_{20}$, showed a reduced θ_{sk} of 20º at the velocity of 50 m/s[168]. SAF skyrmion is another avenue to suppress the skyrmion Hall effect. θ_{sk} was suppressed down to just a few degrees at skyrmion velocities of 1 m/s in Pt/Co/CoFeB/Ir/Co/CoFeB/W by Dohi *et al.*, as shown in Fig. 3.3.3(a)[217]. A direct comparison to FM skyrmions in Pt/Co/CoFeB/Ir showed θ_{sk} of approximately 20º for the same velocity. In addition, without gyrotropic forces, the driving force by SOT are significantly more effective in driving skyrmions, as shown in Fig.

3.3.3(b), where an order less current density is required in SAF skyrmion compared to FM skyrmion to achieve similar velocity.

Along the nanotrack edges, skyrmion-edge repulsion was directly observed by Jiang *et al*. as the skyrmions showed oscillatory motion when driven towards the edge by the skyrmion Hall effect[201]. While analysing Thiele's equation by considering edge repulsion predicts an increase in skyrmion velocity along the track, the opposite was observed experimentally[201,260]. Skyrmions close to the edges travel with lower velocity and exhibit higher pinning current than regions far from the edges, which are likely to be caused by higher non-uniformity and defects along track edges from fabrication processes.

Temperature being critical in skyrmion stability and nucleation, its effects on the current-induced motion was investigated by Litzius *et al.* [138]. Skyrmion velocity increased with temperature due to the strengthening of SOT. θ_{sk} was unaffected due to limited change in skyrmion rigidity due to temperature. Nonetheless, thermally robust properties close to room temperatures are ideal.

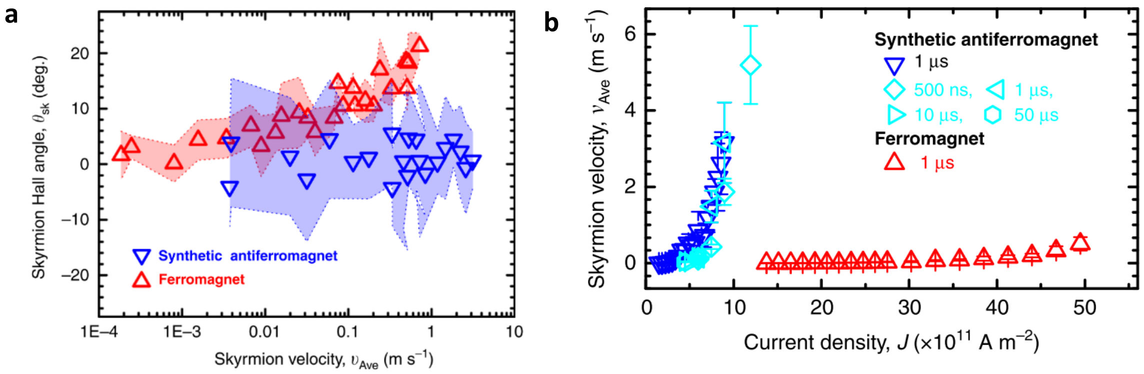

Figure 3.3.3| (a) Skyrmion Hall angle dependence on skyrmion velocity comparison between a synthetic antiferromagnet and ferromagnet structure. (b) Enhancement of skyrmion velocity in the synthetic antiferromagnet Pt/Co/CoFeB/Ir/Co/CoFeB/W[217].

SOT can also drive DDI skyrmions that are not Neel in configuration. As demonstrated by Montoya *et al.*, by depositing $[Fe/Gd]_{100}$ with a bottom Pt layer and top Ta layer, the Bloch skyrmions were still driven by SOT against the direction of electron flow[191]. The motion was found aligned to be driven by SOT induced by the bottom Pt layer acting on the Neel cap of the thick FM layer. Thus, SOT-driven motion remains accessible for Bloch skyrmions by fabricating high repetition multilayers.

The studies in BDMI are limited compared to the magnetic multilayers due to the more stringent fabrication processes and necessary low-temperature measurement for most of the materials. Current-driven skyrmion motion in BDMI materials is limited to the STT mechanism. One main advantage of magnetic skyrmions over domain walls is their low depinning current triggering. The first report of low pinning current was performed by Jonietz *et al.* on MnSi at the order of 10^6 A/m^2. Limited by the SANS used as a means of observation, a temperature gradient parallel to the current was used to generate current-induced rotation[324]. Another low pinning current measurement of 10^6 A/m^2 in MnSi was measured electrically by Schulz *et al.* using the additional Hall effect contribution by the moving skyrmion lattice[325]. Direct observation current-induced motion of skyrmions in FeGe was later demonstrated by Yu *et al.* using LTEM[326] and reported a similarly low pinning current of 10^5 A/m^2.

Table 3.3.1| List of magnetic multilayers' electrical current-driven skyrmion dynamics' parameters including direction (Dir), depinning current, range of skyrmion Hall angle. For skyrmion motion direction, + and – corresponds to the conventional electrical current and electron current direction. The last two columns provide a set of current densities and the corresponding skyrmion velocities for reference.

Material	**Dir.**	**Depinning Current (A/m^2)**	**Skyrmion Hall Angle (°)**	**Current (A/m^2)**	**Velocity (m/s)**
Ta/CoFeB/TaO$_x$[192]	–	1×10^8	-	4.5×10^8	2.5×10^{-5}
[Pt/Co/Ta]$_{15}$[194]	+	2×10^{11}	-	3.5×10^{11}	50
[Pt/CoFeB/MgO]$_{15}$[194,222]	+	2×10^{11}	0 – 32	5.1×10^{11}	110
Ta/CoFeB/TaO$_x$[201]	–	6×10^9	0 – 32	6.2×10^{10}	0.75
Pt/Ni/Co/Ni/Au/Ni/Co/Ni/Pt[127]	+	2.5×10^{11}	-	4.5×10^{11}	65
[W/CoFeB/MgO]$_{15}$[224]	+	-	-	-	-
[Pt/Ir/Co]$_{10}$[128]	+	2.85×10^{11}	-	2.85×10^{11}	0.04
[Pt/CoFeB/MgO]$_{20}$[135]	+	-		1.6×10^{11}	10
Pt/Co/Os/Pt[165]	+	2×10^8	-	1.2×10^9	1.4×10^{-5}
[Pt/GdFeCo/MgO]$_{20}$[168]	+	-	0 – 20	3.55×10^{11}	50
Pt/Co/MgO	+	3.2×10^{11}	0 – 50	6.8×10^{11}	100
Pt/Co/CoFeB/Ir/Co/CoFeB/W[217]	+	2×10^{11}	0	1.2×10^{12}	5
[Pt/CoB/Ir]$_5$[173]	+	-	9	5.6×10^{11}	5
Pt/[Gd/Fe]$_{100}$/Ta[191]	+				

Kagawa *et al.* highlighted the undesirable current-induced topological unwinding of skyrmion strings in thick bulk MnSi where the skyrmion strings extend across the material[38]. In 2018, Shibata *et al.* investigated the motion of metastable hexagonally packed skyrmion clusters amid helical domains, reporting a higher pinning current density of 10^9 A/m^2 due to increased potential barriers to translate the domain boundary[48]. Increased temperature assists in propagation, aligned with previous reports as the motion involve thermally activated creep motion at current densities just above pinning current[48,326]. Okuyama *et al.*, reported a friction-like phenomenon at the edges of the device that causes inhomogenous rotation of the skyrmion lattice in MnSi[327]. In contrast to multilayer skyrmions, BDMI skyrmions are typically stabilized as aggregates or closely packed clusters. Yu *et al*. showed that these skyrmion aggregates undergo internal rotations in addition to their translational motion[52].

3.3.3 Temperature Gradient

The first reported skyrmion motion was detected using the combination of temperature gradient and electrical current injection in MnSi to induce the rotation of skyrmion lattice[324]. The primary role of the temperature gradient in this work was to generate an inhomogeneous spin torque. Mochizuki *et al*. later demonstrated that a pure temperature gradient alone could induce the rotation of the skyrmion lattice in Cu2OSeO3[328]. A radial temperature gradient formed using electron beam illumination drove a CW rotation above a critical electron irradiation density. The temperature gradient generated longitudinal magnons and transverse magnons along the temperature gradient due to the magnetic field induced by the magnetic skyrmions, causing the rotation[328].

In 2020, Wang *et al*. investigated the effects of a temperature gradient on magnetic skyrmion in magnetic multilayers [Ta/CoFeB/MgO]$_{15}$ directly using on-chip heaters instead of illumination[139]. Isolated skyrmions diffused from the hot region to cold region, as the combined effects of magnon spin torque, thermoelectric current's torque and the entropic gradient associated with the temperature gradient[62,329].

3.3.4 Electric field

Electric field-induced rotation skyrmion lattice was first reported by White *et al*. in the insulating multiferroic Cu_2OSeO_3[81]. Note that the application of an electric field on a skyrmion lattice does not generate a rotation. The electric field determined the angle of the skyrmion lattice formed via a magnetic field sweep. The angle of rotation varied linearly with the applied electric field. The skyrmion rotation was achieved via a magneto-electric coupling between the electric dipole and the external electric field[79,81]. White *et al*. later extended this work to show a small oscillating magnetic field under a fixed electric field can induce the rotation of skyrmion lattice towards a saturation angle that extends up to 25º [83]. The small oscillating magnetic field was required to overcoming pinning.

In 2019, Ma *et al*. demonstrated a directional translation of magnetic skyrmions in Pt/CoNi/Pt/CoNi/Pt/SiO_2 performed using an electric field illustrated in Fig. 3.3.4[220]. In this work, the material was fabricated with a thickness gradient and a corresponding magnetic anisotropy gradient. As the electric field was applied across the whole track, magnetic anisotropy was modulated to generate a domain in the lower thickness that pushes the skyrmion up the track under an increasing electric field. However, a thickness gradient will not be feasible for extended tracks. Hence an alternative scheme of electric field variation across a uniform track proposed in our work in Chapter 7 is required and remains to be experimentally demonstrated.

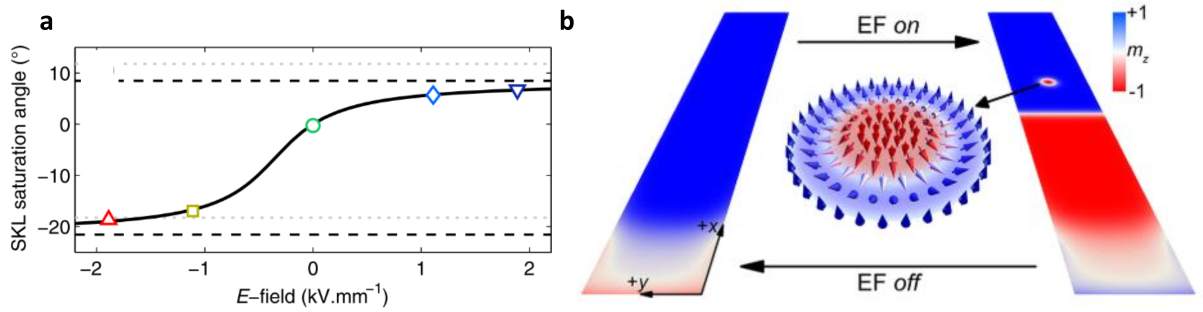

Figure 3.3.4| (a) Skyrmion lattice's saturation angle triggered by a small oscillating magnetic field in the presence of an electric field in Cu_2OSeO_3[83]. (b) Schematic of electric field-induced nucleation and motion of skyrmion along a gradient[220].

3.3.5 Microwave

The first microwave excitation on magnetic skyrmions was performed by Onose *et al*. on Cu_2OSeO_3[78]. The magnetic skyrmions exhibit three key modes: CW rotational, CCW rotational and breathing modes. The rotational modes correspond to the circular motion of the skyrmion core off its equilibrium position. In contrast, the breathing mode corresponds to the periodic expansion and contraction of the skyrmion core. The rotational and breathing modes are excited by magnetic field oscillations parallel and perpendicular to the skyrmion lattice plane, respectively. Okamura *et al*. revealed the nonreciprocal directional dichroism (NDD) of microwaves, where microwave absorption differs for opposite propagation directions due to magneto-electric coupling in Cu_2OSeO_3[82]. In 2015, Schwarze *et al*. extended the materials investigated across more BDMI materials, including MnSi, FeCoSi, and Cu_2OSeO_3 with metallic, semiconducting and insulating conductivities, respectively[35]. A universal behaviour in excitation frequency was identified across all materials and can be characterized based on the Dzyaloshinskii-Moriya energy, a critical internal field energy and shape anisotropy. Metastable skyrmions also displayed additional contribution due to deformation and elongation[96]. For GaV_4S_8 that stabilizes Neel skyrmions and has a strong perpendicular magnetic anisotropy, a different microwave response was detected[330]. The resonant frequencies of the breathing mode were suppressed by magnetic anisotropy to be lower than the CCW mode. Extending the previous work on NDD, Okamura *et al*. investigated GaV_4S_8 and reported a similar behaviour of dichroism[331].

Resonant signatures of magnetic skyrmions were also reported in spin current nano-oscillator on $Pt/[Co/Ni]_5$ by Liu *et al.*[332] and magnetic tunnel junctions that stabilize a single skyrmion by confinement by Penthorn *et al.*[280]. In a recent report by Satywali *et al.*, the magnetic multilayer $[Ir/Fe/Co/Pt]_{20}$ showed two frequency modes corresponding to the CCW gyration of the skyrmion core and an additional higher frequency CCW precession of the inter-skyrmion regions[333]. Notably, CW precession of the skyrmions was not detected in this work due to the magnetic anisotropy and Neel skyrmion configuration that diminished the CW mode’s intensity and enhanced the frequency beyond the detectable range.

3.3.6 Brownian Motion

At room temperature, thermal fluctuations acting on isolated skyrmions manifest as a random Brownian motion, particularly in materials with low pinning potential. In 2019, Zázvorka *et al*. investigated this Brownian motion of skyrmions in Ta/CoFeB/Ta/MgO for temperatures close to room temperature[163]. The random trajectories of the skyrmions and linearly increasing mean squared displacement with time was as expected from Brownian motion, as shown in Fig. 3.3.5(a). An exponentially increasing diffusion coefficient with temperature was also measured. Exploiting this motion, Zázvorka *et al*. additionally demonstrated its application as a reshuffler device. Nozaki *et al*. subsequently demonstrated the voltage control of the diffusion constant in W/FeB/Ir/MgO as shown in Fig. 3.3.5(b)[174]. The diffusion constant increased with voltage while perpendicular magnetic anisotropy decreased. The voltage-controlled diffusion constant was speculated to originate from the modification of skyrmion size and shape and reduced pinning landscape. Zhao *et al*. later showed that the Brownian gyromotion of skyrmions was even topology dependent[158].

For applications in Brownian computing, Jibiki *et al*. introduced a fabrication approach to minimize skyrmion pinning[164]. Instead of etching magnetic skyrmion tracks that cause unwanted non-uniformity and pinning, particularly at track junctions, the tracks were patterned by depositing a capping SiO_2 layer, leaving the ferromagnetic layer undamaged. The confining geometry of the nanodevices is also critical in determining skyrmion diffusion, confirmed by Song *et al*. in triangular devices in Ta/CoFeB/Ta/MgO as shown in Fig. 3.3.6[207]. The commensurability between the device geometry and skyrmion quantity determines the stability of skyrmion positions, as highlighted in the case of 3, 6, and 10 skyrmions being confined in a triangular device in Fig. 3.3.6(a)–(b).

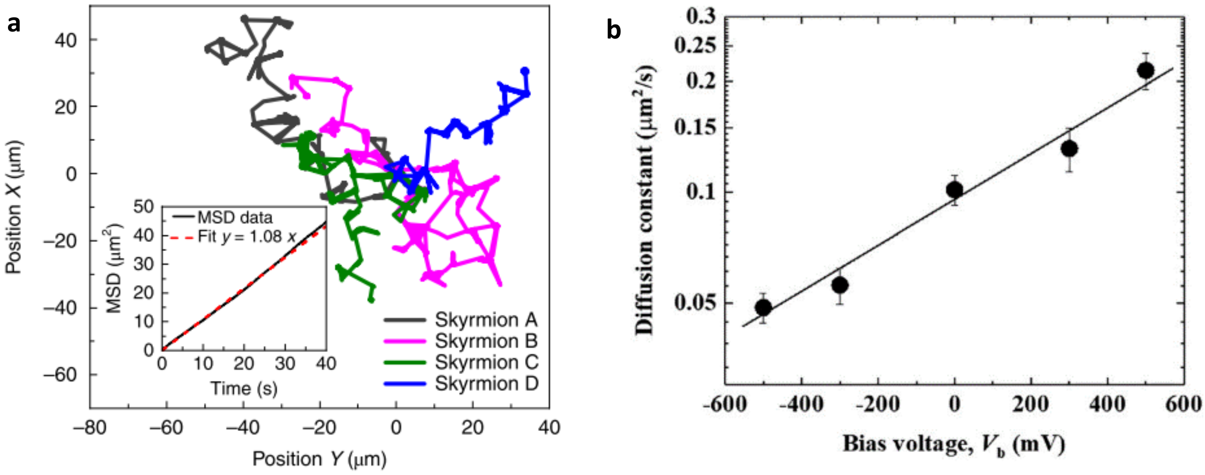

Figure 3.3.5| (a) Skyrmion trajectory at 296K in Ta/CoFeB/Ta/MgO. Inset is the plot of mean squared of skyrmion displacement with time[163]. (b) Voltage dependence of skyrmion diffusion constant in W/FeB/Ir/MgO[174].

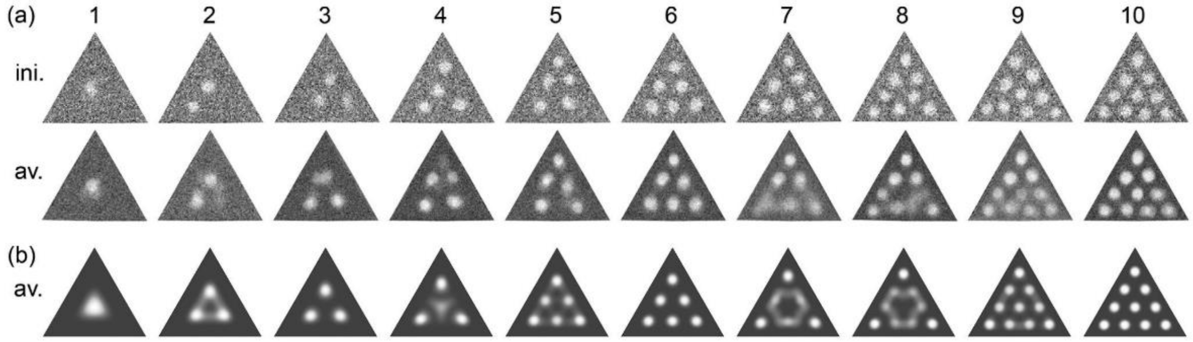

Figure 3.3.6| (a) Experimental images of the initial skyrmion state and time-averaged states with different skyrmion quantity. (b) Time-average skyrmion trajectories evaluated via simulations[207].

3.4 Skyrmion Observation and Detection Techniques

This section discusses the various skyrmion observation and detection techniques ranging from scattering, electrical detection, magnetic susceptibility and imaging using various means including electron, x-ray, scanning probes, and optical light[17].

3.4.1 Scattering and Illumination

The first observation of magnetic skyrmions was performed indirectly via small-angle neutron scattering (SANS) in MnSi, as shown in Fig. 3.4.1(a)[28]. The technique is performed by illuminating a monochromatic and collimated neutron beam on the sample and collecting the scattering pattern on a two-dimensional position-sensitive detector behind the sample. SANS is used to probe mesoscopic physical and magnetic structures at the length scales of 1 nm to 1000 nm[334]. This scattering technique is suitable for investigating the ordered magnetic structures like skyrmion lattice and helices. Magnetic skyrmions return the characteristic 3**q** scattering pattern with sixfold symmetry, as shown in Fig. 3.4.1(a), while helices will produce single **q** scattering patterns[28]. Figure 3.4.1(b) shows the scattering pattern when two domains of magnetic skyrmions are present for the case of $Fe_{0.8}Co_{0.2}Si$[75] and highlights the possible complex scattering patterns that require careful interpretation, particularly for less ordered multidomain, transitioning, or mixed state. SANS was used to characterize many BDMI materials like $Mn_{1-x}Fe_xSi$[75], Cu_2OSeO_3[80], GaV_4S_8[20], $Co_8Zn_8Mn_4$[97], $Mn_{1-x}Fe_xGe$[69], and GaV_4S_8[110]. While SANS is useful in identifying and acquiring general spin phase diagrams, real-space imaging techniques are necessary to further directly observe the skyrmion.

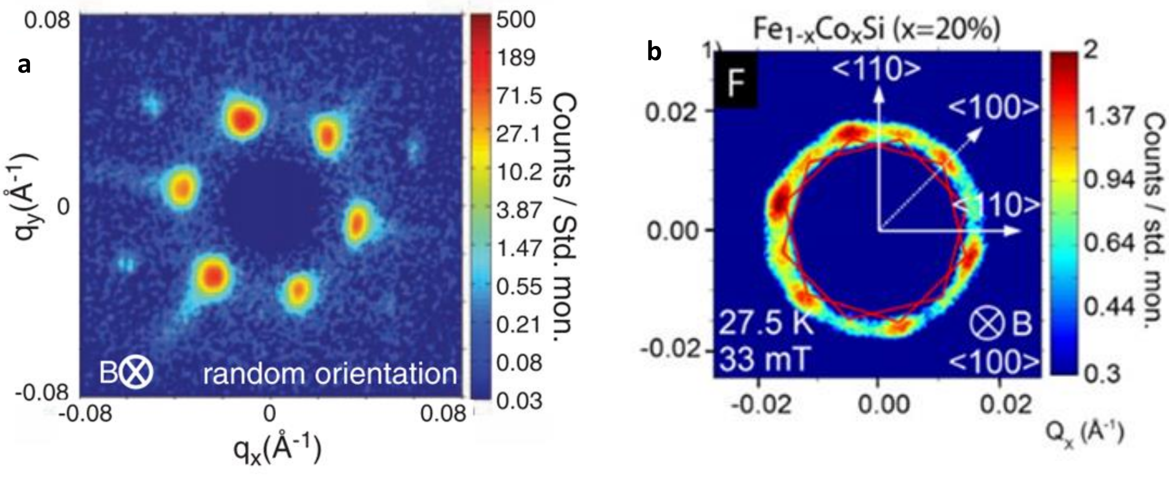

Figure 3.4.1| SANS scattering intensity of magnetic skyrmions in (a) MnSi[28], and (b) $Fe_{0.8}Co_{0.2}Si$[75].

The first real-space observation of magnetic skyrmion was performed using Lorentz transmission electron microscopy (LTEM) in $Fe_{0.5}Co_{0.5}Si$, as shown in Fig. 3.4.2(a)[335]. LTEM images magnetic structures down to 2 nm resolution based on the Lorentz force interaction between the electron beam and magnetic induction by the local magnetization of the sample[336]. The LTEM technique is sensitive to IP winding of magnetization at the domain walls. Based on the winding, the electrons will either converge or diverge to give brighter or darker regions in the Fresnel mode, where the image is defocussed. In combination with the transport-of-intensity equation evaluation, one can even derive a quantitative measure of the IP magnetization[337,338]. Thus, LTEM is suitable for Bloch skyrmions found in a majority of BDMI materials[37,97,104,281,335]. In addition, magnetic multilayers without DMI such as $[Fe/Gd]_{80}$ can stabilize Bloch skyrmions of both helicities corresponding to CW and CCW winding of the skyrmions[190]. Skyrmions with different helicities are easily identifiable from LTEM images as they form opposite contrast, as shown in Fig. 3.4.2(b). LTEM was also used to confirm the formation of a three-dimensional hedgehog lattice in MnGe, as shown in Fig. 3.4.2(c)[18].

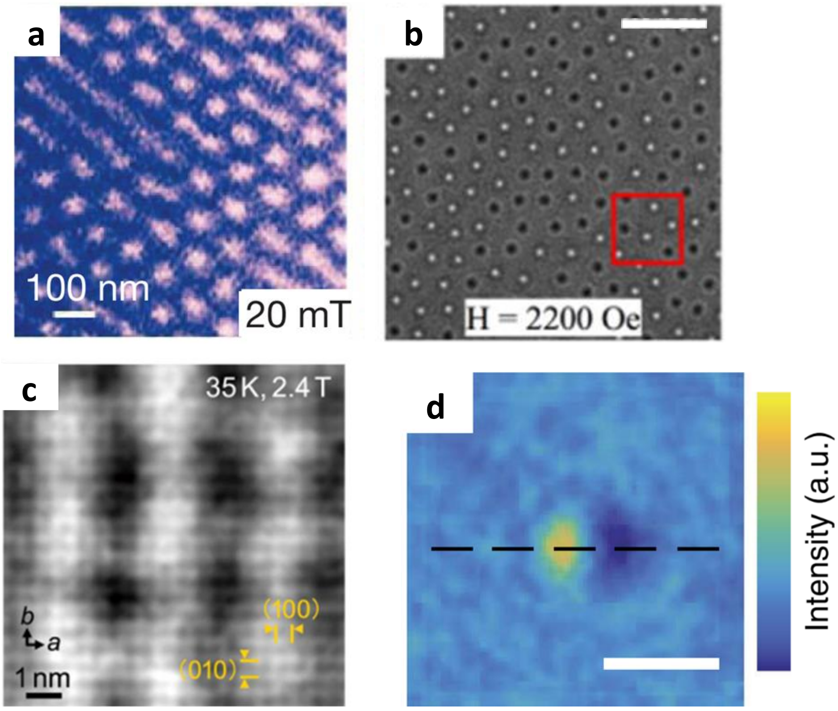

Figure 3.4.2| (a) Overfocussed LTEM image of mixed helical and Bloch magnetic skyrmion state in $Fe_{0.5}Co_{0.5}Si$[335]. (b) Underfocussed LTEM image of Bloch magnetic skyrmions with both helicities in $[Fe/Gd]_{50}$[190] . (c) Underfocussed LTEM image of the hedgehog lattice in MnGe[18]. (d) Tilted LTEM image of a Neel magnetic skyrmion in $[Pd/Co]_5$[180].

For Neel skyrmions, the electron deflection occurs along the domain wall resulting in no divergence or convergence of the electrons, thus generating no magnetic contrast[180]. However, Pollard *et al*. demonstrated Neel skyrmion imaging in magnetic multilayer $[Pd/Co]_5$ by tilting the sample to generate a non-zero curl in magnetization perpendicular to the electron beam and generate contrast, as shown in Fig. 3.4.2(b)[180]. Thus, LTEM are applicable to magnetic multilayers like Pt/Co/Ta[146], Pt/CoW[199], and Ta/CoFeB/MgO[161]. LTEM can identify Neel skyrmions, but their chirality remains hidden. Jiang *et al*. proposes distinguishing Neel skyrmions' chirality using the slight asymmetry and difference in image contrast when tilted in opposite angles but remains too challenging in resolving the signal from the noise[339].

More advanced electron microscopy techniques like electron holography and differential phase contrast (DPC) scanning transmission electron microscopy (STEM) are also available for skyrmion imaging. Electron holography was used to resolve magnetic skyrmion structure at better resolutions and evaluate the magnetic structure across its thickness critical for skyrmion strings and magnetic bobbers by the quantitative measure of the electron phase shifts[45,50,60]. The scanning approach of DPC-STEM offers quantitative measurement at an even better spatial resolution down to the 1 nm resolution useful for investigating detailed skyrmion structure, at the expense of temporal resolution[340-343]. Another electron-based magnetic imaging is scanning electron microscopy with polarization analysis (SEMPA) and spin-polarized low-energy electron microscopy (SPLEEM). SEMPA derives surface magnetization configuration based on the emitted secondary electron's polarization[216,344] while SPLEEM utilizes the magnetization-dependent backscattering of spin-polarized electrons off a magnetic surface[204,345].

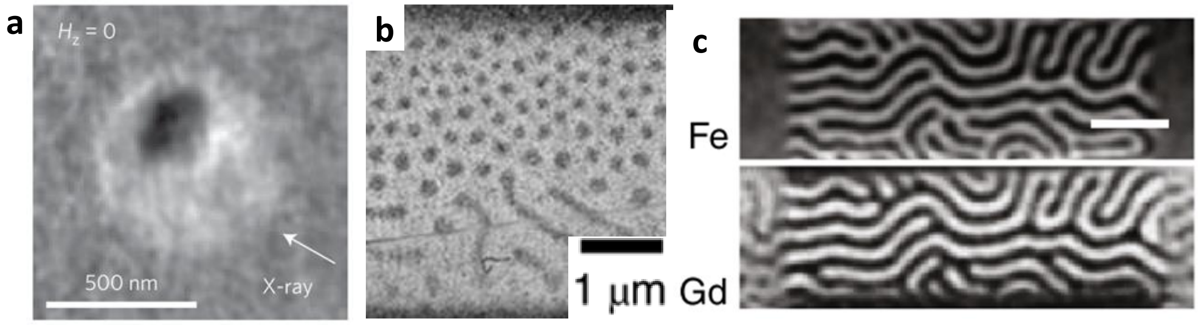

Figure 3.4.3| (a) X-PEEM image of a magnetic skyrmion in a Pt/Co/MgO nanodot where brightness depends on degree of alignment to direction of x-ray that was incident at a grazing angle of 16º [202]. (b) MTXM image of a mixed skyrmion and stripe state in $[Ta/CoFeB/MgO]_{15}$ where brightness corresponds to the perpendicular magnetization magnitude[139]. (c) STXM image of labyrinth domain in GdFeCo resolved by Fe and Gd atoms by tuning of photon energy. Scale bar, 1 μm[168]

Besides electrons, X-ray is another critical tool to probe magnetization via x-ray photoemission electron microscopy (X-PEEM), magnetic transmission x-ray microscopy (MTXM) and scanning transmission x-ray microscopy (STXM)[346]. These imaging techniques fundamentally operates on the phenomenon of x-ray magnetic circular dichroism (XMCD), where circularly polarized X-ray of opposite polarization exhibits different adsorption. The X-ray-based techniques have a trade-off in spatial resolution compared to electron-based techniques. Still, they come with advantages like element-specific probing of magnetization by tuning photon energy and even probing specifically spin or orbital magnetic moments[346].

For X-PEEM, the emitted electron intensity that depends on the projection of the magnetization along the X-ray beam is captured. An X-PEEM image of a magnetic skyrmion on a Pt/Co/MgO nanodot illuminated at a grazing angle of 16º is shown in Fig. 3.4.3(a), with the maximum and minimum brightness at the opposite edges of the skyrmion[202]. X-PEEM is a flexible technique across materials and used in many works on magnetic skyrmions[142,159,160,183,202,221,227,347]. MTXM and STXM differed as full-field imaging and focussed point-like imaging that generates images by spatial scanning. Thus, MTXM has the temporal advantage in investigating fast skyrmion dynamics[135]. Otherwise, MTXM remains useful as simply an imaging technique in other works[135,176,190,191,225]. An MTXM image is presented in Fig. 3.4.3(b), where the brightness corresponds to perpendicular magnetization magnitude and shows a mixed skyrmion and stripe state in $[Ta/CoFeB/MgO]_{15}$ [139]. The element-specific capability of X-ray-based imaging is highlighted for the STXM of ferrimagnets like GdFeCo shown in Fig. 3.4.3(c), clearly demonstrating the ferrimagnetic coupling between the Fe and Gd atoms[168]. With a lower temporal resolution of STXM, it is generally used for static imaging of magnetic states in many materials[121,136,138,140,142,151,168,170,173,177,227,348,349], but are also applied in a pump-probe manner to investigate dynamical processes at the ns temporal resolution provided the processes are fully repeatable and deterministic[169,172]. X-ray holography is another imaging technique that provides high spatial precision and drift-free imaging critical for dynamic investigations[211,223,349,350]. Resonant elastic x-ray scattering (REXS) is also available for reciprocal space imaging limited to ordered magnetic states[44,87,90].

Scanning probe-based magnetic microscopy includes spin-polarized scanning tunnelling microscopy (SP-STM), magnetic force microscopy (MFM), and nitrogen-vacancy scanning probe microscopy (NV-SPM). SP-STM operates based on the electrical tunnelling current that depends on the relative alignment between the probe and the local sample magnetization. The atomic-scale resolution of SP-STM is demonstrated in the magnetic skyrmion lattice in Fe monolayer, as shown in Fig. 3.4.4(a). All three magnetization components can be resolved by this technique, thus being useful particularly for investigating details of magnetic structure and configurations[7,123,124,154,197,351-354]. In contrast to SP-STM, MFM indirectly obtains the sample's magnetization via the magnetic force exerted on the magnetic tip by the sample's stray field. Figure 3.4.4(b) shows an MFM image of a mixed skyrmion and stripe state in magnetic multilayer $[Pt/Ir/Co]_{10}$. A similar magnetic exchange force microscopy operates directly based on the exchange interaction between the magnetic tip and the sample magnetization[355,356]. The NV-SPM is similar to MFM but with a significantly higher sensitivity to the magnetic fields and has recently been employed for magnetic skyrmion studies[147,203,357].

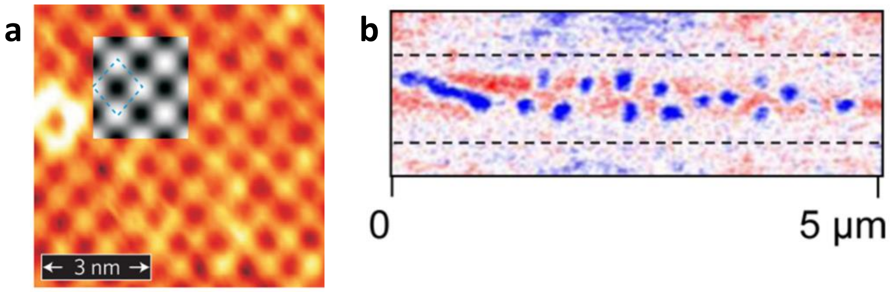

Figure 3.4.4| (a) SP-STM image of magnetic skyrmion lattice in Fe monolayer deposited on Ir(111)[3]. (b) MFM image of a mixed skyrmion and stripe state in magnetic multilayer $[Pt/Ir/Co]_{10}$ [128].

Finally, magneto-optical Kerr microscopy is another common magnetic imaging technique, easily accessible compared to the electron or X-ray-based techniques. The key limiting factor is the spatial resolution constraint by the diffraction limit of optical light in the range of hundreds of nanometers. However, this resolution remains sufficient for most of the magnetic skyrmions found in magnetic multilayers, thus they are commonly applied in many works, including our work presented in Chapters 5 and 6[129,132,143,153,156,157,164-166,174,207,211,217,220,260]. The principle of this microscopy is the magneto-optical Kerr effect (MOKE), where the polarization change upon reflection is magnetization dependent. Detailed discussion on this microscopy technique is presented in Section 4.2.2.

3.4.2 Electrical Detection

Electrical properties and signals are crucial detection methods for applications in electronic devices. The imaging techniques presented in Section 3.4.1 are valuable for research investigations but impractical to be embedded into technological devices. Magnetic information can be probed electrically using various phenomena, including Hall resistance, magnetoresistance, and Nernst effect. However, a critical consideration is required regarding electrical signals that can carry magnetic signals representing magnetization information but not a specific spin texture. The electrical Hall resistance can be resolved into three main sources: ordinary Hall effect, anomalous Hall effect, and topological Hall effect[65,131,358,359]. A detailed discussion of electrical Hall resistance is presented in Section 4.2.3 as it was used in our work presented in Chapters 5 and 6.

In a magnetic tunnel junction (MTJ), the structure itself constitutes a magnetization detector based on tunnelling magnetoresistance (TMR). The electrical resistance depends on the relative alignment between the free and reference layer. An MTJ can be designed with narrow dimensions comparable to the magnetic skyrmion to restrict the stable states within the MTJ layer to be either a single magnetic skyrmion or the ferromagnetic state[280,296]. In this manner, the intermediate magnetoresistance can be directly associated with certainty to the existence of a magnetic skyrmion.

Apart from TMR applied in MTJ and SP-STM, Hanneken *et al.* demonstrated that the winding structure of the magnetic skyrmion could generate a tunnelling non-collinear magnetoresistance (NCMR)[360,361]. Instead of requiring a reference layer or magnetized tip, NCMR alone can generate the detectable change in electrical resistance to identify the polar angle evolution across a domain wall or skyrmion. This property is sufficient to characterize several key properties like skyrmion position and size even though it cannot resolve the exact magnetic configuration[125,362,363].

A thermoelectric approach to probe local magnetization and acquiring an image via a scanning protocol was proposed recently[162]. Using a scanning laser source to induce thermal gradients and generate detectable IP charge currents via the anomalous Nernst effect (ANE) and the combination of the spin Seeback effect with the inverse spin Hall effect. By measurement of electrical currents across both the orthogonal IP axis, the magnetization profile can be reconstructed.

3.4.3 Magnetic susceptibility

Magnetic susceptibility is commonly used to identify magnetic phase transitions and map spin texture phases, including magnetic skyrmions in earlier works in the absence of an imaging technique. Magnetic susceptibility is given by $\chi_{DC} = \partial M / \partial H$, quantifying the magnetization response to an external magnetic field. An alternating current (AC) magnetic susceptibility quantifies the magnetization response to an oscillating external magnetic field about a dc magnetic field. Bauer and Pfleiderer comprehensively elucidate both the DC and AC magnetic susceptibility behaviour in a magnetic skyrmion material based on MnSi[364].

As discussed in Section 3.1.3, the spin texture transformation with magnetic field will follow helical, conical, skyrmion lattice, conical, and ferromagnetic states in sequence at the temperature close to the Curie temperature. The divergence between χ_{DC} and real χ_{AC} are found at the critical field ranges where the transition between spin textures occurs for both helical to conical and conical to skyrmion states. The divergence occurs as a response to macroscopic spin textures at very slow time scales like helical state reorientation. The magnetic skyrmion phase is identifiable from an apparent dip and plateau in both χ_{DC} and real χ_{AC} [46,64,77,89,103,107,364].

3.5 Skyrmionic Technologies

This section highlights the technological application of magnetic skyrmions centred in memory and computing, followed by several other applications beyond those fields.

3.5.1 Storage and Memory

The main application of magnetic skyrmions is nanoscale information carriers, thus immediately becoming relevant for high-density storage and memory technologies[28,70,219,253]. The magnetic skyrmion's topological nature provides it with further stability and reliability from deformation and defects[4,6]. Notably, their low pinning current propelled their application as mobile and electrically controllable mobile information carriers, particularly in a memory architecture like the racetrack memory[324-326]. The racetrack memory architecture initially proposed by Parkin *et al*. constitutes a concept of using a magnetic nanowire or track carrying mobile domain walls and stationary domain wall generating, annihilating, and reading elements along the nanowire[365]. Magnetic skyrmions with topological stability and lower pinning currents naturally became the preferred information carrier over domain walls for racetrack memory devices[366].

Using the presence and absence of magnetic skyrmions to present the binary bit of information, the thermally induced random drifting of the skyrmions will cause data corruption[163,174]. Artificial pinning structures to confine skyrmion at specific points along the track is an option[367,368]. Zheng *et al*. alternatively proposed using a continuous magnetic skyrmion and bobbers chain, where a bobber replaces the role of the skyrmion's absence to maintain their relative positions along the track[50]. Jena *et al*. later demonstrated a similar scheme that uses antiskyrmions instead of chiral bobbers[369]. For skyrmion propagation, the skyrmion Hall effect is of the primary concern. A synthetic antiferromagnetic structure or antiferromagnetic material can nullify the gyrotropic force[168,217]. Alternatively, edge modifications such as magnetic anisotropy and thickness can enhance the confining potential to sustain skyrmion motion up to larger velocities[317,370]. Juge *et al*. fabricated confining skyrmion tracks on a magnetic film via ion irradiation that lowered the magnetic anisotropy and DMI of the irradiated regions[160]. The data in the racetrack memory needs to be shifted to the desired position for reading and writing and requires excess space to accommodate these shifts. Thus, Zhang *et al*. proposed a circular racetrack design that does not require those excessive space and could be driven using magnetic field gradients, as shown in Fig. 3.5.1(b)[371]. Zhang *et al*. recently proposed a perpendicular track architecture to enhance information density, as shown in Fig. 3.5.1(c), and demonstrated its feasibility experimentally in thin BDMI material, Cu_2OSeO_3 [94].

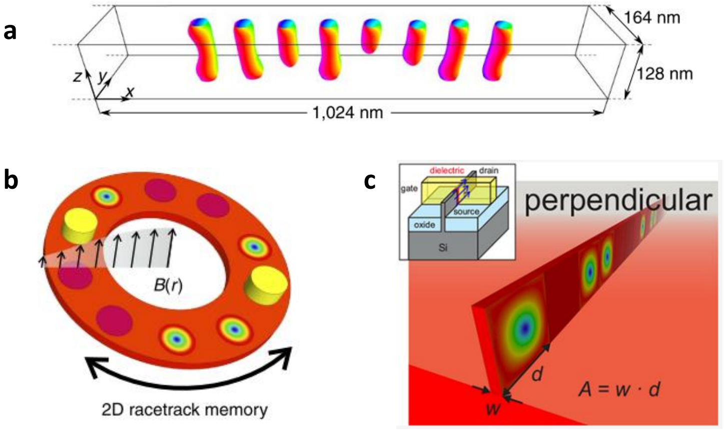

Figure 3.5.1| (a) Magnetic skyrmion and bobber chain used to maintain relative separation between data[50]. (c) Circular racetrack memory design[371]. (c) Illustration of a perpendicular magnetic skyrmion track[94].

Besides utilizing the mobile properties of magnetic skyrmions, their stability continues to make them reliable information carriers in static systems. The concerns surrounding skyrmion propagation can be removed in these systems, leaving the focus on just the nucleation and annihilation processes. The quantized magnetic skyrmions offer reliable multistate properties in a static memory element like a magnetic tunnel junction[372]. The magnetic tunnel junction also simultaneously operates as nucleation, annihilation, and detection of the magnetic skyrmions[296].

3.5.2 Computing

The variety of magnetic skyrmion excitations and their mobility allows magnetic skyrmions to be directly used for computations besides representing data. In 2015, Zhang *et al*. proposed skyrmion OR and AND logic gates based on the magnetic track design, as shown in Fig. 3.5.2(a)[373]. These logic gates operated based on the skyrmion-skyrmion merger at the structural constrictions. Xing *et al*. later designed NOT, NAND, and NOR gates based on a trapped domain wall-skyrmion collision. By exploiting VCMA that can erect barriers for magnetic skyrmions along the magnetic track, Luo *et al*. showed a reconfigurable logic device that performs AND, NAND, OR, and NOR logic functions[258]. In a twist of fate, the skyrmion Hall effect viewed as detrimental for racetrack memory is essential for the logic device, in addition to skyrmion-skyrmion repulsion[258]. More skyrmionic designs are later proposed by Mankalale *et al*. [374]and Zhang *et al*. [375], as shown in Fig. 3.5.2(d). Chauwin *et al*. also designed a skyrmion logic system that performed reversible computations where the information carriers are preserved in the circuit[376]. While many skyrmion logic devices have been proposed, their experimental demonstration is yet to be realized.

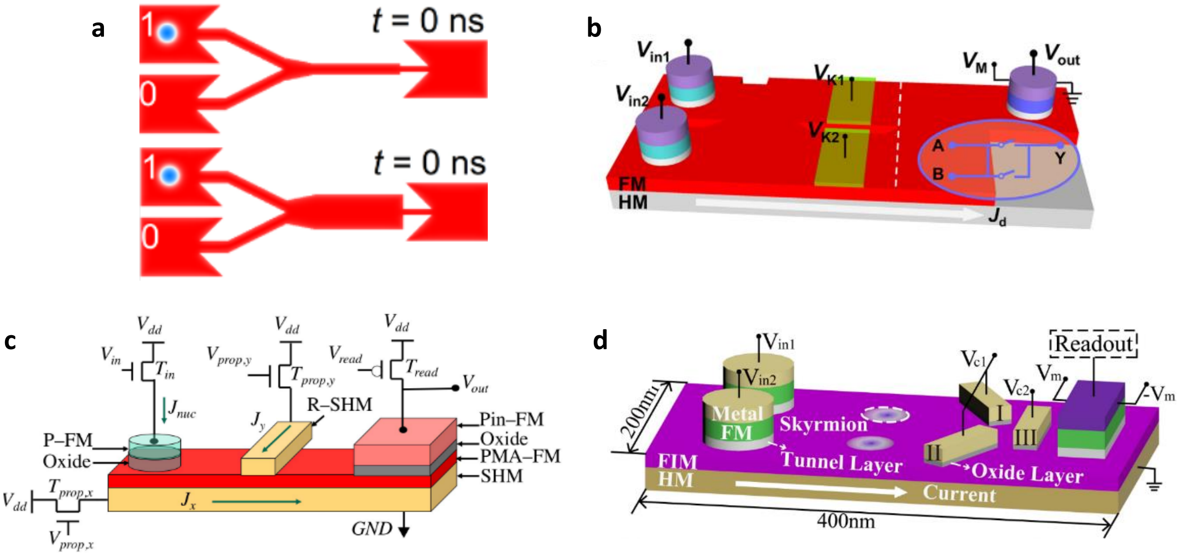

Figure 3.5.2| (a) OR and AND logic gate by track design[373]. (b) Reconfigurable skyrmion logic gate using voltage-controlled skyrmion barriers[258]. (c) NOR logic gate by using an additional current injection along the track[374]. (d) Reconfigurable AND, OR, XOR using three voltage-controlled pads[375].

Beyond basic logic operations, magnetic skyrmion applications are also extended to unconventional computing like neuromorphic computing, probabilistic computing, reservoir computing and Brownian computing.

Neuromorphic computing refers to the computing technique that mimics the human brains' function. The brain consists of a network of approximately 86 billion interconnected neurons that communicate via electrical pulses triggered under specific conditions. The simplest form of neuromorphic computing requires a network of neurons connected by weighted synapses. Neurons act as the signal computing element in the network, while the synapse regulates signal connection strength between each neuron[377]. The synapse only needs to carry information of its weight. Thus, a device that could hold a range of skyrmion quantities can easily be applied for this function as proposed in many works[378-383]. An artificial synapse was demonstrated experimentally by Song *et al*. using a Hall cross device with an injection tip as shown in Fig. 3.5.3(a)[170]. The skyrmions at the Hall cross can be accumulated or depopulated depending on the current direction.

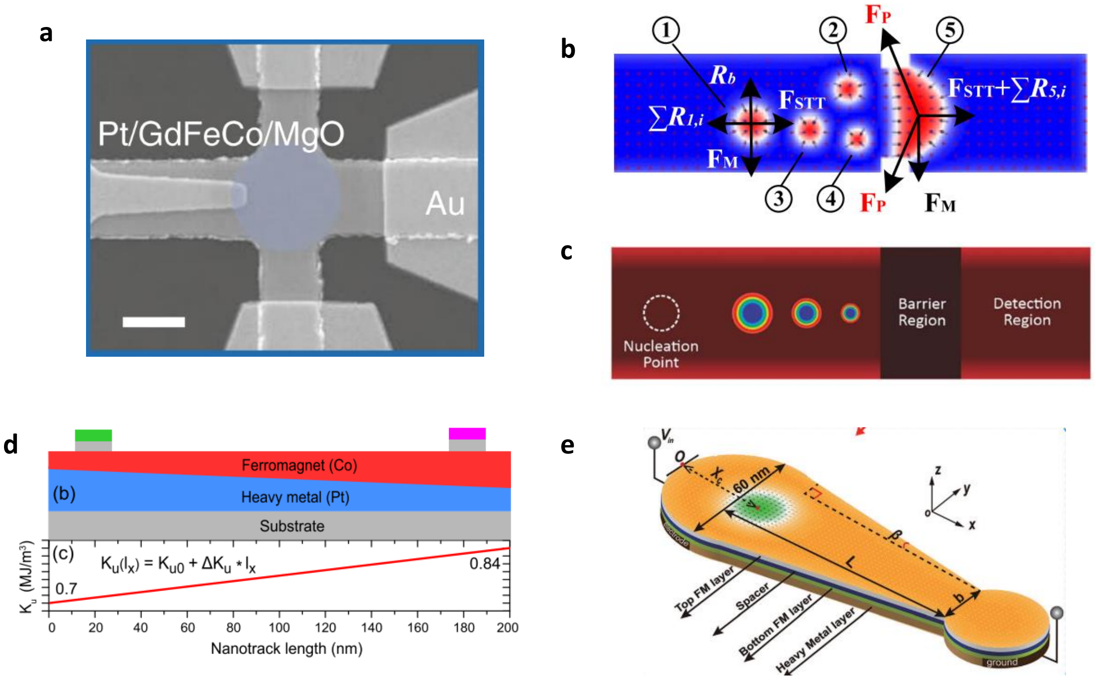

Figure 3.5.3| (a) Experimental magnetic skyrmion-based artificial synapse device**[170]**. (b) IF neuron based on pinned domain[384]. (c) IF neuron based on a magnetic anisotropy barrier[385]. (d) LIF neuron based current-driven skyrmion on anisotropy gradient[386]. (e) LIF neuron based current-driven skyrmion with geometrical constriction[387].

Among the variety in the type of biological neuron, the integrate-and-fire (IF) neuron triggers depending on the accumulate signal inputs[388]. He *et al*. numerically demonstrates this function using a pinned domain that inhibits the propagation of magnetic skyrmions up to a certain quantity before they can depin the domain and reach the detector at the end of the device, as shown in Fig. 3.5.3(b)[384]. Bindal *et al*. proposed a similar design that uses a magnetic anisotropy barrier which can only be surpassed by a minimum number of skyrmions as shown in Fig. 3.5.3(c)[385]. Li *et al*. proposed a more complex leaky integrate-and-fire neuron (LIF) where the accumulated signal in the neuron decays over time[386]. In the device shown in Fig. 3.5.3(d), the driving current is the input signal, the accumulation of signal is represented by the skyrmion's position, and the anisotropy gradient drives the skyrmion away from the detector to perform the leaky function. Chen *et al*. proposed a similar LIF neuron where the leaky function is achieved by geometrical constriction, as shown in Fig 3.5.3(d)[387]. Another LIF neuron was suggested by Liang *et al.* using a magnetic skyrmion in a nano-oscillator. The magnetic skyrmion has an equilibrium position at the centre of the device but can be increasingly driven into circular motion away from the centre by spin current injection[389]. A resonate-and-fire was also proposed using the oscillating breathing mode of a magnetic skyrmion in an MTJ[390].

Probabilistic or stochastic computing is a computing scheme that processes randomized bit-streams as probabilities instead of precise numerical values. This computing scheme benefits from significantly lower numerical operations for highly complex computations that do not require high numerical precision[391]. Pinna *et al.* first proposed applying magnetic skyrmions as a reshuffler device, and later experimentally achieved by Zázvorka *et al.*, as shown in Fig. 3.5.4(a)[163,259]. The reshuffler device utilizes the thermally induced random diffusive motion of the magnetic skyrmions to converts an input stream of magnetic skyrmions into a randomized stream as an output while conserving the number of skyrmions.

Reservoir computing is a form of recursive neural network that is useful for temporal or sequential recognition tasks like voice recognition[392,393]. Inputs are fed into a reservoir containing an interconnected and complex system of nodes with internal feedback loops due to their interconnectivity, and their transient responses are obtained as outputs[394]. The reservoir only requires a non-linear response and short term memory. Thus, the potential systems that can implement this are very wide. Only the collective response or output of the reservoir is weighted and trained instead of details within the reservoir to conserve significant computations[392]. Magnetic skyrmions were proposed as potential reservoir nodes using their non-linear resistive behaviour by Prychynenko *et al.* [395,396]. Clusters of magnetic skyrmions with different polarities are used as a skyrmion fabric or the reservoir as shown in Fig. 3.5.4(b). A dumbbell-shaped skyrmion device was also demonstrated as a reservoir node using its non-linear dependence of spatial position with the injected current[397].

Brownian computing is an ultralow energy-consuming computing technique that operates based on ambient thermal fluctuations[398]. When discrete particles like magnetic skyrmions are placed in a circuit or complex network of tracks, Brownian motion, albeit random, can drive the skyrmions across the whole circuit like a search operation. With intentional circuit design referred to as Brownian circuits, these random walks of particles and their interactions can be incorporated to perform computational capabilities. Jibiki *et al*. overcame one of the challenges in fabricating a skyrmion Brownian circuit that is pinning induced at the circuit junctions due to defects produced from etching processes[164]. They experimentally demonstrated pinning-free junctions by fabricating the tracks by deposition of a patterned SiO_2 layer instead of etching.

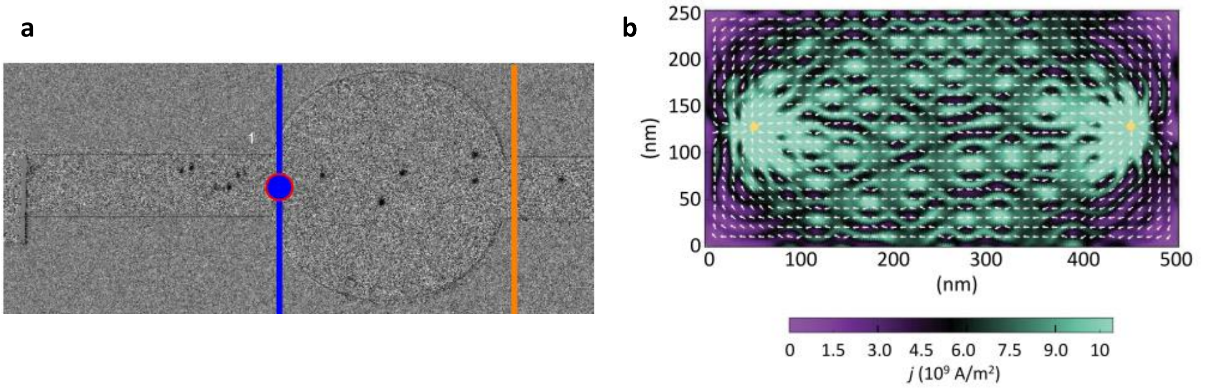

Figure 3.5.4| (a) Reshuffler device for probabilistic computing[163]. (b) Current density distribution across a skyrmion fabric for reservoir computing[396].

3.5.3 Other Applications

Magnonic crystals are artificial devices with periodic modulations in magnetic properties to manipulate magnon or spin wave dispersion. Instead of fabricating the modulation via material or device design, a periodic array of magnetic skyrmions was demonstrated as an effective magnonic crystal by Ma *et al*.[399]. The periodic skyrmion array generates band gaps that inhibit spin wave propagation within these gap frequencies and are even tunable by skyrmion size and out-of-plane magnetic field. A similar function was demonstrated by Wang *et al*. for the case of two-dimensional skyrmion lattice[400].

Nano-oscillators are critical as on-chip microwave signal generators and detectors for magnonic applications. In these devices, a sustained oscillating response from a steady excitation is required. The earliest design of a skyrmion nano-oscillator was proposed by Zhang *et al*. in the form of an MTJ structure, as shown in Fig.3.5.5(a)[401]. The structure consists of a free layer hosting a magnetic skyrmion separated from the uniformly magnetized fixed layer by a spacer with an electrode that is much smaller on top of the free layer. The size of the electrode must be smaller to induce a non-uniform current density and spin current injected from the fixed layer into the free layer. The spin current exerts a spin-transfer torque that drives the skyrmion away from the centre of the device into a circular motion. Garcia-Sanzhez *et al*. next proposed using a fixed layer with a vortex configuration to generate a diverging spin current for a device with a uniform size[402]. The confining potential due to skyrmion-edge interaction determines the gyration frequency. Thus, edge modifications via magnetic anisotropy or DMI could tune the gyration frequency and reported in later works[403-405]. SAF skyrmions were also demonstrated to exhibit gyration with suppressed radius when one skyrmion is driven into circular motion by STT drags the other by SAF coupling along the same trajectory[406].

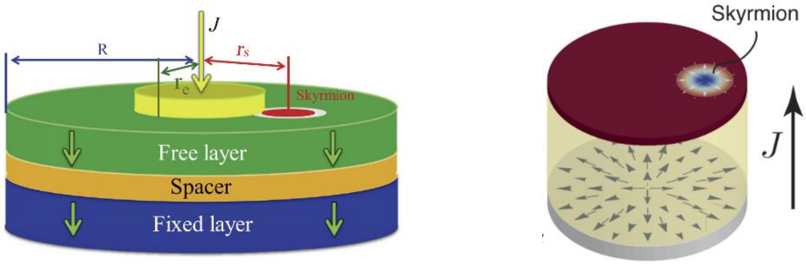

Figure 3.5.5| Magnetic skyrmion-based spin-torque nano-oscillators using (a) uniformly magnetized fixed layer and narrow electrode[401], and (b) vortex magnetized fixed layer[402].

References

1 R. Y. Q. Xun. Emerging Scientists Supplementary Issue II: Topological Circuits - A Stepping Stone in the Topological Revolution. *Molecular Frontiers Journal*, 1-6, doi:10.1142/S2529732520970020 (2020).

2 O. A. Tretiakov & O. Tchernyshyov. Vortices in thin ferromagnetic films and the skyrmion number. *Phys. Rev. B* **75**, 012408, doi:10.1103/PhysRevB.75.012408 (2007).

3 S. Heinze, K. von Bergmann, M. Menzel, *et al.* Spontaneous atomic-scale magnetic skyrmion lattice in two dimensions. *Nat. Phys.* **7**, 713-718, doi:10.1038/nphys2045 (2011).

4 N. Nagaosa & Y. Tokura. Topological properties and dynamics of magnetic skyrmions. *Nat. Nanotech.* **8**, 899-911, doi:10.1038/nnano.2013.243 (2013).

5 N. Romming, C. Hanneken, M. Menzel, *et al.* Writing and Deleting Single Magnetic Skyrmions. *Science* **341**, 636, doi:10.1126/science.1240573 (2013).

6 G. Finocchio, F. Büttner, R. Tomasello, *et al.* Magnetic skyrmions: from fundamental to applications. *J. Phys. D: Appl. Phys.* **49**, 423001, doi:10.1088/0022-3727/49/42/423001 (2016).

7 N. Romming, A. Kubetzka, C. Hanneken, *et al.* Field-Dependent Size and Shape of Single Magnetic Skyrmions. *Phys. Rev. Lett.* **114**, 177203, doi:10.1103/PhysRevLett.114.177203 (2015).

8 H.-B. Braun. Fluctuations and instabilities of ferromagnetic domain-wall pairs in an external magnetic field. *Phys. Rev. B* **50**, 16485-16500, doi:10.1103/PhysRevB.50.16485 (1994).

9 A. Kubetzka, O. Pietzsch, M. Bode, *et al.* Spin-polarized scanning tunneling microscopy study of 360º walls in an external magnetic field. *Phys. Rev. B* **67**, 020401, doi:10.1103/PhysRevB.67.020401 (2003).

10 F. Büttner, I. Lemesh & G. S. D. Beach. Theory of isolated magnetic skyrmions: From fundamentals to room temperature applications. *Sci. Rep.* **8**, 4464, doi:10.1038/s41598-018-22242-8 (2018).

11 A. A. Belavin & A. M. Polyakov. Metastable states of two-dimensional isotropic ferromagnets. *Soviet Journal of Experimental and Theoretical Physics Letters* **22**, 245 (1975).

12 A. D. Verga. Skyrmion to ferromagnetic state transition: A description of the topological change as a finite-time singularity in the skyrmion dynamics. *Phys. Rev. B* **90**, 174428, doi:10.1103/PhysRevB.90.174428 (2014).

13 A. O. Leonov, T. L. Monchesky, N. Romming, *et al.* The properties of isolated chiral skyrmions in thin magnetic films. *New J. Phys.* **18**, 065003, doi:10.1088/1367-2630/18/6/065003 (2016).

14 B. Heil, A. Rosch & J. Masell. Universality of annihilation barriers of large magnetic skyrmions in chiral and frustrated magnets. *Phys. Rev. B* **100**, 134424, doi:10.1103/PhysRevB.100.134424 (2019).

15 A. Derras-Chouk, E. M. Chudnovsky & D. A. Garanin. Thermal collapse of a skyrmion. *J. Appl. Phys.* **126**, 083901, doi:10.1063/1.5109728 (2019).

16 A. Bernand-Mantel, C. B. Muratov & T. M. Simon. Unraveling the role of dipolar versus Dzyaloshinskii-Moriya interactions in stabilizing compact magnetic skyrmions. *Phys. Rev. B* **101**, 045416, doi:10.1103/PhysRevB.101.045416 (2020).

17 X. Zhang, Y. Zhou, K. Mee Song, *et al.* Skyrmion-electronics: writing, deleting, reading and processing magnetic skyrmions toward spintronic applications. *Journal of Physics: Condensed Matter* **32**, 143001, doi:10.1088/1361-648x/ab5488 (2020).

18 T. Tanigaki, K. Shibata, N. Kanazawa, *et al.* Real-Space Observation of Short-Period Cubic Lattice of Skyrmions in MnGe. *Nano Lett.* **15**, 5438-5442, doi:10.1021/acs.nanolett.5b02653 (2015).

19 X. Z. Yu, W. Koshibae, Y. Tokunaga, *et al.* Transformation between meron and skyrmion topological spin textures in a chiral magnet. *Nature* **564**, 95-98, doi:10.1038/s41586-018-0745-3 (2018).

20 I. Kézsmárki, S. Bordács, P. Milde, *et al.* Néel-type skyrmion lattice with confined orientation in the polar magnetic semiconductor GaV_4S_8. *Nat. Mater.* **14**, 1116-1122, doi:10.1038/nmat4402 (2015).

21 A. K. Nayak, V. Kumar, T. Ma, *et al.* Magnetic antiskyrmions above room temperature in tetragonal Heusler materials. *Nature* **548**, 561-566, doi:10.1038/nature23466 (2017).

22 S. Seki, X. Z. Yu, S. Ishiwata, *et al.* Observation of Skyrmions in a Multiferroic Material. *Science* **336**, 198, doi:10.1126/science.1214143 (2012).

23 E. Ruff, S. Widmann, P. Lunkenheimer, *et al.* Multiferroicity and skyrmions carrying electric polarization in GaV_4S_8. *Sci. Adv.* **1**, e1500916, doi:10.1126/sciadv.1500916 (2015).

24 J. Beille, J. Voiron & M. Roth. Long period helimagnetism in the cubic B20 $Fe_xCo_{1-x}Si$ and $Co_xMn_{1-x}Si$ alloys. *Solid State Communications* **47**, 399-402, doi:10.1016/0038-1098(83)90928-6 (1983).

25 Y. Tokura & N. Kanazawa. Magnetic Skyrmion Materials. *Chemical Reviews* **121**, 2857-2897, doi:10.1021/acs.chemrev.0c00297 (2020).

26 A. S. Sukhanov, A. Heinemann, L. Kautzsch, *et al.* Robust metastable skyrmions with tunable size in the chiral magnet $FePtMo_3N$. *Phys. Rev. B* **102**, 140409, doi:10.1103/PhysRevB.102.140409 (2020).

27 J. Kindervater, T. Adams, A. Bauer, *et al.* Evolution of magnetocrystalline anisotropies in $Mn_{1-x}Fe_xSi$ and $Mn_{1-x}Co_xSi$ as inferred from small-angle neutron scattering and bulk properties. *Phys. Rev. B* **101**, 104406, doi:10.1103/PhysRevB.101.104406 (2020).

28 S. Mühlbauer, B. Binz, F. Jonietz, *et al.* Skyrmion Lattice in a Chiral Magnet. *Science* **323**, 915, doi:10.1126/science.1166767 (2009).

29 A. Neubauer, C. Pfleiderer, B. Binz, *et al.* Topological Hall Effect in the A Phase of MnSi. *Phys. Rev. Lett.* **102**, 186602, doi:10.1103/PhysRevLett.102.186602 (2009).

30 M. Lee, W. Kang, Y. Onose, *et al.* Unusual Hall Effect Anomaly in MnSi under Pressure. *Phys. Rev. Lett.* **102**, 186601, doi:10.1103/PhysRevLett.102.186601 (2009).

31 N. Kanazawa, Y. Onose, T. Arima, *et al.* Large Topological Hall Effect in a Short-Period Helimagnet MnGe. *Phys. Rev. Lett.* **106**, 156603, doi:10.1103/PhysRevLett.106.156603 (2011).

32 R. Ritz, M. Halder, C. Franz, *et al.* Giant generic topological Hall resistivity of MnSi under pressure. *Phys. Rev. B* **87**, 134424, doi:10.1103/PhysRevB.87.134424 (2013).

33 A. Chacon, A. Bauer, T. Adams, *et al.* Uniaxial Pressure Dependence of Magnetic Order in MnSi. *Phys. Rev. Lett.* **115**, 267202, doi:10.1103/PhysRevLett.115.267202 (2015).

34 Y. Nii, T. Nakajima, A. Kikkawa, *et al.* Uniaxial stress control of skyrmion phase. *Nat. Commun.* **6**, 8539, doi:10.1038/ncomms9539 (2015).

35 T. Schwarze, J. Waizner, M. Garst, *et al.* Universal helimagnon and skyrmion excitations in metallic, semiconducting and insulating chiral magnets. *Nat. Mater.* **14**, 478-483, doi:10.1038/nmat4223 (2015).

36 T. Yokouchi, N. Kanazawa, A. Tsukazaki, *et al.* Formation of In-plane Skyrmions in Epitaxial MnSi Thin Films as Revealed by Planar Hall Effect. *Journal of the Physical Society of Japan* **84**, 104708, doi:10.7566/JPSJ.84.104708 (2015).

37 X. Yu, A. Kikkawa, D. Morikawa, *et al.* Variation of skyrmion forms and their stability in MnSi thin plates. *Phys. Rev. B* **91**, 054411, doi:10.1103/PhysRevB.91.054411 (2015).

38 F. Kagawa, H. Oike, W. Koshibae, *et al.* Current-induced viscoelastic topological unwinding of metastable skyrmion strings. *Nat. Commun.* **8**, 1332, doi:10.1038/s41467-017-01353-2 (2017).

39 T. Nakajima, H. Oike, A. Kikkawa, *et al.* Skyrmion lattice structural transition in MnSi. *Sci. Adv.* **3**, e1602562, doi:10.1126/sciadv.1602562 (2017).

40 T. Yokouchi, S. Hoshino, N. Kanazawa, *et al.* Current-induced dynamics of skyrmion strings. *Sci. Adv.* **4**, eaat1115, doi:10.1126/sciadv.aat1115 (2018).

41 S. V. Grigoriev, N. M. Potapova, S. A. Siegfried, *et al.* Chiral Properties of Structure and Magnetism in $Mn_{1-x}Fe_xGe$ Compounds: When the Left and the Right are Fighting, Who Wins? *Phys. Rev. Lett.* **110**, 207201, doi:10.1103/PhysRevLett.110.207201 (2013).

42 N. Kanazawa, M. Kubota, A. Tsukazaki, *et al.* Discretized topological Hall effect emerging from skyrmions in constricted geometry. *Phys. Rev. B* **91**, 041122, doi:10.1103/PhysRevB.91.041122 (2015).

43 K. Shibata, J. Iwasaki, N. Kanazawa, *et al.* Large anisotropic deformation of skyrmions in strained crystal. *Nat. Nanotech.* **10**, 589-592, doi:10.1038/nnano.2015.113 (2015).

44 Y. Yamasaki, D. Morikawa, T. Honda, *et al.* Dynamical process of skyrmion-helical magnetic transformation of the chiral-lattice magnet FeGe probed by small-angle

resonant soft x-ray scattering. *Phys. Rev. B* **92**, 220421, doi:10.1103/PhysRevB.92.220421 (2015).

45 C. Jin, Z.-A. Li, A. Kovács, *et al.* Control of morphology and formation of highly geometrically confined magnetic skyrmions. *Nat. Commun.* **8**, 15569, doi:10.1038/ncomms15569 (2017).

46 A. S. Ahmed, J. Rowland, B. D. Esser, *et al.* Chiral bobbers and skyrmions in epitaxial FeGe/Si(111) films. *Phys. Rev. Mater.* **2**, 041401, doi:10.1103/PhysRevMaterials.2.041401 (2018).

47 G. Berruto, I. Madan, Y. Murooka, *et al.* Laser-Induced Skyrmion Writing and Erasing in an Ultrafast Cryo-Lorentz Transmission Electron Microscope. *Phys. Rev. Lett.* **120**, 117201, doi:10.1103/PhysRevLett.120.117201 (2018).

48 K. Shibata, T. Tanigaki, T. Akashi, *et al.* Current-Driven Motion of Domain Boundaries between Skyrmion Lattice and Helical Magnetic Structure. *Nano Lett.* **18**, 929-933, doi:10.1021/acs.nanolett.7b04312 (2018).

49 X. Yu, D. Morikawa, T. Yokouchi, *et al.* Aggregation and collapse dynamics of skyrmions in a non-equilibrium state. *Nat. Phys.* **14**, 832-836, doi:10.1038/s41567-018-0155-3 (2018).

50 F. Zheng, F. N. Rybakov, A. B. Borisov, *et al.* Experimental observation of chiral magnetic bobbers in B20-type FeGe. *Nat. Nanotech.* **13**, 451-455, doi:10.1038/s41565-018-0093-3 (2018).

51 F. Rendell-Bhatti, R. J. Lamb, J. W. van der Jagt, *et al.* Spontaneous creation and annihilation dynamics and strain-limited stability of magnetic skyrmions. *Nat. Commun.* **11**, 3536, doi:10.1038/s41467-020-17338-7 (2020).

52 X. Z. Yu, D. Morikawa, K. Nakajima, *et al.* Motion tracking of 80-nm-size skyrmions upon directional current injections. *Sci. Adv.* **6**, eaaz9744, doi:10.1126/sciadv.aaz9744 (2020).

53 J. C. Gallagher, K. Y. Meng, J. T. Brangham, *et al.* Robust Zero-Field Skyrmion Formation in FeGe Epitaxial Thin Films. *Phys. Rev. Lett.* **118**, 027201, doi:10.1103/PhysRevLett.118.027201 (2017).

54 N. Kanazawa, J. H. Kim, D. S. Inosov, *et al.* Possible skyrmion-lattice ground state in the B20 chiral-lattice magnet MnGe as seen via small-angle neutron scattering. *Phys. Rev. B* **86**, 134425, doi:10.1103/PhysRevB.86.134425 (2012).

55 Y. Shiomi, N. Kanazawa, K. Shibata, *et al.* Topological Nernst effect in a three-dimensional skyrmion-lattice phase. *Phys. Rev. B* **88**, 064409, doi:10.1103/PhysRevB.88.064409 (2013).

56 N. Kanazawa, J. S. White, H. M. Rønnow, *et al.* Topological spin-hedgehog crystals of a chiral magnet as engineered with magnetic anisotropy. *Phys. Rev. B* **96**, 220414, doi:10.1103/PhysRevB.96.220414 (2017).

57 Y. Fujishiro, N. Kanazawa, T. Shimojima, *et al.* Large magneto-thermopower in MnGe with topological spin texture. *Nat. Commun.* **9**, 408, doi:10.1038/s41467-018-02857-1 (2018).

58 N. Kanazawa, A. Kitaori, J. S. White, *et al.* Direct Observation of the Statics and Dynamics of Emergent Magnetic Monopoles in a Chiral Magnet. *Phys. Rev. Lett.* **125**, 137202, doi:10.1103/PhysRevLett.125.137202 (2020).

59 T. Adams, S. Mühlbauer, A. Neubauer, *et al.* Skyrmion Lattice Domains in $Fe_{1-x}Co_xSi$. *Journal of Physics: Conference Series* **200**, 032001, doi:10.1088/1742-6596/200/3/032001 (2010).

60 H. S. Park, X. Yu, S. Aizawa, *et al.* Observation of the magnetic flux and three-dimensional structure of skyrmion lattices by electron holography. *Nat. Nanotech.* **9**, 337-342, doi:10.1038/nnano.2014.52 (2014).

61 A. Bauer, M. Garst & C. Pfleiderer. History dependence of the magnetic properties of single-crystal $Fe_{1-x}Co_xSi$. *Phys. Rev. B* **93**, 235144, doi:10.1103/PhysRevB.93.235144 (2016).

62 J. Wild, T. N. G. Meier, S. Pöllath, *et al.* Entropy-limited topological protection of skyrmions. *Sci. Adv.* **3**, e1701704, doi:10.1126/sciadv.1701704 (2017).

63 P. Milde, E. Neuber, A. Bauer, *et al.* Surface pinning and triggered unwinding of skyrmions in a cubic chiral magnet. *Phys. Rev. B* **100**, 024408, doi:10.1103/PhysRevB.100.024408 (2019).

64 B. Balasubramanian, P. Manchanda, R. Pahari, *et al.* Chiral Magnetism and High-Temperature Skyrmions in B20-Ordered Co-Si. *Phys. Rev. Lett.* **124**, 057201, doi:10.1103/PhysRevLett.124.057201 (2020).

65 C. Franz, F. Freimuth, A. Bauer, *et al.* Real-Space and Reciprocal-Space Berry Phases in the Hall Effect of $Mn_{1-x}Fe_xSi$. *Phys. Rev. Lett.* **112**, 186601, doi:10.1103/PhysRevLett.112.186601 (2014).

66 T. Yokouchi, N. Kanazawa, A. Tsukazaki, *et al.* Stability of two-dimensional skyrmions in thin films of $Mn_{1-x}Fe_xSi$ investigated by the topological Hall effect. *Phys. Rev. B* **89**, 064416, doi:10.1103/PhysRevB.89.064416 (2014).

67 K. Shibata, X. Z. Yu, T. Hara, *et al.* Towards control of the size and helicity of skyrmions in helimagnetic alloys by spin–orbit coupling. *Nat. Nanotech.* **8**, 723-728, doi:10.1038/nnano.2013.174 (2013).

68 E. Altynbaev, N. Martin, A. Heinemann, *et al.* Onset of a skyrmion phase by chemical substitution in MnGe-based chiral magnets. *Phys. Rev. B* **101**, 100404, doi:10.1103/PhysRevB.101.100404 (2020).

69 E. Altynbaev, S. A. Siegfried, E. Moskvin, *et al.* Hidden quantum phase transition in $Mn_{1-x}Fe_xGe$ evidenced by small-angle neutron scattering. *Phys. Rev. B* **94**, 174403, doi:10.1103/PhysRevB.94.174403 (2016).

70 Y. Fujishiro, N. Kanazawa, T. Nakajima, *et al.* Topological transitions among skyrmion- and hedgehog-lattice states in cubic chiral magnets. *Nat. Commun.* **10**, 1059, doi:10.1038/s41467-019-08985-6 (2019).

71 M. J. Stolt, X. Sigelko, N. Mathur, *et al.* Chemical Pressure Stabilization of the Cubic B20 Structure in Skyrmion Hosting $Fe_{1-x}Co_xGe$ Alloys. *Chemistry of Materials* **30**, 1146-1154, doi:10.1021/acs.chemmater.7b05261 (2018).

72 C. S. Spencer, J. Gayles, N. A. Porter, *et al.* Helical magnetic structure and the anomalous and topological Hall effects in epitaxial B20 $Fe_{1-y}Co_yGe$ films. *Phys. Rev. B* **97**, 214406, doi:10.1103/PhysRevB.97.214406 (2018).

73 M. J. Stolt, S. Schneider, N. Mathur, *et al.* Electrical Detection and Magnetic Imaging of Stabilized Magnetic Skyrmions in $Fe_{1-x}Co_xGe$ ($x < 0.1$) Microplates. *Advanced Functional Materials* **29**, 1805418, doi:10.1002/adfm.201805418 (2019).

74 H. Oike, A. Kikkawa, N. Kanazawa, *et al.* Interplay between topological and thermodynamic stability in a metastable magnetic skyrmion lattice. *Nat. Phys.* **12**, 62-66, doi:10.1038/nphys3506 (2016).

75 C. Pfleiderer, T. Adams, A. Bauer, *et al.* Skyrmion lattices in metallic and semiconducting B20 transition metal compounds. *Journal of Physics: Condensed Matter* **22**, 164207, doi:10.1088/0953-8984/22/16/164207 (2010).

76 A. Chacon, L. Heinen, M. Halder, *et al.* Observation of two independent skyrmion phases in a chiral magnetic material. *Nat. Phys.* **14**, 936-941, doi:10.1038/s41567-018-0184-y (2018).

77 M. Halder, A. Chacon, A. Bauer, *et al.* Thermodynamic evidence of a second skyrmion lattice phase and tilted conical phase in Cu_2OSeO_3. *Phys. Rev. B* **98**, 144429, doi:10.1103/PhysRevB.98.144429 (2018).

78 Y. Onose, Y. Okamura, S. Seki, *et al.* Observation of Magnetic Excitations of Skyrmion Crystal in a Helimagnetic Insulator Cu_2OSeO_3. *Phys. Rev. Lett.* **109**, 037603, doi:10.1103/PhysRevLett.109.037603 (2012).

79 S. Seki, S. Ishiwata & Y. Tokura. Magnetoelectric nature of skyrmions in a chiral magnetic insulator Cu_2OSeO_3. *Phys. Rev. B* **86**, 060403, doi:10.1103/PhysRevB.86.060403 (2012).

80 S. Seki, J. H. Kim, D. S. Inosov, *et al.* Formation and rotation of skyrmion crystal in the chiral-lattice insulator Cu_2OSeO_3. *Phys. Rev. B* **85**, 220406, doi:10.1103/PhysRevB.85.220406 (2012).

81 J. S. White, I. Levatić, A. A. Omrani, *et al.* Electric field control of the skyrmion lattice in Cu_2OSeO_3. *Journal of Physics: Condensed Matter* **24**, 432201, doi:10.1088/0953-8984/24/43/432201 (2012).

82 Y. Okamura, F. Kagawa, M. Mochizuki, *et al.* Microwave magnetoelectric effect via skyrmion resonance modes in a helimagnetic multiferroic. *Nat. Commun.* **4**, 2391, doi:10.1038/ncomms3391 (2013).

83 J. S. White, K. Prša, P. Huang, *et al.* Electric-Field-Induced Skyrmion Distortion and Giant Lattice Rotation in the Magnetoelectric Insulator Cu_2OSeO_3. *Phys. Rev. Lett.* **113**, 107203, doi:10.1103/PhysRevLett.113.107203 (2014).

84 N. Ogawa, S. Seki & Y. Tokura. Ultrafast optical excitation of magnetic skyrmions. *Sci. Rep.* **5**, 9552, doi:10.1038/srep09552 (2015).

85 Y. Okamura, F. Kagawa, S. Seki, *et al.* Transition to and from the skyrmion lattice phase by electric fields in a magnetoelectric compound. *Nat. Commun.* **7**, 12669, doi:10.1038/ncomms12669 (2016).

86 S. Seki, Y. Okamura, K. Kondou, *et al.* Magnetochiral nonreciprocity of volume spin wave propagation in chiral-lattice ferromagnets. *Phys. Rev. B* **93**, 235131, doi:10.1103/PhysRevB.93.235131 (2016).

87 S. L. Zhang, A. Bauer, H. Berger, *et al.* Imaging and manipulation of skyrmion lattice domains in Cu_2OSeO_3. *Appl. Phys. Lett.* **109**, 192406, doi:10.1063/1.4967499 (2016).

88 P. Huang, M. Cantoni, A. Kruchkov, *et al.* In Situ Electric Field Skyrmion Creation in Magnetoelectric Cu_2OSeO_3. *Nano Lett.* **18**, 5167-5171, doi:10.1021/acs.nanolett.8b02097 (2018).

89 F. Qian, L. J. Bannenberg, H. Wilhelm, *et al.* New magnetic phase of the chiral skyrmion material Cu_2OSeO_3. *Sci. Adv.* **4**, eaat7323, doi:10.1126/sciadv.aat7323 (2018).

90 S. Zhang, G. van der Laan, J. Müller, *et al.* Reciprocal space tomography of 3D skyrmion lattice order in a chiral magnet. *Proceedings of the National Academy of Sciences* **115**, 6386, doi:10.1073/pnas.1803367115 (2018).

91 L. J. Bannenberg, H. Wilhelm, R. Cubitt, *et al.* Multiple low-temperature skyrmionic states in a bulk chiral magnet. *npj Quantum Materials* **4**, 11, doi:10.1038/s41535-019-0150-7 (2019).

92 M. T. Birch, R. Takagi, S. Seki, *et al.* Increased lifetime of metastable skyrmions by controlled doping. *Phys. Rev. B* **100**, 014425, doi:10.1103/PhysRevB.100.014425 (2019).

93 T. Nomura, X. X. Zhang, S. Zherlitsyn, *et al.* Phonon Magnetochiral Effect. *Phys. Rev. Lett.* **122**, 145901, doi:10.1103/PhysRevLett.122.145901 (2019).

94 S. Zhang, D. M. Burn, N. Jaouen, *et al.* Robust Perpendicular Skyrmions and Their Surface Confinement. *Nano Lett.* **20**, 1428-1432, doi:10.1021/acs.nanolett.9b05141 (2020).

95 S. Seki, M. Garst, J. Waizner, *et al.* Propagation dynamics of spin excitations along skyrmion strings. *Nat. Commun.* **11**, 256, doi:10.1038/s41467-019-14095-0 (2020).

96 A. Aqeel, J. Sahliger, T. Taniguchi, *et al.* Microwave Spectroscopy of the Low-Temperature Skyrmion State in Cu_2OSeO_3. *Phys. Rev. Lett.* **126**, 017202, doi:10.1103/PhysRevLett.126.017202 (2021).

97 Y. Tokunaga, X. Z. Yu, J. S. White, *et al.* A new class of chiral materials hosting magnetic skyrmions beyond room temperature. *Nat. Commun.* **6**, 7638, doi:10.1038/ncomms8638 (2015).

98 K. Karube, J. S. White, N. Reynolds, *et al.* Robust metastable skyrmions and their triangular–square lattice structural transition in a high-temperature chiral magnet. *Nat. Mater.* **15**, 1237-1242, doi:10.1038/nmat4752 (2016).

99 K. Karube, J. S. White, D. Morikawa, *et al.* Skyrmion formation in a bulk chiral magnet at zero magnetic field and above room temperature. *Phys. Rev. Mater.* **1**, 074405, doi:10.1103/PhysRevMaterials.1.074405 (2017).

100 K. Karube, J. S. White, D. Morikawa, *et al.* Disordered skyrmion phase stabilized by magnetic frustration in a chiral magnet. *Sci. Adv.* **4**, eaar7043, doi:10.1126/sciadv.aar7043 (2018).

101 K. Karube, J. S. White, V. Ukleev, *et al.* Metastable skyrmion lattices governed by magnetic disorder and anisotropy in β-Mn-type chiral magnets. *Phys. Rev. B* **102**, 064408, doi:10.1103/PhysRevB.102.064408 (2020).

102 J. D. Bocarsly, C. Heikes, C. M. Brown, *et al.* Deciphering structural and magnetic disorder in the chiral skyrmion host materials $Co_xZn_yMn_z$ (x+y+z=20). *Phys. Rev. Mater.* **3**, 014402, doi:10.1103/PhysRevMaterials.3.014402 (2019).

103 K. Karube, K. Shibata, J. S. White, *et al.* Controlling the helicity of magnetic skyrmions in a β-Mn-type high-temperature chiral magnet. *Phys. Rev. B* **98**, 155120, doi:10.1103/PhysRevB.98.155120 (2018).

104 W. Li, C. Jin, R. Che, *et al.* Emergence of skyrmions from rich parent phases in the molybdenum nitrides. *Phys. Rev. B* **93**, 060409, doi:10.1103/PhysRevB.93.060409 (2016).

105 L. Kautzsch, J. D. Bocarsly, C. Felser, *et al.* Controlling Dzyaloshinskii-Moriya interactions in the skyrmion host candidates $FePd_{1-x}Pt_xMo_3N$. *Phys. Rev. Mater.* **4**, 024412, doi:10.1103/PhysRevMaterials.4.024412 (2020).

106 B. W. Qiang, N. Togashi, S. Momose, *et al.* Room-temperature magnetic skyrmion in epitaxial thin films of $Fe_{2-x}Pd_xMo_3N$ with the filled β-Mn-type chiral structure. *Appl. Phys. Lett.* **117**, 142401, doi:10.1063/5.0024071 (2020).

107 Y. Fujima, N. Abe, Y. Tokunaga, *et al.* Thermodynamically stable skyrmion lattice at low temperatures in a bulk crystal of lacunar spinel GaV_4Se_8. *Phys. Rev. B* **95**, 180410, doi:10.1103/PhysRevB.95.180410 (2017).

108 T. Kurumaji, T. Nakajima, V. Ukleev, *et al.* Neel-Type Skyrmion Lattice in the Tetragonal Polar Magnet $VOSe_2O_5$. *Phys. Rev. Lett.* **119**, 237201, doi:10.1103/PhysRevLett.119.237201 (2017).

109 A. N. Bogdanov & D. A. Yablonskii. Thermodynamically stable "vortices" in magnetically ordered crystals. The mixed state of magnets *Soviet Physics Journal of Experimental and Theoretical Physics* **68**, 101-103 (1989).

110 S. Bordács, A. Butykai, B. G. Szigeti, *et al.* Equilibrium Skyrmion Lattice Ground State in a Polar Easy-plane Magnet. *Sci. Rep.* **7**, 7584, doi:10.1038/s41598-017-07996-x (2017).

111 A. O. Leonov & I. Kézsmárki. Skyrmion robustness in noncentrosymmetric magnets with axial symmetry: The role of anisotropy and tilted magnetic fields. *Phys. Rev. B* **96**, 214413, doi:10.1103/PhysRevB.96.214413 (2017).

112 T. Kurumaji, T. Nakajima, A. Feoktystov, *et al.* Direct Observation of Cycloidal Spin Modulation and Field-induced Transition in Néel-type Skyrmion-hosting $VOSe_2O_5$. *Journal of the Physical Society of Japan* **90**, 024705, doi:10.7566/JPSJ.90.024705 (2021).

113 L. Peng, R. Takagi, W. Koshibae, *et al.* Controlled transformation of skyrmions and antiskyrmions in a non-centrosymmetric magnet. *Nat. Nanotech.* **15**, 181-186, doi:10.1038/s41565-019-0616-6 (2020).

114 J. Jena, B. Göbel, T. Ma, *et al.* Elliptical Bloch skyrmion chiral twins in an antiskyrmion system. *Nat. Commun.* **11**, 1115, doi:10.1038/s41467-020-14925-6 (2020).

115 S. V. Grigoriev, V. A. Dyadkin, E. V. Moskvin, *et al.* Helical spin structure of MnFeSi under a magnetic field: Small angle neutron diffraction study. *Phys. Rev. B* **79**, 144417, doi:10.1103/PhysRevB.79.144417 (2009).

116 V. Jaccarino, G. K. Wertheim, J. H. Wernick, *et al.* Paramagnetic Excited State of FeSi. *Phys. Rev.* **160**, 476-482, doi:10.1103/PhysRev.160.476 (1967).

117 D. Shinoda & S. Asanabe. Magnetic Properties of Silicides of Iron Group Transition Elements. *Journal of the Physical Society of Japan* **21**, 555-555, doi:10.1143/JPSJ.21.555 (1966).

118 X. Z. Yu, N. Kanazawa, Y. Onose, *et al.* Near room-temperature formation of a skyrmion crystal in thin-films of the helimagnet FeGe. *Nat. Mater.* **10**, 106-109, doi:10.1038/nmat2916 (2011).

119 S. V. Grigoriev, S. A. Siegfried, E. V. Altynbayev, *et al.* Flip of spin helix chirality and ferromagnetic state in $Fe_{1-x}Co_xGe$ compounds. *Phys. Rev. B* **90**, 174414, doi:10.1103/PhysRevB.90.174414 (2014).

120 J. F. DiTusa, S. B. Zhang, K. Yamaura, *et al.* Magnetic, thermodynamic, and electrical transport properties of the noncentrosymmetric B20 germanides MnGe and CoGe. *Phys. Rev. B* **90**, 144404, doi:10.1103/PhysRevB.90.144404 (2014).

121 C. Moreau-Luchaire, C. Moutafis, N. Reyren, *et al.* Additive interfacial chiral interaction in multilayers for stabilization of small individual skyrmions at room temperature. *Nat. Nanotech.* **11**, 444, doi:10.1038/nnano.2015.313 (2016).

122 A. Soumyanarayanan, M. Raju, A. L. Gonzalez Oyarce, *et al.* Tunable room-temperature magnetic skyrmions in Ir/Fe/Co/Pt multilayers. *Nat. Mater.* **16**, 898-904, doi:10.1038/nmat4934 (2017).

123 J. Brede, N. Atodiresei, V. Caciuc, *et al.* Long-range magnetic coupling between nanoscale organic–metal hybrids mediated by a nanoskyrmion lattice. *Nat. Nanotech.* **9**, 1018-1023, doi:10.1038/nnano.2014.235 (2014).

124 P.-J. Hsu, A. Kubetzka, A. Finco, *et al.* Electric-field-driven switching of individual magnetic skyrmions. *Nat. Nanotech.* **12**, 123-126, doi:10.1038/nnano.2016.234 (2017).

125 A. Kubetzka, C. Hanneken, R. Wiesendanger, *et al.* Impact of the skyrmion spin texture on magnetoresistance. *Phys. Rev. B* **95**, 104433, doi:10.1103/PhysRevB.95.104433 (2017).

126 J. Hagemeister, N. Romming, K. von Bergmann, *et al.* Stability of single skyrmionic bits. *Nat. Commun.* **6**, 8455, doi:10.1038/ncomms9455 (2015).

127 A. Hrabec, J. Sampaio, M. Belmeguenai, *et al.* Current-induced skyrmion generation and dynamics in symmetric bilayers. *Nat. Commun.* **8**, 15765, doi:10.1038/ncomms15765 (2017).

128 W. Legrand, D. Maccariello, N. Reyren, *et al.* Room-Temperature Current-Induced Generation and Motion of sub-100 nm Skyrmions. *Nano Lett.* **17**, 2703-2712, doi:10.1021/acs.nanolett.7b00649 (2017).

129 M. Schott, A. Bernand-Mantel, L. Ranno, *et al.* The Skyrmion Switch: Turning Magnetic Skyrmion Bubbles on and off with an Electric Field. *Nano Lett.* **17**, 3006-3012, doi:10.1021/acs.nanolett.7b00328 (2017).

130 N. K. Duong, M. Raju, A. P. Petrović, *et al.* Stabilizing zero-field skyrmions in Ir/Fe/Co/Pt thin film multilayers by magnetic history control. *Appl. Phys. Lett.* **114**, 072401, doi:10.1063/1.5080713 (2019).

131 M. Raju, A. Yagil, A. Soumyanarayanan, *et al.* The evolution of skyrmions in Ir/Fe/Co/Pt multilayers and their topological Hall signature. *Nat. Commun.* **10**, 696, doi:10.1038/s41467-018-08041-9 (2019).

132 C. C. I. Ang, W. Gan, G. D. H. Wong, *et al.* Electrical Control of Skyrmion Density via Skyrmion-Stripe Transformation. *Phys. Rev. Appl.* **14**, 054048, doi:10.1103/PhysRevApplied.14.054048 (2020).

133 N. K. Duong, R. Tomasello, M. Raju, *et al.* Magnetization reversal signatures of hybrid and pure Néel skyrmions in thin film multilayers. *APL Materials* **8**, 111112, doi:10.1063/5.0022033 (2020).

134 M. Ma, C. C. I. Ang, Y. Li, *et al.* Enhancement of zero-field skyrmion density in $[Pt/Co/Fe/Ir]_2$ multilayers at room temperature by the first-order reversal curve. *J. Appl. Phys.* **127**, 223901, doi:10.1063/5.0004432 (2020).

135 S. Woo, K. M. Song, H.-S. Han, *et al.* Spin-orbit torque-driven skyrmion dynamics revealed by time-resolved X-ray microscopy. *Nat. Commun.* **8**, 15573, doi:10.1038/ncomms15573 (2017).

136 I. Lemesh, K. Litzius, M. Böttcher, *et al.* Current-Induced Skyrmion Generation through Morphological Thermal Transitions in Chiral Ferromagnetic Heterostructures. *Adv. Mater.* **30**, 1805461, doi:10.1002/adma.201805461 (2018).

137 A. Casiraghi, H. Corte-León, M. Vafaee, *et al.* Individual skyrmion manipulation by local magnetic field gradients. *Commun. Phys.* **2**, 145, doi:10.1038/s42005-019-0242-5 (2019).

138 K. Litzius, J. Leliaert, P. Bassirian, *et al.* The role of temperature and drive current in skyrmion dynamics. *Nat. Electron* **3**, 30-36, doi:10.1038/s41928-019-0359-2 (2020).

139 Z. Wang, M. Guo, H.-A. Zhou, *et al.* Thermal generation, manipulation and thermoelectric detection of skyrmions. *Nat. Electron* **3**, 672-679, doi:10.1038/s41928-020-00489-2 (2020).

140 K. Zeissler, M. Mruczkiewicz, S. Finizio, *et al.* Pinning and hysteresis in the field dependent diameter evolution of skyrmions in Pt/Co/Ir superlattice stacks. *Sci. Rep.* **7**, 15125, doi:10.1038/s41598-017-15262-3 (2017).

141 D. Maccariello, W. Legrand, N. Reyren, *et al.* Electrical detection of single magnetic skyrmions in metallic multilayers at room temperature. *Nat. Nanotech.* **13**, 233-237, doi:10.1038/s41565-017-0044-4 (2018).

142 K. Zeissler, S. Finizio, K. Shahbazi, *et al.* Discrete Hall resistivity contribution from Néel skyrmions in multilayer nanodiscs. *Nat. Nanotech.* **13**, 1161-1166, doi:10.1038/s41565-018-0268-y (2018).

143 S. Sugimoto, S. Kasai, E. Anokhin, *et al.* Nonequilibrium skyrmion accumulation induced by direct current in Ir/Co/Pt heterostructure. *Appl. Phys. Express* **12**, 073002, doi:10.7567/1882-0786/ab2901 (2019).

144 S. Sugimoto, W. Koshibae, S. Kasai, *et al.* Nonlocal accumulation, chemical potential, and Hall effect of skyrmions in Pt/Co/Ir heterostructure. *Sci. Rep.* **10**, 1009, doi:10.1038/s41598-020-57818-w (2020).

145 T. Yokouchi, S. Sugimoto, B. Rana, *et al.* Creation of magnetic skyrmions by surface acoustic waves. *Nat. Nanotech.* **15**, 361-366, doi:10.1038/s41565-020-0661-1 (2020).

146 M. He, G. Li, Z. Zhu, *et al.* Evolution of topological skyrmions across the spin reorientation transition in Pt/Co/Ta multilayers. *Phys. Rev. B* **97**, 174419, doi:10.1103/PhysRevB.97.174419 (2018).

147 Y. Dovzhenko, F. Casola, S. Schlotter, *et al.* Magnetostatic twists in room-temperature skyrmions explored by nitrogen-vacancy center spin texture reconstruction. *Nat. Commun.* **9**, 2712, doi:10.1038/s41467-018-05158-9 (2018).

148 S. Zhang, J. Zhang, Y. Wen, *et al.* Creation of a thermally assisted skyrmion lattice in Pt/Co/Ta multilayer films. *Appl. Phys. Lett.* **113**, 192403, doi:10.1063/1.5053983 (2018).

149 S. Zhang, J. Zhang, Y. Wen, *et al.* Determination of chirality and density control of Néel-type skyrmions with in-plane magnetic field. *Commun. Phys.* **1**, 36, doi:10.1038/s42005-018-0040-5 (2018).

150 S. Zhang, J. Zhang, Q. Zhang, *et al.* Direct writing of room temperature and zero field skyrmion lattices by a scanning local magnetic field. *Appl. Phys. Lett.* **112**, 132405, doi:10.1063/1.5021172 (2018).

151 S. Saha, M. Zelent, S. Finizio, *et al.* Formation of Neel-type skyrmions in an antidot lattice with perpendicular magnetic anisotropy. *Phys. Rev. B* **100**, 144435, doi:10.1103/PhysRevB.100.144435 (2019).

152 D. Toneto, R. B. da Silva, L. S. Dorneles, *et al.* First order reversal curve Hall analysis of zero-field skyrmions on Pt/Co/Ta multilayers. *J. Phys. D: Appl. Phys.* **53**, 395001, doi:10.1088/1361-6463/ab95be (2020).

153 S. Zhang, X. Zhang, J. Zhang, *et al.* Direct imaging of an inhomogeneous electric current distribution using the trajectory of magnetic half-skyrmions. *Sci. Adv.* **6**, eaay1876, doi:10.1126/sciadv.aay1876 (2020).

154 M. Hervé, B. Dupé, R. Lopes, *et al.* Stabilizing spin spirals and isolated skyrmions at low magnetic field exploiting vanishing magnetic anisotropy. *Nat. Commun.* **9**, 1015, doi:10.1038/s41467-018-03240-w (2018).

155 S.-G. Je, P. Vallobra, T. Srivastava, *et al.* Creation of Magnetic Skyrmion Bubble Lattices by Ultrafast Laser in Ultrathin Films. *Nano Lett.* **18**, 7362-7371, doi:10.1021/acs.nanolett.8b03653 (2018).

156 T. Srivastava, W. Lim, I. Joumard, *et al.* Mapping different skyrmion phases in double wedges of Ta/FeCoB/TaO$_x$ trilayers. *Phys. Rev. B* **100**, 220401(R), doi:10.1103/PhysRevB.100.220401 (2019).

157 Z. Wang, X. Zhang, J. Xia, *et al.* Generation and Hall effect of skyrmions enabled using nonmagnetic point contacts. *Phys. Rev. B* **100**, 184426, doi:10.1103/PhysRevB.100.184426 (2019).

158 L. Zhao, Z. Wang, X. Zhang, *et al.* Topology-Dependent Brownian Gyromotion of a Single Skyrmion. *Phys. Rev. Lett.* **125**, 027206, doi:10.1103/PhysRevLett.125.027206 (2020).

159 R. Juge, S.-G. Je, D. de Souza Chaves, *et al.* Magnetic skyrmions in confined geometries: Effect of the magnetic field and the disorder. *J. Magn. Magn. Mater.* **455**, 3-8, doi:10.1016/j.jmmm.2017.10.030 (2018).

160 R. Juge, K. Bairagi, K. G. Rana, *et al.* Helium Ions Put Magnetic Skyrmions on the Track. *Nano Lett.*, doi:10.1021/acs.nanolett.1c00136 (2021).

161 Z. Qin, Y. Wang, S. Zhu, *et al.* Stabilization and Reversal of Skyrmion Lattice in Ta/CoFeB/MgO Multilayers. *ACS Applied Materials & Interfaces* **10**, 36556-36563, doi:10.1021/acsami.8b12694 (2018).

162 R. Iguchi, S. Kasai, K. Koshikawa, *et al.* Thermoelectric microscopy of magnetic skyrmions. *Sci. Rep.* **9**, 18443, doi:10.1038/s41598-019-54833-4 (2019).

163 J. Zázvorka, F. Jakobs, D. Heinze, *et al.* Thermal skyrmion diffusion used in a reshuffler device. *Nat. Nanotech.* **14**, 658-661, doi:10.1038/s41565-019-0436-8 (2019).

164 Y. Jibiki, M. Goto, E. Tamura, *et al.* Skyrmion Brownian circuit implemented in continuous ferromagnetic thin film. *Appl. Phys. Lett.* **117**, 082402, doi:10.1063/5.0011105 (2020).

165 R. Tolley, S. A. Montoya & E. E. Fullerton. Room-temperature observation and current control of skyrmions in Pt/Co/Os/Pt thin films. *Phys. Rev. Mater.* **2**, doi:10.1103/PhysRevMaterials.2.044404 (2018).

166 G. Yu, A. Jenkins, X. Ma, *et al.* Room-Temperature Skyrmions in an Antiferromagnet-Based Heterostructure. *Nano Lett.* **18**, 980-986, doi:10.1021/acs.nanolett.7b04400 (2018).

167 D. Bhattacharya, S. A. Razavi, H. Wu, *et al.* Creation and annihilation of non-volatile fixed magnetic skyrmions using voltage control of magnetic anisotropy. *Nat. Electron* **3**, 539-545, doi:10.1038/s41928-020-0432-x (2020).

168 S. Woo, K. M. Song, X. Zhang, *et al.* Current-driven dynamics and inhibition of the skyrmion Hall effect of ferrimagnetic skyrmions in GdFeCo films. *Nat. Commun.* **9**, 959, doi:10.1038/s41467-018-03378-7 (2018).

169 S. Woo, K. M. Song, X. Zhang, *et al.* Deterministic creation and deletion of a single magnetic skyrmion observed by direct time-resolved X-ray microscopy. *Nat. Electron* **1**, 288-296, doi:10.1038/s41928-018-0070-8 (2018).

170 K. M. Song, J.-S. Jeong, B. Pan, *et al.* Skyrmion-based artificial synapses for neuromorphic computing. *Nat. Electron*, doi:10.1038/s41928-020-0385-0 (2020).

171 L. Wang, Q. Feng, Y. Kim, *et al.* Ferroelectrically tunable magnetic skyrmions in ultrathin oxide heterostructures. *Nat. Mater.* **17**, 1087-1094, doi:10.1038/s41563-018-0204-4 (2018).

172 S. Finizio, K. Zeissler, S. Wintz, *et al.* Deterministic Field-Free Skyrmion Nucleation at a Nanoengineered Injector Device. *Nano Lett.* **19**, 7246-7255, doi:10.1021/acs.nanolett.9b02840 (2019).

173 K. Zeissler, S. Finizio, C. Barton, *et al.* Diameter-independent skyrmion Hall angle observed in chiral magnetic multilayers. *Nat. Commun.* **11**, 428, doi:10.1038/s41467-019-14232-9 (2020).

174 T. Nozaki, Y. Jibiki, M. Goto, *et al.* Brownian motion of skyrmion bubbles and its control by voltage applications. *Appl. Phys. Lett.* **114**, 012402, doi:10.1063/1.5070101 (2019).

175 K.-Y. Meng, A. S. Ahmed, M. Baćani, *et al.* Observation of Nanoscale Skyrmions in $SrIrO_3$/$SrRuO_3$ Bilayers. *Nano Lett.* **19**, 3169-3175, doi:10.1021/acs.nanolett.9b00596 (2019).

176 J. A. Brock, S. A. Montoya, M.-Y. Im, *et al.* Energy-efficient generation of skyrmion phases in Co/Ni/Pt-based multilayers using Joule heating. *Phys. Rev. Mater.* **4**, 104409, doi:10.1103/PhysRevMaterials.4.104409 (2020).

177 Y. Guang, I. Bykova, Y. Liu, *et al.* Creating zero-field skyrmions in exchange-biased multilayers through X-ray illumination. *Nat. Commun.* **11**, 949, doi:10.1038/s41467-020-14769-0 (2020).

178 M. Li, A. Rai, A. Pokhrel, *et al.* Formation of zero-field skyrmion arrays in asymmetric superlattices. *Appl. Phys. Lett.* **117**, 112403, doi:10.1063/5.0024265 (2020).

179 X. Palermo, N. Reyren, S. Mesoraca, *et al.* Tailored Flux Pinning in Superconductor-Ferromagnet Multilayers with Engineered Magnetic Domain Morphology From Stripes to Skyrmions. *Phys. Rev. Appl.* **13**, 014043, doi:10.1103/PhysRevApplied.13.014043 (2020).

180 S. D. Pollard, J. A. Garlow, J. Yu, *et al.* Observation of stable Néel skyrmions in cobalt/palladium multilayers with Lorentz transmission electron microscopy. *Nat. Commun.* **8**, 14761, doi:10.1038/ncomms14761 (2017).

181 S. D. Pollard, J. A. Garlow, K.-W. Kim, *et al.* Bloch Chirality Induced by an Interlayer Dzyaloshinskii-Moriya Interaction in Ferromagnetic Multilayers. *Phys. Rev. Lett.* **125**, 227203, doi:10.1103/PhysRevLett.125.227203 (2020).

182 Y. Wu, S. Zhang, J. Zhang, *et al.* Néel-type skyrmion in WTe_2/Fe_3GeTe_2 van der Waals heterostructure. *Nat. Commun.* **11**, 3860, doi:10.1038/s41467-020-17566-x (2020).

183 M. Yang, Q. Li, R. V. Chopdekar, *et al.* Creation of skyrmions in van der Waals ferromagnet Fe_3GeTe_2 on $(Co/Pd)_n$ superlattice. *Sci. Adv.* **6**, eabb5157, doi:10.1126/sciadv.abb5157 (2020).

184 K. von Bergmann, S. Heinze, M. Bode, *et al.* Observation of a Complex Nanoscale Magnetic Structure in a Hexagonal Fe Monolayer. *Phys. Rev. Lett.* **96**, 167203, doi:10.1103/PhysRevLett.96.167203 (2006).

185 Y. Deng, Y. Yu, Y. Song, *et al.* Gate-tunable room-temperature ferromagnetism in two-dimensional Fe_3GeTe_2. *Nature* **563**, 94-99, doi:10.1038/s41586-018-0626-9 (2018).

186 M. Heide, G. Bihlmayer & S. Blügel. Dzyaloshinskii-Moriya interaction accounting for the orientation of magnetic domains in ultrathin films: Fe/W(110). *Phys. Rev. B* **78**, 140403, doi:10.1103/PhysRevB.78.140403 (2008).

187 B. Kaplan & G. A. Gehring. The domain structure in ultrathin magnetic films. *J. Magn. Magn. Mater.* **128**, 111-116, doi:10.1016/0304-8853(93)90863-W (1993).

188 I. Lemesh, F. Büttner & G. S. D. Beach. Accurate model of the stripe domain phase of perpendicularly magnetized multilayers. *Phys. Rev. B* **95**, 174423, doi:10.1103/PhysRevB.95.174423 (2017).

189 M. T. Johnson, P. J. H. Bloemen, F. J. A. d. Broeder, *et al.* Magnetic anisotropy in metallic multilayers. *Reports on Progress in Physics* **59**, 1409-1458, doi:10.1088/0034-4885/59/11/002 (1996).

190 S. A. Montoya, S. Couture, J. J. Chess, *et al.* Tailoring magnetic energies to form dipole skyrmions and skyrmion lattices. *Phys. Rev. B* **95**, 024415, doi:10.1103/PhysRevB.95.024415 (2017).

191 S. A. Montoya, R. Tolley, I. Gilbert, *et al.* Spin-orbit torque induced dipole skyrmion motion at room temperature. *Phys. Rev. B* **98**, 104432, doi:10.1103/PhysRevB.98.104432 (2018).

192 W. Jiang, P. Upadhyaya, W. Zhang, *et al.* Blowing magnetic skyrmion bubbles. *Science* **349**, 283, doi:10.1126/science.aaa1442 (2015).

193 K. Chesnel, A. S. Westover, C. Richards, *et al.* Morphological stripe-bubble transition in remanent magnetic domain patterns of Co/Pt multilayer films and its dependence on Co thickness. *Phys. Rev. B* **98**, 224404, doi:10.1103/PhysRevB.98.224404 (2018).

194 S. Woo, K. Litzius, B. Krüger, *et al.* Observation of room-temperature magnetic skyrmions and their current-driven dynamics in ultrathin metallic ferromagnets. *Nat. Mater.* **15**, 501-506, doi:10.1038/nmat4593 (2016).

195 G. Yu, P. Upadhyaya, X. Li, *et al.* Room-Temperature Creation and Spin–Orbit Torque Manipulation of Skyrmions in Thin Films with Engineered Asymmetry. *Nano Lett.* **16**, 1981-1988, doi:10.1021/acs.nanolett.5b05257 (2016).

196 J. Brandão, D. A. Dugato, R. L. Seeger, *et al.* Observation of magnetic skyrmions in unpatterned symmetric multilayers at room temperature and zero magnetic field. *Sci. Rep.* **9**, 4144, doi:10.1038/s41598-019-40705-4 (2019).

197 P.-J. Hsu, L. Rózsa, A. Finco, *et al.* Inducing skyrmions in ultrathin Fe films by hydrogen exposure. *Nat. Commun.* **9**, 1571, doi:10.1038/s41467-018-04015-z (2018).

198 K. Fallon, S. Hughes, K. Zeissler, *et al.* Controlled Individual Skyrmion Nucleation at Artificial Defects Formed by Ion Irradiation. *Small* **16**, 1907450, doi:10.1002/smll.201907450 (2020).

199 T. Lin, H. Liu, S. Poellath, *et al.* Observation of room-temperature magnetic skyrmions in Pt/Co/W structures with a large spin-orbit coupling. *Phys. Rev. B* **98**, 174425, doi:10.1103/PhysRevB.98.174425 (2018).

200 M. Li, D. Lau, M. De Graef, *et al.* Lorentz TEM investigation of chiral spin textures and N\'eel Skyrmions in asymmetric $[Pt/(Co/Ni)_M/Ir]_N$ multi-layer thin films. *Phys. Rev. Mater.* **3**, 064409, doi:10.1103/PhysRevMaterials.3.064409 (2019).

201 W. Jiang, X. Zhang, G. Yu, *et al.* Direct observation of the skyrmion Hall effect. *Nat. Phys.* **13**, 162, doi:10.1038/nphys3883 (2016).

202 O. Boulle, J. Vogel, H. Yang, *et al.* Room-temperature chiral magnetic skyrmions in ultrathin magnetic nanostructures. *Nat. Nanotech.* **11**, 449-454, doi:10.1038/nnano.2015.315 (2016).

203 K. G. Rana, A. Finco, F. Fabre, *et al.* Room-Temperature Skyrmions at Zero Field in Exchange-Biased Ultrathin Films. *Phys. Rev. Appl.* **13**, 044079, doi:10.1103/PhysRevApplied.13.044079 (2020).

204 G. Chen, A. Mascaraque, A. T. N'Diaye, *et al.* Room temperature skyrmion ground state stabilized through interlayer exchange coupling. *Appl. Phys. Lett.* **106**, 242404, doi:10.1063/1.4922726 (2015).

205 S. Rohart & A. Thiaville. Skyrmion confinement in ultrathin film nanostructures in the presence of Dzyaloshinskii-Moriya interaction. *Phys. Rev. B* **88**, 184422, doi:10.1103/PhysRevB.88.184422 (2013).

206 X. Zhang, G. P. Zhao, H. Fangohr, *et al.* Skyrmion-skyrmion and skyrmion-edge repulsions in skyrmion-based racetrack memory. *Sci. Rep.* **5**, 7643, doi:10.1038/srep07643 (2015).

207 C. Song, N. Kerber, J. Rothörl, *et al.* Commensurability between Element Symmetry and the Number of Skyrmions Governing Skyrmion Diffusion in Confined Geometries. *Advanced Functional Materials* **n/a**, 2010739, doi:10.1002/adfm.202010739 (2021).

208 K. Fallon, S. McVitie, W. Legrand, *et al.* Quantitative imaging of hybrid chiral spin textures in magnetic multilayer systems by Lorentz microscopy. *Phys. Rev. B* **100**, 214431, doi:10.1103/PhysRevB.100.214431 (2019).

209 W. Legrand, J.-Y. Chauleau, D. Maccariello, *et al.* Hybrid chiral domain walls and skyrmions in magnetic multilayers. *Sci. Adv.* **4**, eaat0415, doi:10.1126/sciadv.aat0415 (2018).

210 C. C. I. Ang, W. Gan, G. D. H. Wong, *et al.* Temperature-modulated magnetic skyrmion phases and transformations analysis from first-order reversal curve study. *Phys. Rev. B* **103**, 144409, doi:10.1103/PhysRevB.103.144409 (2021).

211 L. Caretta, M. Mann, F. Büttner, *et al.* Fast current-driven domain walls and small skyrmions in a compensated ferrimagnet. *Nat. Nanotech.* **13**, 1154-1160, doi:10.1038/s41565-018-0255-3 (2018).

212 C. D. Stanciu, A. V. Kimel, F. Hansteen, *et al.* Ultrafast spin dynamics across compensation points in ferrimagnetic GdFeCo: The role of angular momentum compensation. *Phys. Rev. B* **73**, 220402, doi:10.1103/PhysRevB.73.220402 (2006).

213 M. Binder, A. Weber, O. Mosendz, *et al.* Magnetization dynamics of the ferrimagnet CoGd near the compensation of magnetization and angular momentum. *Phys. Rev. B* **74**, 134404, doi:10.1103/PhysRevB.74.134404 (2006).

214 S. S. P. Parkin & D. Mauri. Spin engineering: Direct determination of the Ruderman-Kittel-Kasuya-Yosida far-field range function in ruthenium. *Phys. Rev. B* **44**, 7131-7134, doi:10.1103/PhysRevB.44.7131 (1991).

215 W. Legrand, D. Maccariello, F. Ajejas, *et al.* Room-temperature stabilization of antiferromagnetic skyrmions in synthetic antiferromagnets. *Nat. Mater.* **19**, 34-42, doi:10.1038/s41563-019-0468-3 (2020).

216 M. J. Meijer, J. Lucassen, F. Kloodt-Twesten, *et al.* Magnetic Chirality Controlled by the Interlayer Exchange Interaction. *Phys. Rev. Lett.* **124**, 207203, doi:10.1103/PhysRevLett.124.207203 (2020).

217 T. Dohi, S. DuttaGupta, S. Fukami, *et al.* Formation and current-induced motion of synthetic antiferromagnetic skyrmion bubbles. *Nat. Commun.* **10**, 5153, doi:10.1038/s41467-019-13182-6 (2019).

218 A. Sonntag, J. Hermenau, S. Krause, *et al.* Thermal Stability of an Interface-Stabilized Skyrmion Lattice. *Phys. Rev. Lett.* **113**, 077202, doi:10.1103/PhysRevLett.113.077202 (2014).

219 A. Schlenhoff, P. Lindner, J. Friedlein, *et al.* Magnetic Nano-skyrmion Lattice Observed in a Si-Wafer-Based Multilayer System. *ACS Nano* **9**, 5908-5912, doi:10.1021/acsnano.5b01146 (2015).

220 C. Ma, X. Zhang, J. Xia, *et al.* Electric Field-Induced Creation and Directional Motion of Domain Walls and Skyrmion Bubbles. *Nano Lett.* **19**, 353-361, doi:10.1021/acs.nanolett.8b03983 (2019).

221 R. Juge, S.-G. Je, D. d. S. Chaves, *et al.* Current-Driven Skyrmion Dynamics and Drive-Dependent Skyrmion Hall Effect in an Ultrathin Film. *Phys. Rev. Appl.* **12**, 044007, doi:10.1103/PhysRevApplied.12.044007 (2019).

222 K. Litzius, I. Lemesh, B. Krüger, *et al.* Skyrmion Hall effect revealed by direct time-resolved X-ray microscopy. *Nat. Phys.* **13**, 170, doi:10.1038/nphys4000 (2016).

223 F. Büttner, I. Lemesh, M. Schneider, *et al.* Field-free deterministic ultrafast creation of magnetic skyrmions by spin–orbit torques. *Nat. Nanotech.* **12**, 1040-1044, doi:10.1038/nnano.2017.178 (2017).

224 S. Jaiswal, K. Litzius, I. Lemesh, *et al.* Investigation of the Dzyaloshinskii-Moriya interaction and room temperature skyrmions in W/CoFeB/MgO thin films and microwires. *Appl. Phys. Lett.* **111**, 022409, doi:10.1063/1.4991360 (2017).

225 S.-G. Je, M.-S. Jung, M.-Y. Im, *et al.* Electric current control of creation and annihilation of sub-100 nm magnetic bubbles examined by full-field transmission soft X-ray microscopy. *Curr. Appl. Phys.* **18**, 1201-1204, doi:10.1016/j.cap.2018.06.004 (2018).

226 M. Finazzi, M. Savoini, A. R. Khorsand, *et al.* Laser-Induced Magnetic Nanostructures with Tunable Topological Properties. *Phys. Rev. Lett.* **110**, 177205, doi:10.1103/PhysRevLett.110.177205 (2013).

227 F. Büttner, M. A. Mawass, J. Bauer, *et al.* Thermal nucleation and high-resolution imaging of submicrometer magnetic bubbles in thin thulium iron garnet films with perpendicular anisotropy. *Phys. Rev. Mater.* **4**, 011401, doi:10.1103/PhysRevMaterials.4.011401 (2020).

228 X. Z. Yu, K. Shibata, W. Koshibae, *et al.* Thermally activated helicity reversals of skyrmions. *Phys. Rev. B* **93**, 134417, doi:10.1103/PhysRevB.93.134417 (2016).

229 R. D. Desautels, L. DeBeer-Schmitt, S. A. Montoya, *et al.* Realization of ordered magnetic skyrmions in thin films at ambient conditions. *Phys. Rev. Mater.* **3**, 104406, doi:10.1103/PhysRevMaterials.3.104406 (2019).

230 Z. Hou, W. Ren, B. Ding, *et al.* Observation of Various and Spontaneous Magnetic Skyrmionic Bubbles at Room Temperature in a Frustrated Kagome Magnet with Uniaxial Magnetic Anisotropy. *Adv. Mater.* **29**, 1701144, doi:10.1002/adma.201701144 (2017).

231 Z. Hou, Q. Zhang, G. Xu, *et al.* Creation of Single Chain of Nanoscale Skyrmion Bubbles with Record-High Temperature Stability in a Geometrically Confined Nanostripe. *Nano Lett.* **18**, 1274-1279, doi:10.1021/acs.nanolett.7b04900 (2018).

232 Z. Hou, Q. Zhang, G. Xu, *et al.* Manipulating the Topology of Nanoscale Skyrmion Bubbles by Spatially Geometric Confinement. *ACS Nano* **13**, 922-929, doi:10.1021/acsnano.8b09689 (2019).

233 Z. Hou, Q. Zhang, X. Zhang, *et al.* Current-Induced Helicity Reversal of a Single Skyrmionic Bubble Chain in a Nanostructured Frustrated Magnet. *Adv. Mater.* **32**, 1904815, doi:10.1002/adma.201904815 (2020).

234 S.-G. Je, H.-S. Han, S. K. Kim, *et al.* Direct Demonstration of Topological Stability of Magnetic Skyrmions via Topology Manipulation. *ACS Nano* **14**, 3251-3258, doi:10.1021/acsnano.9b08699 (2020).

235 M.-G. Han, J. A. Garlow, Y. Liu, *et al.* Topological Magnetic-Spin Textures in Two-Dimensional van der Waals $Cr_2Ge_2Te_6$. *Nano Lett.* **19**, 7859-7865, doi:10.1021/acs.nanolett.9b02849 (2019).

236 B. Ding, Z. Li, G. Xu, *et al.* Observation of Magnetic Skyrmion Bubbles in a van der Waals Ferromagnet Fe_3GeTe_2. *Nano Lett.* **20**, 868-873, doi:10.1021/acs.nanolett.9b03453 (2020).

237 M. Nakamura, D. Morikawa, X. Yu, *et al.* Emergence of Topological Hall Effect in Half-Metallic Manganite Thin Films by Tuning Perpendicular Magnetic Anisotropy. *Journal of the Physical Society of Japan* **87**, 074704, doi:10.7566/JPSJ.87.074704 (2018).

238 L. Peng, Y. Zhang, W. Wang, *et al.* Real-Space Observation of Nonvolatile Zero-Field Biskyrmion Lattice Generation in MnNiGa Magnet. *Nano Lett.* **17**, 7075-7079, doi:10.1021/acs.nanolett.7b03792 (2017).

239 X. Z. Yu, Y. Tokunaga, Y. Kaneko, *et al.* Biskyrmion states and their current-driven motion in a layered manganite. *Nat. Commun.* **5**, 3198, doi:10.1038/ncomms4198 (2014).

240 D. Morikawa, X. Z. Yu, Y. Kaneko, *et al.* Lorentz transmission electron microscopy on nanometric magnetic bubbles and skyrmions in bilayered manganites $La_{1.2}Sr_{1.8}(Mn_{1-y}Ru_y)_2O_7$ with controlled magnetic anisotropy. *Appl. Phys. Lett.* **107**, 212401, doi:10.1063/1.4936078 (2015).

241 L. Balents. Spin liquids in frustrated magnets. *Nature* **464**, 199-208, doi:10.1038/nature08917 (2010).

242 *Introduction to Frustrated Magnetism*. 1 edn, XXVI, 682 (Springer-Verlag Berlin Heidelberg, 2011).

243 J. E. Greedan. Geometrically frustrated magnetic materials. *Journal of Materials Chemistry* **11**, 37-53, doi:10.1039/B003682J (2001).

244 Y. Fujishiro, N. Kanazawa & Y. Tokura. Engineering skyrmions and emergent monopoles in topological spin crystals. *Appl. Phys. Lett.* **116**, 090501, doi:10.1063/1.5139488 (2020).

245 T. Okubo, S. Chung & H. Kawamura. Multiple-q States and the Skyrmion Lattice of the Triangular-Lattice Heisenberg Antiferromagnet under Magnetic Fields. *Phys. Rev. Lett.* **108**, 017206, doi:10.1103/PhysRevLett.108.017206 (2012).

246 A. O. Leonov & M. Mostovoy. Multiply periodic states and isolated skyrmions in an anisotropic frustrated magnet. *Nat. Commun.* **6**, 8275, doi:10.1038/ncomms9275 (2015).

247 P. Sutcliffe. Skyrmion Knots in Frustrated Magnets. *Phys. Rev. Lett.* **118**, 247203, doi:10.1103/PhysRevLett.118.247203 (2017).

248 T. Kurumaji, T. Nakajima, M. Hirschberger, *et al.* Skyrmion lattice with a giant topological Hall effect in a frustrated triangular-lattice magnet. *Science* **365**, 914, doi:10.1126/science.aau0968 (2019).

249 M. Hirschberger, T. Nakajima, M. Kriener, *et al.* High-field depinned phase and planar Hall effect in the skyrmion host Gd_2PdSi_3. *Phys. Rev. B* **101**, 220401, doi:10.1103/PhysRevB.101.220401 (2020).

250 H. Zhang, Q. Huang, L. Hao, *et al.* Anomalous magnetoresistance in centrosymmetric skyrmion-lattice magnet Gd_2PdSi_3. *New J. Phys.* **22**, 083056, doi:10.1088/1367-2630/aba650 (2020).

251 M. Hirschberger, T. Nakajima, S. Gao, *et al.* Skyrmion phase and competing magnetic orders on a breathing kagomé lattice. *Nat. Commun.* **10**, 5831, doi:10.1038/s41467-019-13675-4 (2019).

252 N. D. Khanh, T. Nakajima, X. Yu, *et al.* Nanometric square skyrmion lattice in a centrosymmetric tetragonal magnet. *Nat. Nanotech.* **15**, 444-449, doi:10.1038/s41565-020-0684-7 (2020).

253 S. Ishiwata, M. Tokunaga, Y. Kaneko, *et al.* Versatile helimagnetic phases under magnetic fields in cubic perovskite $SrFeO_3$. *Phys. Rev. B* **84**, 054427, doi:10.1103/PhysRevB.84.054427 (2011).

254 J. H. Kim, A. Jain, M. Reehuis, *et al.* Competing Exchange Interactions on the Verge of a Metal-Insulator Transition in the Two-Dimensional Spiral Magnet $Sr_3Fe_2O_7$. *Phys. Rev. Lett.* **113**, 147206, doi:10.1103/PhysRevLett.113.147206 (2014).

255 M. Azhar & M. Mostovoy. Incommensurate Spiral Order from Double-Exchange Interactions. *Phys. Rev. Lett.* **118**, 027203, doi:10.1103/PhysRevLett.118.027203 (2017).

256 S. Ishiwata, T. Nakajima, J. H. Kim, *et al.* Emergent topological spin structures in the centrosymmetric cubic perovskite $SrFeO_3$. *Phys. Rev. B* **101**, 134406, doi:10.1103/PhysRevB.101.134406 (2020).

257 X. Zhang, Y. Zhou, M. Ezawa, *et al.* Magnetic skyrmion transistor: skyrmion motion in a voltage-gated nanotrack. *Sci. Rep.* **5**, 11369, doi:10.1038/srep11369 (2015).

258 S. Luo, M. Song, X. Li, *et al.* Reconfigurable Skyrmion Logic Gates. *Nano Lett.* **18**, 1180-1184, doi:10.1021/acs.nanolett.7b04722 (2018).

259 D. Pinna, F. Abreu Araujo, J. V. Kim, *et al.* Skyrmion Gas Manipulation for Probabilistic Computing. *Phys. Rev. Appl.* **9**, 064018, doi:10.1103/PhysRevApplied.9.064018 (2018).

260 G. Yu, P. Upadhyaya, Q. Shao, *et al.* Room-Temperature Skyrmion Shift Device for Memory Application. *Nano Lett.* **17**, 261-268, doi:10.1021/acs.nanolett.6b04010 (2017).

261 C. Schütte & A. Rosch. Dynamics and energetics of emergent magnetic monopoles in chiral magnets. *Phys. Rev. B* **90**, 174432, doi:10.1103/PhysRevB.90.174432 (2014).

262 S.-Z. Lin & A. Saxena. Dynamics of Dirac strings and monopolelike excitations in chiral magnets under a current drive. *Phys. Rev. B* **93**, 060401, doi:10.1103/PhysRevB.93.060401 (2016).

263 P. F. Bessarab, V. M. Uzdin & H. Jónsson. Method for finding mechanism and activation energy of magnetic transitions, applied to skyrmion and antivortex annihilation. *Computer Physics Communications* **196**, 335-347, doi:10.1016/j.cpc.2015.07.001 (2015).

264 I. S. Lobanov, H. Jónsson & V. M. Uzdin. Mechanism and activation energy of magnetic skyrmion annihilation obtained from minimum energy path calculations. *Phys. Rev. B* **94**, 174418, doi:10.1103/PhysRevB.94.174418 (2016).

265 D. Stosic, J. Mulkers, B. Van Waeyenberge, *et al.* Paths to collapse for isolated skyrmions in few-monolayer ferromagnetic films. *Phys. Rev. B* **95**, 214418, doi:10.1103/PhysRevB.95.214418 (2017).

266 S. von Malottki, B. Dupé, P. F. Bessarab, *et al.* Enhanced skyrmion stability due to exchange frustration. *Sci. Rep.* **7**, 12299, doi:10.1038/s41598-017-12525-x (2017).

267 S. von Malottki, P. F. Bessarab, S. Haldar, *et al.* Skyrmion lifetime in ultrathin films. *Phys. Rev. B* **99**, 060409, doi:10.1103/PhysRevB.99.060409 (2019).

268 L. Desplat, D. Suess, J. V. Kim, *et al.* Thermal stability of metastable magnetic skyrmions: Entropic narrowing and significance of internal eigenmodes. *Phys. Rev. B* **98**, 134407, doi:10.1103/PhysRevB.98.134407 (2018).

269 W. Münzer, A. Neubauer, T. Adams, *et al.* Skyrmion lattice in the doped semiconductor FeCoSi. *Phys. Rev. B* **81**, 041203, doi:10.1103/PhysRevB.81.041203 (2010).

270 P. Milde, D. Köhler, J. Seidel, *et al.* Unwinding of a Skyrmion Lattice by Magnetic Monopoles. *Science* **340**, 1076-1080, doi:10.1126/science.1234657 (2013).

271 P. F. Bessarab, V. M. Uzdin & H. Jónsson. Harmonic transition-state theory of thermal spin transitions. *Phys. Rev. B* **85**, 184409, doi:10.1103/PhysRevB.85.184409 (2012).

272 V. M. Uzdin, M. N. Potkina, I. S. Lobanov, *et al.* Energy surface and lifetime of magnetic skyrmions. *J. Magn. Magn. Mater.* **459**, 236-240, doi:10.1016/j.jmmm.2017.10.100 (2018).

273 C. Wang, H. Du, X. Zhao, *et al.* Enhanced Stability of the Magnetic Skyrmion Lattice Phase under a Tilted Magnetic Field in a Two-Dimensional Chiral Magnet. *Nano Lett.* **17**, 2921-2927, doi:10.1021/acs.nanolett.7b00135 (2017).

274 Z. Qin, C. Jin, H. Xie, *et al.* Size-tunable skyrmion bubbles in Ta/CoFeB/MgO multilayers. *J. Phys. D: Appl. Phys.* **51**, 425001, doi:10.1088/1361-6463/aadd59 (2018).

275 A. G. Temiryazev, M. P. Temiryazeva, A. V. Zdoroveyshchev, *et al.* Formation of a Domain Structure in Multilayer CoPt Films by Magnetic Probe of an Atomic Force Microscope. *Physics of the Solid State* **60**, 2200-2206, doi:10.1134/S1063783418110318 (2018).

276 A. K. C. Tan, J. Lourembam, X. Chen, *et al.* Skyrmion generation from irreversible fission of stripes in chiral multilayer films. *Phys. Rev. Mater.* **4**, 114419, doi:10.1103/PhysRevMaterials.4.114419 (2020).

277 V. M. Uzdin, M. N. Potkina, I. S. Lobanov*, et al.* The effect of confinement and defects on the thermal stability of skyrmions. *Phys. B (Amsterdam, Neth.)* **549**, 6-9, doi:10.1016/j.physb.2017.09.040 (2018).

278 S.-Z. Lin. Edge instability in a chiral stripe domain under an electric current and skyrmion generation. *Phys. Rev. B* **94**, 020402, doi:10.1103/PhysRevB.94.020402 (2016).

279 K. Everschor-Sitte, M. Sitte, T. Valet, *et al.* Skyrmion production on demand by homogeneous DC currents. *New J. Phys.* **19**, 092001, doi:10.1088/1367-2630/aa8569 (2017).

280 N. E. Penthorn, X. Hao, Z. Wang*, et al.* Experimental Observation of Single Skyrmion Signatures in a Magnetic Tunnel Junction. *Phys. Rev. Lett.* **122**, 257201, doi:10.1103/PhysRevLett.122.257201 (2019).

281 X. Yu, D. Morikawa, Y. Tokunaga*, et al.* Current-Induced Nucleation and Annihilation of Magnetic Skyrmions at Room Temperature in a Chiral Magnet. *Adv. Mater.* **29**, 1606178, doi:10.1002/adma.201606178 (2017).

282 S.-Z. Lin, C. Reichhardt, C. D. Batista*, et al.* Driven Skyrmions and Dynamical Transitions in Chiral Magnets. *Phys. Rev. Lett.* **110**, 207202, doi:10.1103/PhysRevLett.110.207202 (2013).

283 L. D. Anh, P. N. Hai, Y. Kasahara*, et al.* Modulation of ferromagnetism in (In,Fe)As quantum wells via electrically controlled deformation of the electron wave functions. *Phys. Rev. B* **92**, 161201, doi:10.1103/PhysRevB.92.161201 (2015).

284 V. L. Korenev, I. V. Kalitukha, I. A. Akimov*, et al.* Low voltage control of exchange coupling in a ferromagnet-semiconductor quantum well hybrid structure. *Nat. Commun.* **10**, 2899, doi:10.1038/s41467-019-10774-0 (2019).

285 O. O. Brovko, P. Ruiz-Díaz, T. R. Dasa*, et al.* Controlling magnetism on metal surfaces with non-magnetic means: electric fields and surface charging. *Journal of Physics: Condensed Matter* **26**, 093001, doi:10.1088/0953-8984/26/9/093001 (2014).

286 Y. Ba, S. Zhuang, Y. Zhang*, et al.* Electric-field control of skyrmions in multiferroic heterostructure via magnetoelectric coupling. *Nat. Commun.* **12**, 322, doi:10.1038/s41467-020-20528-y (2021).

287 M. Endo, S. Kanai, S. Ikeda, *et al.* Electric-field effects on thickness dependent magnetic anisotropy of sputtered MgO/$Co_{40}Fe_{40}B_{20}$/Ta structures. *Appl. Phys. Lett.* **96**, 212503, doi:10.1063/1.3429592 (2010).

288 K. Kita, D. W. Abraham, M. J. Gajek, *et al.* Electric-field-control of magnetic anisotropy of $Co_{0.6}Fe_{0.2}B_{0.2}$/oxide stacks using reduced voltage. *J. Appl. Phys.* **112**, 033919, doi:10.1063/1.4745901 (2012).

289 W.-G. Wang, M. Li, S. Hageman, *et al.* Electric-field-assisted switching in magnetic tunnel junctions. *Nat. Mater.* **11**, 64-68, doi:10.1038/nmat3171 (2012).

290 K. Nawaoka, S. Miwa, Y. Shiota, *et al.* Voltage induction of interfacial Dzyaloshinskii–Moriya interaction in Au/Fe/MgO artificial multilayer. *Appl. Phys. Express* **8**, 063004, doi:10.7567/apex.8.063004 (2015).

291 T. Koyama, Y. Nakatani, J. i. Ieda, *et al.* Electric field control of magnetic domain wall motion via modulation of the Dzyaloshinskii-Moriya interaction. *Sci. Adv.* **4**, eaav0265, doi:10.1126/sciadv.aav0265 (2018).

292 T. Srivastava, M. Schott, R. Juge, *et al.* Large-Voltage Tuning of Dzyaloshinskii–Moriya Interactions: A Route toward Dynamic Control of Skyrmion Chirality. *Nano Lett.* **18**, 4871-4877, doi:10.1021/acs.nanolett.8b01502 (2018).

293 J. Suwardy, K. Nawaoka, J. Cho, *et al.* Voltage-controlled magnetic anisotropy and voltage-induced Dzyaloshinskii-Moriya interaction change at the epitaxial Fe(001)/MgO(001) interface engineered by Co and Pd atomic-layer insertion. *Phys. Rev. B* **98**, 144432, doi:10.1103/PhysRevB.98.144432 (2018).

294 W. Zhang, H. Zhong, R. Zang, *et al.* Electrical field enhanced interfacial Dzyaloshinskii-Moriya interaction in MgO/Fe/Pt system. *Appl. Phys. Lett.* **113**, 122406, doi:10.1063/1.5050447 (2018).

295 L. Gerhard, T. K. Yamada, T. Balashov, *et al.* Magnetoelectric coupling at metal surfaces. *Nat. Nanotech.* **5**, 792-797, doi:10.1038/nnano.2010.214 (2010).

296 S. Kasai, S. Sugimoto, Y. Nakatani, *et al.* Voltage-controlled magnetic skyrmions in magnetic tunnel junctions. *Appl. Phys. Express* **12**, 083001, doi:10.7567/1882-0786/ab2baa (2019).

297 A. J. Kruchkov, J. S. White, M. Bartkowiak, *et al.* Direct electric field control of the skyrmion phase in a magnetoelectric insulator. *Sci. Rep.* **8**, 10466, doi:10.1038/s41598-018-27882-4 (2018).

298 J. S. White, I. Živković, A. J. Kruchkov, *et al.* Electric-Field-Driven Topological Phase Switching and Skyrmion-Lattice Metastability in Magnetoelectric Cu_2OSeO_3. *Phys. Rev. Appl.* **10**, 014021, doi:10.1103/PhysRevApplied.10.014021 (2018).

299 C. Jia, S. Onoda, N. Nagaosa, *et al.* Bond electronic polarization induced by spin. *Phys. Rev. B* **74**, 224444, doi:10.1103/PhysRevB.74.224444 (2006).

300 C. Jia, S. Onoda, N. Nagaosa, *et al.* Microscopic theory of spin-polarization coupling in multiferroic transition metal oxides. *Phys. Rev. B* **76**, 144424, doi:10.1103/PhysRevB.76.144424 (2007).

301 A. Kirilyuk, A. V. Kimel & T. Rasing. Ultrafast optical manipulation of magnetic order. *Reviews of Modern Physics* **82**, 2731-2784, doi:10.1103/RevModPhys.82.2731 (2010).

302 E. Beaurepaire, J. C. Merle, A. Daunois, *et al.* Ultrafast Spin Dynamics in Ferromagnetic Nickel. *Phys. Rev. Lett.* **76**, 4250-4253, doi:10.1103/PhysRevLett.76.4250 (1996).

303 C. D. Stanciu, F. Hansteen, A. V. Kimel, *et al.* All-Optical Magnetic Recording with Circularly Polarized Light. *Phys. Rev. Lett.* **99**, 047601, doi:10.1103/PhysRevLett.99.047601 (2007).

304 S. Mangin, M. Gottwald, C. H. Lambert, *et al.* Engineered materials for all-optical helicity-dependent magnetic switching. *Nat. Mater.* **13**, 286-292, doi:10.1038/nmat3864 (2014).

305 C. H. Lambert, S. Mangin, B. S. D. C. S. Varaprasad, *et al.* All-optical control of ferromagnetic thin films and nanostructures. *Science* **345**, 1337, doi:10.1126/science.1253493 (2014).

306 T. Ogasawara, N. Iwata, Y. Murakami, *et al.* Submicron-scale spatial feature of ultrafast photoinduced magnetization reversal in TbFeCo thin film. *Appl. Phys. Lett.* **94**, 162507, doi:10.1063/1.3123256 (2009).

307 W. Koshibae & N. Nagaosa. Creation of skyrmions and antiskyrmions by local heating. *Nat. Commun.* **5**, 5148, doi:10.1038/ncomms6148 (2014).

308 N. S. Gusev, A. V. Sadovnikov, S. A. Nikitov, *et al.* Manipulation of the Dzyaloshinskii--Moriya Interaction in Co/Pt Multilayers with Strain. *Phys. Rev. Lett.* **124**, 157202, doi:10.1103/PhysRevLett.124.157202 (2020).

309 I. Levatić, P. Popčević, V. Šurija, *et al.* Dramatic pressure-driven enhancement of bulk skyrmion stability. *Sci. Rep.* **6**, 21347, doi:10.1038/srep21347 (2016).

310 S. Seki, Y. Okamura, K. Shibata, *et al.* Stabilization of magnetic skyrmions by uniaxial tensile strain. *Phys. Rev. B* **96**, 220404, doi:10.1103/PhysRevB.96.220404 (2017).

311 T. Nakajima, V. Ukleev, K. Ohishi, *et al.* Uniaxial-stress Effects on Helimagnetic Orders and Skyrmion Lattice in Cu_2OSeO_3. *Journal of the Physical Society of Japan* **87**, 094709, doi:10.7566/JPSJ.87.094709 (2018).

312 L. Deng, H.-C. Wu, A. P. Litvinchuk, *et al.* Room-temperature skyrmion phase in bulk Cu_2OSeO_3 under high pressures. *Proceedings of the National Academy of Sciences* **117**, 8783, doi:10.1073/pnas.1922108117 (2020).

313 C. Feng, F. Meng, Y. Wang, *et al.* Field-Free Manipulation of Skyrmion Creation and Annihilation by Tunable Strain Engineering. *Advanced Functional Materials* **31**, 2008715, doi:10.1002/adfm.202008715 (2021).

314 A. A. Thiele. Steady-State Motion of Magnetic Domains. *Phys. Rev. Lett.* **30**, 230-233, doi:10.1103/PhysRevLett.30.230 (1973).

315 C. Reichhardt & C. J. Olson Reichhardt. Noise fluctuations and drive dependence of the skyrmion Hall effect in disordered systems. *New J. Phys.* **18**, 095005, doi:10.1088/1367-2630/18/9/095005 (2016).

316 R. Tomasello, E. Martinez, R. Zivieri, *et al.* A strategy for the design of skyrmion racetrack memories. *Sci. Rep.* **4**, 6784, doi:10.1038/srep06784 (2014).

317 H. T. Fook, W. L. Gan, I. Purnama, *et al.* Mitigation of Magnus Force in Current-Induced Skyrmion Dynamics. *IEEE Trans. Magn.* **51**, 1-4, doi:10.1109/TMAG.2015.2433677 (2015).

318 S. Bhatti & S. N. Piramanayagam. Effect of Dzyaloshinskii–Moriya Interaction Energy Confinement on Current-Driven Dynamics of Skyrmions. *physica status solidi (RRL) – Rapid Research Letters* **13**, 1900090, doi:10.1002/pssr.201900090 (2019).

319 A. V. Khvalkovskiy, V. Cros, D. Apalkov, *et al.* Matching domain-wall configuration and spin-orbit torques for efficient domain-wall motion. *Phys. Rev. B* **87**, 020402, doi:10.1103/PhysRevB.87.020402 (2013).

320 S. Emori, U. Bauer, S.-M. Ahn, *et al.* Current-driven dynamics of chiral ferromagnetic domain walls. *Nat. Mater.* **12**, 611-616, doi:10.1038/nmat3675 (2013).

321 S.-Z. Lin, C. Reichhardt, C. D. Batista, *et al.* Particle model for skyrmions in metallic chiral magnets: Dynamics, pinning, and creep. *Phys. Rev. B* **87**, 214419, doi:10.1103/PhysRevB.87.214419 (2013).

322 P. J. Metaxas, J. P. Jamet, A. Mougin, *et al.* Creep and Flow Regimes of Magnetic Domain-Wall Motion in Ultrathin Pt/Co/Pt Films with Perpendicular Anisotropy. *Phys. Rev. Lett.* **99**, 217208, doi:10.1103/PhysRevLett.99.217208 (2007).

323 W. Jiang, W. Zhang, G. Yu, *et al.* Mobile Néel skyrmions at room temperature: status and future. *AIP Adv.* **6**, 055602, doi:10.1063/1.4943757 (2016).

324 F. Jonietz, S. Mühlbauer, C. Pfleiderer, *et al.* Spin Transfer Torques in MnSi at Ultralow Current Densities. *Science* **330**, 1648, doi:10.1126/science.1195709 (2010).

325 T. Schulz, R. Ritz, A. Bauer, *et al.* Emergent electrodynamics of skyrmions in a chiral magnet. *Nat. Phys.* **8**, 301-304, doi:10.1038/nphys2231 (2012).

326 X. Z. Yu, N. Kanazawa, W. Z. Zhang, *et al.* Skyrmion flow near room temperature in an ultralow current density. *Nat. Commun.* **3**, 988, doi:10.1038/ncomms1990 (2012).

327 D. Okuyama, M. Bleuel, J. S. White, *et al.* Deformation of the moving magnetic skyrmion lattice in MnSi under electric current flow. *Commun. Phys.* **2**, 79, doi:10.1038/s42005-019-0175-z (2019).

328 M. Mochizuki, X. Z. Yu, S. Seki, *et al.* Thermally driven ratchet motion of a skyrmion microcrystal and topological magnon Hall effect. *Nat. Mater.* **13**, 241-246, doi:10.1038/nmat3862 (2014).

329 A. A. Kovalev & Y. Tserkovnyak. Thermoelectric spin transfer in textured magnets. *Phys. Rev. B* **80**, 100408, doi:10.1103/PhysRevB.80.100408 (2009).

330 D. Ehlers, I. Stasinopoulos, V. Tsurkan, *et al.* Skyrmion dynamics under uniaxial anisotropy. *Phys. Rev. B* **94**, 014406, doi:10.1103/PhysRevB.94.014406 (2016).

331 Y. Okamura, S. Seki, S. Bordács, *et al.* Microwave Directional Dichroism Resonant with Spin Excitations in the Polar Ferromagnet GaV_4S_8. *Phys. Rev. Lett.* **122**, 057202, doi:10.1103/PhysRevLett.122.057202 (2019).

332 R. H. Liu, W. L. Lim & S. Urazhdin. Dynamical Skyrmion State in a Spin Current Nano-Oscillator with Perpendicular Magnetic Anisotropy. *Phys. Rev. Lett.* **114**, 137201, doi:10.1103/PhysRevLett.114.137201 (2015).

333 B. Satywali, V. P. Kravchuk, L. Pan, *et al.* Microwave resonances of magnetic skyrmions in thin film multilayers. *Nat. Commun.* **12**, 1909, doi:10.1038/s41467-021-22220-1 (2021).

334 S. Mühlbauer, D. Honecker, É. A. Périgo, *et al.* Magnetic small-angle neutron scattering. *Reviews of Modern Physics* **91**, 015004, doi:10.1103/RevModPhys.91.015004 (2019).

335 X. Z. Yu, Y. Onose, N. Kanazawa, *et al.* Real-space observation of a two-dimensional skyrmion crystal. *Nature* **465**, 901-904, doi:10.1038/nature09124 (2010).

336 J. Tang, L. Kong, W. Wang, *et al.* Lorentz transmission electron microscopy for magnetic skyrmions imaging. *Chinese Physics B* **28**, 087503, doi:10.1088/1674-1056/28/8/087503 (2019).

337 S. Bajt, A. Barty, K. A. Nugent, *et al.* Quantitative phase-sensitive imaging in a transmission electron microscope. *Ultramicroscopy* **83**, 67-73, doi:10.1016/S0304-3991(99)00174-6 (2000).

338 K. Ishizuka & B. Allman. Phase measurement of atomic resolution image using transport of intensity equation. *Journal of Electron Microscopy* **54**, 191-197, doi:10.1093/jmicro/dfi024 (2005).

339 W. Jiang, S. Zhang, X. Wang, *et al.* Quantifying chiral exchange interaction for Néel-type skyrmions via Lorentz transmission electron microscopy. *Phys. Rev. B* **99**, 104402, doi:10.1103/PhysRevB.99.104402 (2019).

340 T. Matsumoto, Y.-G. So, Y. Kohno, *et al.* Direct observation of Σ7 domain boundary core structure in magnetic skyrmion lattice. *Sci. Adv.* **2**, e1501280, doi:10.1126/sciadv.1501280 (2016).

341 D. McGrouther, R. J. Lamb, M. Krajnak, *et al.* Internal structure of hexagonal skyrmion lattices in cubic helimagnets. *New J. Phys.* **18**, 095004, doi:10.1088/1367-2630/18/9/095004 (2016).

342 S. McVitie, S. Hughes, K. Fallon, *et al.* A transmission electron microscope study of Néel skyrmion magnetic textures in multilayer thin film systems with large interfacial chiral interaction. *Sci. Rep.* **8**, 5703, doi:10.1038/s41598-018-23799-0 (2018).

343 T. Matsumoto, Y.-G. So, Y. Ikuhara, *et al.* Direct visualization of nucleation intermediate state of magnetic skyrmion from helical stripes assisted by artificial surface pits. *J. Magn. Magn. Mater.* **531**, 167976, doi:10.1016/j.jmmm.2021.167976 (2021).

344 D. A. Gilbert, B. B. Maranville, A. L. Balk, *et al.* Realization of ground-state artificial skyrmion lattices at room temperature. *Nat. Commun.* **6**, 8462, doi:10.1038/ncomms9462 (2015).

345 N. Rougemaille & A. K. Schmid. Magnetic imaging with spin-polarized low-energy electron microscopy. *The European Physical Journal - Applied Physics* **50**, 20101, doi:10.1051/epjap/2010048 (2010).

346 P. Fischer. Frontiers in imaging magnetism with polarized x-rays. *Frontiers in Physics* **2**, doi:10.3389/fphy.2014.00082 (2015).

347 J. Li, A. Tan, K. W. Moon, *et al.* Tailoring the topology of an artificial magnetic skyrmion. *Nat. Commun.* **5**, 4704, doi:10.1038/ncomms5704 (2014).

348 S. Meyer, M. Perini, S. von Malottki, *et al.* Isolated zero field sub-10 nm skyrmions in ultrathin Co films. *Nat. Commun.* **10**, 3823, doi:10.1038/s41467-019-11831-4 (2019).

349 M. T. Birch, D. Cortés-Ortuño, L. A. Turnbull, *et al.* Real-space imaging of confined magnetic skyrmion tubes. *Nat. Commun.* **11**, 1726, doi:10.1038/s41467-020-15474-8 (2020).

350 F. Büttner, C. Moutafis, M. Schneider, *et al.* Dynamics and inertia of skyrmionic spin structures. *Nat. Phys.* **11**, 225, doi:10.1038/nphys3234 (2015).

351 K. v. Bergmann, A. Kubetzka, O. Pietzsch, *et al.* Interface-induced chiral domain walls, spin spirals and skyrmions revealed by spin-polarized scanning tunneling microscopy. *Journal of Physics: Condensed Matter* **26**, 394002, doi:10.1088/0953-8984/26/39/394002 (2014).

352 M. Cinchetti. Topology communicates. *Nat. Nanotech.* **9**, 965-966, doi:10.1038/nnano.2014.284 (2014).

353 J. Sassmannshausen, A. Kubetzka, P.-J. Hsu, *et al.* Pb-induced skyrmions in a double layer of Fe on Ir(111). *Phys. Rev. B* **98**, 144443, doi:10.1103/PhysRevB.98.144443 (2018).

354 D. Cortés-Ortuño, N. Romming, M. Beg, *et al.* Nanoscale magnetic skyrmions and target states in confined geometries. *Phys. Rev. B* **99**, 214408, doi:10.1103/PhysRevB.99.214408 (2019).

355 R. Wiesendanger. Spin mapping at the nanoscale and atomic scale. *Reviews of Modern Physics* **81**, 1495-1550, doi:10.1103/RevModPhys.81.1495 (2009).

356 J. Grenz, A. Köhler, A. Schwarz, *et al.* Probing the Nano-Skyrmion Lattice on Fe/Ir(111) with Magnetic Exchange Force Microscopy. *Phys. Rev. Lett.* **119**, 047205, doi:10.1103/PhysRevLett.119.047205 (2017).

357 A. Jenkins, M. Pelliccione, G. Yu, *et al.* Single-spin sensing of domain-wall structure and dynamics in a thin-film skyrmion host. *Phys. Rev. Mater.* **3**, 083801, doi:10.1103/PhysRevMaterials.3.083801 (2019).

358 L. Vistoli, W. Wang, A. Sander, *et al.* Giant topological Hall effect in correlated oxide thin films. *Nat. Phys.* **15**, 67-72, doi:10.1038/s41567-018-0307-5 (2019).

359 P. Bruno, V. K. Dugaev & M. Taillefumier. Topological Hall Effect and Berry Phase in Magnetic Nanostructures. *Phys. Rev. Lett.* **93**, 096806, doi:10.1103/PhysRevLett.93.096806 (2004).

360 C. Hanneken, F. Otte, A. Kubetzka, *et al.* Electrical detection of magnetic skyrmions by tunnelling non-collinear magnetoresistance. *Nat. Nanotech.* **10**, 1039-1042, doi:10.1038/nnano.2015.218 (2015).

361 T. L. Monchesky. Detection with unpolarized currents. *Nat. Nanotech.* **10**, 1008-1009, doi:10.1038/nnano.2015.226 (2015).

362 D. M. Crum, M. Bouhassoune, J. Bouaziz, *et al.* Perpendicular reading of single confined magnetic skyrmions. *Nat. Commun.* **6**, 8541, doi:10.1038/ncomms9541 (2015).

363 M. Perini, S. Meyer, A. Kubetzka, *et al.* Electrical Detection of Domain Walls and Skyrmions in Co Films Using Noncollinear Magnetoresistance. *Phys. Rev. Lett.* **123**, 237205, doi:10.1103/PhysRevLett.123.237205 (2019).

364 A. Bauer & C. Pfleiderer. Magnetic phase diagram of MnSi inferred from magnetization and ac susceptibility. *Phys. Rev. B* **85**, 214418, doi:10.1103/PhysRevB.85.214418 (2012).

365 S. S. P. Parkin, M. Hayashi & L. Thomas. Magnetic Domain-Wall Racetrack Memory. *Science* **320**, 190, doi:10.1126/science.1145799 (2008).

366 A. Fert, V. Cros & J. Sampaio. Skyrmions on the track. *Nat. Nanotech.* **8**, 152-156, doi:10.1038/nnano.2013.29 (2013).

367 J. Sampaio, V. Cros, S. Rohart, *et al.* Nucleation, stability and current-induced motion of isolated magnetic skyrmions in nanostructures. *Nat. Nanotech.* **8**, 839-844, doi:10.1038/nnano.2013.210 (2013).

368 J. Ding, X. Yang & T. Zhu. Manipulating current induced motion of magnetic skyrmions in the magnetic nanotrack. *J. Phys. D: Appl. Phys.* **48**, 115004, doi:10.1088/0022-3727/48/11/115004 (2015).

369 J. Jena, B. Göbel, V. Kumar, *et al.* Evolution and competition between chiral spin textures in nanostripes with D_{2d} symmetry. *Sci. Adv.* **6**, eabc0723, doi:10.1126/sciadv.abc0723 (2020).

370 I. Purnama, W. L. Gan, D. W. Wong, *et al.* Guided current-induced skyrmion motion in 1D potential well. *Sci. Rep.* **5**, 10620, doi:10.1038/srep10620 (2015).

371 S. L. Zhang, W. W. Wang, D. M. Burn, *et al.* Manipulation of skyrmion motion by magnetic field gradients. *Nat. Commun.* **9**, 2115, doi:10.1038/s41467-018-04563-4 (2018).

372 X. Zhang, W. Cai, X. Zhang, *et al.* Skyrmions in Magnetic Tunnel Junctions. *ACS Applied Materials & Interfaces* **10**, 16887-16892, doi:10.1021/acsami.8b03812 (2018).

373 X. Zhang, M. Ezawa & Y. Zhou. Magnetic skyrmion logic gates: conversion, duplication and merging of skyrmions. *Sci. Rep.* **5**, 9400, doi:10.1038/srep09400 (2015).

374 M. G. Mankalale, Z. Zhao, J. Wang, *et al.* SkyLogic—A Proposal for a Skyrmion-Based Logic Device. *IEEE Trans. Electron Devices* **66**, 1990-1996, doi:10.1109/TED.2019.2899263 (2019).

375 Z. Zhang, Y. Zhu, Y. Zhang, *et al.* Skyrmion-Based Ultra-Low Power Electric-Field-Controlled Reconfigurable (SUPER) Logic Gate. *IEEE Electron Device Letters* **40**, 1984-1987, doi:10.1109/LED.2019.2946863 (2019).

376 M. Chauwin, X. Hu, F. Garcia-Sanchez, *et al.* Skyrmion Logic System for Large-Scale Reversible Computation. *Phys. Rev. Appl.* **12**, 064053, doi:10.1103/PhysRevApplied.12.064053 (2019).

377 J. Grollier, D. Querlioz & M. D. Stiles. Spintronic Nanodevices for Bioinspired Computing. *Proceedings of the IEEE* **104**, 2024-2039, doi:10.1109/JPROC.2016.2597152 (2016).

378 Y. Huang, W. Kang, X. Zhang, *et al.* Magnetic skyrmion-based synaptic devices. *Nanotech.* **28**, 08LT02, doi:10.1088/1361-6528/aa5838 (2017).

379 M. Chen, A. Sengupta & K. Roy. Magnetic Skyrmion as a Spintronic Deep Learning Spiking Neuron Processor. *IEEE Trans. Magn.* **54**, 1-7, doi:10.1109/TMAG.2018.2845890 (2018).

380 U. Saxena, D. Kaushik, M. Bansal, *et al.* Low-Energy Implementation of Feed-Forward Neural Network With Back-Propagation Algorithm Using a Spin-Orbit Torque Driven Skyrmionic Device. *IEEE Trans. Magn.* **54**, 1-5, doi:10.1109/TMAG.2018.2853082 (2018).

381 T. Bhattacharya, S. Li, Y. Huang, *et al.* Low-Power (1T1N) Skyrmionic Synapses for Spiking Neuromorphic Systems. *IEEE Access* **7**, 5034-5044, doi:10.1109/ACCESS.2018.2886854 (2019).

382 S. Luo, N. Xu, Z. Guo, *et al.* Voltage-Controlled Skyrmion Memristor for Energy-Efficient Synapse Applications. *IEEE Electron Device Letters* **40**, 635-638, doi:10.1109/LED.2019.2898275 (2019).

383 B. Pan, D. Zhang, X. Zhang, *et al.* Skyrmion-Induced Memristive Magnetic Tunnel Junction for Ternary Neural Network. *IEEE Journal of the Electron Devices Society* **7**, 529-533, doi:10.1109/JEDS.2019.2913637 (2019).

384 Z. He, S. Angizi & D. Fan. Current-Induced Dynamics of Multiple Skyrmions With Domain-Wall Pair and Skyrmion-Based Majority Gate Design. *IEEE Magn. Lett.* **8**, 1-5, doi:10.1109/LMAG.2017.2689721 (2017).

385 N. Bindal, C. A. C. Ian, W. S. Lew, *et al.* Antiferromagnetic skyrmion repulsion based artificial neuron device. *Nanotech.* **32**, 215204, doi:10.1088/1361-6528/abe261 (2021).

386 S. Li, W. Kang, Y. Huang, *et al.* Magnetic skyrmion-based artificial neuron device. *Nanotech.* **28**, 31LT01, doi:10.1088/1361-6528/aa7af5 (2017).

387 X. Chen, W. Kang, D. Zhu, *et al.* A compact skyrmionic leaky–integrate–fire spiking neuron device. *Nanoscale* **10**, 6139-6146, doi:10.1039/C7NR09722K (2018).

388 A. Abusnaina & R. Abdullah. Spiking Neuron Models: A Review. *International Journal of Digital Content Technology and its Applications* **8**, 14-21 (2014).

389 X. Liang, X. Zhang, J. Xia, *et al.* A spiking neuron constructed by the skyrmion-based spin torque nano-oscillator. *Appl. Phys. Lett.* **116**, 122402, doi:10.1063/5.0001557 (2020).

390 M. A. Azam, D. Bhattacharya, D. Querlioz, *et al.* Resonate and fire neuron with fixed magnetic skyrmions. *J. Appl. Phys.* **124**, 152122, doi:10.1063/1.5042308 (2018).

391 J. P. Hayes. in *2015 52nd ACM/EDAC/IEEE Design Automation Conference (DAC).* 1-3.

392 G. Finocchio, M. Di Ventra, K. Y. Camsari, *et al.* The promise of spintronics for unconventional computing. *J. Magn. Magn. Mater.* **521**, 167506, doi:10.1016/j.jmmm.2020.167506 (2021).

393 J. Torrejon, M. Riou, F. A. Araujo, *et al.* Neuromorphic computing with nanoscale spintronic oscillators. *Nature* **547**, 428-431, doi:https://doi.org/10.1038/nature23011 (2017).

394 L. Appeltant, M. C. Soriano, G. Van der Sande, *et al.* Information processing using a single dynamical node as complex system. *Nat. Commun.* **2**, 468, doi:10.1038/ncomms1476 (2011).

395 G. Bourianoff, D. Pinna, M. Sitte, *et al.* Potential implementation of reservoir computing models based on magnetic skyrmions. *AIP Adv.* **8**, 055602, doi:10.1063/1.5006918 (2018).

396 D. Prychynenko, M. Sitte, K. Litzius, *et al.* Magnetic Skyrmion as a Nonlinear Resistive Element: A Potential Building Block for Reservoir Computing. *Phys. Rev. Appl.* **9**, 014034, doi:10.1103/PhysRevApplied.9.014034 (2018).

397 W. Jiang, L. Chen, K. Zhou, *et al.* Physical reservoir computing using magnetic skyrmion memristor and spin torque nano-oscillator. *Appl. Phys. Lett.* **115**, 192403, doi:10.1063/1.5115183 (2019).

398 F. Peper, J. Lee, J. Carmona, *et al.* Brownian Circuits: Fundamentals. *J. Emerg. Technol. Comput. Syst.* **9**, Article 3, doi:10.1145/2422094.2422097 (2013).

399 F. Ma, Y. Zhou, H. B. Braun, *et al.* Skyrmion-Based Dynamic Magnonic Crystal. *Nano Lett.* **15**, 4029-4036, doi:10.1021/acs.nanolett.5b00996 (2015).

400 X.-g. Wang, Y.-Z. Nie, Q.-l. Xia, *et al.* Dynamically reconfigurable magnonic crystal composed of artificial magnetic skyrmion lattice. *J. Appl. Phys.* **128**, 063901, doi:10.1063/5.0012791 (2020).

401 S. Zhang, J. Wang, Q. Zheng, *et al.* Current-induced magnetic skyrmions oscillator. *New J. Phys.* **17**, 023061, doi:10.1088/1367-2630/17/2/023061 (2015).

402 F. Garcia-Sanchez, J. Sampaio, N. Reyren, *et al.* A skyrmion-based spin-torque nano-oscillator. *New J. Phys.* **18**, 075011, doi:10.1088/1367-2630/18/7/075011 (2016).

403 D. Das, B. Muralidharan & A. Tulapurkar. Skyrmion based spin-torque nano-oscillator. *J. Magn. Magn. Mater.* **491**, 165608, doi:10.1016/j.jmmm.2019.165608 (2019).

404 Y. Feng, J. Xia, L. Qiu, *et al.* A skyrmion-based spin-torque nano-oscillator with enhanced edge. *J. Magn. Magn. Mater.* **491**, 165610, doi:10.1016/j.jmmm.2019.165610 (2019).

405 J. H. Guo, J. Xia, X. C. Zhang, *et al.* A ferromagnetic skyrmion-based nano-oscillator with modified profile of Dzyaloshinskii-Moriya interaction. *J. Magn. Magn. Mater.* **496**, 165912, doi:10.1016/j.jmmm.2019.165912 (2020).

406 S. Zhou, C. Zheng, X. Chen, *et al.* Skyrmion-based spin-torque nano-oscillator in synthetic antiferromagnetic nanodisks. *J. Appl. Phys.* **128**, 033907, doi:10.1063/5.0013402 (2020).

Chapter 4 Experimental and Simulation Methods

In this chapter, we detail the experimental techniques used for device fabrication and characterization. We also describe the numerical methods used for micromagnetic simulations performed using Mumax3.

4.1 Device Fabrication

In this section, the fabrication of the magnetic multilayer thin film Hall cross devices used in the experiments of Chapters 5 and 6 are described. The complete process involved a series of deposition, lithography, etching, and lift-off processes.

The process begins with substrate preparation and cleaning. A thermally oxidized silicon wafer was used as the substrate. The wafer was cleaved into 1 cm by 1 cm squares to ease subsequent lithography and characterization processes. These wafers were cleaned using an ultrasonic cleaner in an acetone bath, then an isopropanol bath, and finally dried using a nitrogen jet.

The fabrication of the device can be approached by either lithography–deposition–lift-off process or deposition–lithography–etching process. Our work used the latter as the magnetic multilayer is extremely sensitive to each layer's thickness and deposition conditions. Delicate tuning and multiple depositions were required to optimize the desired magnetic multilayer with magnetic skyrmions. Thus, the initial lithography process was avoided to minimize time lost. Depositing a full thin film across the wafer instead of directly fabricating the Hall crosses was also helpful for intermediate characterization such as VSM and MOKE.

The prepared wafers were deposited with the magnetic multilayer thin film by magnetron sputtering under ultra-high vacuum (UHV). Some of the wafers were used for thin-film characterization, while others were fabricated into Hall cross. For the Hall cross fabrication, the wafers first underwent an electron beam lithography (EBL) process to pattern the structure onto the film. With the patterned photoresist protecting the Hall cross regions on the thin film, ion beam etching (IBE) was performed to remove the materials in the unprotected regions, leaving the Hall cross structure.

Electrical contact pads were deposited via the lithography–deposition–lift-off process. The electrical contact pads were patterned onto the completed Hall cross structure by EBL with the desired regions unprotected by the photoresist. Next, the conductive metal was deposited by magnetron sputtering across the film. Finally, the photoresist was lifted off along with the materials deposited on top of it, leaving behind the desired contact pads. The completed devices were then ready for their subsequent characterization and experiments.

The process described above provides a handy overview of the complete procedure. The increased complexity of each step, magnetron sputtering, EBL, and ion beam etching are further detailed in the respective subsections.

4.1.1 Magnetron Sputtering Deposition

Sputtering deposition is a form of physical vapour deposition technique widely used in thin-film manufacturing and coatings, particularly in the semiconductor industry. It can be applied to a wide range of materials ranging across metals, semiconductors, and insulators. The term sputtering refers to ejecting atoms from a solid material due to the bombardment of energetic particles. The capturing of these ejected atoms onto a substrate is its application in thin film deposition.

A basic schematic of the sputtering deposition system is shown in Fig. 4.1.1. The key components are the target, substrate, argon plasma in a UHV chamber, and power supply. The target refers to the intended material for deposition and must be of very high purity. These targets are typically produced via casting or sintering. The substrate is positioned to capture the ejected atoms from the target. Argon gas is used to create the plasma used for the bombardment of the target because of its relatively high atomic mass and being inert to chemical reactions with the materials. The argon plasma is ignited by applying a high voltage to the target using a power supply. The argon ions in the plasma are accelerated towards the target to bombard and eject the target's surface atoms as intermediate gaseous particles towards the substrate. The deposition is achieved as the flux of ejected atoms lands on the substrate and reforms as solid thin films[1,2].

Magnetron sputtering refers to the additional use of magnetic fields to improve the sputtering process. A magnetic field is introduced right above the sputtering targets using strong permanent magnets placed below them. The magnetic field traps electrons close to the target, generating a localized high plasma density for higher deposition rates at lower pressures.

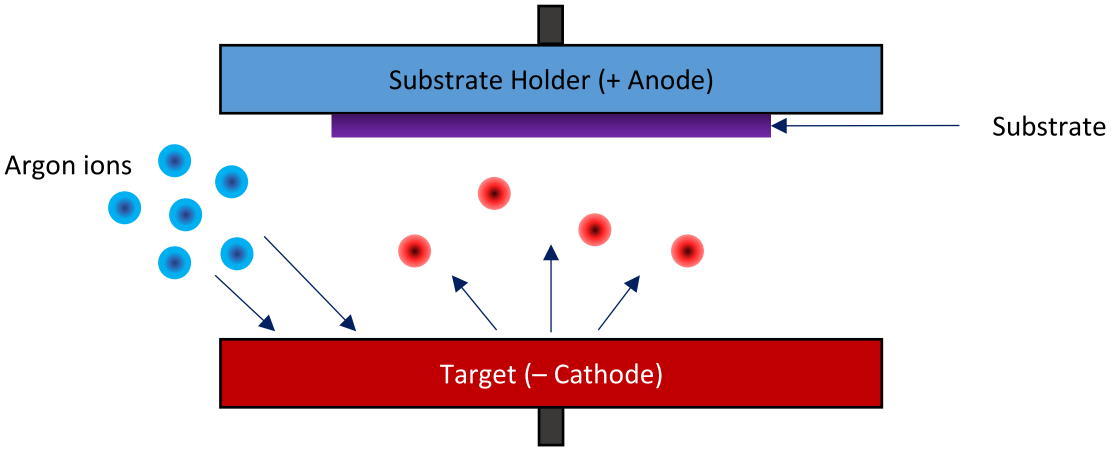

Figure 4.1.1| Schematic of a basic sputtering deposition system and process.

A DC power is typically used for metallic targets, while a radio frequency (RF) power is necessary for insulating targets. If a DC power is used on an insulating target, a positive charge will accumulate over time and cease to attract the Argon ions for the target bombardment. Charge build-up is also highly undesirable because it can lead to arcing, disrupting the sputtering process or damaging the target. An RF power overcomes the charge accumulation issue by discharging it during half its cycle. RF sputtering offers other advantages like a more uniform use of the sputtering target due to the more diffused plasma and resolving the disappearing anode problem that occurs as dielectric coats the anode and disrupts the electric fields[3,4]. However, RF sputtering requires higher voltage and more costly power supplies and offers much slower sputtering rates than DC sputtering[2].

The sputtering system used for deposition is the two custom connected AJA ATC-Orion 8 UHV, as shown in Fig. 4.1.2(a). Sixteen different targets can be installed simultaneously, and wafers can be transferred between the two sputtering chambers for deposition without breaking vacuum that would be critical for materials susceptible to atmospheric oxygen and moisture. Figure 4.1.2(b) shows the internal view of the sputtering chamber with the opened lid. Wafers are attached to a sputtering cassette and suspended at the top of the sputtering chamber by a rotating helicopter blade. At the bottom of the chamber lies the eight sputtering guns with their respective targets installed and positioned in a confocal manner directed at the substrate position for uniform deposition, as shown in Fig. 4.1.2(c). Water cooling is another critical component as ion bombardment raises the target temperature significantly, even more so for materials with poor thermal conductivity. The poor heat dissipation of insulators requires the power applied to these targets to be raised stepwise slowly to avoid creating a steep thermal gradient across the target that can crack the target under thermal stress.

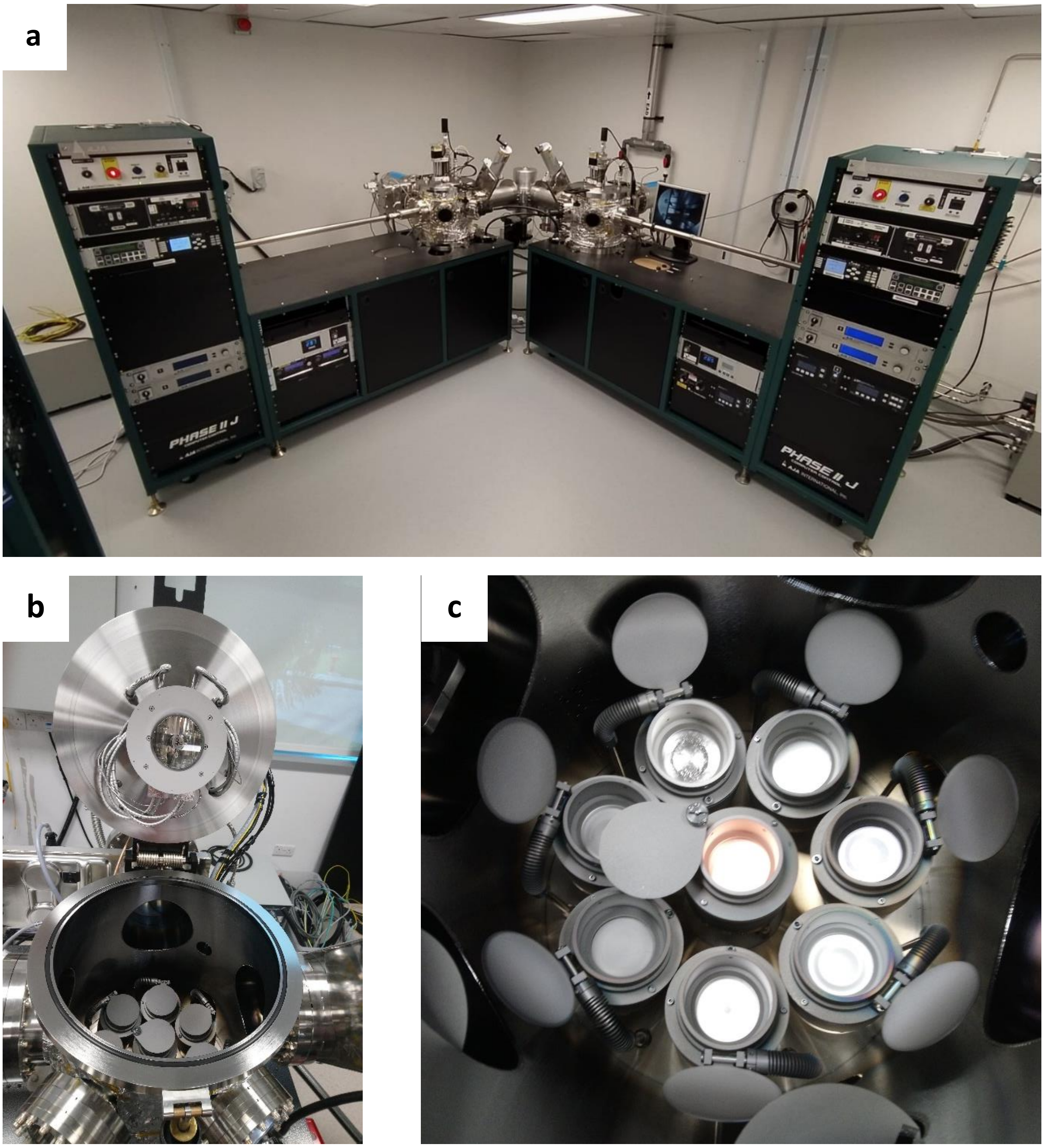

Figure 4.1.2| (a) Two custom connected AJA ATC-Orion 8 UHV sputtering systems. (b) Internal view of the sputtering chamber. (c) A top-down view of the 8 sputtering guns configurations.

The system can achieve base pressure in the UHV regime of 1×10^{-8} Torr under optimal conditioning and is sustained by a CTI cryogenic pump. The cryogenic pump uses liquid helium to cool cryopanels down to temperatures of 11 K that condenses and traps surrounding gas as they lose their kinetic energy when they contact the panels. These panels eventually become saturated over time and require the regeneration process to clean the panels and maintain optimal performance.

The thin film deposition thickness is nominally set based on calibrated values of sputtering rates instead of *in situ* thickness monitoring. A long-duration deposition of the material is performed onto a calibration sample with a small drop of photoresist. After lifting off the photoresist, a step structure is acquired at the edge and measured accurately using the Park Systems NX10 atomic force microscope. The deposition rate is obtained based on the step height divided by the deposition time.

4.1.2 Electron Beam Lithography

EBL is an advanced patterning technique that transfers a computer-aided design structure onto a resist-coated wafer at high resolutions at the order of nanometres. We use the Raith eLINE EBL system, as shown in Fig. 4.1.3. The lithography process involves three key steps: spin coating, exposure, and development of resist. At the start of the lithography process, the choice between either the positive or negative resist is required. A positive resist becomes more soluble after exposure, while the negative resist becomes less soluble.

For the fabrication of the Hall cross on the wafer with the already deposited magnetic multilayer, we use the negative resist ma-N 2403 to protect the exposed region during the subsequent IBE. The negative resist is spin-coated onto the wafer at a high rotation speed of 4500 rpm to achieve a thin resist thickness. The wafer is then soft-baked to vaporize part of the solvent and solidify the resist to be ready for exposure. For exposure, the wafer is inserted into the EBL vacuum system. The EBL system also functions as a scanning electron microscope (SEM) to view the sample surface down to nanometre resolutions. Multiple alignment procedures are performed to ensure the electron beam is well focussed on achieving optimal resolution. The electron beam exposure itself is fully computer-controlled. One limitation of EBL is the long exposure time necessary in exchange for the narrow electron beam required for high resolution. After exposure of the negative resist, it is developed using its corresponding developer ma-D 532 and subsequently stopped using de-ionised water. The development time is critical in determining the produced patterns' dimension accuracy. Over-developing the sample results in wider than intended features, while under-developing the sample leaves unwanted residual resist. After development, the wafer is ready for IBE.

The fabrication of the contact pads is identical but uses a positive resist, Polymethyl methacrylate (PMMA) 950K, and is developed using a mixture of Methyl Isobutyl Ketone (MIBK) and IPA. In this case, after development, the pattern is left exposed and ready for deposition.

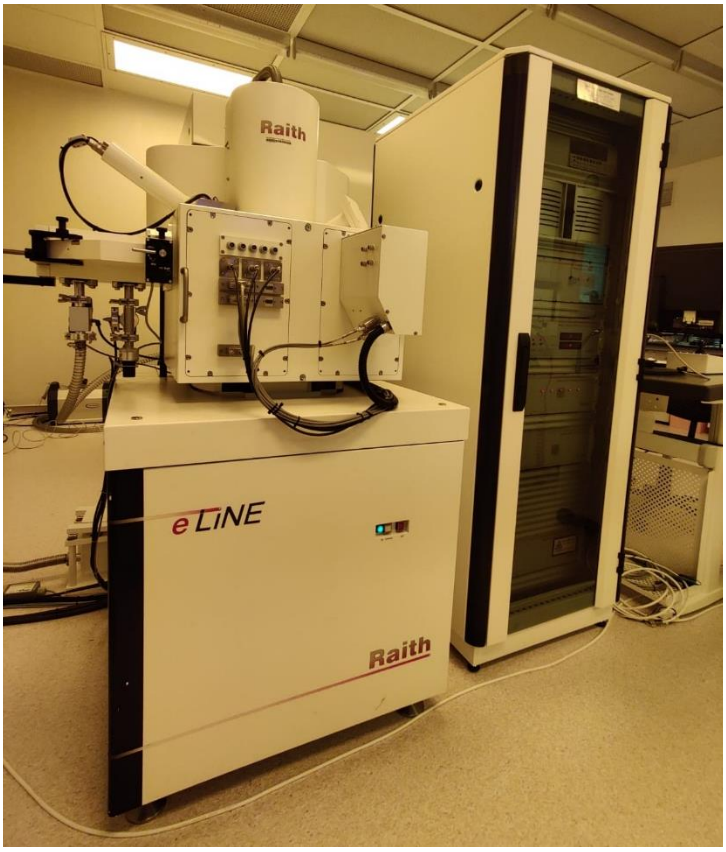

Figure 4.1.3| Raith eLINE EBL system.

4.1.3 Ion Beam Etching

IBE is an anisotropic physical etching process that operates by bombarding the sample with strongly accelerated argon ions to physically dislodge atoms from the sample. IBE is also commonly known as ion milling. The process is analogous to the sputtering deposition process, but instead of bombarding a target material, the ions are directed towards the sample. In contrast, to the sputtering deposition where the argon plasma is generated right above the target, IBE utilizes an argon plasma are generated in a dedicated ion source as uniformity and directionality of the bombarding ions is critical in achieving anisotropic etching. This etching technique occurs via physical collisions instead of a chemical reaction. Thus, it is non-selective and applicable to any material, albeit the etching rate is material dependent. Additional considerations will be required if multiple different materials across the sample are exposed to the ion beam simultaneously. During IBE of our patterned sample with resist covering the regions intended to be retained as the Hall cross, both the resist and the exposed magnetic multilayers are simultaneously etched. Hence, a sufficiently thick resist is necessary to protect the materials beneath it until the exposed regions' etching process is completed.

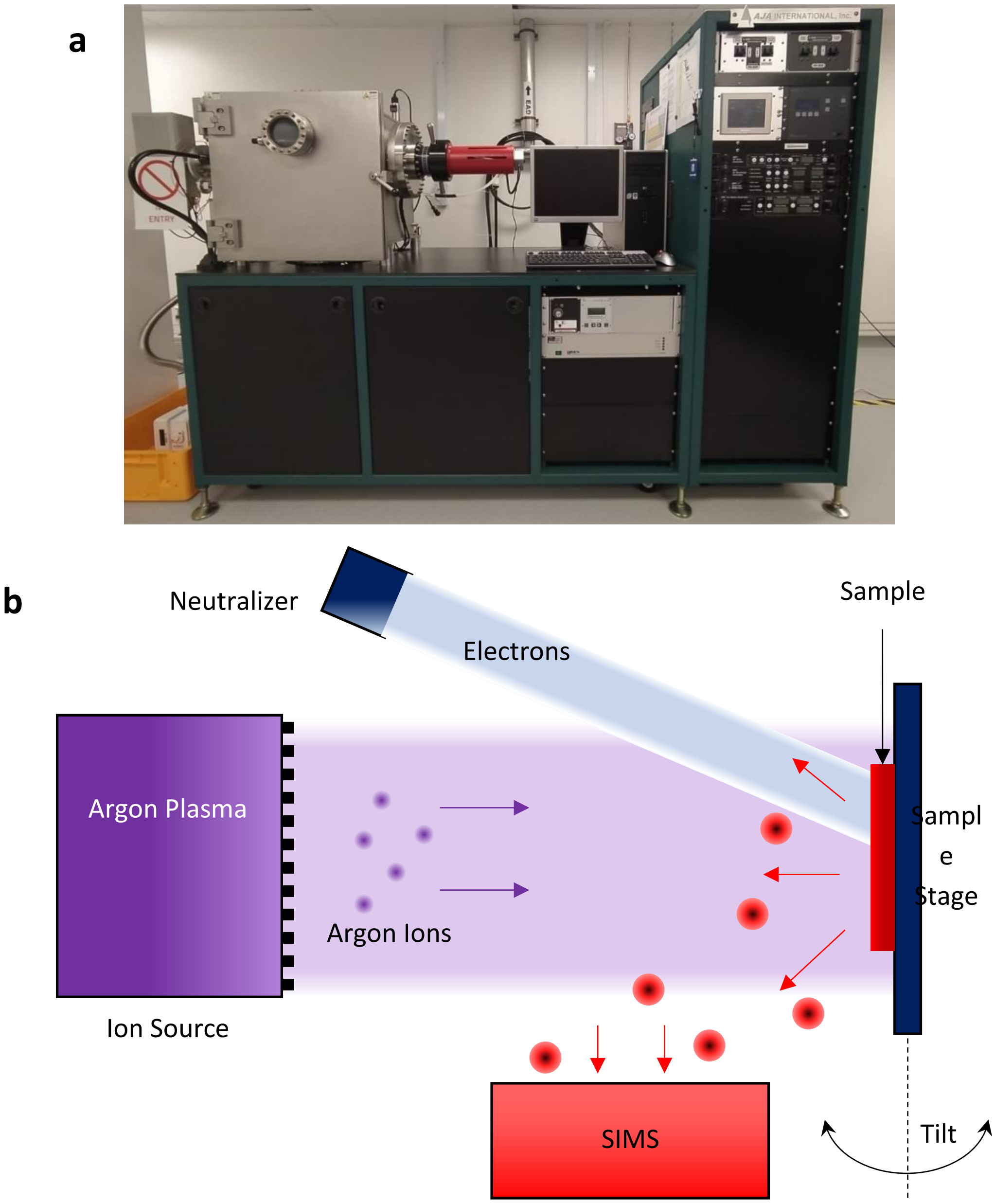

Figure 4.1.3| (a) AJA ATC-2020-IM ion beam etching system. (b) Schematic of an ion beam etching system.

We use the AJA ATC-2020-IM ion beam etching system, as shown in Fig. 4.1.3(a). The schematic of the system is presented in Fig. 4.1.3(b) with the main components of the ion source, neutralizer, sample stage, and a secondary ion mass spectrometer (SIMS). The Kaufman & Robinson RF-ICP ion source generates argon plasma and accelerates argon ions through a graphite grid towards the sample stage. Under bombardment, the sample and sample stage get significantly heated, and water cooling is crucial. Even with water cooling, the etching process is still segmented many times with intermediate pauses for the sample cooling. Excessive heat may dry out and result in difficulty removing the resist on the sample later. The sample stage is also tilted at a slight angle of 10^0 relative argon beam to minimize redeposition; Dislodged materials are scattered in an anisotropic manner, including the sides of features and channels. The small tilt introduces minor etching to clean off the redeposition. The sample stage is also continuously rotated around its central axis for uniform etching.

The continuous bombardment of argon ions on the sample will cause the accumulation of positive charge and eventually terminate the etching process. Hence, a neutralizer is a critical component that supplies electrons and ensures the etching process can be performed continuously. The SIMS *in situ* detects and plots the intensity of specified elements based on their atomic mass over time. Based on the transitions in the selected elements' intensity, the progress of etching and depth can be deduced. After the completion of IBE, the resist is then removed, and the fabrication of the Hall cross is complete.

4.2 Characterization Techniques

This section discusses the three characterization techniques performed on the full film for vibrating sample magnetometer (VSM) and the Hall cross devices for magneto-optical Kerr microscopy, electrical Hall resistance, and first-order reversal curve (FORC).

4.2.1 Vibrating Sample Magnetometer

VSM quantifies the total magnetic moment along the axis under measurement using the voltage induced by the changing magnetic flux of a vibrating magnetic sample given by Faraday's law of induction. We use the LakeShore 8604 shown in Fig. 4.2.1(a) for our experiments.

The main components of the equipment are the piezo-driven vertical oscillator, sample holder, pick up coils, and electromagnets, as shown in Fig. 4.2.1(b). The piezo-driven vertical oscillator vibrates the sample holder at 83 Hz. The measurement axis is fixed as the axis perpendicular to the pickup coil surface; Thus, the vibration axis has to be perpendicular to the measurement axis and is vertical. The sample is attached to the flat surface at the lower end of the sample holder rod using adhesive tape. While the vibration axis and measurement axis are fixed, the sample is free to be rotated by 360º around the central axis of the sample holder to perform both hard and easy axis magnetic hysteresis measurements. The electromagnet poles that sandwich the sample can generate up to 2 T of magnetic field strength depending on the adjustable pole gap distance. The pickup coils are attached to the magnet poles, as shown in Fig. 4.2.1(b). As the magnetic field and pick up coil orientations are fixed, only the magnetic moment along the magnetic field is measurable. The quantitative measurement of the magnetic moment is performed based on the magnitude of pickup coil voltage that was prior calibrated to a reference Ni sphere of 6.92 emu under a magnetic field of 5 kOe.

The VSM used also has the additional single stage variable temperature (SSVT) fixture. The SSVT allows for wide temperature-controlled measurements from 100 K to 900 K. The temperature is controlled using N_2 gas flowed past a cooler immersed in a liquid N_2 dewar and subsequently a heat exchanger before passing the sample for measurements below room temperature. For the above room temperature measurements, argon gas is used instead. The gas is flowed directly to the heat exchanger and then the sample. Extra caution is taken to ensure the sample holder material used is suitable to withstand the temperature.

From the magnetic moment data along the measurement axis against magnetic field strength, many magnetic properties are derivable, including the saturation magnetic moment, coercivity, remanent magnetic moment, exchange bias, and magnetic anisotropy. The perpendicular anisotropy of the magnetic multilayer used in our experiment is identified from the much lower saturation magnetic field under a perpendicular magnetic field than an in-plane magnetic field. More complex measurement techniques like the FORC detailed in section 4.2.4 and used in Chapter 5 can also be performed to derive further information on the magnetic reversal process.

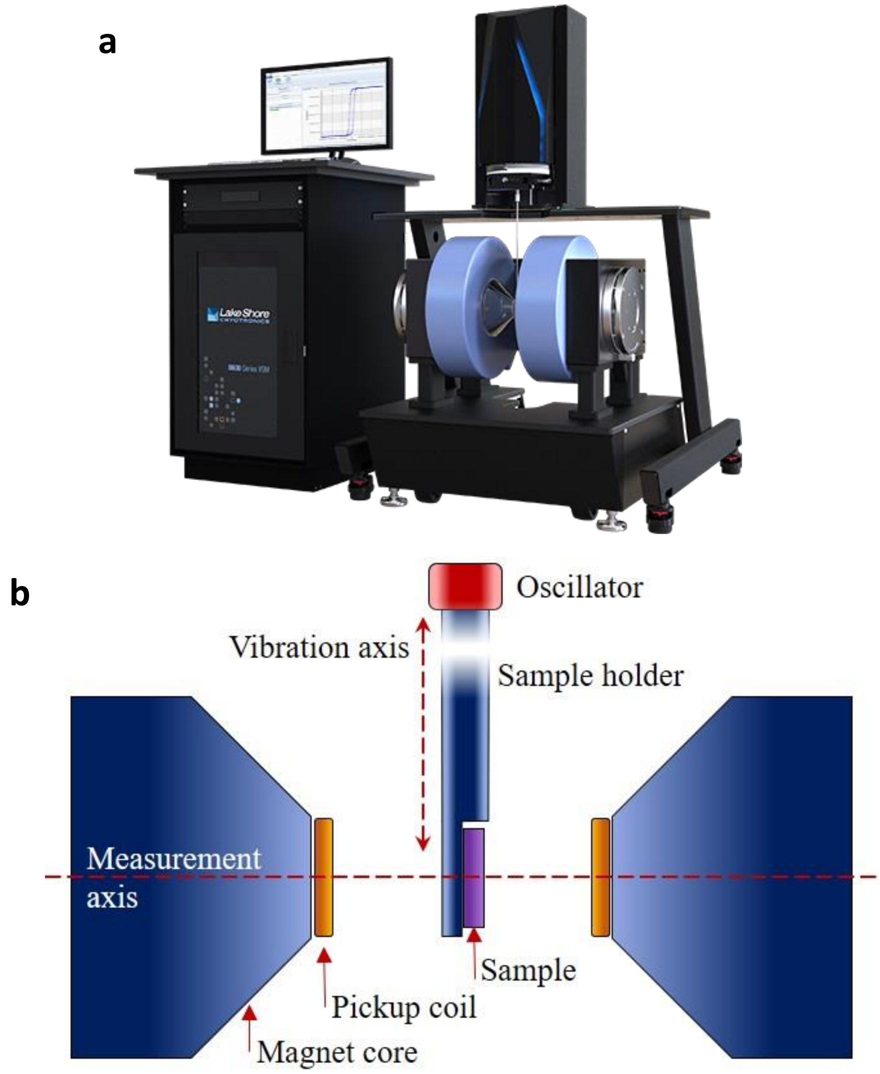

Figure 4.2.1| (a) LakeShore 8604 vibrating sample magnetometer. (b) Schematic of a vibrating sample magnetometer.

4.2.2 Magneto-optical Kerr Microscopy

Magneto-optical Kerr microscopy is a magnetic moment imaging technique that functions based on the magneto-optical Kerr effect (MOKE). MOKE refers to the interaction between an electromagnetic wave and a magnetic material during reflection, resulting in wave polarization change[5-7]. MOKE is similar to the Faraday effect, the interaction between an electromagnetic wave and a magnetic material but during transmission.

The MagVision Kerr imaging system was used, as shown in Fig. 4.2.2(a). It is an epi-illuminated imaging system, as shown in the schematic in Fig. 4.2.2(b). On the right end of Fig. 4.2.2(b), an LED provides the 520 nm green light and is attached to a cooler. The cooler is critical in protecting the LED from burning and maintaining brightness stability. The light is directed to the left, passing through a set of optical lenses, a first linear polarizer, and incident on the beam splitter. The beam splitter reflects half of the incident light downwards through the objective lens and onto the sample. The other half of the incident light transmits to the left, is not used for imaging, and is omitted from the schematic. The light reflected off the sample travels upwards through the objective lens, beam splitter, a second linear polarizer, optical lens, and is captured by a camera. The optical lenses are positioned to provide the Köhler illumination, where the image conjugate planes and illumination conjugate planes are split so that the light source's image does not superimpose onto the sample image at the camera. A homogeneous illumination is also achieved in this configuration.

The two linear polarizers are the critical components that distinguish this system from a basic microscope, and MOKE can be detected. The first linear polarizer is used to generate a linearly polarized incident light on the sample surface. This configuration where the light is incident and reflected perpendicularly from the sample surface is known as the polar configuration. In polar MOKE, the linearly polarized incident light undergoes polarization rotation in opposite directions depending on the perpendicular magnetic moment magnitude and direction. Hence, the second linear polarizer acts as an analyzer of reflected light off the sample that generates regions of differing brightness corresponding to the local perpendicular magnetic moment direction.

The typical small Kerr rotation magnitude of less than a single degree is the main challenge for MOKE imaging[7-9]. Light depolarization is further worsened by highly curved lenses like that in an objective lens. Hence, a trade-off exists between a high numerical aperture to achieve high image resolution and the loss in polarization quality due to lenses' curvature. A correction non-planar lens is used to alleviate the depolarization effect and acquire good MOKE image quality.

Differential imaging further enhances the contrast of MOKE images by taking the difference between two images to detect the change in brightness of the images. For magnetic skyrmions with a negative polarity in a positive ferromagnetic background, the reference image is taken at the positive saturated state, and the contrast of reversed domains, be it skyrmions, stripe or labyrinth domains, will be improved. For differential imaging to be optimal, spatial alignment of the reference image to the other images is vital. The system has real-time 3-

dimensional drift correction of the sample stage that gives stable images for the best images obtained in the differential manner.

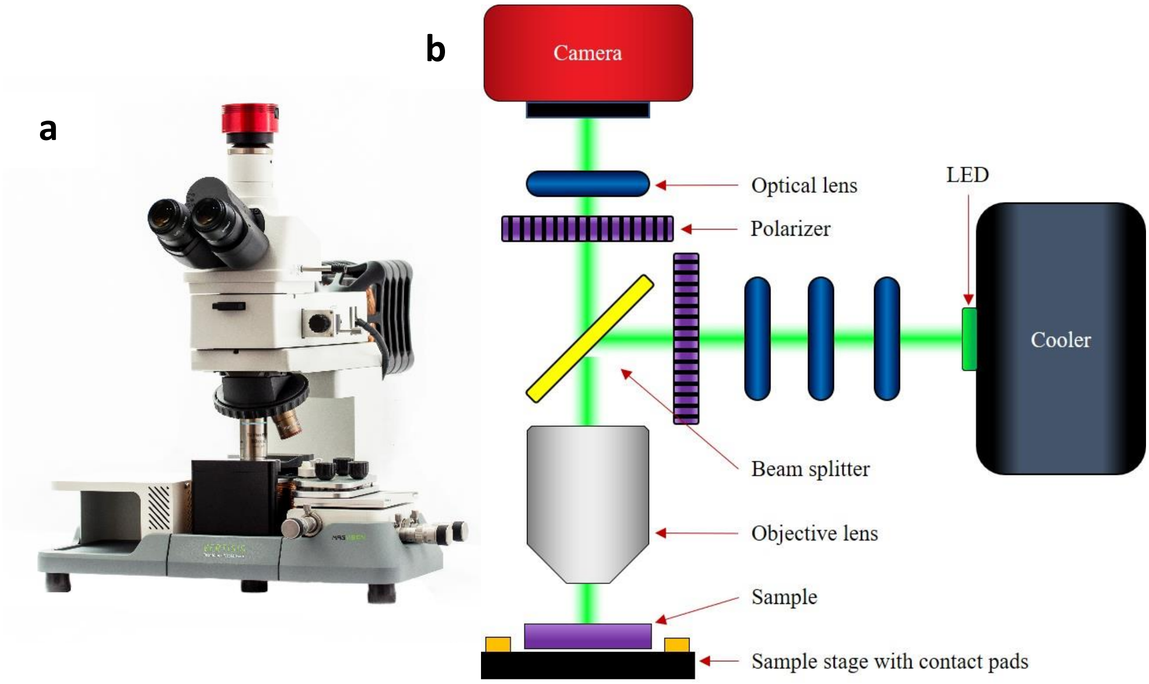

Figure 4.2.2| (a) MagVision Kerr imaging system. (b) Schematic of Kerr imaging system.

4.2.3 Electrical Hall Resistance

Electrical Hall voltage, V_{Hall} refers to the voltage due to the accumulation of charges on opposite transverse edges of the wire when a current flows along the longitudinal axis. Three possible sources of the Hall voltage are a perpendicular magnetic field, perpendicular magnetization in a magnetic wire, and topological magnetic texture. Based on the voltage source, these phenomena are named ordinary Hall effect, anomalous Hall effect (AHE), and topological Hall effect (THE), respectively.

The electrical Hall resistance is defined as the ratio of $R_{Hall} = V_{Hall}/I_x$, assuming the electrical current I flows along $\hat{x}$, analogous to a conductor's electrical resistance, $R_{elec} = V_x / I_x$. Note that electrical Hall resistance does not relate to the physical resistance but share a common formulism. Instead of characterizing the Hall effect using R_{Hall} that is dependent not only on material but also device dimensions, the resistivity ρ_{Hall} is used and is given by,

$$\rho_{Hall} = \frac{E_{Hall}}{j_x}, \tag{4.2.1}$$

where E_{Hall} is the Hall electric field, and j_x is the electrical current density along $\hat{x}$. ρ_{Hall} is analogous to the electrical resistivity, $\rho_{elec} = E_x / j_x$, following a common form of formulism.

The total ρ_{Hall} is given by the summation of contribution by all three sources,

$$\rho_{Hall} = \rho_{OHE} + \rho_{AHE} + \rho_{THE}, \tag{4.2.2}$$

$$\rho_{OHE} = R_{OHE}H + R_{AHE}M + PR_{THE}n_T\Phi_0, \tag{4.2.3}$$

where R_n is the Hall coefficients of their respective mechanisms, H is the magnetic field strength, M is magnetization, P is spin polarization of conduction electrons, n_T is the topological charge density, and $\Phi_0 = h/e$ is the quantum flux[10-13]. For the typical measurement where the current injection axis is defined as $\hat{x}$ and Hall voltage measurement performed along $\hat{y}$, H and M refers to the perpendicular component along $\hat{z}$.

The first term ρ_{OHE} in Eq. 4.2.3 originates from the Lorentz force acting on the flowing conduction electrons. The second term ρ_{AHE} arises in conducting magnetic materials where the magnetic moment within the material provides the effective magnetic field. The final term ρ_{THE} contributes to the effective magnetic field due to the topological configuration of magnetic textures like skyrmions. The individual source's contribution to ρ_{Hall} can be broken down based on the dependence of H and M. R_{OHE} is derived by taking the gradient of ρ_{OHE} at high H where the sample is saturated, thus ρ_{AHE} and ρ_{THE} are constants. $R_{AHE} = S_{AHE}\rho_{elec}^2$ relation is used to determine the second term, where S_{AHE} is a H-independent parameter[14]. Finally, ρ_{THE} is derived as the residual ρ_{Hall} after deduction of the first two terms.

ρ_{THE} is typically small and even more so for skyrmions in magnetic multilayer as compared to bulk DMI materials because of the larger size of skyrmions, and thus lower skyrmion density that relates to ρ_{THE} given in Eq. 4.2.3. Hence, for our work in Chapters 5 and 6, we only focus on R_{Hall} due to AHE to estimate skyrmion density as supported by MOKE images.

4.2.4 First-Order Reversal Curve

The magnetic hysteresis loop is an essential experimental technique, typically used in quantifying magnetic anisotropy by measuring the major hysteresis loop, where the magnetic field is swept from one saturation field to another. However, the major hysteresis loop alone is unable to reveal the underlying magnetic texture or domain behaviour fully. The first-order reversal curve is an advanced magnetic hysteresis technique that systematically quantify magnetization reversal behaviour by obtaining the set of magnetization reversal behaviour across a range of reversal fields. The different magnetization reversal behaviours of different magnetic textures allow for their transitions, and stability to be identified from the FORC data. The analysis of the FORC data is performed based on the Preisach-Krasnoselskii hysteresis model where the domain reversibility is quantified by the FORC distribution, detailed below.

. In the classical Preisach-Krasnoselskii hysteresis model, the magnetic system is assumed to be made up of an infinite set of hysterons described by the elementary hysteresis operator $\hat{\gamma}_{\alpha\beta}(t)$. $\hat{\gamma}_{\alpha\beta}$ outputs ±1 depending on the excitation input $u(t)$, where the output switches to +1 above α and –1 below β, as shown in Fig. 4.2.3(a). The state of the magnetic system $f(t)$ at a particular time t is given by the sum of all its constituent hysterons. $f(t)$ is analogous to net magnetization. Due to the system's hysteretic and history dependent nature, an initial system state is necessary to derive all subsequent states $f(t)$. By taking an arbitrary point in time t_0, where the system is in the $f(t_0)$ state and under the excitation of $u(t_0)$, the system's subsequent state $f(t)$ at any later time t becomes uniquely defined and is given by,

$$f(t) = \iint \mu(\alpha,\beta)\,\hat{\gamma}_{\alpha\beta}u(t) \quad d\alpha d\beta, \tag{4.2.4}$$

where $\mu(\alpha,\beta)$ is the Preisach distribution that describes the weight or distribution of each elementary hysteresis with different α and β. The evaluation of Eq. 4.2.4 is best visualized as a contour plot of μ on the Preisach plane with a vertical axis of α and horizontal axis of β, as shown in Fig. 4.2.3(b–f). μ is only defined within the range of $-u_{sat} \le \alpha, \beta \le u_{sat}$ and $\alpha \ge \beta$. Hence, the Preisach plane is triangular.

The Preisach plane is split into two regions: S_+ where $\hat{\gamma}_{\alpha\beta} = +1$, and S_- where $\hat{\gamma}_{\alpha\beta} = -1$. The change in $u(t)$ is represented as the shift in the S_+ and S_- boundaries. For an intuitive illustration of these shifts, we first take the case of a positively saturated state with $u > u_{sat}$ and performing a negative field sweep. Figure 4.2.3(b) shows the saturated state with S_+ covering the full range of μ. The negative field sweep is represented as the boundary shift leftwards as hysterons with $\beta \geq u(t)$ switched, thus giving the new state shown in Fig. 4.2.3(c). In another case of a negatively saturated state with $u < -u_{sat}$ and performing a positive field sweep. Figure 4.2.3(d) shows the saturated state with S_- covering the full range of μ. The positive field sweep is represented as the boundary shift upwards as hysterons with $\alpha \leq u(t)$ switched, thus giving the new state shown in Fig. 4.2.3(e).

The FORC is used to evaluate μ. The FORC is acquired by the combination of a positive field sweep followed by a negative field sweep or vice versa. The first positive field sweep is performed from a negatively saturated state at $u < -u_{sat}$ to a new field we denote as α_1 giving the resulting state as shown in Fig. 4.2.3(e). The positive field sweep is subsequently performed up to β_1, giving the resulting state as shown in Fig. 4.2.3(f). By defining a new function,

$$F(\alpha,\beta) = \left(f_\alpha - f_{\alpha\beta}\right)/2, \tag{4.2.5}$$

where f_α is the state after the first field sweep, and $f_{\alpha\beta}$ is the state after both field sweeps. This function will correspond to the integral of μ enclosed by the yellow triangle indicated in Fig. 4.2.3(f). Hence, $F(\alpha,\beta)$ can be re-expressed as,

$$F(\alpha,\beta) = \int_{\beta_1}^{\alpha_1} \int_{\beta_1}^{\alpha} \mu \, d\beta d\alpha \,, \tag{4.2.6}$$

and derive the characterizing equation of μ,

$$\mu(\alpha,\beta) = -\frac{1}{2}\frac{\partial^2 f_{\alpha\beta}}{\partial\alpha\partial\beta} = -\frac{1}{2}\frac{\partial^2 M}{\partial H_r \partial H}. \tag{4.2.7}$$

Translating from the general Preisach model to magnetic hysteresis, α, β, and $f_{\alpha\beta}$ corresponds to reversal field H_r, sweeping field H, and M, respectively.

The Preisach-Krasnoselskii hysteresis model used here being one of the simplest hysteresis model is unable to fully characterize the complex magnetic texture transitions found in magnetic skyrmion-stabilizing materials. However, even with the deviation in properties between the ideal hysteron to the varied magnetic textures, some information relating to the magnetic texture transitions can still be derived. Chapter 5 aims to unravel the information that would be easily derivable from the FORC data, particularly on magnetic skyrmions.

The deviations in magnetic system from the model include independent binary switching of its constituent parts, with no intermediary states. The approximation of the binary nature of the hysteron to the experimental system remains valid as the perpendicular magnetic domains primarily switches between up or down, with domain walls much narrower than the domain size. Furthermore, magnetic skyrmions exhibit discretised changes in perpendicular magnetization during nucleation and annihilation. The magnetic skyrmions are considered as discrete particle-like reversed domains, as details of the skyrmion structure are not derivable from magnetization data.

It is important to note that analysis performed using FORC uses the change in net magnetization instead of the magnetization magnitude. The macroscopic net magnetization measurement only provides the relative amount of up and down magnetic moments, with no microscopic detail of their distribution and thus the magnetic textures. However, magnetic textures exhibit different magnetization changes under a magnetic field sweep, thus allowing for the derivation of information on magnetic textures, discussed in Chapter 5.

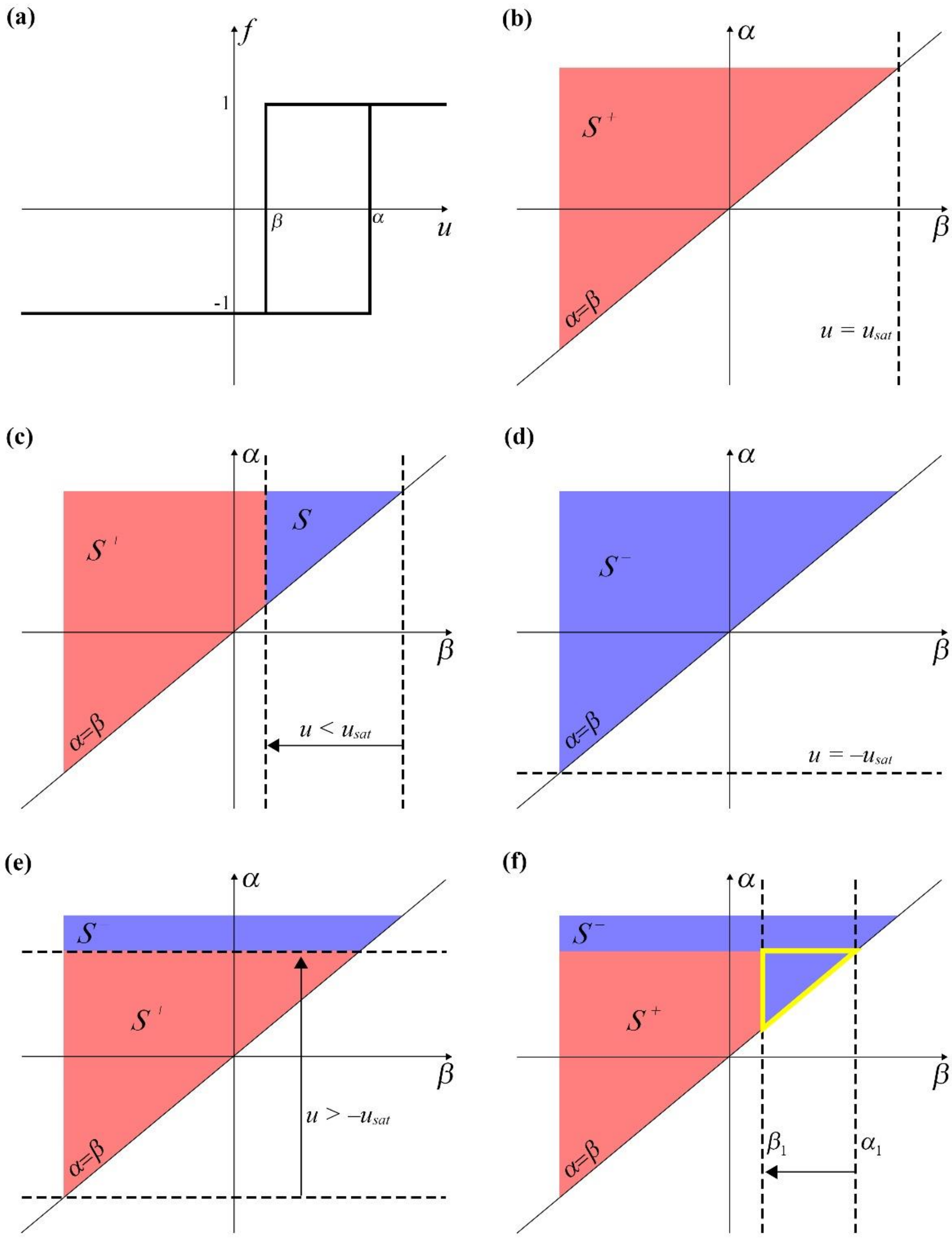

Fig. 4.2.3| (a) Elementary hysteresis element, hysteron. (b-f) Preisach plane at various magnetic state. (b) Positive saturation state. (c) Negative field sweep from positive saturation. (d) Negative saturation state. (e) Positive field sweep from negative saturation. (f) Positive field sweep from negative saturation to α_1 followed by a negative field sweep down to β_1.

4.3 Micromagnetic Simulation

Numerical simulation is an important branch of research investigating complex systems where exact solutions are not readily available and used to elucidate the underlying mechanism of experimentally observed phenomena, like magnetic skyrmions and other nanoscale magnetic textures. For magnetic systems, micromagnetic simulations is a less computationally demanding approach compared to atomistic simulation. In micromagnetic simulations, the material is broken up into cells larger than the atomistic scale. Magnetization is assumed to be uniform within the cell, and all the magnetic interactions are resolved between the cells. Thus, the total number of elements within the simulation can be significantly reduced. However, the range of conditions and limits in which the micromagnetic simulation remains valid shrink by doing so. For instance, frustrated magnets with competing next nearest neighbour interactions cannot be condensed into an effective exchange interaction[15] or investigate skyrmion annihilation via a transitioning state at the atomic scale[16,17]. All the micromagnetic simulation work presented in Chapter 8 was performed using MuMax3[18].

4.3.1 Effective Fields

In this section, we describe the formulism for the magnetic interactions and dynamics used in micromagnetic simulation[18]. Magnetization dynamics is described by the Landau-Lifshitz Gilbert (LLG) equation, given by,

$$\frac{d\vec{m}}{dt} = \gamma \frac{1}{1+\alpha^2}\left(\vec{m}\times\vec{B}_{eff} + \alpha\left(\vec{m}\times\left(\vec{m}\times\vec{B}_{eff}\right)\right)\right), \tag{4.3.1}$$

where $\vec{m}$ is normalized magnetization with magnitude 1, γ is the gyromagnetic ratio, α is Gilbert damping constant, and $\vec{B}_{eff}$ is the effective field. $\vec{B}_{eff}$ is given by the sum of the equivalent fields of all the corresponding magnetic interactions: Heisenberg exchange interaction, magnetostatic interaction, DMI, magnetic anisotropy, externally applied magnetic field. The first term in Eq. 4.3.1 describes the precessional motion of the magnetization around a magnetic field. The second term describes the damping term that gradually aligns magnetization towards the magnetic field and terminates the precessional motion.

The effective field due to Heisenberg exchange interaction $\vec{B}_{exch}$ is given by,

$$\vec{B}_{exch} = 2\frac{A_{ex}}{M_s}\sum_{nn}\frac{\vec{m}_{nn}-\vec{m}}{\Delta_{nn}^2}, \tag{4.3.2}$$

where the summation is performed across all six nearest neighbours of the cell across all three dimensions, $\vec{m}_{nn}$ is the normalized magnetization of the nearest neighbour, Δ_{nn} is the distance between the nearest neighbour cell dependent on the cell dimension. The validity of Eq. 4.3.2 is bounded by small relative angles between the nearest neighbour cells. Thus cell dimensions must be small compared to the exchange length to accurately capture the spatial variation in magnetization[19].

The effective field due to magnetostatic interaction $\vec{B}_{DDI}$, otherwise known as DDI interaction or demagnetization, is given by,

$$\vec{B}_{DDI,i} = M_s\left(\hat{K}_{ij} * \vec{m}_j\right), \tag{4.3.3}$$

where $\hat{K}$ is the DDI kernel. $\vec{B}_{DDI}$ is the most computationally costly part of micromagnetic magnetic simulation due to its long-range nature; each cell interacts with every other cell in the simulation space. Fast Fourier transform (FFT) is used to evaluate the convolution sum of the DDI tensor with magnetization distribution. Equation 4.3.3's validity is limited by the aspect ratio of the cells, as it is computed based on the assumption of constant magnetization across the cell[20,21].

The effective field due to IDMI, $\vec{B}_{DMI}$, is given,

$$\vec{B}_{DMI} = \frac{2D}{M_S}\left(\frac{\partial m_z}{\partial x}, \frac{\partial m_z}{\partial y}, -\frac{\partial m_x}{\partial x} - \frac{\partial m_y}{\partial y}\right), \tag{4.3.4}$$

where D is DMI strength. Equation 4.3.4 is specifically for the case of IDMI where the DMI vector lies within the plane. Like exchange interaction, the accuracy of Eq. 4.3.4 relies closely on the approximation used to compute the gradient values[22,23].

The effective field due to the first order uniaxial magnetic anisotropy is given by,

$$\vec{B}_{Ku} = \frac{2K_u}{M_s}\left(\hat{u} \cdot \vec{m}\right)\vec{u}\ , \tag{4.3.5}$$

where K_u is the uniaxial magnetic anisotropy strength, and $\hat{u}$ is the uniaxial anisotropy axis. Second order uniaxial and cubic anisotropy can also be included, but the role of first-order magnetic anisotropy is sufficient for magnetic skyrmion investigations.

4.3.2 Current Interactions

Magnetic materials can undergo two main electrical current-induced torques: Zhang-Li spin-transfer torque and Slonczewski spin-transfer torque.

Zhang-Li spin-transfer torque refers to the continual exchange of angular momentum from the conduction electron to the local atomic angular momentum as electrical current flow within a ferromagnetic material. As an electron traverse past the first ferromagnetic atom, the electron becomes polarized following the first ferromagnetic atom. When it traverses the second ferromagnetic atom, the electron again becomes polarized following the second ferromagnetic atom, but the angular momentum exchange leaves the second ferromagnetic atom in the state of the first ferromagnetic atom by angular momentum conservation. Thus, the Zhang-Li spin transfer torque results in the translation of non-uniform magnetization in the direction of electron flow. The Zhang-Li spin transfer torque $\vec{\tau}_{ZL}$ is formulated as,

$$\vec{\tau}_{ZL} = \frac{1}{1+\alpha^2}\Big(\left(1+\xi\alpha\right)\vec{m}\times\Big(\vec{m}\times\left(\vec{u}_{ZL}\cdot\nabla\right)\vec{m}\Big)+\left(\xi-\alpha\right)\vec{m}\times\left(\vec{u}_{ZL}\cdot\nabla\right)\vec{m}\Big), \tag{4.3.6}$$

$$\vec{u}_{ZL} = \frac{\mu_B\mu_0}{2e\gamma_0 M_s(1+\xi^2)}\vec{j}\,, \tag{4.3.7}$$

where ξ is the degree of non-adiabaticity, $\vec{u}_{ZL}$ is the spin current density, μ_B is the Bohr magneton, μ_0 is the permeability of free space, e is the elementary charge, and $\vec{j}$ is the current density vector. The first term in Eq. 4.3.6 describes the adiabatic process of nonequilibrium conduction electrons. In contrast, the second term represents the nonadiabatic processes arising from the spatial mistracking of the spins between the conduction electrons and the local magnetization[24].

The Slonczewski spin-transfer torque refers to the torque generated by spin currents injected into the ferromagnetic material. In the early years, spin current injection in magnetic tunnel junctions using electrical currents perpendicular to its structure was of interest. Today, the spotlight is taken over by the spin current injection via the spin Hall effect(SHE). SHE refers to the transverse spin current injected from a heavy metal layer into adjacent ferromagnetic material due to spin-orbit interactions as an unpolarized in-plane current flows through the heavy metal layer. Hence, the torque arising from SHE is also commonly known as spin-orbit torque (SOT) and is given by,

$$\tau_{SHE} = \frac{\mu_B \hbar \theta_{SH} j}{2eM_s d}\left(\vec{m}\times\left(\vec{m}\times\hat{\sigma}\right)\right), \tag{4.3.8}$$

where $\hbar$ is the reduced Planck's constant, θ_{SH} is the spin Hall angle, j is the magnitude of unpolarized current injection in the heavy metal layer, d is the ferromagnetic layer thickness, and $\hat{\sigma}$ is the injected spin current polarization direction.

References

1 J. E. Greene. Review Article: Tracing the recorded history of thin-film sputter deposition: From the 1800s to 2017. *Journal of Vacuum Science & Technology A* **35**, 05C204, doi:10.1116/1.4998940 (2017).

2 P. J. Kelly & R. D. Arnell. Magnetron sputtering: a review of recent developments and applications. *Vacuum* **56**, 159-172, doi:10.1016/S0042-207X(99)00189-X (2000).

3 J. C. Sellers. The disappearing anode myth: strategies and solutions for reactive PVD from single magnetrons. *Surface and Coatings Technology* **94-95**, 184-188, doi:10.1016/S0257-8972(97)00438-6 (1997).

4 P. Mareš, S. Kadlec, M. Dubau, *et al.* Long-term stability and disappearing anode effects during reactive DC and pulsed bipolar magnetron sputtering of Al_2O_3. *Vacuum* **173**, 109161, doi:10.1016/j.vacuum.2019.109161 (2020).

5 Z. Q. Qiu & S. D. Bader. Surface magneto-optic Kerr effect (SMOKE). *J. Magn. Magn. Mater.* **200**, 664-678, doi:10.1016/S0304-8853(99)00311-X (1999).

6 Z. Q. Qiu & S. D. Bader. Surface magneto-optic Kerr effect. *Review of Scientific Instruments* **71**, 1243-1255, doi:10.1063/1.1150496 (2000).

7 in *Classical Optics and its Applications* (ed Masud Mansuripur) 166-181 (Cambridge University Press, 2009).

8 N. Qureshi, H. Schmidt & A. R. Hawkins. Cavity enhancement of the magneto-optic Kerr effect for optical studies of magnetic nanostructures. *Appl. Phys. Lett.* **85**, 431-433, doi:10.1063/1.1774276 (2004).

9 D. Kim, Y.-W. Oh, J. U. Kim, *et al.* Extreme anti-reflection enhanced magneto-optic Kerr effect microscopy. *Nat. Commun.* **11**, 5937, doi:10.1038/s41467-020-19724-7 (2020).

10 L. Vistoli, W. Wang, A. Sander, *et al.* Giant topological Hall effect in correlated oxide thin films. *Nat. Phys.* **15**, 67-72, doi:10.1038/s41567-018-0307-5 (2019).

11 P. Bruno, V. K. Dugaev & M. Taillefumier. Topological Hall Effect and Berry Phase in Magnetic Nanostructures. *Phys. Rev. Lett.* **93**, 096806, doi:10.1103/PhysRevLett.93.096806 (2004).

12 C. Franz, F. Freimuth, A. Bauer, *et al.* Real-Space and Reciprocal-Space Berry Phases in the Hall Effect of $Mn_{1-x}Fe_xSi$. *Phys. Rev. Lett.* **112**, 186601, doi:10.1103/PhysRevLett.112.186601 (2014).

13 M. Raju, A. Yagil, A. Soumyanarayanan, *et al.* The evolution of skyrmions in Ir/Fe/Co/Pt multilayers and their topological Hall signature. *Nat. Commun.* **10**, 696, doi:10.1038/s41467-018-08041-9 (2019).

14 N. Kanazawa, A. Kitaori, J. S. White, *et al.* Direct Observation of the Statics and Dynamics of Emergent Magnetic Monopoles in a Chiral Magnet. *Phys. Rev. Lett.* **125**, 137202, doi:10.1103/PhysRevLett.125.137202 (2020).

15 M. Hoffmann, G. P. Müller & S. Blügel. Atomistic Perspective of Long Lifetimes of Small Skyrmions at Room Temperature. *Phys. Rev. Lett.* **124**, 247201, doi:10.1103/PhysRevLett.124.247201 (2020).

16 P. F. Bessarab, G. P. Müller, I. S. Lobanov, *et al.* Lifetime of racetrack skyrmions. *Sci. Rep.* **8**, 3433, doi:10.1038/s41598-018-21623-3 (2018).

17 D. Cortés-Ortuño, W. Wang, M. Beg, *et al.* Thermal stability and topological protection of skyrmions in nanotracks. *Sci. Rep.* **7**, 4060, doi:10.1038/s41598-017-03391-8 (2017).

18 A. Vansteenkiste, J. Leliaert, M. Dvornik, *et al.* The design and verification of MuMax3. *AIP Adv.* **4**, 107133, doi:10.1063/1.4899186 (2014).

19 M. J. Donahue & D. G. Porter. Exchange energy formulations for 3D micromagnetics. *Phys. B (Amsterdam, Neth.)* **343**, 177-183, doi:10.1016/j.physb.2003.08.090 (2004).

20 R. D. McMichael, M. J. Donahue, D. G. Porter, *et al.* Comparison of magnetostatic field calculation methods on two-dimensional square grids as applied to a micromagnetic standard problem. *J. Appl. Phys.* **85**, 5816-5818, doi:10.1063/1.369929 (1999).

21 S. Lepadatu. Efficient computation of demagnetizing fields for magnetic multilayers using multilayered convolution. *J. Appl. Phys.* **126**, 103903, doi:10.1063/1.5116754 (2019).

22 F. Hellman, A. Hoffmann, Y. Tserkovnyak, *et al.* Interface-induced phenomena in magnetism. *Reviews of Modern Physics* **89**, 025006, doi:10.1103/RevModPhys.89.025006 (2017).

23 A. N. Bogdanov & U. K. Rößler. Chiral Symmetry Breaking in Magnetic Thin Films and Multilayers. *Phys. Rev. Lett.* **87**, 037203, doi:10.1103/PhysRevLett.87.037203 (2001).

24 S. Zhang & Z. Li. Roles of Nonequilibrium Conduction Electrons on the Magnetization Dynamics of Ferromagnets. *Phys. Rev. Lett.* **93**, 127204, doi:10.1103/PhysRevLett.93.127204 (2004).

Chapter 5 Temperature-modulated magnetic skyrmion phases and transformations analysis from first-order reversal curve study

In this chapter, we establish a new skyrmion phase characterization technique using the FORC technique. We first investigate the change in skyrmion stability and phase with increasing temperature using *in situ* magneto-optical Kerr imaging and electrical Hall measurements. After determining the temperature range under study encompasses the critical transition from isolated skyrmions to a closely packed skyrmion lattice, the magnetization FORC was performed via electrical Hall measurements. The correlation between magnetic texture transformations and the FORC distribution features was then established at not only the reversal field, but also the sweeping field that is commonly neglected in analyses. Thus, allowing for an intuitive way of interpreting the otherwise abstract FORC distribution data. This new interpretation of FORC distribution features was then demonstrated to be applicable in identifying skyrmion phases.

5.1 Introduction

FM-HM multilayers commonly stabilize magnetic skyrmions at room temperature as strong IDMI is induced at the FM/HM interface with strong spin-orbit coupling[1,2]. By having many repeats of these FM/HM layers in a stack, DDI is enhanced to stabilize the magnetic skyrmions further[3,4].As the stabilization of the magnetic skyrmion primarily depends on the energy cost of the twisting segment of its structure, the skyrmion stability parameter $\kappa = \pi D / 4\sqrt{A_{ex} K_{eff}}$ derived from domain wall energy given in Eq. 3.1.11 is commonly used to characterize the stability of magnetic skyrmions in these materials[5,6]. As D increases and κ approaches unity, skyrmions become increasingly favourable and exist as isolated skyrmions. However, above unity, the domain wall energy becomes negative, resulting in the proliferation of skyrmions in a packed or lattice configuration[6-8]. Prior studies had reported the tuning of κ via the composition and structure of the multilayer[1,9], and temperature[10,11].

The FORC technique uses a combination of reversal field, sweeping field, and magnetization data to determine irreversible domain transitions. FORC is especially suitable for the characterization of magnetic skyrmions as it reveals magnetic states and transitions that are imperceivable in a major hysteresis loop or even by optical imaging techniques[12]. The FORC technique had been applied to maximize zero-field skyrmions based on the projected FORC distribution peaks onto the reversal fields previously[13,14]. A recent work extended its use to determine a pure Néel skyrmion structure from the disappearance of the FORC distribution trough[15]. Several earlier works investigating similar bubble-stripe transitions attributed the FORC features to the fracturing of magnetic stripes and the skyrmion annihilation at the reversal field[12,16,17]. However, these analyses remain limited to the reversal field or a particular feature, leaving the sweeping field unexplored and its associated information about the system hidden.

In this work, we report the analysis of skyrmion transformations across both the reversal field and the sweeping field using Hall voltage measurement and *in situ* MOKE imaging. The domain transformation processes associated with each FORC distribution peak were identified and proved to be consistent across the skyrmion phases from isolated skyrmion to skyrmion lattice. Furthermore, the divergence in domain-domain separation from its terminal separation in the labyrinth state was revealed as the other vital phenomena determining the FORC features. In addition, a model characterized by the FORC distribution peaks was developed to describe the transformations with increasing κ from which the skyrmion phase and other useful field ranges can be deduced.

5.2 Experimental Details

The material stack used in this experiment, Ta(5)/ Ir(2)/ [Pt(1)/ Co(0.5)/ Fe(0.5)/ Ir(0.8)]$_2$ /Ta(5) (nominal layer thicknesses in nanometers) was chosen for the strong additive IDMI by both the Pt/Co and Fe/Ir interfaces[1]. A thermally oxidized silicon wafer was used as the substrate. The material stack was deposited at room temperature using a magnetron sputtering system (AJA ATC-Orion 8) with a base pressure of 8×10^{-8} Torr or better. Pt, Ta, Ir, and Fe were deposited via direct current (DC) at sputtering pressure of 2.0 mTorr and deposition rates of 0.68, 0.62, 0.37, 0.30 Å/s, respectively. Co was deposited via RF current at sputtering pressure of 3.0 mTorr and deposition rate of 0.26 Å/s. The top and bottom Ta(5) layers were deposited as a protective layer against oxidation and adhesion, respectively. The additional Ir underlayer was added to provide a similar interface for the repeating layers. The Hall cross device with 20 μm × 10 μm widths was subsequently fabricated using a combination of EBL (Raith e-line) and ion milling (AJA ion milling system with Hiden SIMS element detector) techniques.

Magnetic domain imaging was performed using the MagVision Kerr Imaging System, which operates on MOKE. The out-of-plane magnetization is probed in the polar configuration and observed as different brightness levels in the image. Regions of lower brightness correspond to magnetization in the negative out-of-plane direction and vice versa. In addition, the images' colour balance had been adjusted to offer the best contrast for qualitative analysis.

The out-of-plane magnetization used for FORC measurements was measured electrically by Hall voltage induced by AHE across the Hall cross. Lock-in detection of Hall voltage was used to optimize the signal-to-noise ratio. A weak sensing current with the current density of 2.3×10^{9} A/m^2 was used to probe the magnetization and was verified by MOKE images to cause a negligible effect on the magnetic domains.

Electrical measurements and MOKE imaging were performed *in situ*. However, a long exposure time was required to acquire a sufficiently clear MOKE image. Hence, the MOKE images for the hysteresis were taken with stepwise changes in the out-of-plane field instead of a continuous field sweep. For each of the images taken for the FORC sweep, the complete sequence magnetic field sweep from the positive saturation field to the reversal field and up to the desired final field was performed before a MOKE image is taken.

Temperature modulation was performed using a proportional–integral–derivative (PID) controlled thermoelectric cooler. The thermoelectric cooler was secured directly beneath the sample stage with a thermistor attached to the cooler. A microcontroller, Arduino Nano, was programmed to measure temperature using a pre-calibrated thermistor resistance, perform PID computations to control the output of the thermoelectric cooler, and maintain the desired temperature even with ambient fluctuations. A fluctuation of less than 0.1 °C was held for all measurements. By measuring the sample device resistance, the thermal conductivity from the thermoelectric cooler through the stage to the sample device was verified to be reliable, with thermal equilibrium achieved in seconds.

5.3 Temperature-modulated skyrmion phase transition

First, the supporting evidence for the transition of κ across unity occurring within the small temperature range of 18.0 °C to 26.0 °C investigated is presented. Figure 5.1(a) shows a decreasing enclosed area and gradient of the major hysteresis loop with temperature indicating the anisotropy shift towards the film plane[18-20]. The linearly decreasing saturation Hall voltage with temperature relates to the expected decrease in saturation magnetization with temperature, as shown in Fig. 5.1(b). The magneto-optical Kerr effect (MOKE) images of the demagnetized domains obtained using a decreasing alternating field sweep were analyzed by 2-D FFTs to derive their corresponding domain periodicity shown in Fig. 5.1(b)[21-23]. These results in Fig. 5.1(a) and 5.1(b) are consistent with an increasing κ.

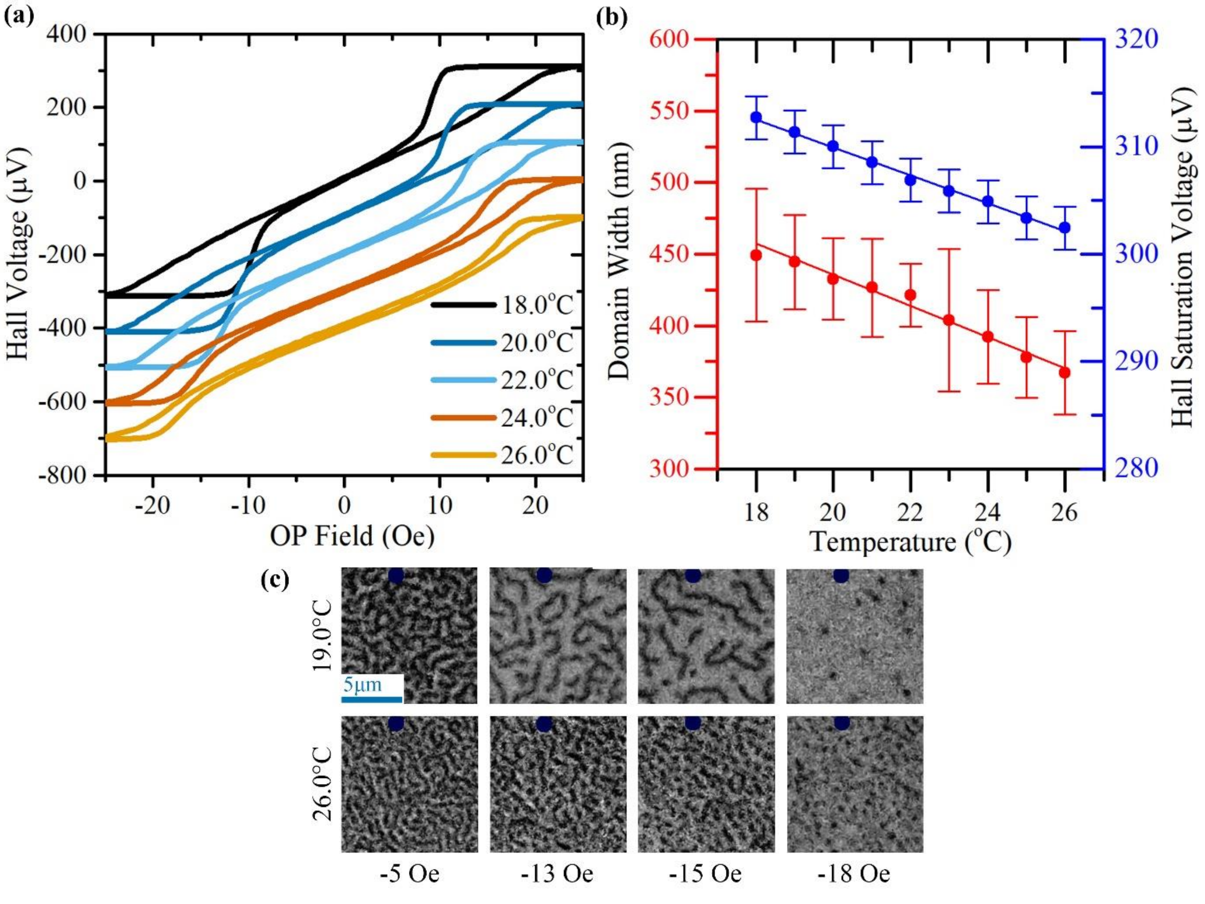

Figure 5.1| (a) Out-of-plane magnetic hysteresis. Each curve has an offset of −100 μV to improve the clarity of the transformation. (b) Plot of domain width of demagnetized domains and saturation Hall Voltages against temperature. (c) MOKE images after a magnetic field sweep from a negative saturated state to the corresponding positive field at the temperature of 19.0 °C and 26.0 °C. Dark blue circles obscure defects to avoid misinterpretation as data[24].

Figure 5.1(c) shows the MOKE images of magnetic domains after the out-of-plane field H_Z was swept from the positive saturation field to their labelled fields at 19.0 °C and 26.0 °C, respectively. At 19.0 °C, the labyrinth domains fracture into long stripe domains, which receded into the isolated skyrmion state with decreasing H_Z. In contrast, at 26.0 °C and H_Z of 5.1 Oe, the domains formed a mix of short stripe segments and skyrmions domains instead of the labyrinth configuration. As H_Z was further decreased, these stripe segments fractured into the densely packed skyrmion lattice configuration. Hence, the temperature range of 18.0 °C to 26.0 °C used in this investigation encompasses the state of isolated skyrmions with $\kappa < 1$ to the skyrmion lattice with $\kappa > 1$.

5.4 First-order reversal curve distribution analysis

FORCs were obtained following the sequence of magnetic field sweeps illustrated in Fig. 5.2(a). To get a single FORC, H_Z is first swept from a large positive field sufficient to attain the saturated state H_{Sat} to the lower or negative reversal field H_R following the blue dashed line shown in Fig. 5.2(a). This field sweep is hereon referred to as the negative field sweep (–FS). From the reversal field H_R, the direction of magnetic field sweep is reversed and swept back to H_{Sat} following the solid red line while measuring magnetization $M\left(H_R, H_Z\right)$. This field sweep is hereon referred to as the positive field sweep (+FS). Multiple FORCs are repeated for the desired H_R range to compute the FORC distribution ρ given by, $\rho = -(\partial^2 M / \partial H_R \partial H_Z)/2$. Irreversible transitions are identified from regions of non-zero ρ on the FORC diagram. ρ is calculated by smoothing and fitting the magnetization data following the locally weighted second-order polynomial regression method^{25}. Smoothing is necessary to overcome the noise in the raw magnetization data, particularly for high resolution reversal field steps that are comparable to the magnetization data's noise. Degree of smoothing was raised up to the point where majority of the noise was removed, with limited loss in signal.

Figure 5.2(b) shows a schematic contour plot of ρ, also known as the FORC diagram, in the negative H_R and H_Z range with the two main features of magnetic skyrmions that are an upper peak and a lower trough-peak pair. Figure 5.3(a)–(i) show these features translating in the negative H_Z direction with increasing temperature, implying the single remaining peak at 26.0 °C corresponds to the same peak of the trough-peak pair at 19.0 °C^{26}. These irreversible transitions associated with each non-zero ρ feature can only be fully described as the combination of two switching events, one associated with each field sweep. Therefore, the emergence of a peak or trough is analyzed as a cause-effect relation, where a switching event during the –FS alters the subsequent switching event during the +FS.

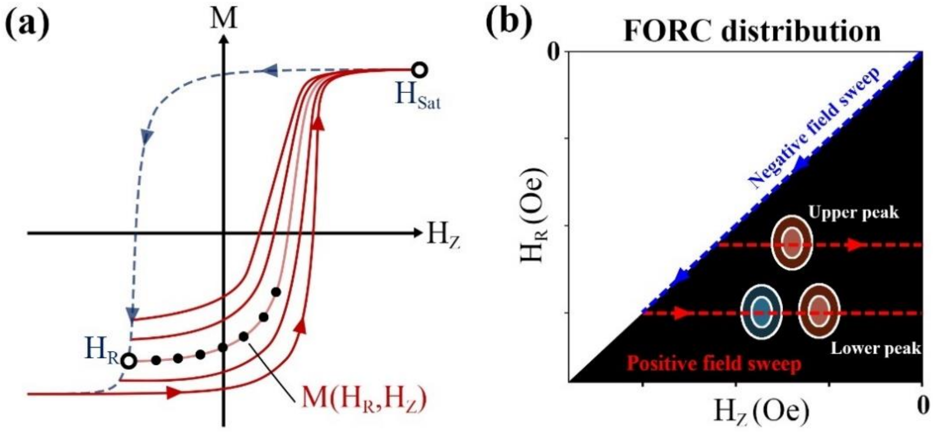

Figure 5.2| (a) Schematic for field sweeps of FORC measurements. (b) FORC distribution contour plot of magnetic skyrmions schematic. The blue and red dashed lines indicate the negative and positive field sweeps of interest for analysis, respectively.

Using *in situ* MOKE imaging, the domain transformations are identified along the three critical magnetic field sweeps indicated in Fig. 5.2(b). The –FS sweep represented as a blue dashed line along the diagonal, and two +FS intersecting the upper peak, and the lower trough-peak pair represented as horizontal red dashed lines. Here, we will focus on demonstrating the consistent domain transformation associated with each FORC feature by comparing the MOKE images at 19.0 °C for isolated skyrmions and 26.0 °C for skyrmion lattice, presented in Fig. 5.4 and 5.6. The same description can also be verified for 23.0 °C, as shown in Fig. 5.5. The FORC diagram, original FORC, and MOKE images are presented in a single figure for a more accessible and intuitive analysis of the FORC features.

The magnetic domains along the –FS down to H_R of the upper peak shown in Fig. 5.4(c) for 19.0 °C and Fig. 5.6(c) for 26.0 °C, both show stripe domains fracturing into shorter segments and skyrmions, leaving a mixture of stripe and skyrmions. However, the domains in Fig. 5.4(c) are far apart with sparse skyrmions. In contrast, skyrmion density is significantly larger in Fig. 5.6(c) and maintains domain-domain separation close to its terminal separation. Terminal separation refers to the minimum stable gap between skyrmions or stripes. This gap is analogous to the domain width approached by the broader domain in a labyrinth with an increasing magnetic field in previous works[22,23]. Under a sufficiently large magnetic field, domain-domain separation diverges beyond this terminal width and approaches saturation. At H_R of the lower peak, Fig. 5.4(c) and 5.6(c) both show the process of skyrmion annihilation from a pure skyrmion state. This process is entirely consistent between both temperatures, but Fig. 5.6(c) shows smaller skyrmions and significantly larger skyrmion density.

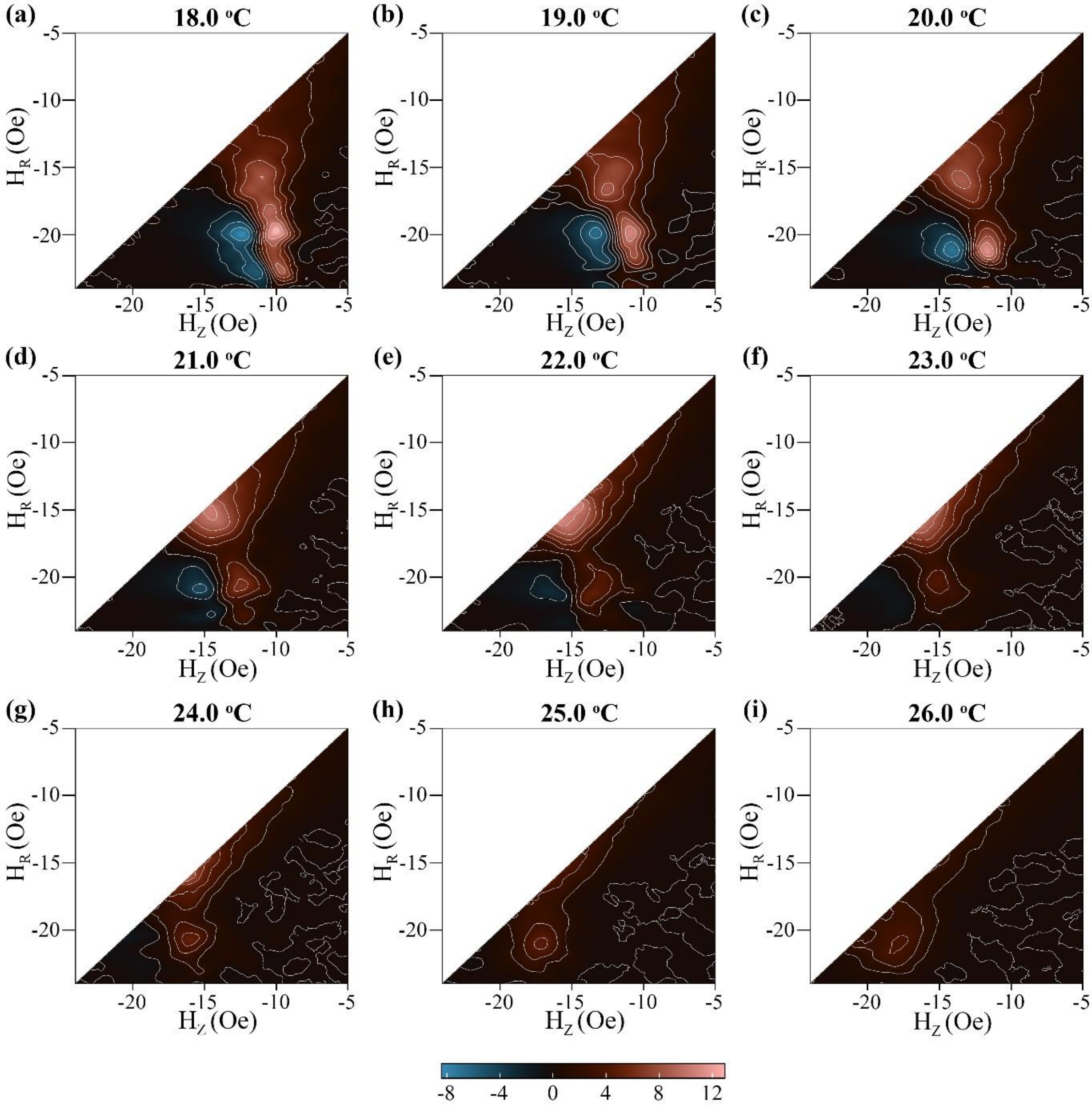

Figure 5.3| Contour plot of FORC distribution at (a) 18.0 °C, (b) 19.0 °C, (c) 20.0 °C, (d) 21.0 °C, (e) 22.0 °C, (f) 23.0 °C, (g) 24.0 °C, (h) 25.0 °C, and (i) 26.0 °C, respectively.

For the +FS along the upper peak from H_R = –16 Oe shown in Fig. 5.4(d) for 19.0 °C and H_R = –15 Oe shown in Fig. 5.6(d) for 26.0 °C, both showed the increase in stripe domains at the expense of skyrmion annihilation as H_Z is swept past the FORC peak. The transformation in Fig. 5.4(d) involves a significant increase in domains as the stripes propagate to fill the gaps between the domains. In contrast, initially close to terminal separation domains showed little change in domain area due to skyrmion-to-stripe transformation in Fig. 5.6(d). A maximum rate of domain propagation is also associated with the field of H_Z = –13 Oe, where ρ is maximum at 19.0 °C.

For the +FS along the lower peak from H_R = –20 Oe shown in Fig. 5.4(e) for 19.0 °C and H_R = –21 Oe shown in Fig. 5.6(e) for 26.0 °C, both transformations began from a pure skyrmions state at their H_R and subsequently approached the terminal separation as H_Z was swept across the FORC peak. However, at 19.0 °C, the skyrmions elongate into stripe domains to fill the sample and approach terminal separation, as shown in Fig. 5.4(e). In this process, the skyrmions were annihilated by transformation into stripes resulting in negligible skyrmion density at the final field. In contrast, skyrmion nucleation occurred to fill the gaps at 26.0 °C, as shown in Fig. 5.6(e). For the FORC trough found at 19.0°C with H_R = –20 Oe, no significant change to the initial pure skyrmions state was observed for H_Z < –15 Oe. As H_Z was further increased, transformations shown in Fig. 5.4(e) commenced in tandem with the emergence of the trough.

The FORC plot as colored lines based on ρ in Fig. 5.4(a) shows that the peaks and trough arise from the convergence and the divergence of the FORCs, respectively. The converging FORCs here correspond to the nucleation of new domains or the propagation of existing domains towards a densely packed state with terminal domain separation as shown in Fig. 5.4(d)–(e), and 5.6(e). The terminal separation state was identified by the uniformity of the domain-domain separation across the sample that converges to the terminal value. There are no wide regions in the ferromagnetic state at terminal separation available for expansion, and domains can only expand by coalescence. The negative FORC distribution trough with diverging FORCs arise due to the skyrmion-to-stripe transformation from a limited number of residual skyrmions being initiated at a higher field than skyrmion nucleation [27]. For low stability skyrmions, skyrmion-to-stripe transformation occurs readily during the +FS before skyrmion nucleation is triggered at lower fields, accounting for most of the magnetization change close to saturation fields. Thus, the further H_R is from the saturation field, the more residual skyrmions are available for skyrmion-to-stripe transformation, leading to the diverging FORCs signature.

Based on the domain image analyses, H_R and H_Z of the peaks correspond to processes across the whole region of non-zero ρ associated with the peak rather than domain states at the peak. The upper peak's H_R corresponds to the fracturing of stripe domains into a mixture of stripes and skyrmions, while the upper peak's H_Z corresponds to the propagation of stripes towards terminal separation. The lower peak's H_R corresponds to the annihilation of skyrmions from a pure skyrmion state, while the lower peak's H_Z corresponds to the skyrmion nucleation or stripe propagation towards terminal separation. Both H_Z peaks represent the transition towards terminal separation, and the domains were observed to reach terminal separation at the edge of the peak where ρ becomes zero.

While previous works had identified the fracturing and annihilation process during the –FS[12-15,28-30], the lack of analysis of the process associated with the +FS can lead to incomplete descriptions of the peaks. One main contradiction is the process of stripe fracturing into multiple shorter segments or skyrmions that continues to occur even when the upper peak had been almost completely translated off the FORC diagram. From the analysis of the sweeping field, the translation of the upper peak towards negative H_Z and its eventual disappearance directly relates to the extent of domain-domain separation divergence from terminal separation even though the process associated with the reversal field continues to occur. The irreversible process of stripe fracturing into skyrmions persisting as seen from their zero-field skyrmion density dependence on H_R with minimal FORC features highlights the limitation of the FORC technique in quantifying microscopic irreversible domain transformations using the macroscopic measurement of magnetization. However, ironically at the same time, demonstrating the high sensitivity of the FORC technique that remains useful even with such a small residual peak.

This FORC analysis can generalized to identify the transition between any magnetic phases within the limits of several requirements. The magnetization response of the magnetic phases under magnetic field sweeps differs and has sufficiently large variation in magnetization to be detected experimentally. Note that the analysis identifies transitions, instead of verifying the type of magnetic texture present directly. Given the requirement of variations in magnetization, the application of this analysis technique to antiferromagnetic or synthetic antiferromagnetic skyrmions will be challenging as they exhibit net zero magnetization. Ferrimagnetic systems with a small uncompensated magnetic moment is expected to generate a similar FORC diagram but signal may be overwhelmed by noise. Alternatively, a SAF structure consisting of a ferromagnetic layer coupled to a rare-earth transition-metal ferrimagnetic layer can produce pronounced anomalous Hall and magneto-optical signal, as reported by Xu et al. recently[31]. The rare earth metal contributes little to the magnetic signal due to their weak coupling with conduction-electron spins, leading to a net electrical and optical signal even with zero net magnetization.

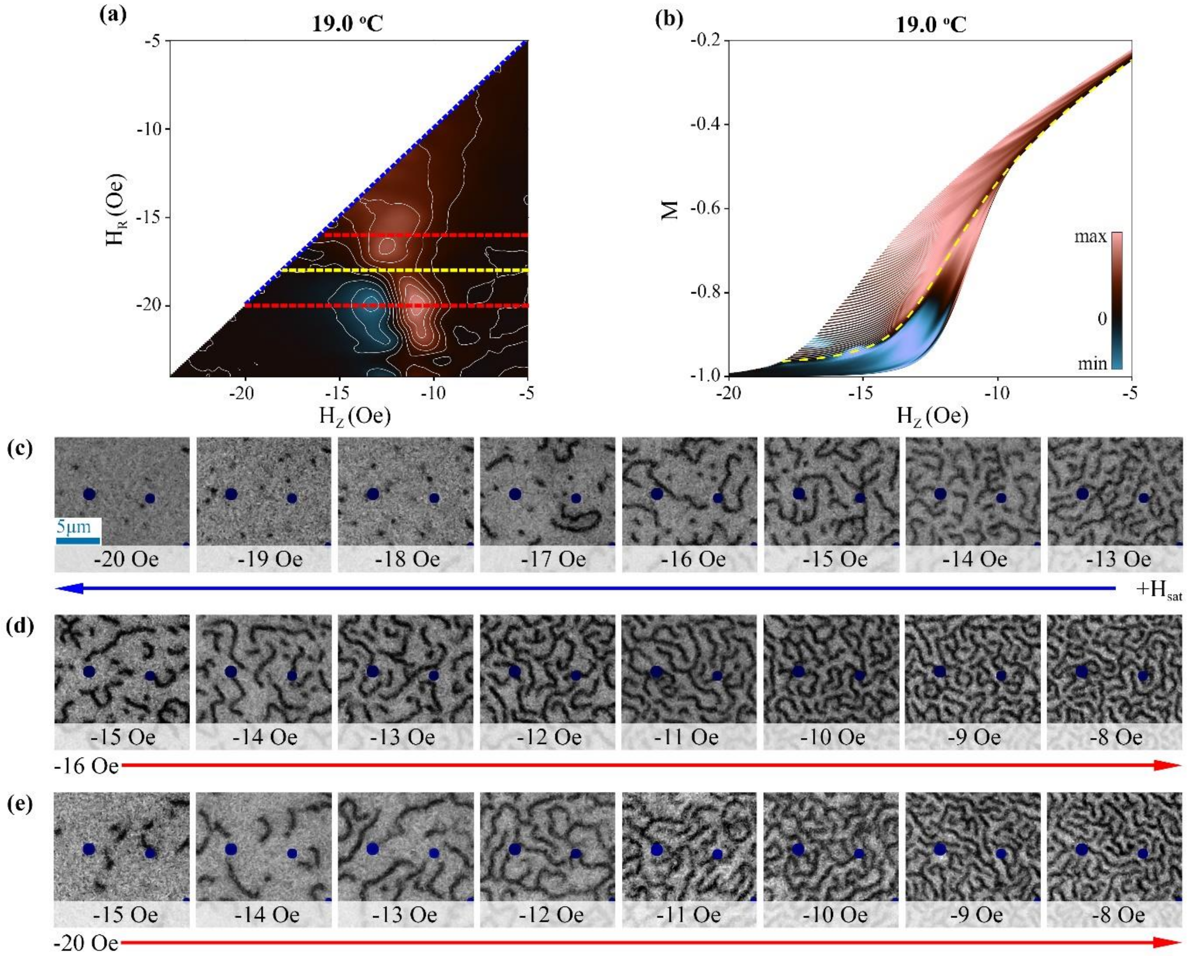

Figure 5.4| (a) Contour plot of FORC distribution at 19.0 °C. The yellow dashed line corresponds to the valley in the FORC distribution. (b) Plot of coloured reversal curves based on the FORC distribution at 19.0 °C. (c) MOKE images during the negative field sweep corresponding to the dashed blue line in (a). (d) MOKE images during the positive field sweep corresponding to the upper dashed red line in (a). (e) MOKE images during the positive field sweep corresponding to the lower dashed red line in (a).

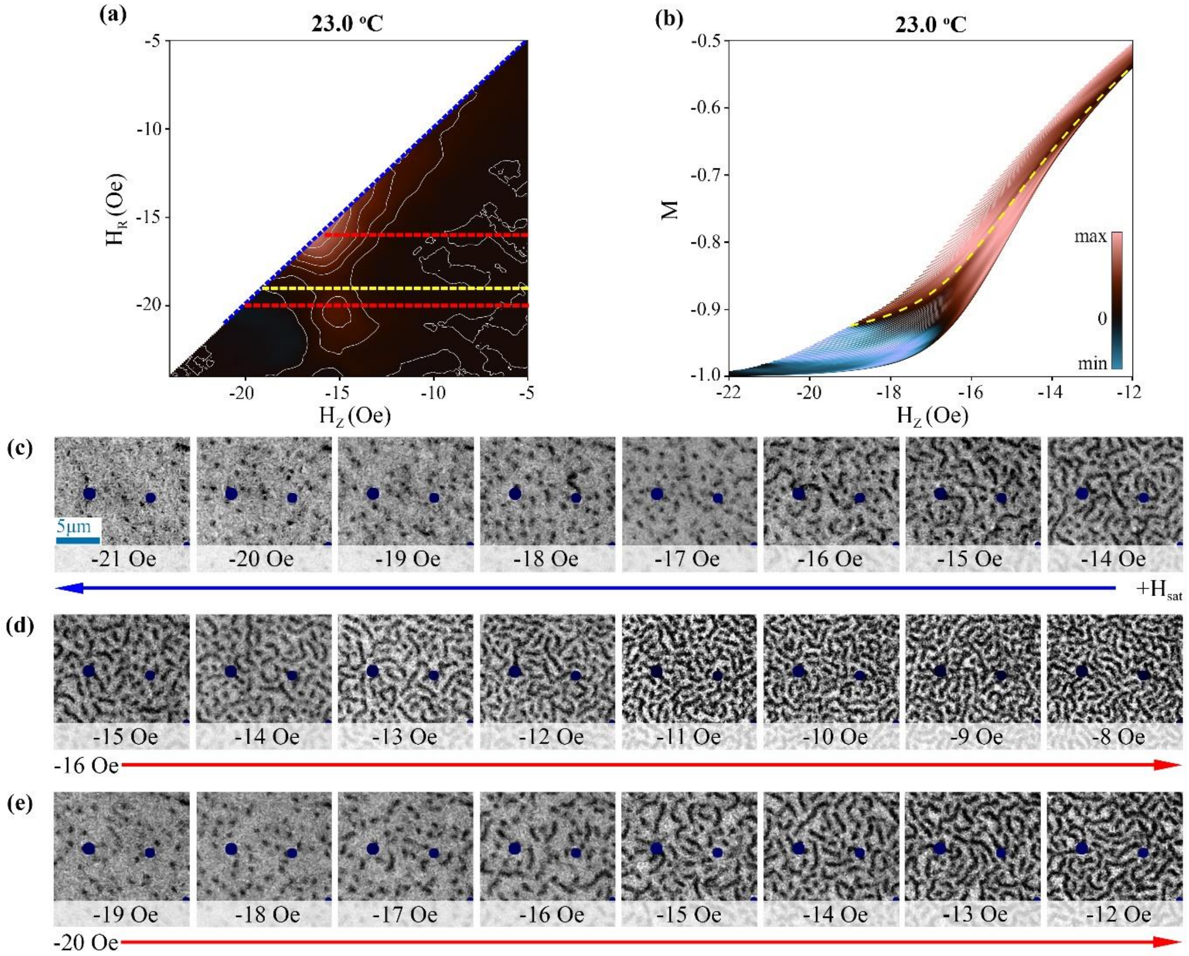

Figure 5.5| (a) Contour plot of FORC distribution at 23.0 °C. The yellow dashed line corresponds to the valley in the FORC distribution. (b) Plot of coloured reversal curves based on the FORC distribution at 23.0 °C. The colour has been normalized to its minimum and maximum FORC distribution magnitude (c) MOKE images during the negative field sweep corresponding to the dashed blue line in (a). (d) MOKE images during the positive field sweep corresponding to the upper dashed red line in (a). (e) MOKE images during the positive field sweep corresponding to the lower dashed red line in (a).

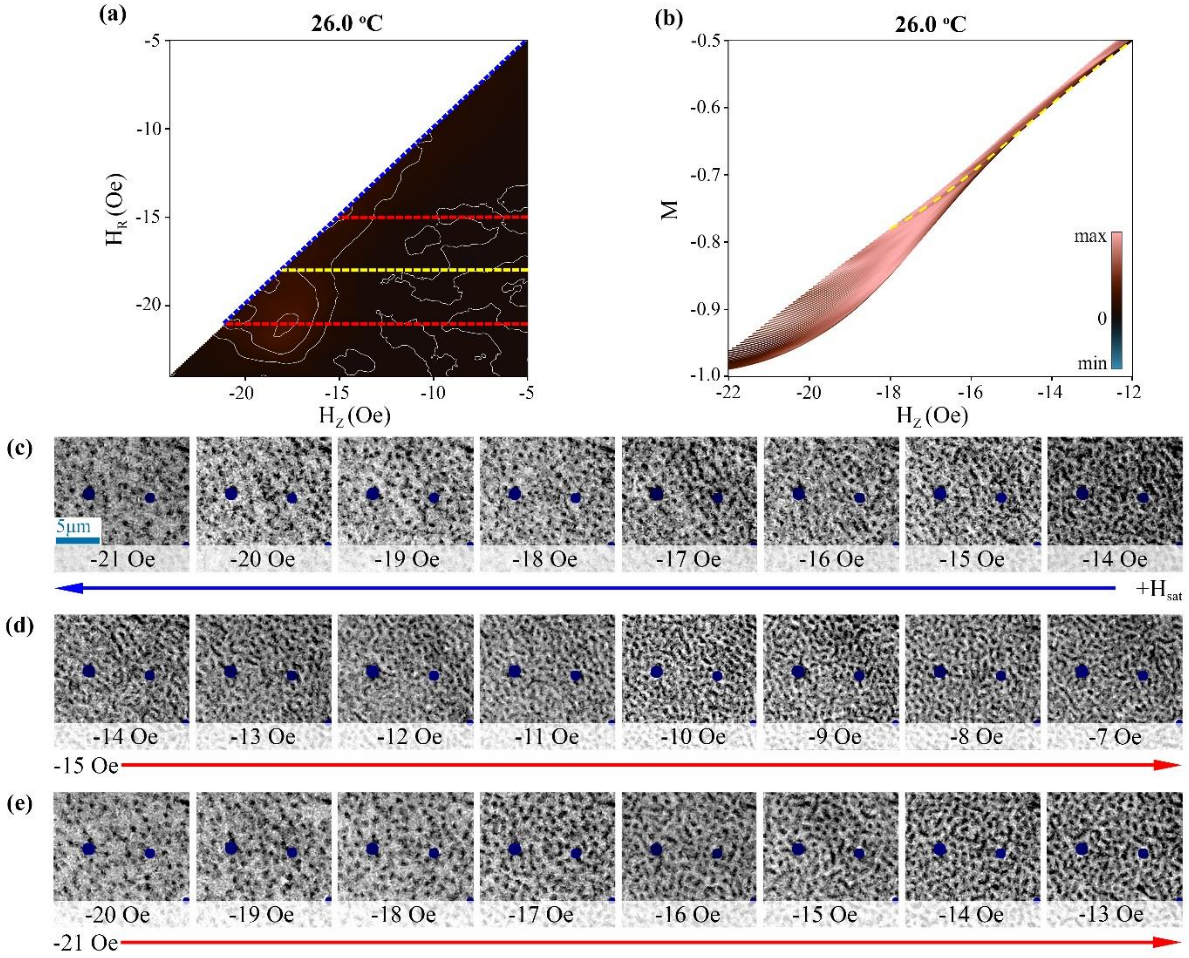

Figure 5.6| (a) Contour plot of FORC distribution at 26.0 °C. The yellow dashed line corresponds to the valley in the FORC distribution. (b) Plot of coloured reversal curves based on the FORC distribution at 26.0 °C. The colour has been normalized to its minimum and maximum FORC distribution magnitude (c) MOKE images during the negative field sweep corresponding to the dashed blue line in (a). (d) MOKE images during the positive field sweep corresponding to the upper dashed red line in (a). (e) MOKE images during the positive field sweep corresponding to the lower dashed red line in (a).

5.5 Skyrmion phase model

Figure 5.7 serves as a valuable model for the changes in the upper and lower FORC distribution peaks with respect to magnetic skyrmion phase and stability. The upper and lower peaks correspond to the FORC distribution peaks on the FORC diagram that occur at the reversal field of approximately 75% of the saturation magnetic field, and 100% of the saturation magnetic field, respectively. From the film's major hysteresis loop, the lower and upper peaks are approximately found at magnetic fields where the magnetization of the forward and backward magnetic field sweep converge, signifying the transition of magnetic textures. The horizontal axis in Fig. 5.7 can be assumed to be analogous with increasing κ, as previously discussed in Chapter 5.3. Note that the coloured bar plotted around the fitted lines are used to signify the peaks corresponding to a specific process, rather than a specific state. The specific range of magnetic fields whereby the process persists can be derived alternatively from the region of non-zero FORC distribution on the FORC diagram.

H_Z of the upper and lower peaks form a pair of linearly decreasing parallel lines, but H_Z of the upper peak converges to its corresponding H_R above the temperature of 22.0 °C. H_R of the lower peak increased and upper peak decreased with temperature respectively at a slow rate. The divergence of the upper peak's H_R and H_Z at lower temperatures is associated with the isolated skyrmion phase. It represents the existence of a field range where domains remain insensitive to field changes and is far from terminal separation after being fractured into shorter stripe segments or undergone skyrmion annihilation. At high temperatures, the translation of the upper peak towards the negative H_Z direction and eventually off the FORC diagram represents the decreasing divergence from terminal separation as domain wall energy decreases, leading to the domains being stabilized up to larger fields. This model applies to the class of magnetic skyrmions stabilized in magnetic multilayers by combining interfacial-DMI and dipolar interactions. These magnetic skyrmions exhibit the state transitions between the labyrinth, stripe, skyrmion, and saturated states with a magnetic field and typically have the bow-tie-shaped major hysteresis loop[1,32].

As the upper peak represents the process of skyrmion fracturing and the lower peak represents the pure skyrmion state, a critical field above which stripes are entirely annihilated lies between them. The valley, which refers to the field of minimum ρ as projected onto the reversal field, showed alignment with the MOKE images for the minimum reversal field for the pure skyrmion state. The lower edge of the bottom peak represents the reversal field for true saturation, where all skyrmions are annihilated. The true saturation field is typically larger than that derived from a major hysteresis loop due to the negligible magnetization signal by residual skyrmions close to saturation. Still, these residual skyrmions can induce clear FORC peaks. Our work provides an intuitive form of analysis for the otherwise abstract FORC distribution and extended the use of FORC to determine skyrmion stability and phase. Using the information of magnetization changes in addition to magnetization magnitude, FORC provides detailed identification of magnetic texture transitions, and their stable magnetic field ranges. While the current work only demonstrates its application on magnetic skyrmions, this analysis can be generalized to magnetic texture transitions that show varied magnetization response.

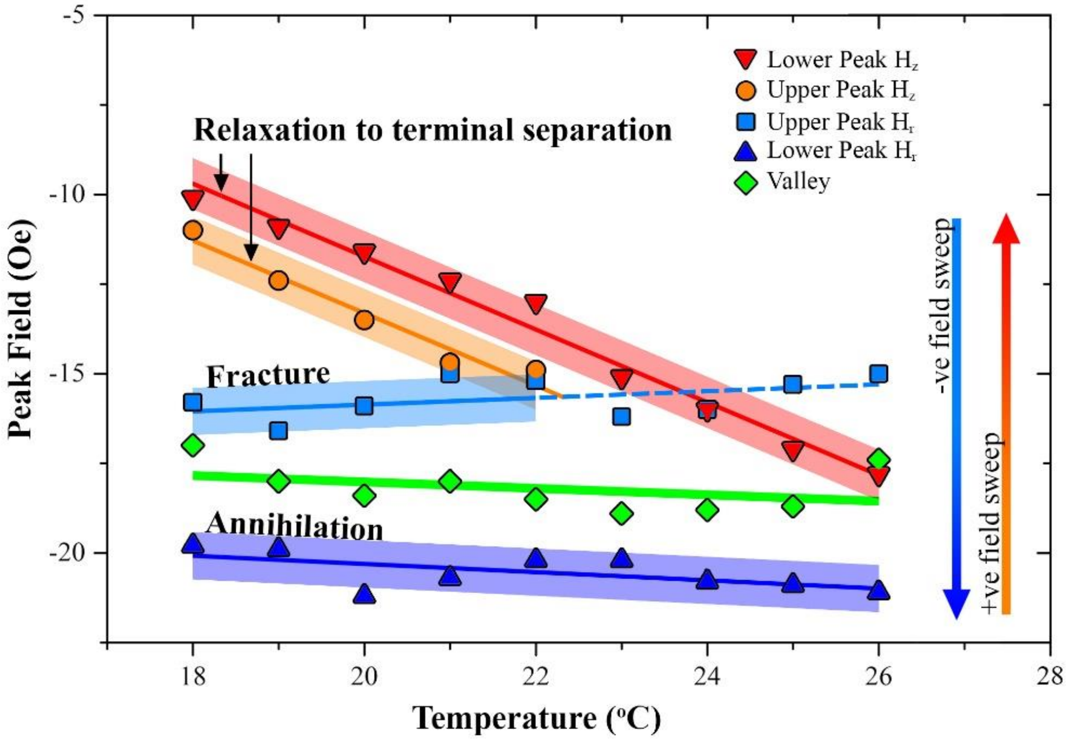

Figure 5.7| Plot of the fields of the FORC distribution peaks against temperature. All plots are linearly fitted. The bars signify the processes occur across a range of field. The valley represents the field of minimum FORC distribution between the peaks as projected onto the reversal field. Above 22 °C, the upper peak's H_Z converges to its H_R plotted as the dotted line.

5.6 Conclusion

In conclusion, we report that the two peaks in the FORC distribution of a skyrmion sample correspond to the fracturing of stripe domains and the annihilation of skyrmions for the upper and lower peak, respectively, at the reversal field. Both the peaks correspond to the propagation and/or nucleation of domains to reach terminal domain separation at the sweeping field. Divergence from terminal domain separation is found to be essential for the microscopic domain transformations to develop macroscopic irreversibility detectable *via* the FORC technique. Based on both the reversal field and sweeping field of the FORC distribution peaks, a model was developed to describe FORCs transitioning from isolated skyrmions to the skyrmion lattice phase. Our study clarifies the significance of the FORC features to characterize skyrmion phases and derive useful magnetic field ranges for the desired magnetic state and transformations, which is beneficial to advancing research on magnetic skyrmions.

References

1 A. Soumyanarayanan, M. Raju, A. L. Gonzalez Oyarce, *et al.* Tunable room-temperature magnetic skyrmions in Ir/Fe/Co/Pt multilayers. *Nat. Mater.* **16**, 898-904, doi:10.1038/nmat4934 (2017).

2 C. Moreau-Luchaire, C. Moutafis, N. Reyren, *et al.* Additive interfacial chiral interaction in multilayers for stabilization of small individual skyrmions at room temperature. *Nat. Nanotech.* **11**, 444, doi:10.1038/nnano.2015.313 (2016).

3 M. Ezawa. Giant Skyrmions Stabilized by Dipole-Dipole Interactions in Thin Ferromagnetic Films. *Phys. Rev. Lett.* **105**, 197202, doi:10.1103/PhysRevLett.105.197202 (2010).

4 I. Lemesh & G. S. D. Beach. Twisted domain walls and skyrmions in perpendicularly magnetized multilayers. *Phys. Rev. B* **98**, 104402, doi:10.1103/PhysRevB.98.104402 (2018).

5 A. Bogdanov & A. Hubert. Thermodynamically stable magnetic vortex states in magnetic crystals. *J. Magn. Magn. Mater.* **138**, 255-269, doi:10.1016/0304-8853(94)90046-9 (1994).

6 S. Rohart & A. Thiaville. Skyrmion confinement in ultrathin film nanostructures in the presence of Dzyaloshinskii-Moriya interaction. *Phys. Rev. B* **88**, 184422, doi:10.1103/PhysRevB.88.184422 (2013).

7 A. Fert, N. Reyren & V. Cros. Magnetic skyrmions: advances in physics and potential applications. *Nat. Rev. Mater.* **2**, 17031, doi:10.1038/natrevmats.2017.31 (2017).

8 A. Siemens, Y. Zhang, J. Hagemeister, *et al.* Minimal radius of magnetic skyrmions: statics and dynamics. *New J. Phys.* **18**, 045021, doi:10.1088/1367-2630/18/4/045021 (2016).

9 T. Srivastava, W. Lim, I. Joumard, *et al.* Mapping different skyrmion phases in double wedges of Ta/FeCoB/TaO$_x$ trilayers. *Phys. Rev. B* **100**, 220401(R), doi:10.1103/PhysRevB.100.220401 (2019).

10 S. Zhang, J. Zhang, Y. Wen, *et al.* Creation of a thermally assisted skyrmion lattice in Pt/Co/Ta multilayer films. *Appl. Phys. Lett.* **113**, 192403, doi:10.1063/1.5053983 (2018).

11 D. A. Garanin, E. M. Chudnovsky, S. Zhang, *et al.* Thermal creation of skyrmions in ferromagnetic films with perpendicular anisotropy and Dzyaloshinskii-Moriya interaction. *J. Magn. Magn. Mater.* **493**, 165724, doi:10.1016/j.jmmm.2019.165724 (2020).

12 A. S. Westover, K. Chesnel, K. Hatch, *et al.* Enhancement of magnetic domain topologies in Co/Pt thin films by fine tuning the magnetic field path throughout the hysteresis loop. *J. Magn. Magn. Mater.* **399**, 164-169, doi:10.1016/j.jmmm.2015.09.040 (2016).

13 N. K. Duong, M. Raju, A. P. Petrović, *et al.* Stabilizing zero-field skyrmions in Ir/Fe/Co/Pt thin film multilayers by magnetic history control. *Appl. Phys. Lett.* **114**, 072401, doi:10.1063/1.5080713 (2019).

14 M. Ma, C. C. I. Ang, Y. Li, *et al.* Enhancement of zero-field skyrmion density in [Pt/Co/Fe/Ir]$_2$ multilayers at room temperature by the first-order reversal curve. *J. Appl. Phys.* **127**, 223901, doi:10.1063/5.0004432 (2020).

15 N. K. Duong, R. Tomasello, M. Raju, *et al.* Magnetization reversal signatures of hybrid and pure Néel skyrmions in thin film multilayers. *APL Materials* **8**, 111112, doi:10.1063/5.0022033 (2020).

16 B. J. Kirby, J. E. Davies, K. Liu, *et al.* Vertically graded anisotropy in Co/Pd multilayers. *Phys. Rev. B* **81**, 100405, doi:10.1103/PhysRevB.81.100405 (2010).

17 J. E. Davies, O. Hellwig, E. E. Fullerton, *et al.* Magnetization reversal of Co/Pt multilayers: Microscopic origin of high-field magnetic irreversibility. *Phys. Rev. B* **70**, 224434, doi:10.1103/PhysRevB.70.224434 (2004).

18 J. Brandão, D. A. Dugato, R. L. Seeger, *et al.* Observation of magnetic skyrmions in unpatterned symmetric multilayers at room temperature and zero magnetic field. *Sci. Rep.* **9**, 4144, doi:10.1038/s41598-019-40705-4 (2019).

19 R. Tolley, S. A. Montoya & E. E. Fullerton. Room-temperature observation and current control of skyrmions in Pt/Co/Os/Pt thin films. *Phys. Rev. Mater.* **2**, doi:10.1103/PhysRevMaterials.2.044404 (2018).

20 M. He, G. Li, Z. Zhu, *et al.* Evolution of topological skyrmions across the spin reorientation transition in Pt/Co/Ta multilayers. *Phys. Rev. B* **97**, 174419, doi:10.1103/PhysRevB.97.174419 (2018).

21 B. Buford, P. Dhagat & A. Jander. Estimating Exchange Stiffness of Thin Films With Perpendicular Anisotropy Using Magnetic Domain Images. *IEEE Magn. Lett.* **7**, 1-5, doi:10.1109/LMAG.2016.2611681 (2016).

22 I. Lemesh, F. Büttner & G. S. D. Beach. Accurate model of the stripe domain phase of perpendicularly magnetized multilayers. *Phys. Rev. B* **95**, 174423, doi:10.1103/PhysRevB.95.174423 (2017).

23 S. Jaiswal, K. Litzius, I. Lemesh, *et al.* Investigation of the Dzyaloshinskii-Moriya interaction and room temperature skyrmions in W/CoFeB/MgO thin films and microwires. *Appl. Phys. Lett.* **111**, 022409, doi:10.1063/1.4991360 (2017).

24 C. C. I. Ang, W. Gan, G. D. H. Wong, *et al.* Electrical Control of Skyrmion Density via Skyrmion-Stripe Transformation. *Phys. Rev. Appl.* **14**, 054048, doi:10.1103/PhysRevApplied.14.054048 (2020).

25 R. J. Harrison & J. M. Feinberg. FORCinel: An improved algorithm for calculating first-order reversal curve distributions using locally weighted regression smoothing. *Geochemistry, Geophysics, Geosystems* **9**, doi:10.1029/2008gc001987 (2008).

26 F. Crameri. Geodynamic diagnostics, scientific visualisation and StagLab 3.0. *Geosci. Model Dev.* **11**, 2541-2562, doi:10.5194/gmd-11-2541-2018 (2018).

27 J. E. Davies, O. Hellwig, E. E. Fullerton, *et al.* Frustration driven stripe domain formation in Co/Pt multilayer films. *Appl. Phys. Lett.* **95**, 022505, doi:10.1063/1.3179553 (2009).

28 A. K. C. Tan, J. Lourembam, X. Chen, *et al.* Skyrmion generation from irreversible fission of stripes in chiral multilayer films. *Phys. Rev. Mater.* **4**, 114419, doi:10.1103/PhysRevMaterials.4.114419 (2020).

29 X. Wang, Y. Wei, K. He, *et al.* Effect of the repeat number and Co layer thickness on the magnetization reversal process in $[Pt/Co(x)]_N$ multilayers. *J. Phys. D: Appl. Phys.* **53**, 215001, doi:10.1088/1361-6463/ab78d7 (2020).

30 D. Toneto, R. B. da Silva, L. S. Dorneles, *et al.* First order reversal curve Hall analysis of zero-field skyrmions on Pt/Co/Ta multilayers. *J. Phys. D: Appl. Phys.* **53**, 395001, doi:10.1088/1361-6463/ab95be (2020).

31 T. Xu, H.-A. Zhou, Y. Dong, *et al.* Fully Compensated Synthetic Antiferromagnets with Pronounced Anomalous Hall and Magneto-Optical Responses. *Phys. Rev. Appl.* **16**, 044056, doi:10.1103/PhysRevApplied.16.044056 (2021).

32 S. D. Pollard, J. A. Garlow, J. Yu, *et al.* Observation of stable Néel skyrmions in cobalt/palladium multilayers with Lorentz transmission electron microscopy. *Nat. Commun.* **8**, 14761, doi:10.1038/ncomms14761 (2017).

Chapter 6 Skyrmion Nucleation and Annihilation via Current-induced Skyrmion- Stripe Transformations

Beyond the skyrmion stability investigation presented in Chapter 5, technological application of skyrmions additionally require reliable techniques to selectively nucleate or annihilate skyrmions, particularly using electrical currents. In this chapter, we investigate the current density-dependent skyrmion-stripe transformation in Pt/Co/Fe/Ir magnetic multilayer to further contribute to the understanding of electrical current-induced skyrmion excitation. High current density pulses induced a densely packed skyrmion state commonly reported in many other studies, and skyrmion nucleation is expected to lessen at a lower current density. However, in the regime where pinning effects became significant, current-induced skyrmion annihilation and skyrmion-to-stripe transformation were observed. Kerr imaging reveals that the rapidly expanding stripes crowd out and annihilate the skyrmions under a low current pulse before quickly decaying and leaving behind a sparse skyrmion population. Our findings establish an additional requirement of minimum operating current density in the design of skyrmionic devices to avoid unintended skyrmion deletion. In addition, this skyrmion annihilation was strategically demonstrated as a technique for skyrmion density control using solely current modulation.

6.1 Introduction

Electrical current has been the primary propagation technique of magnetic skyrmions for their CMOS compatibility and availability of SOT in magnetic multilayers[1-4]. Besides propagation, electrical currents pulses can be used for skyrmion nucleation[1,5-8], annihilation[8], and magnetic texture transformations[7,9,10]. Hence, a comprehensive understanding of all forms of electrical excitations will be necessary for reliable performance. The stripe to skyrmion transformation has been reported in previous works as a skyrmion nucleation technique[1,5-7], where stripe domains are initially nucleated via magnetic field sweeps and subsequently broken into skyrmions by current pulses. In articles reporting the current-induced formation of stripes, these stripes were not shown to be created from skyrmions[9] or investigated at a magnetic field where these stripes show decay into skyrmions thereafter[7,10]. In a recent work, the current-induced skyrmion-to-stripe transformation was reported, but the underlying mechanism remains unclear[11].

In this work, we observed the current density dependence of the current-induced magnetization state transformation. A high current density induced the nucleation of skyrmions whereas, a low current density induced skyrmion-to-stripe transformation and skyrmion annihilation. The conditions required for the low current-induced transformation were millisecond pulses and out-of-plane magnetic fields with a skyrmion ground state. The electrical control of skyrmion density was demonstrated using unipolar current pulses to activate the different current-induced magnetization states by utilizing the observed phenomena.

6.2 Experimental details

Ta(5)/ Ir(2)/ [Pt(1)/ Co(0.5)/ Fe(0.5)/ Ir(0.8)]2/ Ta(5) (nominal layer thicknesses in nanometres) stack was grown on thermally oxidized silicon wafer by magnetron sputtering system (AJA ATC-Orion 8) at room temperature. The base pressure of the vacuum chamber was better than 8×10^{-8} Torr, and a range of sputtering pressures of 2.0 ~ 3.0 mTorr was used during the film deposition. The bottom Ta layer was used as an adhesive underlayer, while the additional Ir(2) underlayer was added to provide a similar interface for the repeating layers. The top Ta(5) layer was used as a protective layer against oxidation. The film stack was patterned into a 20 µm × 10 µm Hall cross structure using EBL and ion milling techniques.

Images of magnetic domains were captured using MagVision Kerr Imaging System, which operates on the magneto-optical Kerr effect in the polar configuration. In the polar configuration, the out-of-plane magnetization was probed and observed as different brightness levels in the image. In the images, regions of lower brightness correspond to magnetization in the negative out-of-plane direction and vice versa. The images' colour balance has been adjusted to offer the best contrast for qualitative analysis.

The four-point configuration was used to measure Hall resistance using Keithley 2401 sourcemeter. The measuring current was passed across the wider bar, while the Hall resistance measurement was performed across the narrow bar. The measuring current had a current density of 1.38 × 10^9 A/m^2 and a duration of 85 ms.

6.3 Electrical current-induced skyrmion-stripe transformation

The patterned Hall cross structure's optical micrograph is shown in Fig. 6.1(a). An out-of-plane magnetic field H_Z of 18.8 Oe was applied to initialize a magnetic state with only skyrmions. Upon applying a magnetic field, the magnetization evolved gradually towards the equilibrium state. The sample was left idle for 3 minutes to reach its equilibrium state. Current density ranging from 1.11 × 10^{10} A/m^2 to 7.75 × 10^{10} A/m^2 was investigated. For each current density, 30 pulses of 10 ms duration were injected across the wide bar, as indicated in Fig. 6.1(a). The subsequent relaxation process after these pulse injections was monitored by the Hall resistance R_{Hall}. A positive ΔR_{Hall} represents an increase in net magnetization in the direction of H_Z and implies the annihilation of stripes or skyrmions and vice versa. The zero level for ΔR_{Hall} is 910 mΩ.

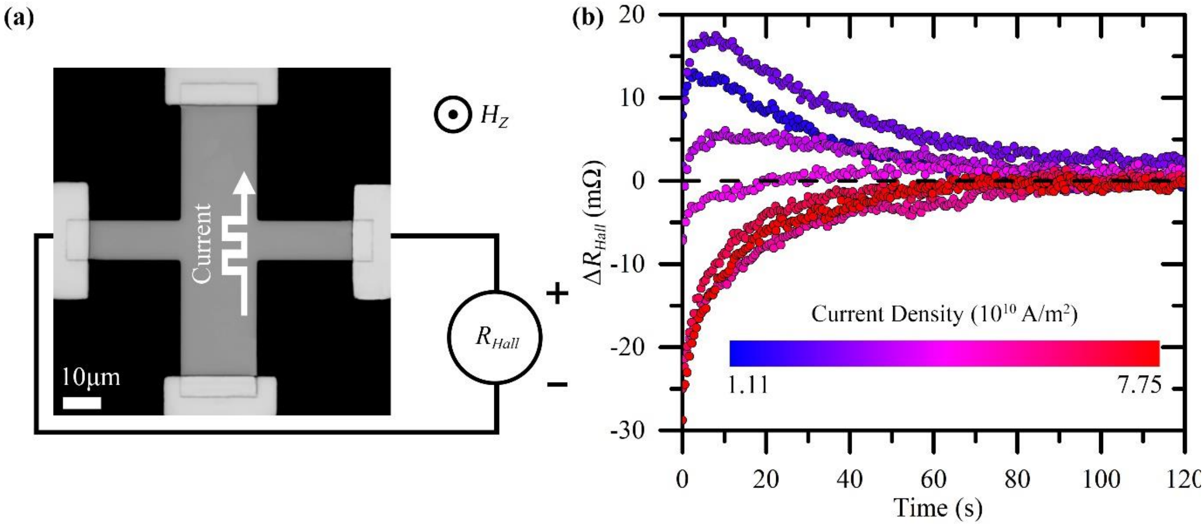

Figure 6.1| Hall resistance measurement of the current-induced magnetization transformation's relaxation process. (a) Measurement setup consisting of a Hall cross with widths of 20 μm and 10 μm. Electrical currents were injected through the wider Hall bar while Hall resistance was measured across the narrow bar. (b) Time evolution of Hall resistance change after 30 current pulses of 10 ms were injected for current densities ranging from 1.11 × 10^{10} A/m2 to 7.75 × 10^{10} A/m^2. Error bars are omitted from the graph for clarity, and the data have a standard deviation of 6 mΩ or less.

The different current-induced magnetization states were deduced based on the ΔR_{Hall} evolution during the relaxation process. From Fig. 6.1(b), the low current density pulses induced a relaxation process with ΔR_{Hall} initially increasing up to a peak before decaying into the final equilibrium state. The highest ΔR_{Hall} peak was observed at the current density of 2.21 × 10^{10} A/m^2. With further current density increase up to 3.32 × 10^{10} A/m^2, the ΔR_{Hall} peak decreased in magnitude and eventually vanished at 3.88 × 10^{10} A/m^2. At current densities larger than 3.88 × 10^{10} A/m^2, ΔR_{Hall} showed a sharp initial drop lower than equilibrium and increased at a decreasing rate towards the equilibrium state. Lastly, ΔR_{Hall} remained almost identical for current densities above 5.54 × 10^{10} A/m^2, suggesting that the current-induced magnetization states and their relaxation process reached a limiting condition.

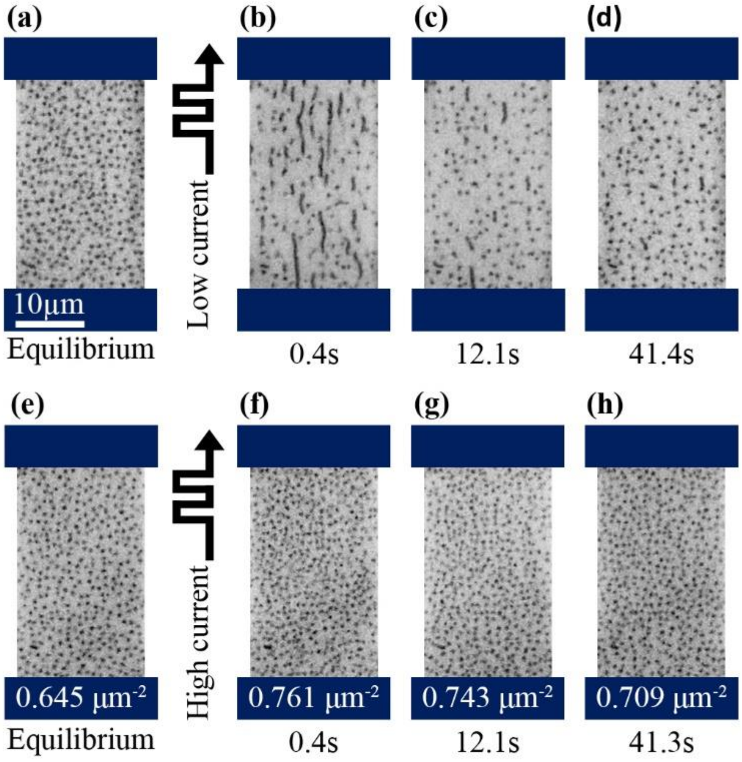

Figure 6.2| MOKE images of current-induced magnetic states and their relaxation process back to equilibrium. (a) Magnetization state at equilibrium. After the injection of 2.21 × 10^{10} A/m^2 current pulses, the skyrmions were transformed into a mixed state of stripes and skyrmions at (b) t = 0.4 s. Magnetization state at (c) t = 12.1 s and (d) t = 41.4 s after current injection. (e) Magnetization state at equilibrium with skyrmion density of 0.645 μm^{-2}. After the injection of 7.20 × 10^{10} A/m^2 current pulses, a state with a higher skyrmion density of 0.761 μm^{-2} was observed at (f) t = 0.4 s. The high skyrmion density state showed a gradual reduction in density at (g) t = 12.1 s and (h) t = 41.3 s, with skyrmion density of 0.743 μm^{-2}, and 0.709 μm^{-2} respectively. The states in (d) and (h) eventually return to the equilibrium state.

Magneto-optical Kerr effect (MOKE) imaging was performed to observe the different current-induced magnetization states' relaxation process dependence on electrical current density. Figure 6.2(a) shows the equilibrium state of the wire where the wire was densely packed with magnetic skyrmions. Figures 6.2(b)-(d) show the MOKE images taken at 0.4 s, 12.1 s, and 41.4 s, respectively, after injecting current pulses of 2.21×10^{10} A/m^2. The pulses decreased skyrmion density and formed stripes simultaneously. These stripes crowded out the skyrmions and annihilated part of the skyrmion population into the ferromagnetic state. These stripes subsequently shrank into skyrmions, leaving behind regions in the ferromagnetic state. With time, the spontaneous nucleation of skyrmions gradually filled the wire, as shown in Fig. 6.2(d), and returned to the equilibrium state. The ΔR_{Hall} peak observed in Fig. 6.1(b) can then be attributed to the two competing processes: the shrinking of stripes into skyrmions that increase R_{Hall}, and the spontaneous nucleation of skyrmions that decrease R_{Hall}.

In contrast, the high current density pulses of 7.20×10^{10} A/m^2 induced the proliferation of skyrmions raising the skyrmion density from 0.645 μm^{-2} to 0.761 μm^{-2} as shown in Fig. 6.2(e) and (f). The skyrmion density gradually reduced to 0.743 μm^{-2} and 0.709 μm^{-2} as shown in Fig. 6.2(g) and (h). This transformation is visually subtle but remains in agreement with the negative initial ΔR_{Hall} results shown in Fig. 6.1(b), representing the nucleation of skyrmions. While a larger current can be expected to nucleate more skyrmions, skyrmion-skyrmion repulsion limits skyrmion density[12,13]. Even though the skyrmion density can be raised above the equilibrium state, it is not stable, and excess skyrmions will annihilate until the equilibrium skyrmion density is reached.

The long time scale of magnetic state transitions is primarily due to the thermally-activated transitions between the ferromagnetic state and skyrmion state. The creeping motion of stripe domains as it shrinks back into skyrmions is also in the time scale of seconds. Still, ultimately the transition time is dominated by the even slower spontaneous nucleation and annihilation of skyrmions.

6.4 Skyrmion transformation dependence on current pulse duration

The wire was initialized following the same procedure as in Section 6.3; an out-of-plane magnetic field of 18.8 Oe was applied and left idle for 3 minutes. However, only a single current pulse was used in this section. While the negative ΔR_{Hall} induced by higher current densities remain observable for pulse durations as short as 10 μs, the ΔR_{Hall} peak associated with lower current densities becomes barely observable for a pulse duration of 1 ms or less. Based on the mechanism of the magnetic texture transformations due to low current excitation revealed in the previous section, the relative magnitude of the ΔR_{Hall} peak correlates to the number of stripe domains formed and the general effectiveness of the low current pulse in decreasing skyrmion density. The ΔR_{Hall} peak increases with pulse duration, as shown in the inset of Fig. 6.3(a). Figure 6.3(a) shows that the maximum ΔR_{Hall} quickly saturates with pulse durations above 10 ms. Comparing Fig. 6.3(b) and (c), the increased ΔR_{Hall} peak corresponded to a lower minimum skyrmion density reached due to the increased number of stripes formed. Figure 6.3(d) showed that the stripe formation does not increase indefinitely and approaches a limiting number of stripes.

In investigating the skyrmion-to-stripe transformation mechanism, the stripes tended to form from several spots on the wire after a low current injection. Also, stripes of differing lengths in the current direction consistently formed from these same spots that correspond to pinning sites. Thus, the stripes formed via skyrmion-pinning site interactions, where a pinned skyrmion at a defect elongate due to the current pulse's propagative force. Similar elongation phenomena were recently reported, where stripes extend from the edges of existing domains using current injections[14,15]. As shown in Fig. 6.3(e), the pinning potential map of the wire was generated using images from 100 iterations of stripe formation cycles. In each iteration, the wire was first left idle to reach equilibrium, followed by injecting a single low current density pulse and imaged once right after. The pinned ends of the stripe domains formed were identified in each image and summed across all iterations to generate an overall spatial pinning potential across the wire.

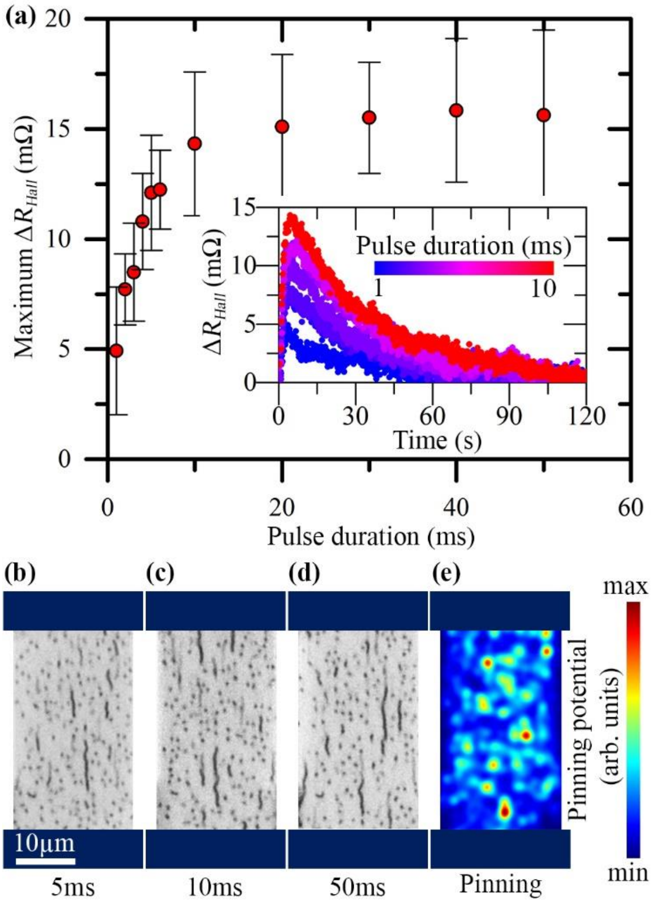

Figure 6.3| Current-induced stripe formation dependence on pulse duration. (a) The plot of maximum Hall resistance change during the relaxation process after low current pulse injection against pulse duration. The inset provides the plot of Hall resistance change over time for pulse durations ranging from 1 ms to 10 ms. Error bars correspond to the standard deviation. MOKE images are taken immediately after current pulse injections with a pulse duration of (b) 5 ms, (c) 10 ms, and (d) 50 ms, respectively. (e) Relative pinning potential along the wire was obtained from 100 images of skyrmion-to-stripe transformation.

6.5 Labyrinth, stripe, and skyrmion current-induced transformation

The observations for the low current density transformation presented thus far had been performed at H_Z of 18.8 Oe, a field close to the saturation field where densely packed skyrmions characterized the ground state. The current-induced transformations were also investigated for the full range of H_Z below saturation, where the ground state ranged from labyrinth domains to stripes and skyrmions. The investigation was executed similarly using 30 pulses of 10 ms at a current density of 2.21×10^{10} A/m^2.

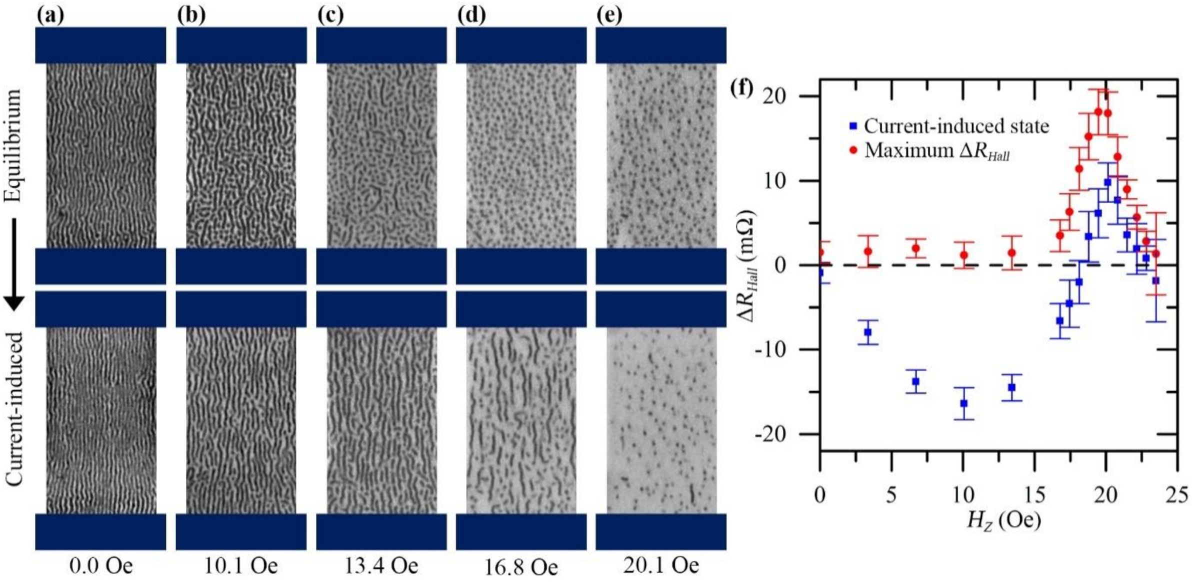

Figure 6.4| Current-induced magnetization state dependence on the out-of-plane magnetic field. MOKE images of their equilibrium and current-induced magnetization state at (a) 0.0 Oe, (b) 10.1 Oe, (c) 13.4 Oe, (d) 16.8 Oe, and (e) 20.1 Oe. (f) The plot of the initial current-induced state's Hall resistance change and its corresponding maximum Hall resistance change during relaxation against out-of-plane magnetic field. Error bars correspond to the standard deviation.

In the absence of an external magnetic field, the ground state of the wire is the labyrinth configuration. Current injection transformed the initial labyrinth domain into parallel stripes aligned in the current direction, as shown in Fig. 6.4(a). Increasing H_Z to 13.4 Oe, skyrmions with diameters of approximately 700 nm started to form while the labyrinth domains break into stripes. In this range of H_Z, the current-induced magnetization states began to form shorter stripes that remain aligned in the current direction, as shown in Fig. 6.4(b) and (c). The current-induced magnetization states formed in the range of 0.0 Oe to 10.1 Oe were stable and did not show significant changes in domain texture over time.

For the H_Z range of 13.4 Oe and 20.1 Oe, the current-induced formation of stripe domains was observed in Fig. 6.4(d) and (e), which then shrank over time into skyrmions by the same process previously given in Fig. 6.2. By comparing Fig. 6.4(d) and (e), fewer and shorter stripes are formed with increasing H_Z. Skyrmion diameter also shrank down to approximately 500 nm. At the saturation field of 23.5 Oe, the current-induced phenomenon was no longer observed due to the immense Zeeman energy that restricted any transformation into other magnetic configurations.

In Fig. 6.4(f), the current-induced phenomena are analyzed quantitatively by comparing the maximum ΔR_{Hall} achieved during relaxation at each magnetic field. A clear peak is found at approximately 20 Oe. A common trend is seen between the current-induced state ΔR_{Hall} and maximum ΔR_{Hall} within the H_Z range of 16.8 Oe and 23.5 Oe. This H_Z range also closely coincides with the diverging segment of the magnetic hysteresis, where irreversible magnetization transformations occur.

6.6 Skyrmion density control

The contrasting magnetization states induced by high and low current density injection present an opportunity for applications in skyrmion density control using a unipolar current. A series of current pulses alternating between low (2.21×10^{10} A/m^2) and high (5.54×10^{10} A/m^2) current density was injected, as shown in Fig. 6.5. The magnetization state can be interchangeably transformed between low and high skyrmion density states by injecting low and high current density currents. Although these states eventually return to the equilibrium state, this technique remains applicable to skyrmions with higher thermal stability and can be used to produce non-volatile state transformations.

Based on the evidence presented above, the skyrmion-to-stripe transformation was found to occur under the condition of i) out-of-plane magnetic field where stripes are unstable, and only skyrmions are stabilized, ii) long pulse duration at the order of milliseconds, and iii) low current magnitude range of 1.11×10^{10} A/m^2 to 3.32×10^{10} A/m^2. Thus, by utilizing this phenomenon, one can achieve two-way skyrmion density modulation under a constant magnetic field.

Pinning sites are expected in materials with Pt/Co due to the sputtering process, defects, its polycrystalline structure, and grain boundaries. As current density increases, the skyrmions are less likely to be pinned, explaining the lack of stripe nucleation at high current density. On the other hand, higher current density injection induces nucleation of skyrmions with a higher density than that of the equilibrium state.

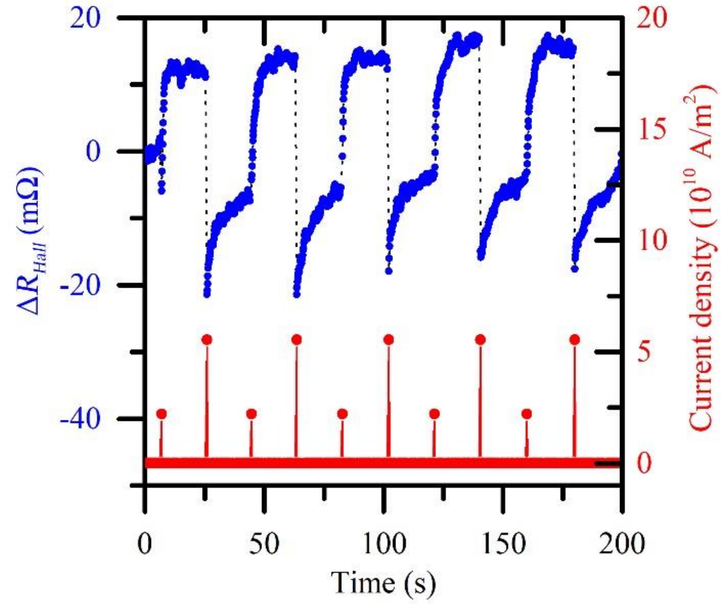

Figure 6.5| Demonstration of electrical control of skyrmion density. The plot of Hall resistance change as a measure of skyrmion density over time due to alternating pulses of low (2.21 × 10^{10} A/m^2) and high (5.51 × 10^{10} A/m^2) current densities.

Joule heating has been closely associated with magnetic texture transformations and skyrmion nucleation in literature[6-8,16,17], but was found to be negligible and not the main contributor to the current-induced skyrmion-to-stripe transformation or current-induced skyrmion annihilation in this work. The current pulses used in the study produced were found to have no measurable increase in temperature. However, by applying a larger pulse width of 352 ms, we could establish an upper bound of 1 K change in temperature, as shown in Fig. 6.6. Hence, the current-induced phenomena observed in this work are unlikely due to Joule heating.

While the skyrmion-to-stripe transformation depends on the current pulse duration in milliseconds, it is due to the slow elongation of the domain in the creep regime. The nucleation mechanism of skyrmions under high current density can be attributed to spin-orbit torque-induced nucleation in non-uniform pinning potential[10,18]. The presence of spin-orbit torque in our multilayer was evident from the current-driven motion of magnetic skyrmions along the current direction, as shown in the supplementary video in Ref[19]. Hence, pinning potential is the critical property involved in skyrmion nucleation, skyrmion annihilation, and skyrmion-to-stripe transformation.

The time scale of magnetic texture transformation shown in Fig. 6.1(b) was intentionally adjusted to the order of seconds and tens of seconds by adjusting the out-of-plane magnetic field and matching the MOKE images' exposure time. With higher out-of-plane magnetic fields, stripe domains become less favourable, as shown in Fig. 6.4(a-e), and the time scale of the transformation decreases. With tuning of the operating out-of-plane magnetic field and fabricating artificial pinning sites, the volatile nature of the stripes formed from skyrmion-to-stripe transformation at a pinning site can be applied in neuromorphic devices. For instance, mimicking a leaky-integrate fire neuron requires the property of potential decay after excitation, and artificial synapses with short-term plasticity where their state is only temporarily retained. Nonetheless, the primary phenomenon raised in the manuscript, skyrmion-to-stripe transformation due to pinning, remains a valuable consideration for the design of future skyrmionic devices.

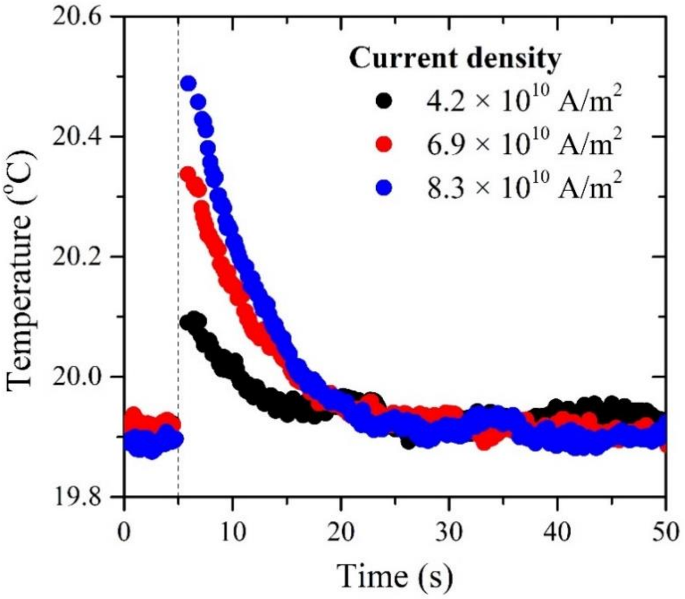

Figure 6.6| Measured device temperature after injection of 352 ms current pulse at different current densities. Temperature between 0.0s to 5.0 s serves as the baseline for the room temperature. The 352 ms current pulse was injected at 5.0s indicated by the vertical dotted line.

6.7 Conclusion

In conclusion, we report the observation of current-induced skyrmion annihilation and skyrmion-stripe transformation at low current density due to pinning effects. By utilizing this phenomenon together with the nucleation of skyrmions at high current density, its application as a technique for skyrmion density control will only require a unipolar electrical current. The current-induced skyrmion annihilation reported here will also bear implications on the operating current densities of future skyrmionic devices where pinning effects are significant. Thus, our study further advances the understanding of current-induced phenomena on magnetic skyrmions to develop future skyrmionic devices.

References

1 W. Jiang, P. Upadhyaya, W. Zhang, *et al.* Blowing magnetic skyrmion bubbles. *Science* **349**, 283, doi:10.1126/science.aaa1442 (2015).

2 S. Woo, K. Litzius, B. Krüger, *et al.* Observation of room-temperature magnetic skyrmions and their current-driven dynamics in ultrathin metallic ferromagnets. *Nat. Mater.* **15**, 501-506, doi:10.1038/nmat4593 (2016).

3 S. Woo, K. M. Song, H.-S. Han, *et al.* Spin-orbit torque-driven skyrmion dynamics revealed by time-resolved X-ray microscopy. *Nat. Commun.* **8**, 15573, doi:10.1038/ncomms15573 (2017).

4 S. A. Montoya, R. Tolley, I. Gilbert, *et al.* Spin-orbit torque induced dipole skyrmion motion at room temperature. *Phys. Rev. B* **98**, 104432, doi:10.1103/PhysRevB.98.104432 (2018).

5 W. Jiang, W. Zhang, G. Yu, *et al.* Mobile Néel skyrmions at room temperature: status and future. *AIP Adv.* **6**, 055602, doi:10.1063/1.4943757 (2016).

6 W. Legrand, D. Maccariello, N. Reyren, *et al.* Room-Temperature Current-Induced Generation and Motion of sub-100 nm Skyrmions. *Nano Lett.* **17**, 2703-2712, doi:10.1021/acs.nanolett.7b00649 (2017).

7 I. Lemesh, K. Litzius, M. Böttcher, *et al.* Current-Induced Skyrmion Generation through Morphological Thermal Transitions in Chiral Ferromagnetic Heterostructures. *Adv. Mater.* **30**, 1805461, doi:10.1002/adma.201805461 (2018).

8 S.-G. Je, M.-S. Jung, M.-Y. Im, *et al.* Electric current control of creation and annihilation of sub-100 nm magnetic bubbles examined by full-field transmission soft X-ray microscopy. *Curr. Appl. Phys.* **18**, 1201-1204, doi:10.1016/j.cap.2018.06.004 (2018).

9 G. Yu, P. Upadhyaya, Q. Shao, *et al.* Room-Temperature Skyrmion Shift Device for Memory Application. *Nano Lett.* **17**, 261-268, doi:10.1021/acs.nanolett.6b04010 (2017).

10 F. Büttner, I. Lemesh, M. Schneider, *et al.* Field-free deterministic ultrafast creation of magnetic skyrmions by spin–orbit torques. *Nat. Nanotech.* **12**, 1040-1044, doi:10.1038/nnano.2017.178 (2017).

11 T. Srivastava, W. Lim, I. Joumard, *et al.* Mapping different skyrmion phases in double wedges of Ta/FeCoB/TaO$_x$ trilayers. *Phys. Rev. B* **100**, 220401(R), doi:10.1103/PhysRevB.100.220401 (2019).

12 S.-Z. Lin, C. Reichhardt, C. D. Batista, *et al.* Particle model for skyrmions in metallic chiral magnets: Dynamics, pinning, and creep. *Phys. Rev. B* **87**, 214419, doi:10.1103/PhysRevB.87.214419 (2013).

13 X. Zhang, G. P. Zhao, H. Fangohr, *et al.* Skyrmion-skyrmion and skyrmion-edge repulsions in skyrmion-based racetrack memory. *Sci. Rep.* **5**, 7643, doi:10.1038/srep07643 (2015).

14 Y. Hirata, D.-H. Kim, S. K. Kim, *et al.* Vanishing skyrmion Hall effect at the angular momentum compensation temperature of a ferrimagnet. *Nat. Nanotech.* **14**, 232-236, doi:10.1038/s41565-018-0345-2 (2019).

15 S. Zhang, X. Zhang, J. Zhang, *et al.* Direct imaging of an inhomogeneous electric current distribution using the trajectory of magnetic half-skyrmions. *Sci. Adv.* **6**, eaay1876, doi:10.1126/sciadv.aay1876 (2020).

16 A. Hrabec, J. Sampaio, M. Belmeguenai, *et al.* Current-induced skyrmion generation and dynamics in symmetric bilayers. *Nat. Commun.* **8**, 15765, doi:10.1038/ncomms15765 (2017).

17 W. Akhtar, A. Hrabec, S. Chouaieb, *et al.* Current-Induced Nucleation and Dynamics of Skyrmions in a Co-based Heusler Alloy. *Phys. Rev. Appl.* **11**, 034066, doi:10.1103/PhysRevApplied.11.034066 (2019).

18 S. Woo, K. M. Song, X. Zhang, *et al.* Deterministic creation and deletion of a single magnetic skyrmion observed by direct time-resolved X-ray microscopy. *Nat. Electron* **1**, 288-296, doi:10.1038/s41928-018-0070-8 (2018).

19 C. C. I. Ang, W. Gan, G. D. H. Wong, *et al.* Electrical Control of Skyrmion Density via Skyrmion-Stripe Transformation. *Phys. Rev. Appl.* **14**, 054048, doi:10.1103/PhysRevApplied.14.054048 (2020).

Chapter 7 Synthetic Antiferromagnetic Skyrmion Dynamics on a Magnetic Anisotropy Gradient

In addition to skyrmion nucleation and annihilation, reliable control of skyrmion mobility is critical to fully exploit their particle-like nature for skyrmionic applications. In this chapter, skyrmion motion driven using voltage-induced magnetic anisotropy gradient was investigated, as an alternative to the conventional electrical current spin torques that require high current densities and face performance deterioration associated with Joule heating. Moreover, the investigation was performed on synthetic antiferromagnetically coupled skyrmions, instead of ferromagnetic skyrmions. An analytical model for an energy-efficient skyrmion propagation in an antiferromagnetically coupled bilayer structure using a magnetic anisotropy gradient was derived. The interlayer skyrmion coupling provides a strong restoring force between the skyrmions, which prevents annihilation and increases their forward velocity up to the order of km/s. For materials with a low Gilbert damping parameter, the interlayer skyrmion coupling force can be amplified up to ten times, with a corresponding increase in velocity. Furthermore, the analytical model also provides insights into the dynamics of skyrmion pinning and the relaxation of asymmetric skyrmion pairs in bilayer-coupled skyrmion systems.

7.1 Introduction

In implementing a magnetic skyrmion racetrack memory, the transport techniques explored thus far have been mainly limited to the use of spin-polarized electrical current injection, which utilizes STT and/or SOT. Experimental transport measurements based on such mechanisms showed that high current densities in the order of 10^{12} A/m^2 are required to achieve practical velocities exceeding 100 m/s[1,2]. The elevated temperatures at such high current densities can drastically reduce skyrmion propagation, and the risk of skyrmion annihilation also increases significantly[3-5].

A wide range of alternative propagation techniques has been proposed to overcome Joule heating and for applications in insulating skyrmions. These alternatives include magnetic field gradients[6-8], electric field gradients[9], temperature gradients[10-12], spin waves, and magnons[13-15]. These systems face various challenges in their implementation and scalability, while spin waves face attenuation and scattering about each skyrmion along a long nanowire. The use of a magnetic anisotropy gradient (MAG) for skyrmion propagation is favoured for its ease of electrical integration and control[16-20]. MAG exerts a force on skyrmions towards regions with lower magnetic anisotropy strength K_u [21-23]. Such a propagation system can be operated using electric fields that can modulate K_u using VCMA[24-26].

In our work, we derive an analytical model for the dynamics of MAG-driven skyrmion pair in synthetic antiferromagnetic (SAF) bilayer structure. The SAF bilayer structure aims to surpass the velocity limit of the monolayer structure due to the skyrmion Hall effect (SKHE)[27-30]. A restoring force that is almost ten times greater than the original driving force generated by the interlayer SAF exchange coupling raises the maximum possible skyrmion velocity to the order of km/s.

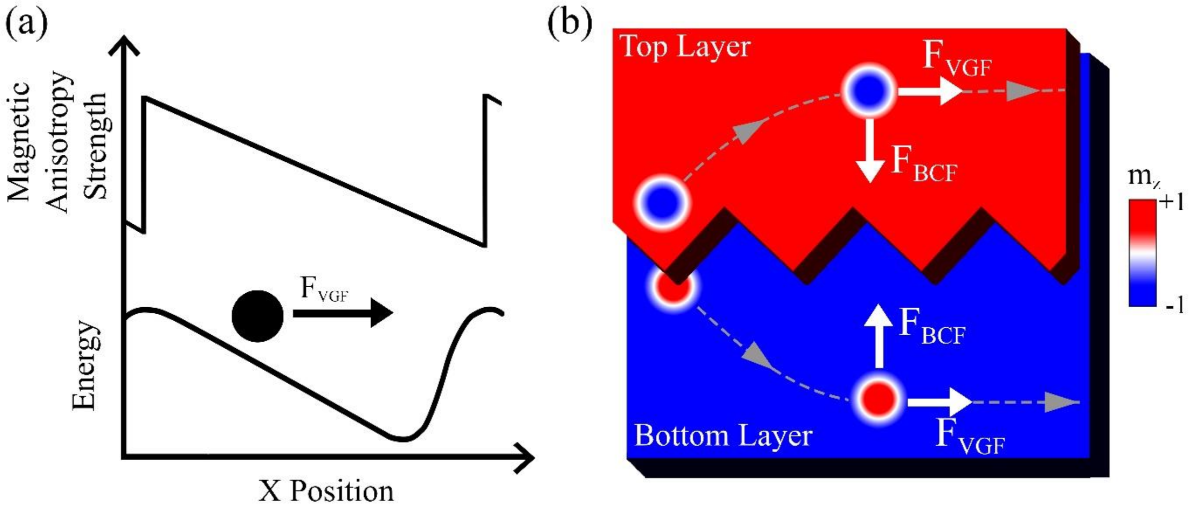

Figure 7.1| Schematic on the operation of a magnetic anisotropy gradient driven skyrmion in a bilayer structure. (a) Magnetic anisotropy strength and energy profile across the wire with a sawtooth configuration to drive the skyrmions. (b) The trajectory of the skyrmions in the bilayer represented in white triangles starts from an overlapping state which then separates and travels parallel to each other at equilibrium velocity. This trajectory is determined by the bilayer coupling force $\vec{F}_{BCF}$ that causes attraction between the skyrmions and the VCMA gradient force $\vec{F}_{VGF}$ that acts along the wire.

The MAG transport scheme operates using a moving MAG generated by external electric fields that shifts in tandem with the magnetic skyrmion to continually exert the MAG force $\vec{F}_{VGF}$ on the skyrmion in the direction of lower K_u, as illustrated in Fig. 7.1(a)–(b). The sawtooth configuration MAG confines the skyrmion within the region of lower K_u as it propagates with the MAG. The moving MAG along the wire can be achieved by applying the corresponding electric field across the region. As this propagation system only utilizes voltage across the track instead of a continuous flow of current for STT or SOT, significant improvement in energy efficiency can be achieved.

Figure 7.1(b) shows that the SAF bilayer structure consists of two antiferromagnetically-coupled FM layers separated by a spacer layer. When driven by $\vec{F}_{VGF}$ along the wire, the skyrmions initially have a diverging trajectory due to the SKHE generated by the gyroscopic force $\vec{F}_g$. The skyrmion in the top and bottom layers carry the same helicity but opposite polarity, resulting in opposite signs of skyrmion topological number N_{Sk} and transverse $\vec{F}_g$. Thus, the top layer's skyrmion is driven towards the upper edge, while the bottom layer's skyrmion is driven towards the lower edge. The bilayer system introduces an attractive bilayer coupling force $\vec{F}_{BCF}$ between the two skyrmions as they are driven apart. The skyrmions achieve steady motion parallel to the wire when the $\vec{F}_g$ that acts perpendicular to velocity is mitigated by $\vec{F}_{BCF}$ and the dissipative force $\vec{F}_d$ that acts against velocity balances $\vec{F}_{VGF}$. Hence, the general trajectory as seen in Fig. 7.1(b) is acquired.

7.2 Numerical methods

Numerical solutions for the skyrmion propagation were evaluated by micromagnetic simulation using MuMax3. Material parameters used for micromagnetic simulation are intralayer exchange stiffness $A_{ex,Intra}$ = 15pJ/m, α = 0.1 , M_s = 580 kA/m, and D = 3 mJ/m. These material parameters are used as the control for investigations on the dependence of skyrmion velocity on individual material parameters. K_u = 0.80 – 1.00 MJ/m^3 values were used across which skyrmions can be nucleated and sustained[31,32]. The interlayer exchange stiffness $A_{ex,Inter}$ was set at the value of 0.45 pJ/m, which is possible by strong antiferromagnetic coupling spacer such as Ru[33-35]. The chosen parameters correspond to the physical system of Pt/Co multilayers[16,31,32].

The simulation cell size was set at 1 nm by 1 nm by 0.4 nm. The bilayer was constructed by having two magnetic layers separated by a non-magnetic layer of 0.4 nm thickness, consisting of material such as Ru or Ir that antiferromagnetically couple the FM layers. The need for an antiferromagnetic coupling layer doesn't necessitate an inverted structure across it. An inverted structure would result in an unwanted opposite IDMI sign for the two FM layers.

Antiferromagnetic coupling remains possible across additional thin layers, allowing for a repeating multilayer for the whole material stack[36].

The MAG is generated stepwise by varying the values of magnetic anisotropy cell by cell along the slope.

7.3 Analytical model for magnetic anisotropy gradient-driven skyrmions

The Thiele equation can model the dynamics of SAF bilayer skyrmions on a MAG proposed above based on the balance of forces acting on the skyrmions. Assuming that the magnetization profile is rigid, the skyrmion's equation of motion can be modelled by the Thiele equation derived from LLG equation[16,37-41]. Recalling the Thiele equation previously discussed in Eq. 3.3.1 is given by,

$$\vec{G}\times\vec{v}-\vec{v}\cdot\overleftrightarrow{D}+\vec{F}_{ext}=0 \ , \tag{7.3.1}$$

where $\vec{G}$ is the gyromagnetic coupling vector, $\vec{v}$ is the drift velocity of the skyrmion's centre of mass, $\overleftrightarrow{D}$ is the dissipative tensor, and $\vec{F}_{ext}$ is conservative external forces acting on the skyrmion. Note that Eq. 7.3.1 differs from Eq. 2 found in Ref.[42] due to differences in the definition of $\vec{G}$ and $\overleftrightarrow{D}$, but both equations are valid and equivalent. The accuracy in quantity of $\vec{G}$ is independent of the Neel or Bloch configuration, but is dependent on the deviations from the assumption of undergoing steady motion at constant velocity without deformation. While $\vec{G}$ is the primary force leading to skyrmion Hall effect, the deformation of skyrmions at high speeds and additional effects like pinning had limited its direct use to determine skyrmion Hall angle as reported in many experimental work[41,43-47].

The first term in Eq. 7.3.1 is referred to as the gyroscopic force $\vec{F}_g$ that acts perpendicular to the direction of propagation $\vec{v}$. This force causes the SKHE that is the deviation in the direction of motion from its driving force. $\vec{F}_g$ is also known as the Magnus force term as it resembles the force generated when a spinning body travels through a viscous fluid that acts perpendicular to the velocity of the body[39,41]. $\vec{G}=(0,0,G)$ for $G=\pm 4\pi N_{sk} M_s d/\gamma$ where d is the magnetic layer thickness, M_s is saturation magnetization, γ is the gyromagnetic. N_{sk} is determined by the combination of skyrmion polarity and helicity. The second term in Eq. 7.3.1 is the dissipative force $\vec{F}_d$ that opposes skyrmion motion. The dissipative tensor is dependent on the details of the skyrmion magnetization profile and $\vec{F}_g$ is described by Eq. 3.3.4 and 3.3.5.

The third term $\vec{F}_{ext}$ describes external forces acting on the magnetic skyrmion and is given by the energy gradient $\vec{F} = -\nabla E$. In this work, $\vec{F}_{VGF}$, and $\vec{F}_{BCF}$ act on the skyrmion pair as shown in Fig. 7.1(b). We will assume the skyrmion pair are far from the wire edge and not included the edge repulsion force in our calculations.

Equation 7.3.1 can be decomposed into two equations given by,

$$Gv_y + D_s v_x = F_x \text{, and} \tag{7.3.2}$$

$$-Gv_x + D_s v_y = F_y \ . \tag{7.3.3}$$

From these two equations, SKHE manifests as a non-vanishing v_y when F_y is zero. Considering a driving force that acts along $\hat{x}$, θ_{sk} is given by,

$$\tan\theta_{sk} = \frac{v_y}{v_x} = \frac{G}{D_s} = \frac{4\pi N_{sk}}{\alpha \iint \partial\vec{m}/\partial x \cdot \partial\vec{m}/\partial x \, dxdy} \ . \tag{7.3.4}$$

In our system of interest, $F_x = \left|\vec{F}_{VGF}\right|$ and $F_y = \left|\vec{F}_{BCF}\right|$. $\vec{F}_{BCF}$ acts between the centre of the skyrmion pair. As the skyrmion pair are driven equally along $\hat{x}$, the skyrmion pair are only displaced along $\hat{y}$, leading to $\vec{F}_{BCF}$ being exclusively along $\hat{y}$. $\vec{F}_{BCF}$ mitigates $\vec{F}_g$ to obtain v_y = 0 m/s. The velocity of the skyrmion parallel to the wire v_x is then given by,

$$v_x = \frac{F_x}{D_s} = -\frac{F_y}{G} \ , \tag{7.3.5}$$

where the ratio of the forces is

$$\left|\vec{F}_{BCF}\right| = \frac{G}{D_s}\left|\vec{F}_{VGF}\right| \ . \tag{7.3.6}$$

From Eq. 7.3.5 and 7.3.6, v_x is dependent on both F_x and F_y. As α is typically small, the ratio of F_y to F_x is large, thus θ_{sk} is large. In our bilayer structure where θ_{sk} = 82.8°, $\left|\vec{F}_{BCF}\right| = 7.95\left|\vec{F}_{VGF}\right|$ and $\vec{F}_{BCF}$ becomes the dominant contributor to v_x. Equation 7.3.5 also shows the inverse relationship between skyrmion velocity and D_s that, in turn, is linear to α. A huge opportunity is presented for material optimization for high skyrmion velocities by being strongly coupled to material parameters.

$\vec{F}_{VGF}$ originates from the inhomogeneous distribution of magnetic anisotropy energy generated using VCMA, and can be quantified by,

$$\left|\vec{F}_{VGF}\right| = -\frac{\partial E_{K_u}}{\partial K_u}\frac{\partial K_u}{\partial x} \text{ and} \tag{7.3.7}$$

$$E_{K_u} = -K_u d \int (1-m_z^2) dxdy, \tag{7.3.8}$$

where m_z is the magnitude of magnetization along $\hat{z}$. From Eq. 7.3.7 and 7.3.8, $\vec{F}_{VGF}$ acts towards the region with lower K_u as observed in the simulation results due to the integral $\int (1-m_z^2) dxdy$ that is dependent on skyrmion size increasing more than linearly with K_u [16]. Thus, $\vec{F}_{VGF}$ also favours and exerts a stronger force on larger skyrmions.

$\vec{F}_{BCF}$ arises from the interlayer exchange coupling of the bilayer skyrmion pair, which forms an energy potential well as a function of the distance between the overlapping skyrmion centres. The potential well provides the restoring force between the skyrmions when they are driven apart. Total exchange energy of the system is given by the integral over the volume of the magnetic layer[48],

$$E_{exchange} = -\int A_{ex} \vec{m} \cdot \left(\frac{\partial^2 \vec{m}}{\partial x^2} + \frac{\partial^2 \vec{m}}{\partial y^2} + \frac{\partial^2 \vec{m}}{\partial z^2} \right) dV \,. \tag{7.3.9}$$

Assuming that the skyrmion profile is rigid, the $\partial^2 \mathbf{m} / \partial x^2$ and $\partial^2 \mathbf{m} / \partial y^2$ terms do not depend on the lateral separation between the skyrmions. Therefore, the interlayer exchange energy E_{BCF} is calculated using only the interaction between the cells directly above or below. $A_{ex,Inter}$ is negative, representing antiferromagnetic coupling. The second-order derivative is then simplified to,

$$E_{BCF} = -A_{ex,Inter} d \int \vec{m}_1 \cdot \left(\frac{\vec{m}_2 - \vec{m}_1}{h^2}\right) dxdy, \tag{7.3.10}$$

where $\vec{m}_1$ is the normalized magnetization on layer 1, $\vec{m}_2$ is the normalized magnetization on layer 2, h is the spacer layer thickness. $\vec{m}_1$ is kept constant while $\vec{m}_2$ is shifted relative to the magnetization of the first layer.

In our analysis, the magnetization profile of the Néel skyrmion $\vec{m} = (m_r, m_\theta, m_z)$ is described in the cylindrical coordinate as it has a radial symmetry which removes its dependence on the azimuthal angle θ. m_r was fitted by the derivative of a Gaussian while m_z was fitted by the Gaussian profile giving,

$$m_r(r) = \frac{r\sqrt{e}}{R} e^{-\frac{r^2}{2R^2}}, \quad m_\theta = 0, \quad m_z(r) = 2^{1-\frac{r^2}{R^2}} - 1, \tag{7.3.11}$$

where r is the radial distance from the centre of the skyrmion and R is the skyrmion radius. Our magnetization profile approximation shows good agreement within the range of K_u investigated. At lower K_u, the magnetization profile deviates from our approximation to resemble that of a chiral bubble domain.

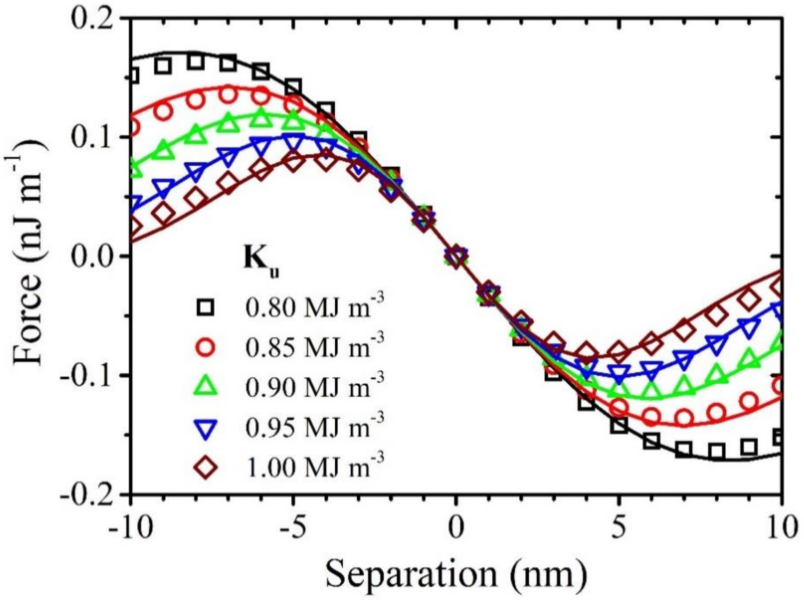

Figure 7.2| Dependence of bilayer coupling force against displacement between the bilayer skyrmions for a range of magnetic anisotropy strength. Numerical results are represented in symbols and the analytical solution given in Eq. 7.3.13 is represented by a solid line.

Using the fitted magnetization profile given in Eq. 7.3.11, the analytical solution derived for E_{BCF} and $\vec{F}_{BCF}$ are,

$$E_{BCF} = -\frac{\pi A_{ex,Inter} d}{2h^2}\left((s^2 - 4R^2) e^{1-\frac{s^2}{4R^2}} + \frac{8R^2}{\ln(2)}\left(2 - 2^{-\frac{s^2}{2R^2}} \right) \right) \text{ and} \tag{7.3.12}$$

$$\vec{F}_{BCF} = \frac{\pi A_{ex,Inter} ds}{2h^2}\left(2^{3-\frac{s^2}{2R^2}} + 2e^{1-\frac{s^2}{4R^2}} - \frac{\left(-4R^2 + s^2\right)}{2R^2} e^{1-\frac{s^2}{4R^2}} \right)\hat{r}, \tag{7.3.13}$$

where s is the bilayer skyrmion pair effective separation. As the skyrmions are driven apart, the skyrmions experience a minor distortion in their profile away from the other skyrmion. s is calculated by taking the weighted position of the skyrmion across its centre.

Figure 7.2 shows the presence of a restoring force. Within the range of s below half their radius, the $\vec{F}_{BCF}$ profile resembles a harmonic oscillator where the gradient is negative and approximately linear. For this range of s, $\vec{F}_{BCF}$ is independent of R and given by,

$$\vec{F}_{BCF} \approx \frac{\pi A_{ex,Inter} d}{h^2}(4+2e^{1})s\hat{r} \ . \tag{7.3.14}$$

As shown in Fig. 7.2, as the bilayer skyrmions are increasingly driven apart by a larger $\vec{F}_g$, $\vec{F}_{BCF}$ reaches a maximum at $s = kR$ where $k = 1.15$ is a dimensionless constant. This is intuitive based on the origin of the force that relies on the skyrmions' overlap that is finite in size. Beyond separation of kR, $\vec{F}_{BCF}$ gradually decreases to zero as the skyrmions become increasingly decoupled and eventually cease to interact with each other for large s. Using Eq. 7.3.14 and $s = kR$, we find the relationship between the theoretical maximum $\vec{F}_{BCF}$ and R is given by,

$$\text{Maximum } \vec{F}_{BCF} \approx 6.65 \times \frac{\pi A_{ex,Inter} Rd}{h^2}\hat{r} \ . \tag{7.3.15}$$

Applying this maximum $\vec{F}_{BCF}$ to Eq. 7.3.5, the theoretical limit in velocity of a skyrmion which is protected from edge annihilation by $\vec{F}_{BCF}$ alone can be derived to be,

$$\text{Maximum } v_x = -\frac{6.65\pi A_{ex,Inter} Rd}{Gh^2} \ . \tag{7.3.16}$$

Using the material parameters considered for this work, the maximum velocity that can be sustained is 10.3 km/s. This maximum velocity can be increased when $\vec{F}_{BCF}$ is complemented by other forces which act towards the centre of the wire, such as edge repulsion force. Edge repulsion force that acts only in the vicinity of the edge requires a wire with a sufficiently thin width to be effective in complementing $\vec{F}_{BCF}$. Enhancement of the edge repulsion force to prevent annihilation can be achieved by engineering the edges using additional magnetic material and VCMA[21,22,49-51].

The closed-form solutions derived here are highly useful in succinctly describing $\vec{F}_{BCF}$ that is essential in SAF skyrmion dynamics. Using these solutions subsequently allow for easy quantitative analysis of skyrmion velocities for different skyrmion sizes and driving forces, and more importantly, the skyrmion velocity limit, in contrast to performing time-consuimg numerical simulations[3].

7.4 Skyrmion velocity dependence on magnetic anisotropy gradient and strength

We investigated the dependence of the skyrmion velocity on MAG and K_u at the centre of the skyrmion. The range of MAG explored ranges from 500 GJ/m^4 to 10 TJ/m^4 which corresponds to a K_u change of 500 J/m^3 and 0.01 MJ/m^3 per nm, respectively. This range is limited by the optimal range of K_u required to stabilize the skyrmions. The size of skyrmions which is dependent on K_u also results in minor expansion of the skyrmions when they are subjected to an increasing MAG.

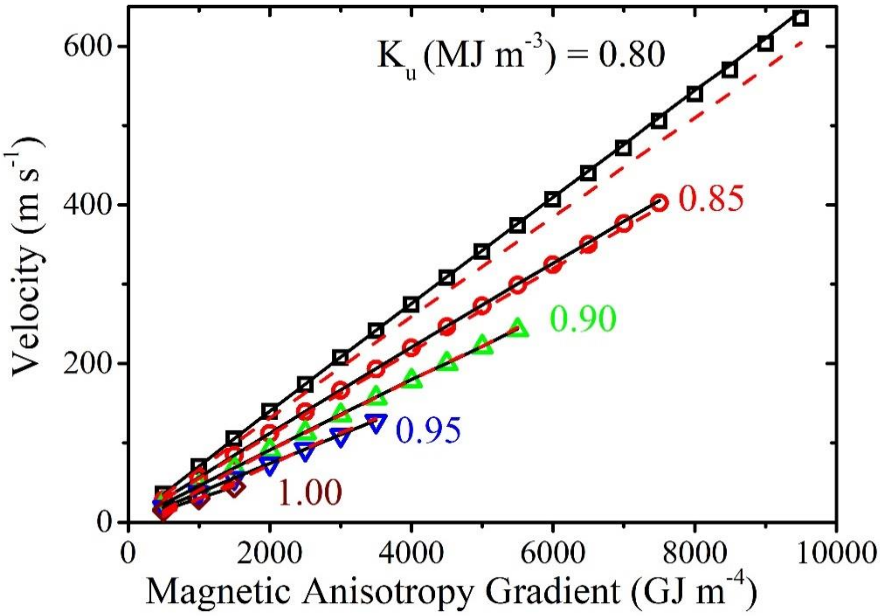

Figure 7.3| Dependence of skyrmion velocity on magnetic anisotropy gradient and strength at the centre of the skyrmion. The solid black line and the broken red line represent the analytical solution derived using the gradient force and bilayer coupling force.

Results presented in Fig. 7.3 verify the linear relationship between skyrmion velocity and K_u gradient shown in Eq. 7.3.7. In addition, Fig. 7.3 shows velocity decrement with increasing K_u magnitude at the centre of the skyrmion due to the reducing $\vec{F}_{VGF}$ and shrinking R discussed previously. The fitted solid and broken line represents the analytical solution derived using $\vec{F}_{VGF}$ and $\vec{F}_{BCF}$ from Eq. 7.3.7 and Eq. 7.3.13, respectively. The accurate agreement between the numerical and analytical solutions supports the validity of our model for both $\vec{F}_{VGF}$ and $\vec{F}_{BCF}$. The accuracy of our model for $\vec{F}_{BCF}$ is limited by the magnetization profile approximation used in Eq. 7.3.11 that is accurate for high K_u skyrmions.

The maximum K_u gradient investigated at 10 TJ/m^4 is possible based on the K_u variation of up to 0.29 MJ/m^3 observed experimentally[52]. This observation has yet to be reported in the system of our interest but nonetheless supports the possibility of realizing such a K_u gradient.

7.5 Skyrmion velocity dependence on the material parameter

MAG-driven skyrmion velocity dependence on α and M_s was investigated at K_u = 0.80 MJ m^{-3} and K_u gradient = 2000 GJ m^{-4}. Figure 7.4 shows the strong inverse relationship between skyrmion velocity and α which is consistent with Eq. 7.3.5. The decrease in α from 0.1 to 0.01 resulted in velocity enhancement from 120 m/s to 1200 m/s shown in Fig. 7.4, surpassing the velocities shown in Fig. 7.3. Even at such velocity, the skyrmion pair remains coupled and protected from edge annihilation. Equation 7.3.16 predicts that $\vec{F}_{BCF}$ can overcome the Magnus force up to the velocity of 10.3 km/s. This relationship makes α a critical material parameter to optimize for higher skyrmion velocity. The range of material parameters investigated was restricted to skyrmions that did not undergo severe deformation during propagation and retained an eccentricity of less than 0.2.

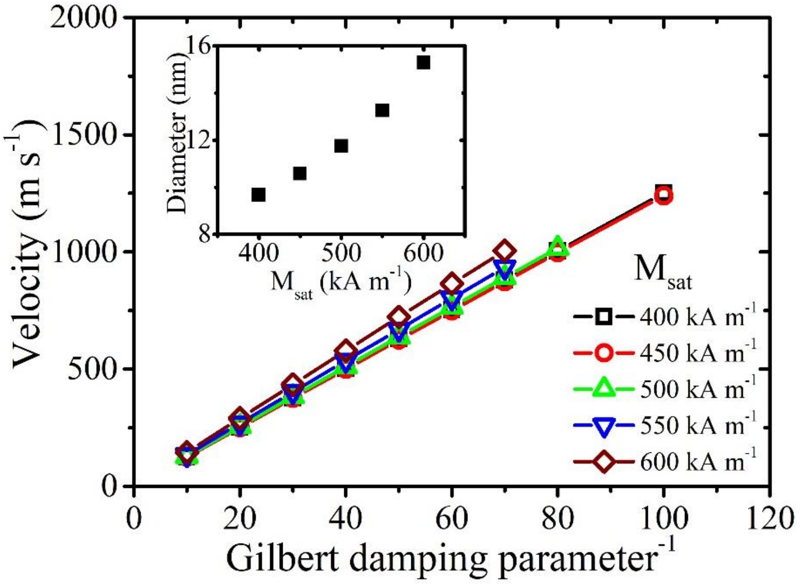

Figure 7.4| Dependence of skyrmion velocity on the inverse of Gilbert damping parameter and saturation magnetization. Inset shows the skyrmion diameter dependence on saturation magnetization.

However, the dependence of skyrmion velocity on M_s is not inversely related, as Eq. 7.3.5 suggests. This disagreement can be explained by the increase in the skyrmion size with M_s and $\vec{F}_{VGF}$. Skyrmion size increases with M_s due to the increase in DDI and decrease in K_{eff}. The inset of Fig. 7.4 shows skyrmion diameter increasing more than linearly with M_s.

Thus, the velocity in Eq. 7.3.5 has a relationship with M_s at the order of more than 1. Hence, skyrmion velocity was observed to increase slightly with M_s.

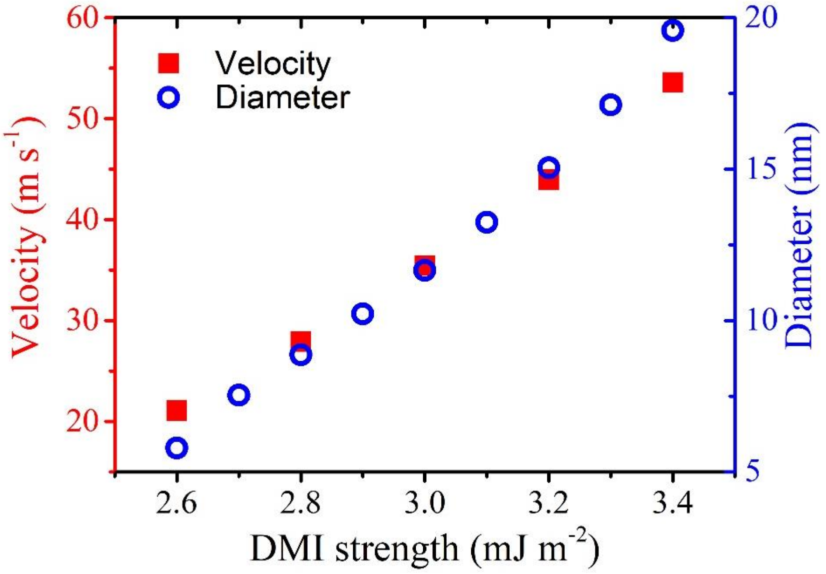

Figure 7.5| Dependence of skyrmion velocity and diameter on DMI strength.

The increase in skyrmion velocity with DMI strength D is due to increased skyrmion diameter like the dependence observed with M_s. While M_s only results in a slight increase in velocity, DMI holds a stronger dependence and results in a more than double velocity increase when D increases from 2.6 mJ/m^2 to 3.2mJ/m^2. However, the magnetic skyrmion is only stable within D of 2.4 mJ m^{-2} to 3.6 mJ m^{-2}, thus voltage-modulation of DMI is also an important consideration when utilizing voltage-controlled systems as it can potentially destabilize and annihilate the skyrmions[53,54].

Note that the increase in skyrmion diameter with D here is only applicable to IDMI skyrmions, where they are stabilized by dipolar interaction and perpendicular magnetic anisotropy[55,56]. An opposite trend in skyrmion diameter will be observed for BDMI skyrmions where they are primarily stabilized by the competition between the ferromagnetic exchange interaction and BDMI[31,57].

7.6 Skyrmion velocity field in a bilayer structure

This section analyzes the dynamics of separated SAF skyrmion pair based on the analytically derived $\vec{F}_{BCF}$ when MAG is removed. Applying $\vec{F}_{BCF}$ to the Thiele's equation given in Eq. 7.3.1, the velocity field of a skyrmion due to the $\vec{F}_{BCF}$ exerted by the other skyrmion can be acquired. The trajectory of a skyrmion in the proximity of another pinned skyrmion follows a spiral configuration that terminates when the skyrmions lie directly over one another. Figure 7.6 shows a skyrmion's velocity field due to $\vec{F}_{BCF}$ by a pinned skyrmion in the other layer. The result shown in Fig. 7.6 can be qualitatively derived from the direction of the force which acts radially towards the centre of the skyrmion and θ_{sk} given in Eq. 7.3.4, which describes the relative angle between the driving force and velocity. The colour in Fig. 7.6 represents the $\left|\vec{F}_{BCF}\right|$ between the skyrmions as shown previously in Fig. 7.2.

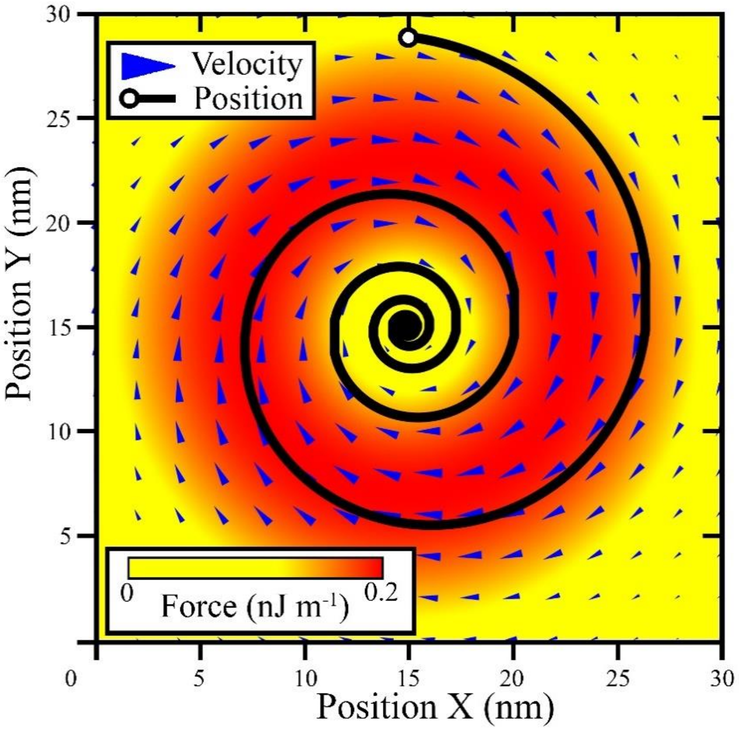

Figure 7.6| Skyrmion velocity profile under a bilayer coupling force with another skyrmion pinned at the center of the spiral trajectory. The trajectory begins at the top, spirals towards the center of the pinned skyrmion, and remains stationary when both skyrmions are overlapped.

In the bilayer structure, the trajectory due to $\vec{F}_{BCF}$ between a freely moving skyrmion (skyrmion 1) on one layer and another skyrmion (skyrmion 2) on the other layer, which has different material parameters are shown in Fig. 7.7. From Eq. 7.3.5, skyrmion velocity is material parameter-dependent, and asymmetry in these parameters can result in spiralling trajectories. The cases where the difference in the material parameters results in the ratio of the velocity of skyrmion 1 to skyrmion 2 to be 0.2, 0.8, and 1.0 are presented in Fig. 7.7. These trajectories were derived analytically using the Thiele's equation, and not numerically evaluated by the change in material parameters. When both skyrmions have identical material parameters (1.0), the two skyrmions converge towards each other in a straight trajectory. Increasingly asymmetric or massive skyrmion 2 for the cases of 0.8 and 0.2 multiple results in the trajectory becoming increasingly spiral and centred around skyrmion 2. At the limit where skyrmion 2 is stationary, the trajectory is shown in Fig. 7.6, where skyrmion 2 does not move while skyrmion 1 spirals towards the centre of skyrmion 2 to the point where they overlap.

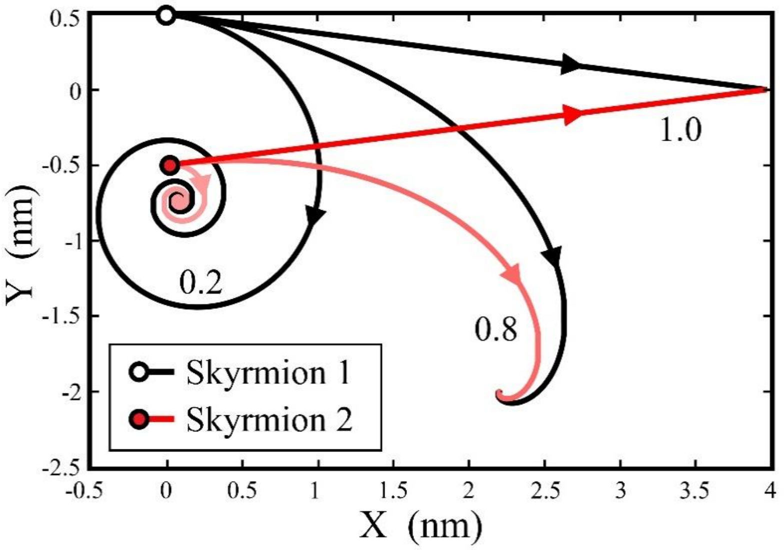

Figure 7.7| Trajectory of two skyrmions in a bilayer structure due to bilayer coupling force where skyrmions 1 and 2 have material parameter discrepancy by the ratio of 1.0, 0.8, and 0.2. The difference in material parameters results in different drift velocities and trajectories that are straight or spiralling motion.

7.7 Discussion on magnetic anisotropy gradient transport and skyrmion Hall effect mitigation

Beyond the search for skyrmion-stable SAF systems, several other considerations must be considered. A continuous electric field gradient can be formed by adopting the multiplexed 3-level racetrack design with high, average, and low voltage stepwise gradients presented by Wang *et al*. and Liu *et al*.[16,20]. In this design, the dimensions of each repeating unit of K_u gradient along the racetrack are dependent on the skyrmion size, maximum K_u variation, and the size of the electrodes. The electrode width is optimized at approximately the diameter of the skyrmion to achieve optimal propagation efficiency[20]. The maximum K_u gradient applicable is then dependent on the maximum K_u variation of the system. In addition, DMI and RKKY interactions can both be tuned by external voltages. From the recent work by

Suwardy *et al.*, which showed a considerable DMI variation of 1.3 mJ m^{-2}, the voltage-induced DMI can significantly affect the skyrmion stability[54]. Hence, the maximum voltage and the corresponding MAG which can be applied may be limited.

The bilayer skyrmion pair can also be driven using a MAG in only one FM layer instead of both FM layers. As one skyrmion experiences a K_u gradient and is driven towards the region of lower K_u, the skyrmion in the other layer will be driven in the same direction due to their exchange coupling. We investigated this propagation at K_u = 0.80 MJ/m^3. A comparison in the velocity of the monolayer and bilayer driven system is given in Fig. 7.8, which shows the magnitude of skyrmion velocity decreasing by half when it is driven in only one of the FM layers.

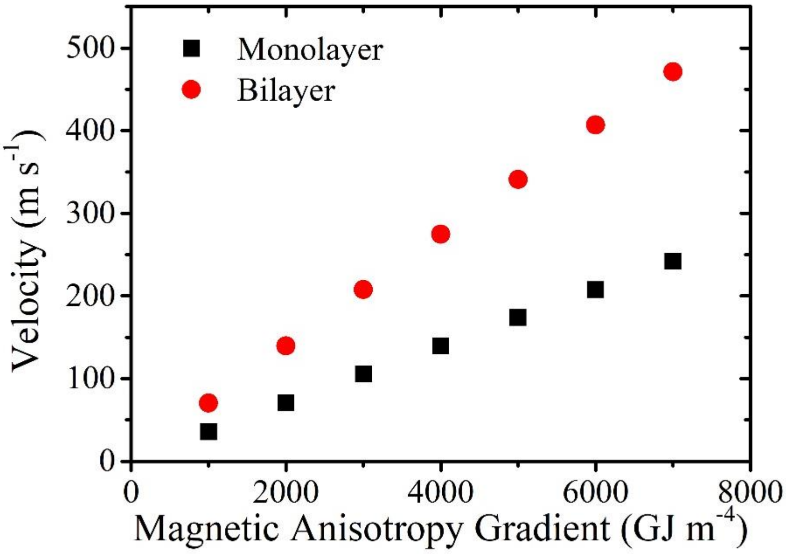

Figure 7.8| Velocity of skyrmion driven by a monolayer and bilayer anisotropy gradient in a synthetic antiferromagnet.

In the monolayer gradient driven skyrmion, the indirectly-driven skyrmion without the anisotropy gradient trails slightly behind the other MAG-driven skyrmion and continues to follow the trajectory given in Fig. 7.1(b). The indirectly-driven skyrmion only trails the MAG-driven skyrmion by a distance much smaller than their separation due to the large skyrmion Hall angle. The indirectly-driven skyrmion has its driving force along the track, previously generated by $\vec{F}_{VGF}$ compensated by $\vec{F}_{BCF}$ that now acts at an angle as opposed to acting only in the transverse direction. The driven skyrmion have this longitudinal force competing against the $\vec{F}_{VGF}$. At equilibrium, both skyrmions will have half the longitudinal force $\vec{F}_{VGF}$ and separation distance of that in the bilayer gradient driven system, supporting the observed decrease in velocity by half.

The MAG propagation technique is also inherently stable against perturbation or variations from dissipation. While voltage-driven techniques are already significantly less dissipative than current-driven techniques, high velocity operation of the MAG can still result in dissipation issues. Elevated temperatures can affect skyrmion size but the MAG system confines the skyrmions to pre-determined spacing, thus not affecting its performance. The sawtooth potential also restrains the skyrmions from Brownian motion beyond its intended site[58,59]. The change in skyrmion velocity due to heat can also be compensated by the MAG operating velocity.

Besides using a system of SAF skyrmions to overcome the skyrmion Hall effect, other proposed approaches include using confining potentials or antiferromagnetic skyrmions. The boundary repulsive force can be enhanced to protect skyrmions from annihilation using boundary material modifications like magnetic anisotropy, DMI strength, or ferromagnetic layer thickness[21,49,60]. However, the enhanced boundary repulsive force still necessitates the skyrmions to travel along the track edge where the repulsive force act. For SAF or antiferromagnetic skyrmions that rely on skyrmion-skyrmion attraction maintain skyrmion displacements close to the centre of the track. Even though antiferromagnetic skyrmions are advantageous due to the lower magnetic damping and potentially higher skyrmion speeds, its experimental exploration remains limited[36,47,61,62]. SAF skyrmions are currently more favourable due to the possibility to adapt from existing ferromagnetic multilayer skyrmion structures[36,47].

7.8 Conclusion

The numerical results from our work on magnetic anisotropy gradient-driven skyrmions in an antiferromagnetically coupled bilayer structure have shown a significant superiority over the monolayer structure due to the restoring force between the skyrmions, which arises from interlayer antiferromagnetic exchange interaction. This restoring force confines the skyrmions to travel along the proximity of the wire centre and prevent edge annihilation. For the range of separation between the coupled skyrmions of less than half its radius, the restoring force resembles a harmonic oscillator which motivates the possibility of nano-oscillator and other applications. The driving force generated by the magnetic anisotropy gradient is dependent on skyrmion size, which can be maximized with a low magnetic anisotropy strength or high saturation magnetization. Skyrmion velocity can also be maximized by utilizing its inverse dependence on the Gilbert damping parameter. We derive the velocity field of a skyrmion from our model of the restoring force, which gave a spiralling configuration and explored the trajectory of two skyrmions with discrepancies in material parameters that returned straight or spiralling trajectories. The dynamics of asymmetric synthetic antiferromagnetically coupled skyrmions with material parameter discrepancies can be investigated further in the future.

References

1 S. Woo, K. Litzius, B. Krüger, *et al.* Observation of room-temperature magnetic skyrmions and their current-driven dynamics in ultrathin metallic ferromagnets. *Nat. Mater.* **15**, 501-506, doi:10.1038/nmat4593 (2016).

2 A. Hrabec, J. Sampaio, M. Belmeguenai, *et al.* Current-induced skyrmion generation and dynamics in symmetric bilayers. *Nat. Commun.* **8**, 15765, doi:10.1038/ncomms15765 (2017).

3 A. Yamaguchi, S. Nasu, H. Tanigawa, *et al.* Effect of Joule heating in current-driven domain wall motion. *Appl. Phys. Lett.* **86**, 012511, doi:10.1063/1.1847714 (2005).

4 C. Schütte, J. Iwasaki, A. Rosch, *et al.* Inertia, diffusion, and dynamics of a driven skyrmion. *Phys. Rev. B* **90**, 174434, doi:10.1103/PhysRevB.90.174434 (2014).

5 R. Tomasello, K. Y. Guslienko, M. Ricci, *et al.* Origin of temperature and field dependence of magnetic skyrmion size in ultrathin nanodots. *Phys. Rev. B* **97**, 060402, doi:10.1103/PhysRevB.97.060402 (2018).

6 K. Everschor, M. Garst, B. Binz, *et al.* Rotating skyrmion lattices by spin torques and field or temperature gradients. *Phys. Rev. B* **86**, 054432, doi:10.1103/PhysRevB.86.054432 (2012).

7 C. Wang, D. Xiao, X. Chen, *et al.* Manipulating and trapping skyrmions by magnetic field gradients. *New J. Phys.* **19**, 083008, doi:10.1088/1367-2630/aa7812 (2017).

8 S. L. Zhang, W. W. Wang, D. M. Burn, *et al.* Manipulation of skyrmion motion by magnetic field gradients. *Nat. Commun.* **9**, 2115, doi:10.1038/s41467-018-04563-4 (2018).

9 Y.-H. Liu, Y.-Q. Li & J. H. Han. Skyrmion dynamics in multiferroic insulators. *Phys. Rev. B* **87**, 100402, doi:10.1103/PhysRevB.87.100402 (2013).

10 L. Kong & J. Zang. Dynamics of an Insulating Skyrmion under a Temperature Gradient. *Phys. Rev. Lett.* **111**, 067203, doi:10.1103/PhysRevLett.111.067203 (2013).

11 S.-Z. Lin, C. D. Batista, C. Reichhardt, *et al.* ac Current Generation in Chiral Magnetic Insulators and Skyrmion Motion induced by the Spin Seebeck Effect. *Phys. Rev. Lett.* **112**, 187203, doi:10.1103/PhysRevLett.112.187203 (2014).

12 M. Mochizuki, X. Z. Yu, S. Seki, *et al.* Thermally driven ratchet motion of a skyrmion microcrystal and topological magnon Hall effect. *Nat. Mater.* **13**, 241-246, doi:10.1038/nmat3862 (2014).

13 J. Iwasaki, A. J. Beekman & N. Nagaosa. Theory of magnon-skyrmion scattering in chiral magnets. *Phys. Rev. B* **89**, 064412, doi:10.1103/PhysRevB.89.064412 (2014).

14 C. Schütte & M. Garst. Magnon-skyrmion scattering in chiral magnets. *Phys. Rev. B* **90**, 094423, doi:10.1103/PhysRevB.90.094423 (2014).

15 X. Zhang, M. Ezawa, D. Xiao, *et al.* All-magnetic control of skyrmions in nanowires by a spin wave. *Nanotech.* **26**, 225701, doi:10.1088/0957-4484/26/22/225701 (2015).

16 X. Wang, W. L. Gan, J. C. Martinez, *et al.* Efficient skyrmion transport mediated by a voltage controlled magnetic anisotropy gradient. *Nanoscale* **10**, 733-740, doi:10.1039/C7NR06482A (2018).

17 R. Tomasello, S. Komineas, G. Siracusano, *et al.* Chiral skyrmions in an anisotropy gradient. *Phys. Rev. B* **98**, 024421, doi:10.1103/PhysRevB.98.024421 (2018).

18 H. Xia, C. Song, C. Jin, *et al.* Skyrmion motion driven by the gradient of voltage-controlled magnetic anisotropy. *J. Magn. Magn. Mater.* **458**, 57-61, doi:10.1016/j.jmmm.2018.02.090 (2018).

19 L. Shen, J. Xia, G. Zhao, *et al.* Dynamics of the antiferromagnetic skyrmion induced by a magnetic anisotropy gradient. *Phys. Rev. B* **98**, 134448, doi:10.1103/PhysRevB.98.134448 (2018).

20 Y. Liu, N. Lei, C. Wang, *et al.* Voltage-Driven High-Speed Skyrmion Motion in a Skyrmion-Shift Device. *Phys. Rev. Appl.* **11**, 014004, doi:10.1103/PhysRevApplied.11.014004 (2019).

21 H. T. Fook, W. L. Gan, I. Purnama, *et al.* Mitigation of Magnus Force in Current-Induced Skyrmion Dynamics. *IEEE Trans. Magn.* **51**, 1-4, doi:10.1109/TMAG.2015.2433677 (2015).

22 P. Upadhyaya, G. Yu, P. K. Amiri, *et al.* Electric-field guiding of magnetic skyrmions. *Phys. Rev. B* **92**, 134411, doi:10.1103/PhysRevB.92.134411 (2015).

23 P. Lai, G. P. Zhao, F. J. Morvan, *et al.* Motion of Skyrmions in Well-Separated Two-Lane Racetracks. *SPIN* **07**, 1740006, doi:10.1142/S2010324717400069 (2017).

24 M. Weisheit, S. Fähler, A. Marty, *et al.* Electric Field-Induced Modification of Magnetism in Thin-Film Ferromagnets. *Science* **315**, 349, doi:10.1126/science.1136629 (2007).

25 C.-G. Duan, J. P. Velev, R. F. Sabirianov, *et al.* Surface Magnetoelectric Effect in Ferromagnetic Metal Films. *Phys. Rev. Lett.* **101**, 137201, doi:10.1103/PhysRevLett.101.137201 (2008).

26 T. Maruyama, Y. Shiota, T. Nozaki, *et al.* Large voltage-induced magnetic anisotropy change in a few atomic layers of iron. *Nat. Nanotech.* **4**, 158, doi:10.1038/nnano.2008.406 (2009).

27 X. Zhang, Y. Zhou & M. Ezawa. Magnetic bilayer-skyrmions without skyrmion Hall effect. *Nat. Commun.* **7**, 10293, doi:10.1038/ncomms10293 (2016).

28 X. Zhang, M. Ezawa & Y. Zhou. Thermally stable magnetic skyrmions in multilayer synthetic antiferromagnetic racetracks. *Phys. Rev. B* **94**, 064406, doi:10.1103/PhysRevB.94.064406 (2016).

29 W. Koshibae & N. Nagaosa. Theory of skyrmions in bilayer systems. *Sci. Rep.* **7**, 42645, doi:10.1038/srep42645 (2017).

30 W. L. Gan, S. Krishnia & W. S. Lew. Efficient in-line skyrmion injection method for synthetic antiferromagnetic systems. *New J. Phys.* **20**, 013029, doi:10.1088/1367-2630/aaa113 (2018).

31 J. Sampaio, V. Cros, S. Rohart, *et al.* Nucleation, stability and current-induced motion of isolated magnetic skyrmions in nanostructures. *Nat. Nanotech.* **8**, 839-844, doi:10.1038/nnano.2013.210 (2013).

32 P. J. Metaxas, J. P. Jamet, A. Mougin, *et al.* Creep and Flow Regimes of Magnetic Domain-Wall Motion in Ultrathin Pt/Co/Pt Films with Perpendicular Anisotropy. *Phys. Rev. Lett.* **99**, 217208, doi:10.1103/PhysRevLett.99.217208 (2007).

33 P. J. H. Bloemen, H. W. van Kesteren, H. J. M. Swagten, *et al.* Oscillatory interlayer exchange coupling in Co/Ru multilayers and bilayers. *Phys. Rev. B* **50**, 13505-13514, doi:10.1103/PhysRevB.50.13505 (1994).

34 S. S. P. Parkin. Systematic variation of the strength and oscillation period of indirect magnetic exchange coupling through the 3d, 4d, and 5d transition metals. *Phys. Rev. Lett.* **67**, 3598-3601, doi:10.1103/PhysRevLett.67.3598 (1991).

35 S. S. P. Parkin, N. More & K. P. Roche. Oscillations in exchange coupling and magnetoresistance in metallic superlattice structures: Co/Ru, Co/Cr, and Fe/Cr. *Phys. Rev. Lett.* **64**, 2304-2307, doi:10.1103/PhysRevLett.64.2304 (1990).

36 W. Legrand, D. Maccariello, F. Ajejas, *et al.* Room-temperature stabilization of antiferromagnetic skyrmions in synthetic antiferromagnets. *Nat. Mater.* **19**, 34-42, doi:10.1038/s41563-019-0468-3 (2020).

37 A. A. Thiele. Steady-State Motion of Magnetic Domains. *Phys. Rev. Lett.* **30**, 230-233, doi:10.1103/PhysRevLett.30.230 (1973).

38 A. Thiaville, Y. Nakatani, J. Miltat, *et al.* Micromagnetic understanding of current-driven domain wall motion in patterned nanowires. *Europhys. Lett.* **69**, 990-996, doi:10.1209/epl/i2004-10452-6 (2005).

39 J. Iwasaki, M. Mochizuki & N. Nagaosa. Universal current-velocity relation of skyrmion motion in chiral magnets. *Nat. Commun.* **4**, 1463, doi:10.1038/ncomms2442 (2013).

40 N. Nagaosa & Y. Tokura. Topological properties and dynamics of magnetic skyrmions. *Nat. Nanotech.* **8**, 899-911, doi:10.1038/nnano.2013.243 (2013).

41 W. Jiang, X. Zhang, G. Yu, *et al.* Direct observation of the skyrmion Hall effect. *Nat. Phys.* **13**, 162, doi:10.1038/nphys3883 (2016).

42 C. C. I. Ang, W. Gan & W. S. Lew. Bilayer skyrmion dynamics on a magnetic anisotropy gradient. *New J. Phys.* **21**, 043006, doi:10.1088/1367-2630/ab1171 (2019).

43 K. Litzius, J. Leliaert, P. Bassirian, *et al.* The role of temperature and drive current in skyrmion dynamics. *Nat. Electron* **3**, 30-36, doi:10.1038/s41928-019-0359-2 (2020).

44 R. Juge, S.-G. Je, D. d. S. Chaves, *et al.* Current-Driven Skyrmion Dynamics and Drive-Dependent Skyrmion Hall Effect in an Ultrathin Film. *Phys. Rev. Appl.* **12**, 044007, doi:10.1103/PhysRevApplied.12.044007 (2019).

45 K. Litzius, I. Lemesh, B. Krüger, *et al.* Skyrmion Hall effect revealed by direct time-resolved X-ray microscopy. *Nat. Phys.* **13**, 170, doi:10.1038/nphys4000 (2016).

46 C. Reichhardt & C. J. Olson Reichhardt. Noise fluctuations and drive dependence of the skyrmion Hall effect in disordered systems. *New J. Phys.* **18**, 095005, doi:10.1088/1367-2630/18/9/095005 (2016).

47 T. Dohi, S. DuttaGupta, S. Fukami, *et al.* Formation and current-induced motion of synthetic antiferromagnetic skyrmion bubbles. *Nat. Commun.* **10**, 5153, doi:10.1038/s41467-019-13182-6 (2019).

48 M. J. Donahue & D. G. Porter. Exchange energy formulations for 3D micromagnetics. *Phys. B (Amsterdam, Neth.)* **343**, 177-183, doi:10.1016/j.physb.2003.08.090 (2004).

49 I. Purnama, W. L. Gan, D. W. Wong, *et al.* Guided current-induced skyrmion motion in 1D potential well. *Sci. Rep.* **5**, 10620, doi:10.1038/srep10620 (2015).

50 P. Lai, G. P. Zhao, H. Tang, *et al.* An Improved Racetrack Structure for Transporting a Skyrmion. *Sci. Rep.* **7**, 45330, doi:10.1038/srep45330 (2017).

51 N. Ran, G. P. Zhao, H. Tang, *et al.* The influence of the edge effect on the skyrmion generation in a magnetic nanotrack. *AIP Adv.* **7**, 025105, doi:10.1063/1.4976726 (2017).

52 T. Nozaki, A. Kozioł-Rachwał, W. Skowroński, *et al.* Large Voltage-Induced Changes in the Perpendicular Magnetic Anisotropy of an MgO-Based Tunnel Junction with an Ultrathin Fe Layer. *Phys. Rev. Appl.* **5**, 044006, doi:10.1103/PhysRevApplied.5.044006 (2016).

53 K. Nawaoka, S. Miwa, Y. Shiota, *et al.* Voltage induction of interfacial Dzyaloshinskii–Moriya interaction in Au/Fe/MgO artificial multilayer. *Appl. Phys. Express* **8**, 063004, doi:10.7567/apex.8.063004 (2015).

54 J. Suwardy, K. Nawaoka, J. Cho, *et al.* Voltage-controlled magnetic anisotropy and voltage-induced Dzyaloshinskii-Moriya interaction change at the epitaxial Fe(001)/MgO(001) interface engineered by Co and Pd atomic-layer insertion. *Phys. Rev. B* **98**, 144432, doi:10.1103/PhysRevB.98.144432 (2018).

55 X. S. Wang, H. Y. Yuan & X. R. Wang. A theory on skyrmion size. *Commun. Phys.* **1**, 31, doi:10.1038/s42005-018-0029-0 (2018).

56 A. Bernand-Mantel, C. B. Muratov & T. M. Simon. Unraveling the role of dipolar versus Dzyaloshinskii-Moriya interactions in stabilizing compact magnetic skyrmions. *Phys. Rev. B* **101**, 045416, doi:10.1103/PhysRevB.101.045416 (2020).

57 A. Fert, V. Cros & J. Sampaio. Skyrmions on the track. *Nat. Nanotech.* **8**, 152-156, doi:10.1038/nnano.2013.29 (2013).

58 L. Zhao, Z. Wang, X. Zhang, *et al.* Topology-Dependent Brownian Gyromotion of a Single Skyrmion. *Phys. Rev. Lett.* **125**, 027206, doi:10.1103/PhysRevLett.125.027206 (2020).

59 T. Nozaki, Y. Jibiki, M. Goto, *et al.* Brownian motion of skyrmion bubbles and its control by voltage applications. *Appl. Phys. Lett.* **114**, 012402, doi:10.1063/1.5070101 (2019).

60 S. Bhatti & S. N. Piramanayagam. Effect of Dzyaloshinskii–Moriya Interaction Energy Confinement on Current-Driven Dynamics of Skyrmions. *physica status solidi (RRL) – Rapid Research Letters* **13**, 1900090, doi:10.1002/pssr.201900090 (2019).

61 L. Caretta, M. Mann, F. Büttner, *et al.* Fast current-driven domain walls and small skyrmions in a compensated ferrimagnet. *Nat. Nanotech.* **13**, 1154-1160, doi:10.1038/s41565-018-0255-3 (2018).

62 S. Woo, K. M. Song, X. Zhang, *et al.* Current-driven dynamics and inhibition of the skyrmion Hall effect of ferrimagnetic skyrmions in GdFeCo films. *Nat. Commun.* **9**, 959, doi:10.1038/s41467-018-03378-7 (2018).

Chapter 8 Conclusion and Future Works

8.1 Conclusion

This thesis presents three main skyrmion works covering critical aspects of skyrmion research for technological applications, including a skyrmion characterization technique, skyrmion nucleation and deletion skyrmion propagation technique, in Chapters 5, 6, and 7, respectively.

In Chapter 5, the FORC technique that reveals irreversible transitions from magnetic field sweeps was applied on the skyrmion-hosting magnetic multilayer, $[Pt/Co/Fe/Ir]_2$. Previous works have reported FORC distribution features analysis based on the reversal field to obtain optimal zero-field skyrmion density[1,2]. Still, analysis based on the sweeping field was yet to be elucidated. Using magneto-optical Kerr imaging, we found the FORC distribution peak along the sweeping field corresponds to the convergence of domain-domain separation towards terminal separation. By extending the FORC analysis across both reversal and sweeping fields, the abstract FORC phase diagram can now be interpreted intuitively. To verify the consistency of this analysis, the FORC was applied across different skyrmion phases ranging from densely packed skyrmion lattice to metastable isolated skyrmions, tuned by temperature modulation. A model to characterize skyrmion phases was then developed based on the apparent trend observed between the FORC distribution and skyrmion density associated with the skyrmion phases.

In Chapter 6, current-induced skyrmion excitation was investigated in the same magnetic multilayer as the previous chapter, $[Pt/Co/Fe/Ir]_{2.}$ Current-induced skyrmion nucleation using dedicated structures[3-6] and uniform track[7-9] had both been demonstrated in other works. As current density is reduced, one would expect less skyrmion nucleation, but skyrmion annihilation was observed instead. Using magneto-optical Kerr imaging, the low current skyrmion annihilation process was driven by a skyrmion-to-stripe transformation due to pinning. The expanding stripe domains crowded out and annihilated skyrmions along the track before decaying back into skyrmion, leaving a sparse skyrmion density. Thus, skyrmion density can be modulated by current density regardless of current polarity. The effectiveness of current-induced annihilation is determined by the balance between skyrmion and stripe stability tuned by the perpendicular field. This work introduces a skyrmion density technique and highlights the need for a minimum current density to avoid unintended skyrmion deletion in skyrmion applications.

In Chapter 7, a voltage-controlled skyrmion propagation technique with significantly higher energy efficiency than conventional current-based methods was investigated numerically. Besides energy efficiency, Joule heating of the track is undesirable for reliable propagation[10-12]. In this propagation system, magnetic skyrmions are driven in tandem with a moving magnetic anisotropy gradient generated using VCMA. SAF skyrmions with suppressed skyrmion Hall effect was investigated instead of FM skyrmions. An analytical model of the SAF skyrmion coupling was developed that accurately describes their dynamics on the magnetic anisotropy gradient. Extending the model to a pair of unidentical or pinned skyrmions, the SAF skyrmion coupling can result in linear or spiralling trajectories. SAF skyrmions propagation by only driving one of the skyrmions by the anisotropy gradient was also shown to be possible, but at half the velocity.

8.2 Future Works

In this section, three future works that extend from the work presented in this thesis are proposed. The field of magnetic skyrmions remains wide with many aspects, including skyrmion stability, reliable nucleation, precise control, and accurate detection with room for investigation and improvement. Given the tremendous progress in recent years, skyrmionic technologies are close within grasp.

8.2.1 Quantitative model for first-order reversal curve distribution of skyrmions in magnetic multilayers

In Chapter 5, we had established an intuitive interpretation of the FORC diagram based on the convergence and divergence of domain-domain separation from their terminal separation. Following the interpretation, the skyrmion phase can be derived based on one of the FORC features, the proximity of the upper peak's reversal field to its sweeping field, or equivalently how close the upper peak is to the edge of the FORC diagram's diagonal. Our work produced a phenomenological model from the experimental data of the FORC peak's reversal and sweeping fields presented in Fig. 5.7. The model is helpful for qualitative determination of the skyrmion phase but is currently limited in deriving a quantitative measure of skyrmion stability that closely relates to the skyrmion phase. We had previously identified that $\kappa = 1$ lies within the temperature range investigated and is likely to lie close to the temperature at which the reversal and sweeping fields of the upper peak intersect. To develop a quantitative model, the experiment first requires an extension to determine their temperature-dependent material properties, including DMI strength, exchange stiffness, and effective perpendicular magnetic anisotropy. Next, numerical replication of the experimental observations can further examine the quantitative relation between the peak field difference of the upper peak and κ. The extension of this model can be highly useful for skyrmionic studies as it bypasses many complex characterization techniques for various material properties to directly obtain κ that is critical for skyrmion stability.

8.2.2 Experimental realization of skyrmion-based artificial neuron

The interest in neuromorphic computing has been blooming in recent years, including the field of magnetic skyrmions, with many proposals for artificial skyrmion synapses[13-18] and neurons[19-22]. While there are plenty of proposals demonstrated numerically, the number of experimental work is still limited[6]. From work presented in Chapter 6 on current-induced skyrmion nucleation and annihilation, the temporal behaviour of the Hall resistance post current injection offers potential application in neuromorphic computing, specifically an artificial leaky-integrate-fire neuron. An LIF neuron requires two main functions: Signal integration or summation and a leaky or decaying potential over time.

For the case of low current injection that leads to the skyrmion-stripe transformation and annihilation, the Hall resistance increases up to a peak before decaying back to the equilibrium, as shown in Fig. 6.1(b). The peak Hall resistance magnitude is pulse duration dependent, as shown in Fig. 6.3(a), suggesting the property of integration where the effect of several short pulses can be additive to generate larger Hall resistance. The leaky property is represented in the gradual decay in Hall resistance back to equilibrium. For high current injection, similar integration property in the decrease in Hall resistance is expected while not explicitly shown, and the gradual decay back to equilibrium also occurs. Thus, both cases are possible to fulfil the required functions. The seconds-long time scale of the Hall resistance transformations in this work was tuned to match the Kerr imaging's exposure time requirements and examine the transformation. The timescale can be significantly reduced by adjusting the perpendicular magnetic field and temperature modulation. Artificial pinning sites can also be intentionally fabricated to improve the reliability of operation.

The operation of the artificial skyrmion is illustrated in Fig. 8.1. Current-induced skyrmion annihilation drives the increment in Hall voltage signal, while the spontaneous nucleation applies a constant decay of the Hall voltage back to equilibrium. The maximum Hall voltage reached is determined by the proximity and duration of the current pulses, a critical Hall voltage can be set as the threshold for the neuron to fire or propagate a signal to the next neuron.

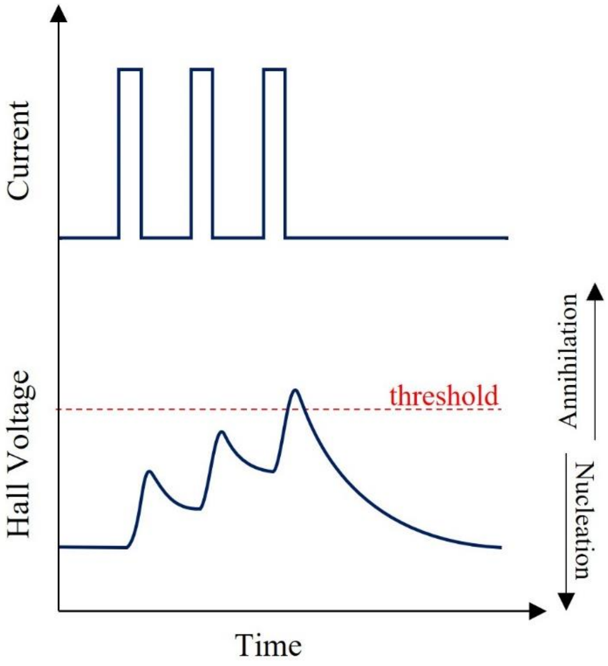

Figure 8.1| Illustration of artificial skyrmion neuron operation driven by current pulses over time.

8.2.3 Experimental demonstration of voltage-driven skyrmion propagation

VCMA has been at the centre of attention as a flexible tool for application in skyrmionic devices as magnetic anisotropy can affect skyrmion stability[23-25], act as barriers of motion[26,27], and drive motion of skyrmions[28-30]. A magnetic anisotropy gradient drives magnetic skyrmions towards the region of lower magnetic anisotropy[31,32], but a smooth and variable anisotropy gradient is challenging to be implemented in practical devices. A non-uniform wire with smooth gradient and electric fields was demonstrated experimentally by Ma *et al*. However, the gradient is fixed, and the range of motion will be limited within the short segment, not applicable for long wires.

The most practical implementation of the proposed voltage-controlled skyrmion propagation by translating magnetic anisotropy gradients presented in Chapter 7 is by discrete magnetic anisotropy steps, as illustrated in Fig. 8.2[29]. Series of discrete electrodes with widths comparable to the skyrmion diameter are fabricated along a uniform wire. The electrodes are divided into sets of threes with a periodic zero, medium, and high voltages to form the corresponding stepwise magnetic anisotropy gradient. With the discrete electrodes, the voltages can be adjusted to drive the magnetic skyrmions to and fro across the full nanowire. Materials of interest for the experiment are the magnetic multilayer with oxide interfaces that exhibit VCMA like Pt/Co/MgO[33,34], W/CoFeB/MgO[35], Pt/GdCo/TaOx[36], and Ta/CoFeB/TaOx[3,37]. The skyrmion diameter in these materials ranges from hundreds to thousands of nanometers. Thus, the fabrication of the discrete electrodes can be done reliably without facing significant challenges like resolution and shorting. The experimental demonstration will be a significant step towards even more energy-efficient skyrmionic devices. Even more complex and precise control of magnetic skyrmions in a two-dimensional plane using these discrete electrodes can be further ventured beyond this work.

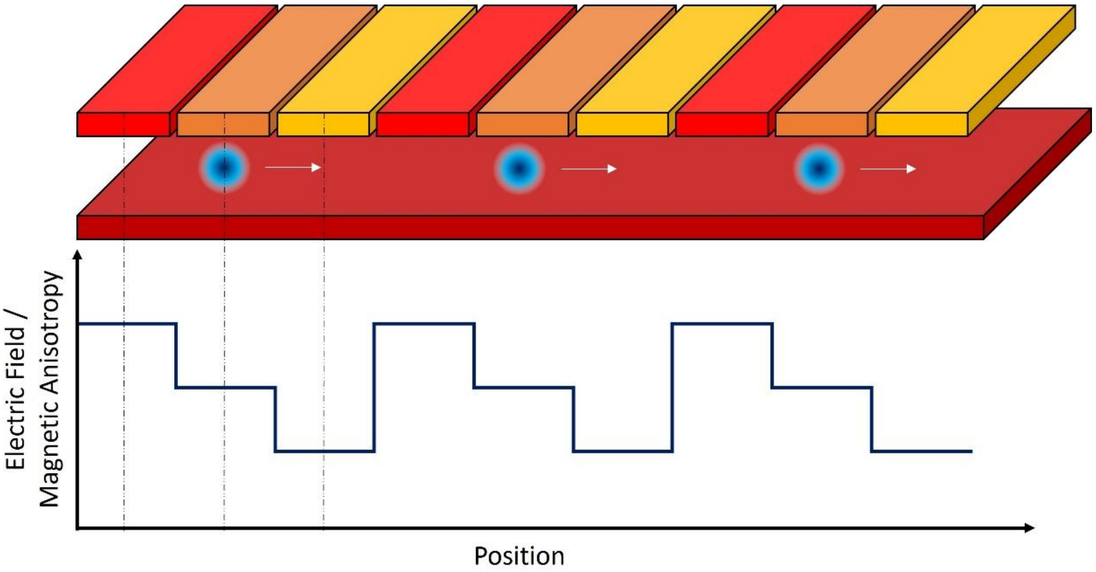

Figure 8.2| Voltage-controlled skyrmion propagation scheme using stepwise magnetic anisotropy produced by discrete electrode along the wire.

References

1 N. K. Duong, M. Raju, A. P. Petrović, *et al.* Stabilizing zero-field skyrmions in Ir/Fe/Co/Pt thin film multilayers by magnetic history control. *Appl. Phys. Lett.* **114**, 072401, doi:10.1063/1.5080713 (2019).

2 M. Ma, C. C. I. Ang, Y. Li, *et al.* Enhancement of zero-field skyrmion density in $[Pt/Co/Fe/Ir]_2$ multilayers at room temperature by the first-order reversal curve. *J. Appl. Phys.* **127**, 223901, doi:10.1063/5.0004432 (2020).

3 W. Jiang, P. Upadhyaya, W. Zhang, *et al.* Blowing magnetic skyrmion bubbles. *Science* **349**, 283, doi:10.1126/science.aaa1442 (2015).

4 A. Hrabec, J. Sampaio, M. Belmeguenai, *et al.* Current-induced skyrmion generation and dynamics in symmetric bilayers. *Nat. Commun.* **8**, 15765, doi:10.1038/ncomms15765 (2017).

5 S. Finizio, K. Zeissler, S. Wintz, *et al.* Deterministic Field-Free Skyrmion Nucleation at a Nanoengineered Injector Device. *Nano Lett.* **19**, 7246-7255, doi:10.1021/acs.nanolett.9b02840 (2019).

6 K. M. Song, J.-S. Jeong, B. Pan, *et al.* Skyrmion-based artificial synapses for neuromorphic computing. *Nat. Electron,* doi:10.1038/s41928-020-0385-0 (2020).

7 K. Everschor-Sitte, M. Sitte, T. Valet, *et al.* Skyrmion production on demand by homogeneous DC currents. *New J. Phys.* **19**, 092001, doi:10.1088/1367-2630/aa8569 (2017).

8 F. Büttner, I. Lemesh, M. Schneider, *et al.* Field-free deterministic ultrafast creation of magnetic skyrmions by spin–orbit torques. *Nat. Nanotech.* **12**, 1040-1044, doi:10.1038/nnano.2017.178 (2017).

9 S. Woo, K. M. Song, X. Zhang, *et al.* Deterministic creation and deletion of a single magnetic skyrmion observed by direct time-resolved X-ray microscopy. *Nat. Electron* **1**, 288-296, doi:10.1038/s41928-018-0070-8 (2018).

10 A. Yamaguchi, S. Nasu, H. Tanigawa, *et al.* Effect of Joule heating in current-driven domain wall motion. *Appl. Phys. Lett.* **86**, 012511, doi:10.1063/1.1847714 (2005).

11 C. Schütte, J. Iwasaki, A. Rosch, *et al.* Inertia, diffusion, and dynamics of a driven skyrmion. *Phys. Rev. B* **90**, 174434, doi:10.1103/PhysRevB.90.174434 (2014).

12 R. Tomasello, K. Y. Guslienko, M. Ricci, *et al.* Origin of temperature and field dependence of magnetic skyrmion size in ultrathin nanodots. *Phys. Rev. B* **97**, 060402, doi:10.1103/PhysRevB.97.060402 (2018).

13 Y. Huang, W. Kang, X. Zhang, *et al.* Magnetic skyrmion-based synaptic devices. *Nanotech.* **28**, 08LT02, doi:10.1088/1361-6528/aa5838 (2017).

14 M. Chen, A. Sengupta & K. Roy. Magnetic Skyrmion as a Spintronic Deep Learning Spiking Neuron Processor. *IEEE Trans. Magn.* **54**, 1-7, doi:10.1109/TMAG.2018.2845890 (2018).

15 U. Saxena, D. Kaushik, M. Bansal, *et al.* Low-Energy Implementation of Feed-Forward Neural Network With Back-Propagation Algorithm Using a Spin-Orbit Torque Driven Skyrmionic Device. *IEEE Trans. Magn.* **54**, 1-5, doi:10.1109/TMAG.2018.2853082 (2018).

16 T. Bhattacharya, S. Li, Y. Huang, *et al.* Low-Power (1T1N) Skyrmionic Synapses for Spiking Neuromorphic Systems. *IEEE Access* **7**, 5034-5044, doi:10.1109/ACCESS.2018.2886854 (2019).

17 S. Luo, N. Xu, Z. Guo, *et al.* Voltage-Controlled Skyrmion Memristor for Energy-Efficient Synapse Applications. *IEEE Electron Device Letters* **40**, 635-638, doi:10.1109/LED.2019.2898275 (2019).

18 B. Pan, D. Zhang, X. Zhang, *et al.* Skyrmion-Induced Memristive Magnetic Tunnel Junction for Ternary Neural Network. *IEEE Journal of the Electron Devices Society* **7**, 529-533, doi:10.1109/JEDS.2019.2913637 (2019).

19 Z. He, S. Angizi & D. Fan. Current-Induced Dynamics of Multiple Skyrmions With Domain-Wall Pair and Skyrmion-Based Majority Gate Design. *IEEE Magn. Lett.* **8**, 1-5, doi:10.1109/LMAG.2017.2689721 (2017).

20 N. Bindal, C. A. C. Ian, W. S. Lew, *et al.* Antiferromagnetic skyrmion repulsion based artificial neuron device. *Nanotech.* **32**, 215204, doi:10.1088/1361-6528/abe261 (2021).

21 S. Li, W. Kang, Y. Huang, *et al.* Magnetic skyrmion-based artificial neuron device. *Nanotech.* **28**, 31LT01, doi:10.1088/1361-6528/aa7af5 (2017).

22 X. Chen, W. Kang, D. Zhu, *et al.* A compact skyrmionic leaky–integrate–fire spiking neuron device. *Nanoscale* **10**, 6139-6146, doi:10.1039/C7NR09722K (2018).

23 M. Schott, A. Bernand-Mantel, L. Ranno, *et al.* The Skyrmion Switch: Turning Magnetic Skyrmion Bubbles on and off with an Electric Field. *Nano Lett.* **17**, 3006-3012, doi:10.1021/acs.nanolett.7b00328 (2017).

24 S. Kasai, S. Sugimoto, Y. Nakatani, *et al.* Voltage-controlled magnetic skyrmions in magnetic tunnel junctions. *Appl. Phys. Express* **12**, 083001, doi:10.7567/1882-0786/ab2baa (2019).

25 D. Bhattacharya, S. A. Razavi, H. Wu, *et al.* Creation and annihilation of non-volatile fixed magnetic skyrmions using voltage control of magnetic anisotropy. *Nat. Electron* **3**, 539-545, doi:10.1038/s41928-020-0432-x (2020).

26 X. Zhang, Y. Zhou, M. Ezawa, *et al.* Magnetic skyrmion transistor: skyrmion motion in a voltage-gated nanotrack. *Sci. Rep.* **5**, 11369, doi:10.1038/srep11369 (2015).

27 S. Luo, M. Song, X. Li, *et al.* Reconfigurable Skyrmion Logic Gates. *Nano Lett.* **18**, 1180-1184, doi:10.1021/acs.nanolett.7b04722 (2018).

28 C. Ma, X. Zhang, J. Xia, *et al.* Electric Field-Induced Creation and Directional Motion of Domain Walls and Skyrmion Bubbles. *Nano Lett.* **19**, 353-361, doi:10.1021/acs.nanolett.8b03983 (2019).

29 X. Wang, W. L. Gan, J. C. Martinez, *et al.* Efficient skyrmion transport mediated by a voltage controlled magnetic anisotropy gradient. *Nanoscale* **10**, 733-740, doi:10.1039/C7NR06482A (2018).

30 Y. Liu, N. Lei, C. Wang, *et al.* Voltage-Driven High-Speed Skyrmion Motion in a Skyrmion-Shift Device. *Phys. Rev. Appl.* **11**, 014004, doi:10.1103/PhysRevApplied.11.014004 (2019).

31 L. Shen, J. Xia, G. Zhao, *et al.* Dynamics of the antiferromagnetic skyrmion induced by a magnetic anisotropy gradient. *Phys. Rev. B* **98**, 134448, doi:10.1103/PhysRevB.98.134448 (2018).

32 R. Tomasello, S. Komineas, G. Siracusano, *et al.* Chiral skyrmions in an anisotropy gradient. *Phys. Rev. B* **98**, 024421, doi:10.1103/PhysRevB.98.024421 (2018).

33 O. Boulle, J. Vogel, H. Yang, *et al.* Room-temperature chiral magnetic skyrmions in ultrathin magnetic nanostructures. *Nat. Nanotech.* **11**, 449-454, doi:10.1038/nnano.2015.315 (2016).

34 R. Juge, S.-G. Je, D. de Souza Chaves, *et al.* Magnetic skyrmions in confined geometries: Effect of the magnetic field and the disorder. *J. Magn. Magn. Mater.* **455**, 3-8, doi:10.1016/j.jmmm.2017.10.030 (2018).

35 S. Jaiswal, K. Litzius, I. Lemesh, *et al.* Investigation of the Dzyaloshinskii-Moriya interaction and room temperature skyrmions in W/CoFeB/MgO thin films and microwires. *Appl. Phys. Lett.* **111**, 022409, doi:10.1063/1.4991360 (2017).

36 L. Caretta, M. Mann, F. Büttner, *et al.* Fast current-driven domain walls and small skyrmions in a compensated ferrimagnet. *Nat. Nanotech.* **13**, 1154-1160, doi:10.1038/s41565-018-0255-3 (2018).

37 W. Jiang, X. Zhang, G. Yu, *et al.* Direct observation of the skyrmion Hall effect. *Nat. Phys.* **13**, 162, doi:10.1038/nphys3883 (2016).

List of Publications

1. **Calvin Ching Ian Ang**, Weiliang Gan, Grayson Dao Hwee Wong & Wen Siang Lew. Temperature-modulated magnetic skyrmion phases and transformations analysis from first-order reversal curve study. Physical Review B 103, 144409 (2021); doi:10.1103/PhysRevB.103.144409

2. **Calvin Ching Ian Ang**, Weiliang Gan, Grayson Dao Hwee Wong & Wen Siang Lew. Electrical Control of Skyrmion Density via Skyrmion-Stripe Transformation. Physical Review Applied 14, 054048 (2021); doi:10.1103/PhysRevApplied.14.054048

3. **Calvin Ching Ian Ang**, Weiliang Gan, Grayson Dao Hwee Wong & Wen Siang Lew. Bilayer skyrmion dynamics on a magnetic anisotropy gradient. New Journal of Physics 21, 043006 (2019); doi:10.1088/1367-2630/ab1171

4. Grayson Dao Hwee Wong, Weiliang Gan, **Calvin Ching Ian Ang**, Wai Cheung Law, Zhan Xu, Feng Xu, Chim Seng Seet, Wen Siang Lew. Reversible strain-induced spin-orbit torque on flexible substrate by mild annealing. Applied Physics Letters, 119, 042402 (2021); doi:10.1063/5.0056995

5. Grayson Dao Hwee Wong, Zhan Xu, Weiliang Gan, **Calvin Ching Ian Ang**, Wai Cheung Law, Jiaxuan Tang, Wen Zhang, Ping Kwan Johnny Wong, Xiaojiang Yu, Andrew Thye Shen Wee, Chim Seng Seet, Wen Siang Lew. Strain-mediated spin-orbit torque enhancement in Pt/Co on flexible substrate. ACS Nano, 15, 5, 8319 (2021); doi:10.1021/acsnano.0c09404

6. Namita Bindal, **Calvin Ching Ian Ang**, Wen Siang Lew & Brajesh Kumar Kaushik. Antiferromagnetic skyrmion repulsion based artificial neuron device. Nanotechnology 32, 215204 (2021); doi:10.1088/1361-6528/abe261

7. Mangyuan Ma, **Calvin Ching Ian Ang**, Yong Li, Zizhao Pan, Weiliang Gan, Wen Siang Lew & Fusheng Ma. Enhancement of zero-field skyrmion density in [Pt/Co/Fe/Ir]2 multilayers at room temperature by the first-order reversal curve. Journal of Applied Physics 127, 223901 (2020); doi:10.1063/5.0004432

8. Grayson Dao Hwee Wong, Wai Cheung Law, Funan Tan, Weiliang Gan, **Calvin Ching Ian Ang**, Zhan Xu, Chim Seng Seet & Wen Siang Lew. Thermal behavior of spin-current generation in Pt_xCu_{1-x} devices characterized through spin-torque ferromagnetic resonance. Scientific Reports 10, 9631 (2020); doi:10.1038/s41598-020-66762-8

9. Lixing Kang, Xuechao Yu, Xiaoxu Zhao, Qingling Ouyang, Jun Di, Manzhang Xu, Dan Tian, Weiliang Gan, **Calvin Ching Ian Ang**, Shoucong Ning, Qundong Fu, Jiadong Zhou, Rajendrannair Govindan Kutty, Ya Deng, Pin Song, Qingsheng Zeng, Stephen J Pennycook, Jun Shen, Ken-T Yong & Zheng Liu. Space-confined microwave synthesis of ternary-layered BiOCl crystals with high-performance ultraviolet photodetection. InfoMat 2, 593-600 (2020); doi:10.1002/inf2.12033

10. Tianli Jin, Funan Tan, **Calvin Ching Ian Ang**, Weiliang Gan, Jiangwei Cao, Wen Siang Lew & SN Piramanayagam. Tilted magnetisation for domain wall pinning in racetrack memory. Journal of Magnetism and Magnetic Materials 489, 1654109 (2019); doi:10.1016/j.jmmm.2019.165410

11. Funan Tan, Weiliang Gan, **Calvin Ching Ian Ang**, Grayson dao Hwee Wong, Hongxi Liu, Francis Poh & Wen Siang Lew. High velocity domain wall propagation using voltage controlled magnetic anisotropy. Scientific Reports 9, 7369 (2019); doi:10.1038/s41598-019-43843-x

12. Qi Ying Wong, Weiliang Gan, Feilong Luo, Gerard Joseph Lim, **Calvin Ching Ian Ang**, Funan Tan, Wai Cheung Law & Wen Siang Lew. In situ Kerr and harmonic measurement in determining current-induced effective fields in MgO/CoFeB/Ta. Journal of Physics D: Applied Physics 51, 115004 (2018); doi:10.1088/1361-6463/aaaedb

13. Mangyuan Ma, Ke Huang, Yong Li, Sihua Li, Qiyuan Feng, **Calvin Ching Ian Ang**; Tianli Jin, Yalin Lu, Qingyou Lu, Wen Siang Lew, Fusheng Ma, Xiao Wang. Nano-engineering the evolution of skyrmion crystal in synthetic antiferromagnets. Submitted.

List of Conferences

1. **Calvin Ching Ian Ang**, WeiLiang Gan, Grayson Dao Hwee Wong, Wen Siang Lew. Skyrmion density modulation via current-induced skyrmion-to-stripe transformation. *INTERMAG 2021, Lyon, France.*

2. **Calvin Ching Ian Ang**, Weiliang Gan, Wen Siang Lew. High speed bilayer skyrmion transport by voltage controlled magnetic anisotropy gradient. *INTERMAG 2018, Singapore.*

3. WeiLiang Gan, **Calvin Ching Ian Ang**, Xuan Wang, and Wen Siang Lew. Skyrmion ratchet for single-electrode skyrmion transport. *2019 Annual Conference on Magnetism and Magnetic Materials (MMM 2019), Las Vegas, USA.*

4. TianLi Jin, Funan Tan, **Calvin Ching Ian Ang**, WeiLiang Gan, Jiangwei Cao, Wen Siang Lew and SN Piramanayagam. Control of domain wall motion with tilted magnetization for domain wall devices. *Joint MMM-INTERMAG 2019, Washington DC, USA.*

5. Tony Hiu Tung Fook, **Calvin Ching Ian Ang**, WeiLiang Gan, Indra Purnama, and Wen Siang Lew. Skyrmion pinning dynamics in nanostructures for diode and symmetric operations. *The 20th International Conference on Magnetism 2015, Barcelona, Spain.*

6. **Calvin Ching Ian Ang**, Tony Hiu Tung Fook, WeiLiang Gan, Indra Purnama, and Wen Siang Lew. Effects of geometry on skyrmion pinning and operation symmetry. *INTERMAG 2015, Beijing, PR China.*

7. Tony Hiu Tung Fook, **Calvin Ching Ian Ang**, WeiLiang Gan, Indra Purnama, and Wen Siang Lew. Mitigation of magnus force in current-induced skyrmion dynamics *INTERMAG 2015, Beijing, PR China.*

8. WeiLiang Gan, Indra Purnama, Shawn De Wei Wong, **Calvin Ching Ian Ang**, Wen Siang Lew. High Speed Transport of 1D Skyrmion Gas. *IEEE Magnetics Symposium 2014, 50th Anniversary of IEEE Magnetics Society, Singapore.*